Experimental and Numerical Studies of Two- and Three-Phase Jets in Crossflow

by

Huan Zhang

A thesis submitted in partial fulfillment of the requirements for the degree of

Doctor of Philosophy

in

Water Resources Engineering

Department of Civil and Environmental Engineering
University of Alberta

Abstract

Multi-phase jet in crossflow (MJC) garnered significant attention across a range of applications, including artificial aeration in oceans, lakes, and rivers. As of yet, the vast majority of the MJC literature focuses on pure gas or solid injection into crossflow, and limited studies pay attention to the much more complex two-phase (e.g., injecting air-water mixture) or three-phase (e.g., injecting air-water-sand mixture) jets in crossflow. This thesis addresses existing knowledge gaps in the field of MJC by conducting fundamental studies on two-phase and three-phase jets in crossflow through a combination of laboratory experiments and numerical simulations.

Bubbly (i.e., air-water mixture) jets in crossflow have been mainly investigated based on physical experiments. To unveil more hydrodynamics of bubbly jets in crossflow, a 3-dimensional model was developed, calibrated and validated by coupling the Euler-Euler two-fluid model with unsteady Reynolds-averaged Navier Stokes (URANS) approach in OpenFOAM. The results showed that the modeled gas void fraction, bubble velocity, water jet centerline trajectory, and jet expansion agree well with the experimental data. Compared to pure water jets, bubbly jets are stretched wider in the vertical direction due to the lift of bubbles and thus dilution is larger. Interestingly, the vorticity at water jet cross-sections of bubbly jets evolves from two vertical "kidney-shapes" to two axisymmetric "thumb-up-shapes".

Although previous studies of bubbly jets in crossflow have been conducted in free-surface crossflow, relevant studies in crossflow with the top solid boundary effects (e.g., in a pipe/conduit or under ice-cover) are much scarce. A series of physical experiments were conducted to investigate the bubble characteristics for bubbly jets in pipe crossflow. The centerline gas void fraction and bubble size increase with distances after bubbles touch the top wall, mainly because

bubbles are prone to gathering to the centerline to form larger bubbles. Good agreement has been achieved between horizontal bubble velocity and the 1/7th power law for water velocity in the pipe, and a correlation was proposed for predicting bubble rise velocity. Furthermore, turbulence characteristics of bubbles (e.g., root-mean-square of bubble fluctuating velocity, bubble turbulence intensity) were investigated for the bubbly jets.

Compared to two-phase flows, gas-liquid-solid three-phase flows (GLSTPF) are inherently complex. The utilization of the Eulerian-Eulerian-Lagrangian (E-E-L) approach for modeling GLSTPF, especially incorporating the population balance model (PBM), has been scarcely reported. A new solver coupling E-E-L approach with PBM was developed in OpenFOAM to simulate GLSTPF. The new solver was successfully compared with the experimental results of bubble size distribution and phase velocities in a three-phase bubble column. The introduction of PBM significantly improved the predictions of bubble rise and solid velocities (by up to 20%) and phase holdups (by up to 30%).

Air-water-sand three-phase jets in crossflow, as an extension of two-phase bubbly jets and a specific case of GLSTPF, have not been previously investigated. A series of physical experiments were conducted to explore air-water-sand three-phase jets in crossflowing water. The results reveal that sand particles that tend to separate from the bubbly region enhance downstream bubble dispersion. The sand concentration at the same level as the nozzle exit typically follows a parabolic distribution in the streamwise direction, and the peak position shifts closer to the source with an increased gas flow rate or reduced slurry flow rate. Finally, dimensionless prediction equations are proposed for the gas void fraction and sand concentration, which agree well with the experimental data ($R^2 = 0.91 - 0.94$).

To comprehensively explore the flow field and particle movement in air-water-sand three-phase jets in crossflow, a large eddy simulation (LES) was conducted based on the developed Eulerian-Eulerian-Lagrangian solver. The results showed that the predicted concentration and velocity of both gas and sand agree well with the experimental data. A pronounced jet expansion of the scalar concentration for the liquid-phase was observed at the location where the leading and the trailing edges of resolved turbulent kinetic energy collapse into one single peak. Sand particles escape from the jet region with a low rising velocity, and then turn downwards and accelerate rapidly to ultimately achieve a relatively uniform settling velocity as they descend to the bed.

Preface

This thesis is an original work by Huan Zhang under the supervision from Dr. Wenming (William) Zhang. It is presented in a paper format and consists of seven chapters.

Chapter 1 is a general introduction on the background, scope, and objectives of this study.

Chapter 2 to 6 are the main contents of this thesis.

Chapter 2 was published as: Zhang, H. and Zhang, W., 2022. Numerical simulation of bubbly jets in crossflow using OpenFOAM. *Physics of Fluids*, 34(12), p.123305. DOI: https://doi.org/10.1063/5.0116853.

Chapter 3 was published as: Zhang, H., Yin, Z., Chen, M. and Zhang, W., 2023. Experiment on bubble characteristics of turbulent bubbly jets in pipe crossflow. *Ocean Engineering*, 271, p.113782. DOI: https://doi.org/10.1016/j.oceaneng.2023.113782.

Chapter 4 was published as: Zhang, H., Yin, Z., Chi, W. and Zhang, W., 2023. A new Eulerian-Eulerian-Lagrangian solver in OpenFOAM and its application in a three-phase bubble column. *Powder Technology*, 426, p.118661. DOI: https://doi.org/10.1016/j.powtec.2023.118661.

Chapter 5 has been submitted as a journal manuscript: Zhang, H., Yin, Z., Zhu, D. Z., and Zhang, W., 2023. Distributions of bubble size, gas void fraction, and sand concentration in air-water-sand three-phase jets in crossflow. *Ocean Engineering*, Under Review.

Chapter 6 is currently being prepared as a journal manuscript.

Chapter 7 contains the general conclusions of this thesis, and provides the suggestions for future research on this topic.

I was responsible for the experimental design, data collection and analysis as well as the manuscript composition. Dr. Z. Yin and Dr. M. Chen assisted with the experimental design and contributed to manuscript edits of Chapter 3. Dr. Z. Yin and Dr. W. Chi assisted with the concept formation and contributed to manuscript edits of Chapter 4. Dr. Z. Yin and Dr. D. Z. Zhu assisted with the experimental design and contributed to manuscript edits of Chapter 5. Dr. Wenming (William) Zhang was the supervisory author and was directly involved with the concept formation, data analysis and manuscript composition.

I also have the following publications during my PhD:

Zhang, H. and Zhang, W., 2023. Experimental study on the characteristics of air-water-sand jets in crossflow. *Proceedings of the 40th IAHR World Congress*, Vienna, Austria, 21-25 August, 2023.

Zhang, H., Zhang, W. and Yin, Z., 2022. Hydrodynamic and dissolved oxygen transport characteristics of an upper and lower water exchange device with regular waves. *Ocean Engineering*, 249, p.110916. DOI: https://doi.org/10.1016/j.oceaneng.2022.110916.

Zhang, H. and Zhang, W., 2021. Numerical simulation of bubbly jets in crossflow. *2021 International Workshop on Sustainable Urban Drainage*, Ningbo, China.

To my family,

Acknowledgements

First and foremost, I express my sincere gratitude to my supervisor, Dr. Wenming (William) Zhang, for providing me with the invaluable opportunity to pursue my doctoral degree and for offering kind support and guidance throughout my research journey. His enthusiasm for research and thoughtful insights have been a constant source of inspiration. I extend my heartfelt thanks for his patience and mentorship throughout every step of this journey.

I would like to extend my secondary acknowledgment to the China Scholarship Council (CSC) Scholarship for their crucial financial support throughout my PhD studies. I am also deeply grateful for the funding provided by the Department of Civil and Environmental Engineering and my supervisor, Dr. Zhang. Additionally, I would like to express my sincere appreciation for the financial support from the Natural Sciences and Engineering Research Council of Canada (NSERC) for the research conducted during my PhD.

I would like to specially thank Perry Fedun for his invaluable technical support in the laboratory setups and computational systems. His dedicated assistance played a crucial role in ensuring the smooth progression of my experiments. I would also like to express my gratitude to the Digital Research Alliance of Canada (alliancecan.ca) for providing powerful computing resources, greatly facilitating my numerical study. Additionally, I extend my thanks to my supervisor, Dr. Zhang, for successfully applying for the Resource Allocation Competition.

Last but not least, I want to express my heartfelt gratitude to my family and my girlfriend, Shaoqing Ji, for their unwavering support and encouragement, which provides me courage and motivation to persevere.

Table of Contents

List of Tables

List of Figures

1. General Introduction

1.1. Research Background

A multi-phase jet in crossflow (MJC) refers to a multi-phase system generated by injecting one or more phases (e.g., air, water, or sand) into a crossflowing fluid phase (e.g., air or water). Compared to a single-phase jet in crossflow, the existence of different phases in MJC increases the complexity of the flow and jet behaviors, such as mixing characteristics, phase interaction, jet trajectory, and flow structures (Socolofsky and Adams, 2002; Zhang and Zhu, 2013; Dong et al., 2020).

Regarding the injection method at the source (nozzle), multi-phase jets in crossflowing water can be categorized into pure gas or sand jets, two-phase bubbly jets (air-water) or slurry jets (water-sand), and three-phase jets (air-water-sand). A pure gas jet is generated by injecting air from submerged nozzles, which can be extended to a bubbly jet with the simultaneous injection of water. Compared to the pure gas injection, the additional water injection at the source for bubbly jets promotes the formation of smaller bubbles that have longer residence times, both enhancing interfacial mass transfer (Lima Neto et al., 2008a, b; Zhang and Zhu, 2013). Furthermore, air-water-sand three-phase jets are generated by the simultaneous injection of air-water-sand mixture, which involve more complex jet behaviors such as the interaction between air bubbles and sand particles.

MJC has received wide attention in many applications including artificial aeration in oceans, lakes, and rivers (Asaeda and Imberger, 1989; Schladow, 1993; McGinnis et al., 2004; Wang et al., 2019), exploitation of offshore natural gas (Zheng et al., 2003), subsea blowouts (Milgram, 1983; Swan and Moros, 1993; Yapa et al., 2010), wastewater treatment (Le Moullec et al., 2008), chemical and nuclear industrial applications (Seol et al., 2007; Zhang et al., 2020), among others.

For instance, Lima Neto et al. (2007) conducted a field study by injecting oxygen into the ice-covered Athabasca River, Canada, to enhance the dissolved oxygen level. The results indicated an absorption efficiency of up to 50% for the injected oxygen, confirming the effectiveness of artificial aeration. Another example is the incident of the Ixtoc 1 subsea blowout in 1979, which was found to contain a mixture of gas, liquid (oil/water), and sand (Jernelöv, 2010). However, monitoring the volume of oil and its dispersion progress using planes or satellites remains challenging. Therefore, there is a critical need to deepen our understanding of the subsea blowout process, including both operational and fundamental aspects.

Nevertheless, previous studies of multiphase jets in crossflow are mainly focused on pure gas jets (i.e., bubble plumes) in crossflow, fewer attentions have been paid to the flow characteristics by injecting gas-liquid mixture (i.e., bubbly jets), which is shown to be more efficient for artificial aeration and mixing processes (Socolofsky and Adams, 2002; Zhang and Zhu, 2013). To the authors' knowledge, no study has been reported on the more complex air-water-sand three-phase jets in crossflow.

1.2. Overall literature review

In this Chapter, an overall literature review is presented, composed of two main aspects: two-phase bubbly jets in crossflow, and air-water-sand three-phase jets in crossflow. More detailed literature for each work can be found in Chapters 2 - 6.

(a) Bubbly jets in crossflow have been mainly studied based on physical experiments. Socolofsky and Adams (2002) conducted physical experiments with various dispersed phases (air, oil, and alcohol) in crossflows, and found that air bubble plumes showed a stronger separation from the entrained ambient water than oil-alcohol plumes as a result of higher slip velocities of bubbles. Zhang (2012) reported that the increase of injected water flow rate was able to break large bubbles into small ones, mainly due to the shear forces exerted on the bubble surface by the water jet. Zhang and Zhu (2013, 2014) conducted a series of physical experiments and observed that the liquid jet trajectory of bubbly jets in crossflow was lifted by the existence of bubbles, and thus the liquid jet thickness and likely the mixing were enhanced. The radial distributions of void fraction, bubble frequency and bubble specific interfacial area generally follow the Gaussian distribution. Several studies have investigated the bubble behaviors in pure gas jets in pipe crossflow (Balzán et al., 2017; Kang et al., 2019; Dhar et al., 2021). However, the effects of the additional water injection and the presence of top pipe wall on bubble behaviors have not been studied.

A few numerical studies have been conducted for gas-oil bubbly jet/plumes in coastal currents under deepwater conditions (Zheng et al., 2003; Chen and Yapa, 2003, 2004; Dissanayake et al., 2018). The numerical models developed by these studies were calibrated with the field or laboratory data, and the effects of gas-phase separation from the liquid-phase jet/plumes, the phase changes and bubble size distribution on the modeling results were considered. However, these researches mainly focused on the evolution of jet/plume (e.g., jet/plume geometries, trajectories, gas dissolution) within a scale of hundreds of meters in deepwater, and the detailed hydrodynamics (e.g., gas/liquid velocity distribution, vorticity) and mixing characteristics were not reported. Meanwhile, limited numerical simulations have been conducted on pure gas injection into liquid crossflow. For instance, Le Moullec (2008) numerically studied a wastewater treatment reactor where air was injected into water crossflow. In their study, the Euler-Euler two-fluid model was applied, coupled with two turbulence models: k-ε and Reynolds Stress Model (RSM). Rek et al. (2017) conducted the numerical modelling of air jet in crossflowing water using the computational fluid dynamics (CFD) code OpenFOAM, and the Volume of Fraction (VOF) method was employed to simulate the interface between bubbles and water. Mitrou (2018) conducted an Eulerian-Lagrangian simulation of gas jet in water crossflow, and investigated the vortex structures caused by the interaction between the two phases.

(b) To the authors' knowledge, no research has been reported on the air-water-sand three-phase jets in crossflow. Nonetheless, various studies have been conducted in different domains, such as fluidized beds and wastewater treatment (Kang et al., 2018; Xie et al., 2022), to investigate three-phase flow phenomena. In the realm of measuring phase properties within three-phase flow, a variety of intrusive and non-intrusive methods have been developed. Intrusive techniques include the use of ultrasonic probes (Bouillard et al., 2001), electrical conductivity probes (Liu et al., 2007), and optical fiber probes (Mokhtari and Chaouki, 2019; Li et al., 2022a). On the other hand, typical non-intrusive methods encompass image processing techniques (Götz et al., 2016; Dong et al., 2019b), electrical resistance tomography (Razzak et al., 2009; Hansen et al., 2019), and phase Doppler anemometry (Gan, 2013). Compared to intrusive methods that are constrained to measuring specific locations at one time, non-intrusive methods offer the advantage of faster data acquisition without perturbing the flow field (Jin et al., 2010). However, it is important to note that non-intrusive methods tend to have high requirements for optical operations (De Oliveira et al., 2015).

For the modeling method of three-phase flow, it can typically be categorized into five types: pseudo two-fluid (Eulerian-Eulerian, i.e., E-E) approach, three-fluid (E-E-E) approach, Eulerian-Eulerian-Lagrangian (E-E-L) approach, Eulerian-Lagrangian-Lagrangian (E-L-L) approach, and volume of fluid-discrete particle model (VOF-DPM) approach. The pros and cons of each method were systematically summarized in Chapter 4. Concerning modeling three-phase flows using the E-E-L model, Wen et al. (2005) investigated flow characteristics of a gas-liquid-solid three-phase fluidized bed, and the modeled local phase holdup and axial liquid velocity agreed with the experimental results. However, only drag force was considered for the fluid-solid interphase coupling, and selection of bubble size was not described. Sedrez et al. (2019) and Sedrez and Shirazi (2021) studied erosion of pipe elbows in GLSTPF using the E-E-L approach in ANSYS FLUENT, but particle effect on fluid behavior and particle-particle collisions were not considered (one-way coupling). To explore the effect of spatial radiation distribution (SRD) on photocatalytic oxidation of methylene blue, Liu et al. (2019a) proposed a SRD model coupling with a reaction kinetic model based on the E-E-L approach in gas-liquid-solid mini-fluidized beds. All the previous researches demonstrated the applicability and reliability of the E-E-L approach on predicting flow characteristics of GLSTPF, but bubble sizes were fixed in these studies without considering the bubble coalescence and breakup, which are however commonly encountered in complex GLSTPF (Ghaffarkhah et al., 2018; Pan et al., 2018; Zhou et al., 2020).

1.3. Knowledge gaps, hypothesis, and research objectives

Based on the comprehensive literature review, several knowledge gaps have been identified and corresponding hypothesis and objectives have been determined.

Specific knowledge gaps, hypothesis, and objectives include:

Gap 1: No CFD study has been reported on bubbly jets in crossflow, and the understanding of this topic is still insufficient: (1) the mixing/dilution characteristics have not been reported; (2) the detailed flow structures, e.g., vortex structures, are still not clear; (3) many hydrodynamic aspects are not revealed, e.g., the water velocity field and vorticity within both air- and water-phases of bubbly jets.

Hypothesis 1: (1) Bubbles in bubbly jets enhance the mixing of liquid-phase; (2) The presence of bubbles in bubbly jets affects the shape and strength of the counter-rotating vortex pair; (3) the liquid-phase will be lifted by bubbles, thereby affecting the liquid-phase trajectory.

Objective 1: To numerically unveil more hydrodynamics of bubbly jets in crossflow, based on Euler-Euler two-fluid model coupled with unsteady Reynolds-averaged Navier Stokes (URANS) approach by using the CFD code OpenFOAM. Particularly, bubble effects on water velocity field and mixing characteristics will be explored.

Gap 2: Studies on bubbly jets in crossflow with the top solid boundary effects (e.g., in a pipe/conduit or under ice-cover) are scarce.

Hypothesis 2: (1) Due to the curvature restriction of the pipe wall, bubbles will gather towards the pipe center plane; (2) the additional injection of water should enhance the bubble velocity fluctuations.

Objective 2: To experimentally investigate the bubble characteristics of bubbly jets in pipe crossflow. Particularly, the boundary effects of pipe wall on bubble properties will be explored, such as the distributions of gas void fraction, bubble diameter, and gas-phase half-width after bubbles reach the top pipe wall.

Gap 3: The applicability and reliability of E-E-L approach need to be further examined due to the limited studies, and in particular, the effects of bubble coalescence and breakup on the accuracy of E-E-L approach have not been investigated; the individual particle motions and flow structures, e.g., vortex structures, have been barely reported in GLSTPF.

Hypothesis 3: (1) The introduction of PBM is expected to enhance the predictive accuracy of the E-E-L approach in modeling GLSTPF; (2) the solid particle velocity is expected to be lower than bubble velocity in a bubble-driven flow.

Objective 3: (1) To develop a new E-E-L solver in OpenFOAM that couples E-E-L approach and PBM for investigating the characteristics of GLSTPF; (2) To evaluate the effect of PBM on the accuracy of the E-E-L approach in modeling GLSTPF.

Gap 4: The characteristics of air-water-sand three-phase jets in crossflow have not been investigated, and in particular, the mutual influence between air bubbles and sand particles on their behaviors are unknown.

Hypothesis 4: (1) The additional injection of sand particles is expected to breakup bubbles into smaller ones; (2) sand particles may drive bubbles to spread further downstream; (3) an increase of gas flow rate is expected to enhance the spreading of sand particles.

Objective 4: To experimentally investigate bubble characteristics and sand transport of air-water-sand three-phase jets in crossflow, and to explore the mutual influence between air bubbles and sand particles on their concentrations.

Gap 5: The air-water-sand three-phase jets in crossflow have not been modeled using the E-E-L approach; the sand transport, flow field, and vortical structures in air-water-sand three-phase jets in crossflow are not clear.

Hypothesis 5: (1) In the bubbly region, the bubble velocity should be higher than the liquid and sand velocities; (2) Sand particles are expected to attain a relatively uniform settling velocity before reaching the bed; (3) vortical structures including shear-layer vortices, wake vortices, and counter-rotating vortex pair are expected to be observed.

Objective 5: To apply the E-E-L approach to the air-water-sand three-phase jets in crossflow, and to investigate the complex velocity field, phase concentrations, particle movement and flow structures.

1.4. Thesis Outline

This thesis investigates the characteristics of two- and three-phase jet in crossflow based on either laboratory experiments or numerical simulations. The focus of two-phase jet is on air-water bubbly jet in crossflow, and the three-phase jet is air-water-sand jet in crossflow. Figure 1-1 shows a brief overview of the five main contents of this thesis. For the bubbly jet in crossflow, the first work aims to numerically unveil more hydrodynamics of bubbly jets in free-surface crossflow (without top boundary effects; Chapter 2); and then the bubble characteristics were investigated experimentally in pipe crossflow (with top boundary effects; Chapter 3). For the air-water-sand three-phase jet in crossflow, a new E-E-L three-phase solver was firstly developed in OpenFOAM, which was successfully validated in a three-phase bubble column (Chapter 4). Subsequently, a series of physical experiments were conducted to explore both bubble and sand properties in air-water-sand three-phase jets in crossflow (Chapter 5). Based on the experimental setup and results, a large eddy simulation was finally performed using the developed three-phase solver in Chapter 4 to investigate the complex flow field and particle movement (Chapter 6).

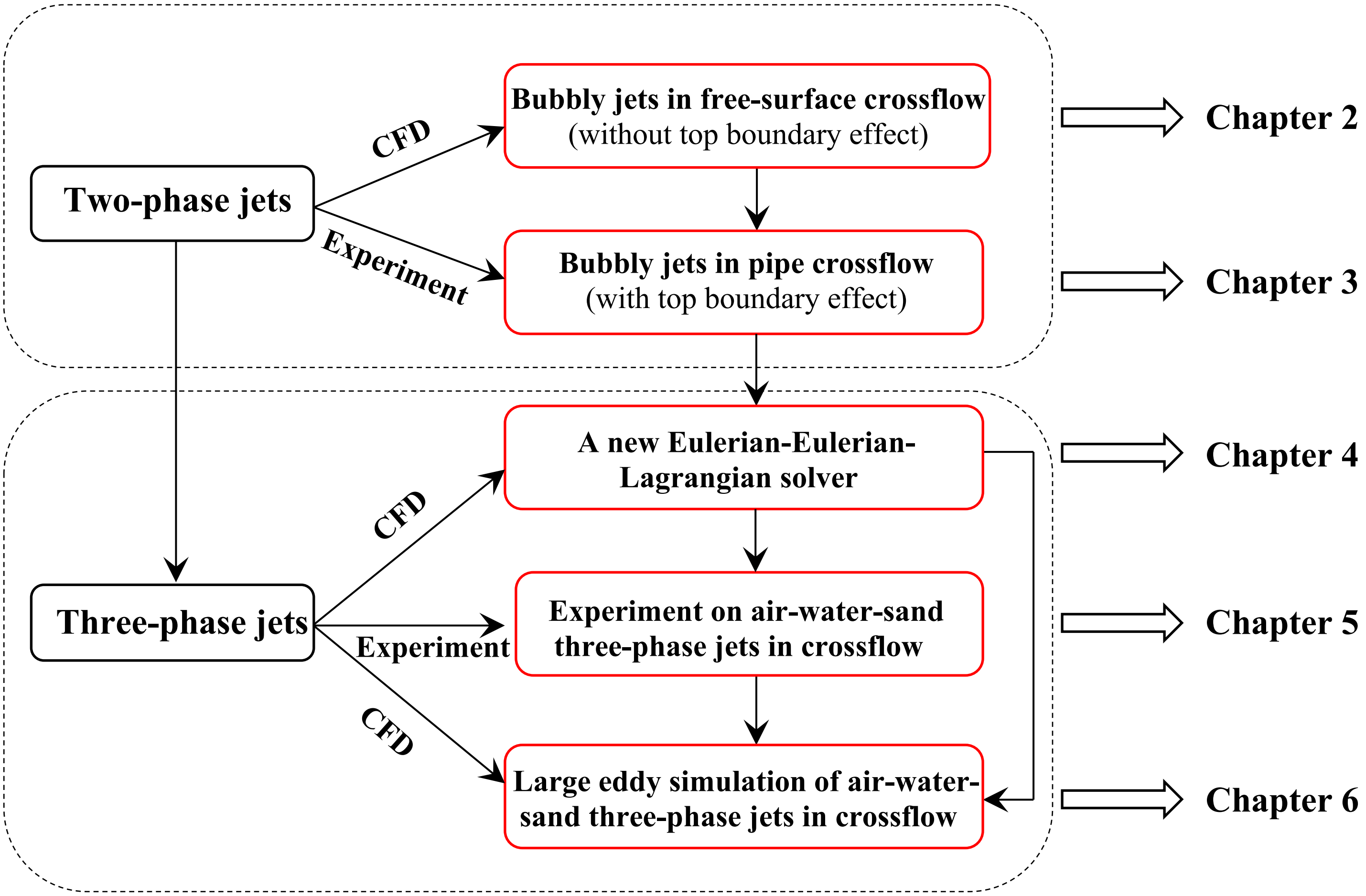

Figure 1-1. The main contents of this thesis from Chapter 2 to Chapter 6, where the red color indicates the five contributions on two- or three-phase jets in crossflow.

The detailed outline of this thesis is organized as follows:

Chapter 2 numerically investigates the hydrodynamics that cannot be measured (or measured easily) for both gas- and water-phases of air-water bubbly jets in crossflow, including the mixing/dilution characteristics, flow structures (e.g., vortex structures), water velocity field and vorticity within both air- and water-phases of bubbly jets.

Chapter 3 reveals the bubble characteristics for bubbly jets in pipe crossflow by conducting a series of physical experiments. The bubble properties (gas-phase trajectory, gas void fraction, bubble diameter, and bubble velocity) were systematically investigated before and after bubbles touch the top pipe wall, based on image processing techniques.

Chapter 4 develops a new solver coupling Eulerian-Eulerian-Lagrangian approach (E-E-L) with population balance model (PBM) in OpenFOAM to simulate gas-liquid-solid three-phase flow. The effects of the PBM model on the accuracy of the E-E-L approach are studied.

Chapter 5 presents a series of physical experiments to investigate air-water-sand three-phase jets in crossflow. The bubble size, gas void fraction, and sand concentration were systematically investigated, and dimensionless prediction equations are proposed for the gas void fraction and sand concentration.

Chapter 6 conducts a large eddy simulation using the developed E-E-L three-phase model, which is calibrated and validated with the experimental data, to numerically investigate the characteristics in air-water-sand three-phase jets in crossflow, such as the flow field, particle movement, and vortical structures.

Chapter 7 provides general conclusions and discusses the future directions of this research.

2. Numerical simulation of bubbly jets in crossflow using OpenFOAM[*]

2.1. Introduction

Multi-phase jet in crossflow (MJC) has received wide attention in many applications including artificial aeration, mixing, subsea blowouts of oil and gas, etc. (Zheng and Yapa, 1998; Socolofsky and Adams, 2002; Zhang and Zhu, 2013; Rek et al., 2017; Dong et al., 2020). As of yet, the vast majority of the MJC literature focuses on pure gas or liquid jets in crossflow, and limited studies pay attention to the much more complex bubby jets in crossflow, which are resulted from the injection of a mixture of multiphase flow (e.g., air-water mixture) in crossflow. As reported by Zhang and Zhu[3], the injection of air-water mixture can produce much smaller bubbles (1.5-3.1 mm), compared to pure air injection (5.5-13.5 mm), and therefore, bubbly jets are more efficient for artificial aeration and mixing. Bubbly jets have been reported to have lower construction and maintenance costs (Lima Neto et al., 2008a).

In the case of pure gas injection into liquid crossflow, experimental investigations of bubble/gas-phase behaviors such as bubble size, rising velocity, gas void fraction, bubble jet penetration and trajectory, are of great interest (Socolofsky and Adams, 2002; Balzán et al., 2017; Kang et al., 2019; Dong et al., 2020; Dong et al., 2021). Compared to an air jet in stagnant liquid, the existence of crossflow affects greatly to the bubble behaviors (Wang and Socolofsky, 2015). For instance, bubbles deform into ellipsoids and spherical cap during rising in the still water,

---

[*] The content of this chapter has been published as: Zhang, H., Zhang, W., 2022. Numerical simulation of bubbly jets in crossflow using OpenFOAM. Phys. Fluids 34(12).

whereas they are observed to be irregularly shaped ellipsoids skewed towards the ambient flow direction under crossflow effect (Xu et al., 2018). As the crossflow velocity increases, the bubbles become smaller and tend to be rounded (Kang et al., 2019). Besides experimental studies, numerical simulations on pure gas injection into liquid crossflow are limited. Le Moullec et al. (2008) numerically studied a wastewater treatment reactor where air was injected into water crossflow. In their study, the Euler-Euler two-fluid model was applied, coupled with two turbulence models: k-ε and Reynolds Stress Model (RSM). Rek et al. (2017) conducted the numerical modelling of air jet in crossflowing water using the computational fluid dynamics (CFD) code OpenFOAM, and the Volume of Fraction (VOF) method was employed to simulate the interface between bubbles and water. Mitrou et al. (2018) conducted an Eulerian-Lagrangian simulation of gas jet in water crossflow, and investigated the vortex structures caused by the interaction between the two phases.

Compared to pure gas jet in water (i.e., bubble plumes), fewer attentions have been paid to injecting gas-liquid mixture (i.e., bubbly jets) into either still liquid or crossflow, which is shown to be more efficient for artificial aeration and mixing processes (Zhang and Zhu, 2013; Pakhomov and Terekhov, 2019; Wang et al., 2019; Yin et al., 2020). Focusing on bubbly jets in stagnant water, Lima Neto et al. (2008) conducted an experimental study to investigate the gas void fraction, bubble size distribution, and velocities of air and water. Based on Lima Neto et al.'s experiment, Wang et al. (2019) further investigated turbulent kinetic energy and entrainment coefficient of bubbly jets in stagnant water using a mixture model. Seo and Kim (2021) experimentally explored the distributions of bubble size and phase velocities, as well as turbulence characteristics in bubbly jets in stagnant water. Pakhomov and Terekhov (2019) numerically studied the structure of a free round bubbly jet in stagnant water by using the Eulerian approach, and found that the additional injection of gas bubbles enhanced the flow turbulence and mixing.

On the other hand, bubbly jets in crossflow have been mainly studied based on physical experiments. Socolofsky and Adams (2002) studied the multi-phase jets into crossflows with pure air, air-oil, and air-alcohol injections. The results showed that, in strong crossflows, the bubbles separate from the liquid phase (oil or alcohol) due to the buoyancy effect. Zhang (2012) reported that the increase of injected water flow rate was able to break large bubbles into small ones, mainly due to the shear forces exerted on the bubble surface by the water jet. Zhang and Zhu (2013) conducted a series of physical experiments and observed that the liquid jet trajectory of bubbly jets in crossflow was lifted by the existence of bubbles, and thus the liquid jet thickness and likely the mixing were enhanced. To better understand the bubbly jets mixing in crossflow, Zhang and Zhu (2014) investigated the visual centerline trajectories of both air-phase and water-phase.

A few numerical studies have been conducted for gas-oil bubbly jet/plumes in coastal currents under deepwater conditions (Zheng et al., 2003; Chen and Yapa, 2003; Chen and Yapa, 2004; Dissanayake et al., 2018). The numerical models developed by these studies were calibrated with the field or laboratory data, and the effects of gas-phase separation from the liquid-phase jet/plumes, the phase changes and bubble size distribution on the modeling results were considered. However, these researches mainly focused on the evolution of jet/plume (e.g., jet/plume geometries, trajectories, gas dissolution) within a scale of hundreds of meters in deepwater, and the detailed hydrodynamics (e.g., gas/liquid velocity distribution, vorticity) and mixing characteristics were not reported.

Based on the comprehensive literature review, there are several knowledge gaps that needs to be investigated on bubbly jets in crossflow: (1) the mixing/dilution characteristics have not been reported; (2) the detailed flow structures, e.g., vortex structures, are still not clear; (3) many hydrodynamic aspects are not revealed, e.g., the water velocity field and vorticity within both air- and water-phases of bubbly jets; (4) no CFD study has been reported.

This paper aims to numerically unveil more hydrodynamics of bubbly jets in crossflow, based on Euler-Euler two-fluid model coupled with unsteady Reynolds-averaged Navier Stokes (URANS) approach by using the CFD code OpenFOAM. The remainder of this paper is organized as follows: the mathematical model and setup details are introduced in Sections 2 and 3. Section 4 presents the numerical results, including model calibration and validation, flow structure and turbulent kinetic energy, water velocity, scalar concentration, vorticity, and water jet centerline trajectories. Finally, conclusions and the future research directions are provided in Section 5.

2.2. Mathematical model formation

2.2.1. Euler-Euler two-fluid model

In the Euler-Euler two-fluid approach, both the continuous liquid phase and the dispersed gas phase are treated as two interpenetrating continua. In this study, both phases were assumed to be adiabatic interactive phases. The continuity and momentum equations were solved for each phase separately (Fard et al., 2020):

$$\frac{\partial(\rho_\varphi \alpha_\varphi)}{\partial t} + \nabla \cdot \left(\rho_\varphi \alpha_\varphi \mathbf{U}_\varphi\right) = 0 \tag{2-1}$$

$$\frac{\partial(\rho_\varphi \alpha_\varphi \mathbf{U}_\varphi)}{\partial t} + \nabla \cdot \left(\rho_\varphi \alpha_\varphi \mathbf{U}_\varphi \mathbf{U}_\varphi\right) = -\alpha_\varphi \nabla P + \alpha_\varphi \rho_\varphi \mathbf{g} - \nabla \cdot \left(\alpha_\varphi \tau_\varphi^{\mathrm{eff}}\right) + \mathbf{F}_\varphi \tag{2-2}$$

where bold letters denote vectors, α_φ represents the fraction of phase φ, ρ_φ is the phase density (constant in this paper), $\mathbf{U}_\varphi$ denotes the ensemble-averaged phase velocity, P is the pressure, $\mathbf{g}$ is the gravitational acceleration vector, and $\mathbf{F}_\varphi$ is the interfacial forces between phases. $\tau_\varphi^{\mathrm{eff}}$ is the effective stress tensor composed of viscous and Reynolds stresses:

$$\tau_\varphi^{\mathrm{eff}} = -\mu_\varphi^{\mathrm{eff}}\left[\nabla\mathbf{U}_\varphi + \left(\nabla\mathbf{U}_\varphi\right)^T - \tfrac{2}{3}\left(\nabla\cdot\mathbf{U}_\varphi\right)\mathrm{I}\right] \tag{2-3}$$

where $\mu_\varphi^{\mathrm{eff}}$ represents the effective viscosity, which is composed of the molecular viscosity μ_φ and the turbulent viscosity μ_φ^{T}.

2.2.2. Interfacial force terms

The term $\mathbf{F}_\varphi$ in Eq. (2-2) represents the inter-phase momentum exchange between phases due to interphase forces. In this study, the total interfacial forces were decomposed into four main terms (Niceno et al., 2008):

$$\mathbf{F}_\varphi = \mathbf{F}_{lg} = -\mathbf{F}_{gl} = \mathbf{F}_D + \mathbf{F}_L + \mathbf{F}_{VM} + \mathbf{F}_{TD} \tag{2-4}$$

where $\mathbf{F}_{lg}$ refers to the momentum transfer from the gas phase to the liquid phase and vice versa for $\mathbf{F}_{gl}$, and $\mathbf{F}_D$, $\mathbf{F}_L$, $\mathbf{F}_{VM}$ and $\mathbf{F}_{TD}$ represent the drag force, lift force, virtual mass force and turbulent dispersion force, respectively. It should be noted that, the lift force tends to reproduce the radial dispersion of bubbles, which has been demonstrated for single bubbles (Dissanayake et al., 2018). However, there are still uncertainties for bubble swarms, and various (negative, zero, positive) values of lift coefficient have been utilized by previous studies (Mohammadi et al., 2019; Liu et al., 2020; Zhu et al., 2020). In the absence of a specific standard for selecting an appropriate value of lift coefficient, the lift force term was not considered in the present simulation, and similar treatment has also been employed in similar studies (Fard et al., 2020; Kannan et al., 2019; Hu et al., 2021).

The drag force originates from the resistance experienced by the dispersed phase (air bubble in this study) moving in the continuous phase (water in this study). For a bubble swarm, the drag force per unit volume was given by (Clift et al., 1978):

$$\mathbf{F}_D = \frac{3}{4}\alpha_{\mathrm{g}} C_D \frac{\rho_l}{d_{\mathrm{b}}}\left|\mathbf{U}_g - \mathbf{U}_l\right|\left(\mathbf{U}_g - \mathbf{U}_l\right) \tag{2-5}$$

where C_D is the drag coefficient and d_{b} is the bubble diameter. Various drag models have been proposed and compared in the literatures (Schiller, 1933; Ishii and Zuber, 1979; Tabib, 2008), and the widely used Schiller-Naumann drag model (Schiller, 1933) was adopted to calculate C_D in this study.

The virtual mass force is resulted from the bubble acceleration that will accelerate the surrounding fluid (Niceno et al., 2008), and was modelled as:

$$\mathbf{F}_{VM} = \alpha_g \rho_l C_{VM}\left(\frac{\mathrm{D}\mathbf{U}_g}{\mathrm{D}t} - \frac{\mathrm{D}\mathbf{U}_l}{\mathrm{D}t}\right) \tag{2-6}$$

where C_{VM} is the virtual mass coefficient, and was fixed to be 0.5 in this study for individual spherical bubbles (Dhotre et al., 2008).

In this URANS simulation, the fluid velocity for calculating interfacial forces was ensemble-averaged value. Therefore, the turbulent dispersion force was included to take into account the random influence of turbulent eddies. As proposed by Lopez de Bertodano et al. (1994), bubbles tend to disperse from high void fraction regions to low void fraction regions under the action of liquid eddies. The turbulent dispersion force can be expressed as:

$$\mathbf{F}_{TD} = C_{TD}\alpha_g \rho_l k_l \nabla\alpha_g \tag{2-7}$$

where k_l is the turbulent kinetic energy of the liquid, and the turbulent dispersion coefficient C_{TD} was taken as 1.0 in this study after testing numerous values to match the experimental measurements.

2.2.3. Turbulence modeling

In this study, two turbulence models, namely the mixture *k*-*ε* model and Reynolds stress model (RSM) were adopted and compared. The mixture *k*-*ε* model uses one set of equations for turbulent kinetic energy (TKE) *k* and turbulent dissipation rate *ε* of the mixture of the liquid and gas phases. This model is able to solve the problem that at high phase fractions, both liquid and gas fluctuate as a unit (Behzadi et al., 2004), and the *k* and *ε* equations describing the model are as follows:

$$\frac{\partial}{\partial t}(\rho_m k_m) + \nabla \cdot (\rho_m \mathbf{U}_m k_m) = \nabla \cdot \frac{\mu_m^T}{\sigma_m} \nabla k_m + P_k^m - \rho_m \varepsilon_m + S_k^m \tag{2-8}$$

$$\frac{\partial}{\partial t}(\rho_m \varepsilon_m) + \nabla \cdot (\rho_m \mathbf{U}_m \varepsilon_m) = \nabla \cdot \frac{\mu_m^T}{\sigma_m} \nabla \varepsilon_m + \frac{\varepsilon_m}{k_m}(C_{\varepsilon 1} P_k^m - C_{\varepsilon 2} \rho_m \varepsilon_m + C_{\varepsilon 3} S_k^m) \tag{2-9}$$

where *m* refers to the mixture of the two phases, and the mixture properties are related to the continuous (liquid) and dispersed (gas) phases as follows,

$$\rho_m = \alpha_l \rho_l + \alpha_g \rho_g \tag{2-10}$$

$$k_m = \left(\alpha_l \frac{\rho_l}{\rho_m} + \alpha_g \frac{\rho_g}{\rho_m} C_t^2\right) k_l \tag{2-11}$$

$$\varepsilon_m = \left(\alpha_l \frac{\rho_l}{\rho_m} + \alpha_g \frac{\rho_g}{\rho_m} C_t^2\right) \varepsilon_l \tag{2-12}$$

$$\mathbf{U}_m = \frac{\alpha_l \rho_l \mathbf{U}_l + \alpha_g \rho_g \mathbf{U}_g C_t^2}{\alpha_l \rho_l + \alpha_g \rho_g C_t^2} \tag{2-13}$$

$$\mu_m^t = \frac{(\alpha_l \mu_l^t + \alpha_g \mu_g^t C_t^2)\rho_m}{\alpha_l \rho_l + \alpha_g \rho_g C_t^2} \tag{2-14}$$

$$P_k^m = \alpha_l P_k^l + \alpha_g P_k^g \tag{2-15}$$

$$S_k^m = S_k^l + S_k^g = -A_g\left[2\alpha_g (C_t - 1)^2 k_l + \eta_l \nabla \alpha_g \cdot \mathbf{U}_r\right] \tag{2-16}$$

The model constants $C_{\varepsilon 1}$, $C_{\varepsilon 2}$, and $C_{\varepsilon 3}$ are 1.44, 1.92, and 1.92, respectively. Eqs. (2-8)-(2-16) are solved with the *twoPhaseEulerFoam* solver within OpenFOAM-v2006, and the detailed solution procedure can be found in Behzadi et al. (2004) and Bhusare et al. (2017).

Regarding the RSM model, turbulence was only considered for the liquid phase in this paper, and bubble induced turbulence source terms were added to the transport equations. The transport equation for the liquid Reynolds stress tensor $\mathbf{R}_l$ reads (Shi et al., 2019):

$$\frac{\partial(\alpha_l \rho_l \mathbf{R}_l)}{\partial t} + \nabla \cdot (\alpha_l \rho_l \mathbf{U}_l \mathbf{R}_l) = \nabla \cdot \left[\alpha_l \left(\mu_l + \rho_l C_s \frac{k_l}{\varepsilon_l} \mathbf{R}_l\right) \nabla \mathbf{R}_l\right] + \alpha_l \rho_l \mathbf{P}_l$$

$$+\alpha_l \rho_l \mathbf{\Phi}_l - \frac{2}{3} \alpha_l \rho_l \varepsilon_l \mathbf{I} + \mathbf{S}_{R,l} \qquad (2\text{-}17)$$

where the turbulent production of Reynolds stress $\mathbf{P}_l$ is given by,

$$\mathbf{P}_l = -\mathbf{R}_l \cdot [\nabla \mathbf{U}_l + (\nabla \mathbf{U}_l)^{\mathrm{T}}] \qquad (2\text{-}18)$$

The pressure-strain term $\mathbf{\Phi}_l$ is modeled as,

$$\mathbf{\Phi}_l = -C_1 \frac{\varepsilon_l}{k_l}\left(\mathbf{R}_l - \frac{2}{3} k_l \mathbf{I}\right) - C_2 \left(\mathbf{P}_l - \frac{2}{3} \mathrm{tr}(\mathbf{P}_l) \mathbf{I}\right) \qquad (2\text{-}19)$$

The liquid turbulent kinetic energy k_l is calculated by,

$$k_l = \frac{1}{2} \mathrm{tr}(\mathbf{R}_l) \qquad (2\text{-}20)$$

$\mathbf{S}_{R,l}$ is the source term of bubble induced turbulence, which was modeled by following Le Moullec et al. (2008) who simulated a pure gas jet in crossflow:

$$\mathbf{S}_{R,l} = \frac{2}{3} \alpha_l C_R \mathbf{F}_D \left|\mathbf{U}_g - \mathbf{U}_l\right| \cdot \mathbf{I} \qquad (2\text{-}21)$$

To close the RSM model, the transport equation of the dissipation rate ε_l needs be solved by follows,

$$\frac{\partial(\alpha_l \rho_l \varepsilon_l)}{\partial t} + \nabla \cdot (\alpha_l \rho_l \mathbf{U}_l \varepsilon_l) = \nabla \cdot \left[\alpha_l \left(\mu_l + \rho_l C_\varepsilon \frac{k_l}{\varepsilon_l} \mathbf{R}_l\right) \nabla \varepsilon_l\right]$$

$$+\alpha_l \rho_l \frac{\varepsilon_l}{k_l}\left[C_{\varepsilon 1} \frac{1}{2} tr(\mathbf{P}_l) - C_{\varepsilon 2} \varepsilon_l\right] + \mathbf{S}_{\varepsilon,l} \qquad (2\text{-}22)$$

where the source term $\mathbf{S}_{\varepsilon,l}$ is calculated as,

$$\mathbf{S}_{\varepsilon,l} = \alpha_l \frac{\varepsilon_l}{k_l} C_{\varepsilon 1} C_\varepsilon \mathbf{F}_D \left|\mathbf{U}_g - \mathbf{U}_l\right| \qquad (2\text{-}23)$$

The model constants are $C_s = 0.22$, $C_1 = 1.8$, $C_2 = 0.6$, $C_R = 1.44$, $C_\varepsilon = 0.15$, $C_{\varepsilon 1} = 1.44$, and $C_{\varepsilon 2} = 1.92$. Note that the RSM model was not coupled with two-phase system in OpenFOAM-v2006, and thus Eqs. (2-17)-(2-23) were implemented in the *twoPhaseEulerFoam* solver in this work.

2.3. Numerical simulation details

2.3.1. Numerical setup and scenarios

The setup of numerical simulation is based on the experimental configuration of Zhang and Zhu (2013). The experiments of bubbly jets in crossflow were conducted in a water flume of 25 × 1.2 × 0.8 m^3 (L × W × H). The water depth and crossflow (cross-sectional-average) velocity were kept at 0.65 m and 0.2 m/s, respectively. This resulted in a turbulent crossflow with a Reynolds number of 249,600. A circular nozzle with a diameter of *d* = 6 mm was set vertically at the center-plane of the flume, and it was 12 cm above the flume bed to avoid the bottom wall effect. To validate the mathematical model and examine 3D hydrodynamics, the same configurations were used in the simulations. The computational domain was reduced to 1.0 m in length (as shown in Figure 2-1) to save the computational time. The nozzle was set at 0.1 m downstream of the crossflow inlet, and the coordinate origin was set at the nozzle exit where the mixture of air and water was injected.

It should be noted that x, y, z are the longitudinal, vertical, transverse directions, respectively; the λ and ξ directions are along the water and gas phase centerlines, respectively, and the η direction is perpendicular to ξ and points downwards.

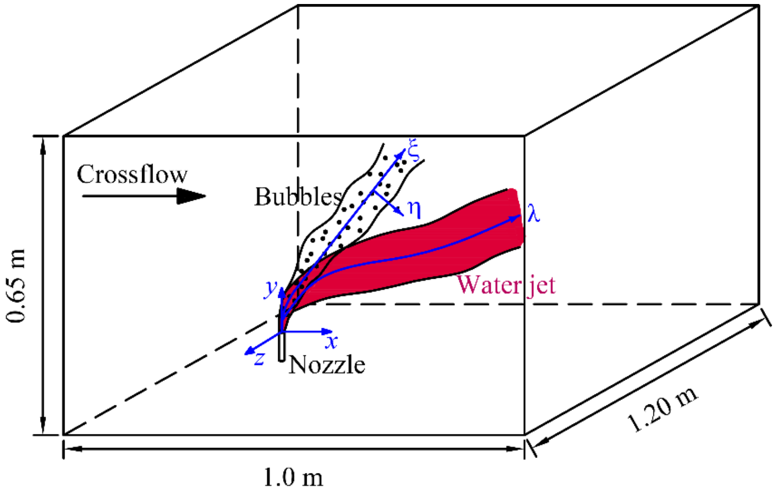

Figure 2-1. Computational domain and the coordinate system.

The boundary conditions were defined as follows. Fixed water velocity was assigned at the crossflow inlet. At the crossflow outlet, velocity was set to inletOutlet, which is normally the same as zero gradient. However, if there is backward flow at the outlet, it switches to a fixed value (zero in this study). At the nozzle exit boundary, the air and water velocities were specified to be fixed values, and the initial gas volume fraction was calculated by $\alpha_0 = Q_g/(Q_g + Q_l)$ (Zhang and Zhu, 2013), where Q_g and Q_l were air and water flow rates, respectively. The turbulence level of water at the crossflow inlet and nozzle exit were specified by (Bhusare et al., 2017) $k_w = \frac{3}{2}(\mathbf{U}_w \mathrm{I})^2$ and $\varepsilon_w = \frac{C_\mu^{3/4} k^{3/2}}{0.07L}$, where the turbulent intensity $\mathrm{I} = 0.16(\mathrm{Re}_w)^{-1/8}$, $C_\mu = 0.09$, and L is the characteristic length (set as hydraulic diameter at the crossflow inlet and nozzle diameter at the nozzle exit). The air phase turbulence properties were only needed to set at the nozzle exit when using the mixture k-ε model. Slip and zero-gradient boundary conditions were imposed at the top surface of the domain for water and air, respectively. The rest surfaces were specified as wall boundaries, and the no-slip boundary conditions were adopted.

Initially, the water was flowing from crossflow inlet to outlet with the same velocity at crossflow inlet, and the hydrostatic pressure distribution at time $t = 0$ was defined in the vertical y direction. No gas and sand particles exist in the channel flow at the initial time, and the scalar concentration is zero in the domain. Based on the experimental observations of Zhang and Zhu (2013), bubble coalescence and breakup mainly occurred near the nozzle ($\xi < 20$d), which is not the focus of this work. Therefore, d_b was fixed as the average value of 3 mm in this study without considering bubble coalescence and breakup. The effect of bubbles deformation was not considered because bubbles with $d_b = 3$ mm can be approximated as spherical bubbles (Clift et al., 1978), for which deformation is not important during rising.

The governing equations were solved using the open source CFD package OpenFOAM v2006 with the *twoPhaseEulerFoam* solver. This solver is based on the finite volume method to discretize the governing equations, and has shown to be stable for transient calculations (Fard et al., 2020). The phase volume fractions were solved based on Eq. (2-1) by using MULES method (Deshpande et al., 2012), and phase fraction boundedness was ensured using a limiter. The PIMPLE algorithm which combines the advantages of PISO (Issa, 1986) and SIMPLE (Patankar, 1980) algorithms was employed for the velocity-pressure coupling. The first order bounded implicit Euler scheme was used for the time derivative terms in the equations, the second order Gauss linear scheme was adopted for the gradient terms, the limited discretization scheme was used for the divergence terms, and the diffusive terms were interpolated with the Gauss linear uncorrected scheme.

The adjustable time step was adopted to satisfy the Courant number requirement $C_o = \Delta t \frac{U_{\max}}{\Delta x_{\min}} < 1$, in which $\Delta x_{\min}$ represents the shortest distances between the computational points. Table 2-1 shows the five scenarios studied in this work, in which the crossflow velocity U_a increased from 0.2 m/s to 0.5 and 1.0 m/s, the air flow rate Q_g were specified as 0 or 3 L/min, and the water flow rate Q_l varied from 3 to 6 L/min, corresponding to the initial gas void fraction α_0 of 0 or 0.5. Moreover, the Cases 0.2-3-3 and 0.2-0-3 were used for model calibration and validation. Each scenario was run for 200 s, and time averaging $\overline{\emptyset} = \frac{1}{200-100}\int_{100}^{200} \emptyset_t dt$ (where $\emptyset_t$ is a generic variable at time t) was performed between 100-200 s when the flow reached statistically stationary turbulence. The numerical simulations were carried out on a cluster with 20 processors for each scenario.

Table 2-1. Summary of numerical scenarios of bubbly jets in this study.

Case I.D.	Crossflow velocity U_a (m/s)	Air flow rate Q_g (L/min)	Water flow rate Q_l (L/min)	Initial gas volume fraction α_0
0.2-0-3	0.2	0	3	0
0.2-0-6	0.2	0	6	0
0.2-3-3	0.2	3	3	0.5
0.5-3-3	0.5	3	3	0.5
1.0-3-3	1.0	3	3	0.5

2.3.2. Grid requirements and grid sensitivity analysis

In this numerical simulation, the grid requirements for Euler-Euler two-fluid model need to be considered. As described by Dhotre et al. (2008), one intrinsic assumption of deriving the Euler-Euler equations is that the grid cell (control volume) size should be larger than the bubble size to encompass all the interfacial details. Therefore, this is a basic requirement for Euler-Euler method that must be strictly satisfied. One important criterion of applying Euler-Euler model is the ratio of grid cell size to bubble diameter Δ/d_b, which is supposed to be larger than 1.5 (Milelli, 2002). By using the Euler-Euler approach, Le Moullec et al. (2008) investigated the characteristics of a pure gas jet in crossflow with $\Delta/d_b = 2.5$. Diaz et al. (2008). conducted a URANS simulation of bubble column and concluded that the coarse mesh (with maximum $\Delta/d_b = 11.2$) agreed better with the experiments, compared with the medium and fine grids. Pfleger and Becker (2001) and Buwa and Ranade (2002) also presented that as the grid cell size decreased, the predicted time-averaged axial velocity differed more from the experimental results. Therefore, it is indispensable to conduct the grid sensitivity analysis before the investigation.

In the current study, four different grid cell sizes, as shown in Table 2-2, were used to compare with the experimental data. Figure 2-2 shows the comparison between the simulated time-averaged gas void fraction (α) by the mixture k-ε model and experimental data for Case 0.2-3-3, in which 20d - 80d represent different cross-sections from the nozzle exit in the ξ direction. It was found that, in both the η and z directions, the overall trends of simulated and experimental distributions of gas void fraction agree well with each other, and Mesh 3 gives the best agreement. However, the distribution of void fraction becomes wider with the increase of mesh sizes, especially in the η direction, and the peak values tend to be larger for the finer grids. This is probably because as the mesh size decreases, the interfacial details between bubbles and surrounding water cannot be fully captured. In the z direction, the differences between Mesh 3 and Mesh 4 decrease, indicating that Mesh 3 is large enough to encompass all the interfacial details in the z direction.

Table 2-2. Main characteristics of the computational mesh.

Mesh	Grid cell size Δ (mm)	Total cell number	Cell partition (x×y×z)	Δ/d_b
1	5	6,460,447	200×130×240	1.6

2	7.5	1,943,123	133×86×160	2.5
3	10	811,791	100×65×120	3.3
4	12	594,869	83×54×100	4

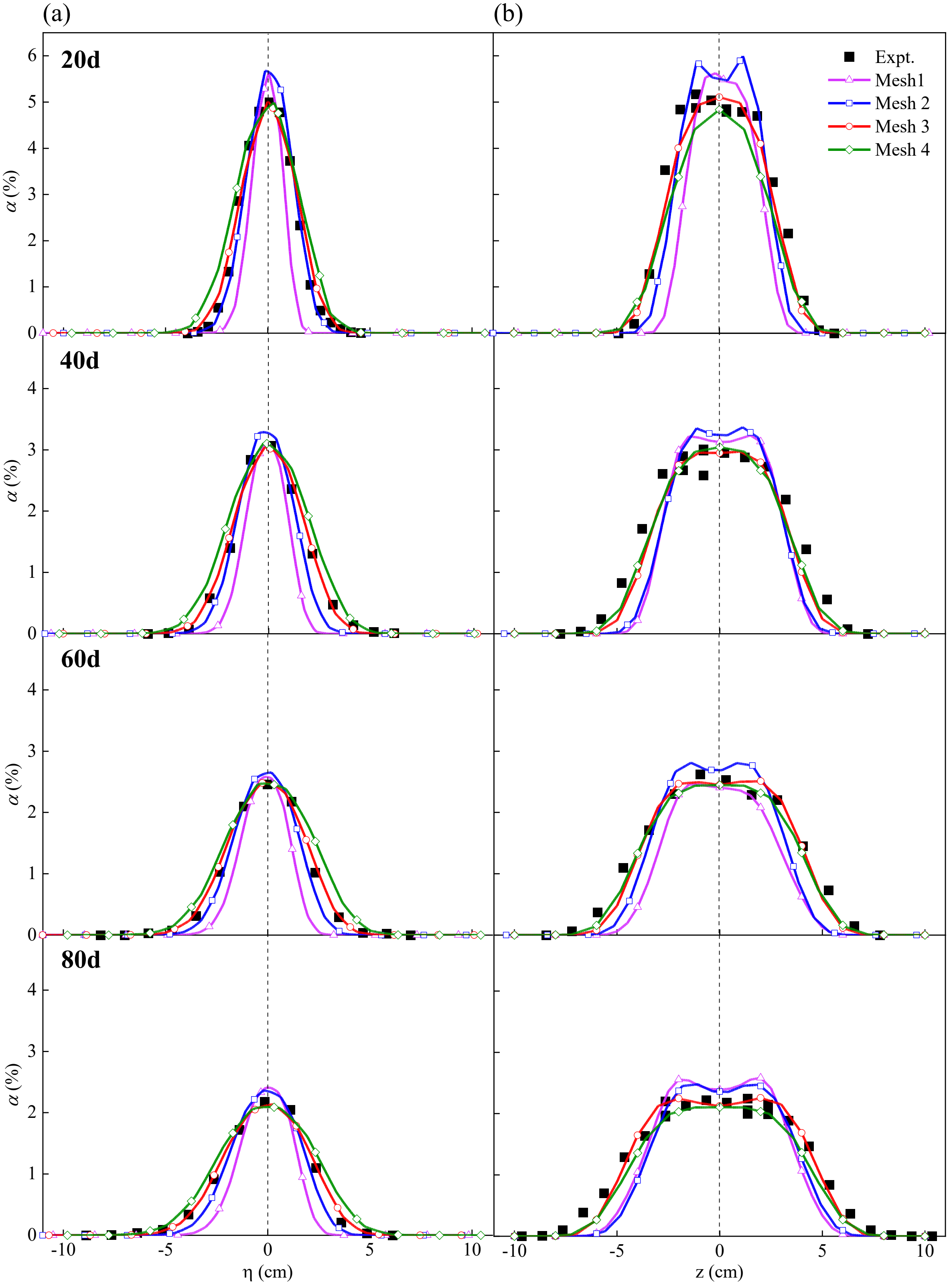
(a)
(b)
20d
40d
60d
80d
α (%)
η (cm)
z (cm)
Expt.
Mesh1
Mesh 2
Mesh 3
Mesh 4
0
1
2
3
4
5
6
-10
-5
0
5
10

Figure 2-2. Comparison between the simulated and experimental time-averaged gas void fraction at Sections 20-80d for Case 0.2-3-3 in the (a) η direction and (b) z direction with different meshes. The experimental results were from Zhang and Zhu (2013).

It should be noted that, the simulated results might be dependent on different mesh sizes due to the grid requirements of the Euler-Euler model, and the predictions by finer meshes were likely to deviate more from the experimental data as reported by many researchers (Liu et al., 2019b; Liu et al., 2020). In this study, Mesh 3 with Δ = 10 mm and Δ/d_b = 3.3 was chosen for the following computations given the accuracy of the prediction and taking the computation time into consideration. Figure 2-3 shows the final grid configuration of the computational domain, and local refinement was implemented near the nozzle, leading to a grid cell size of 1.5 mm in the sub-domain. The grid sensitivity analysis was also conducted near the nozzle, and the differences between several grid cell sizes (0.375-1.5 mm) were relatively small and could be ignored.

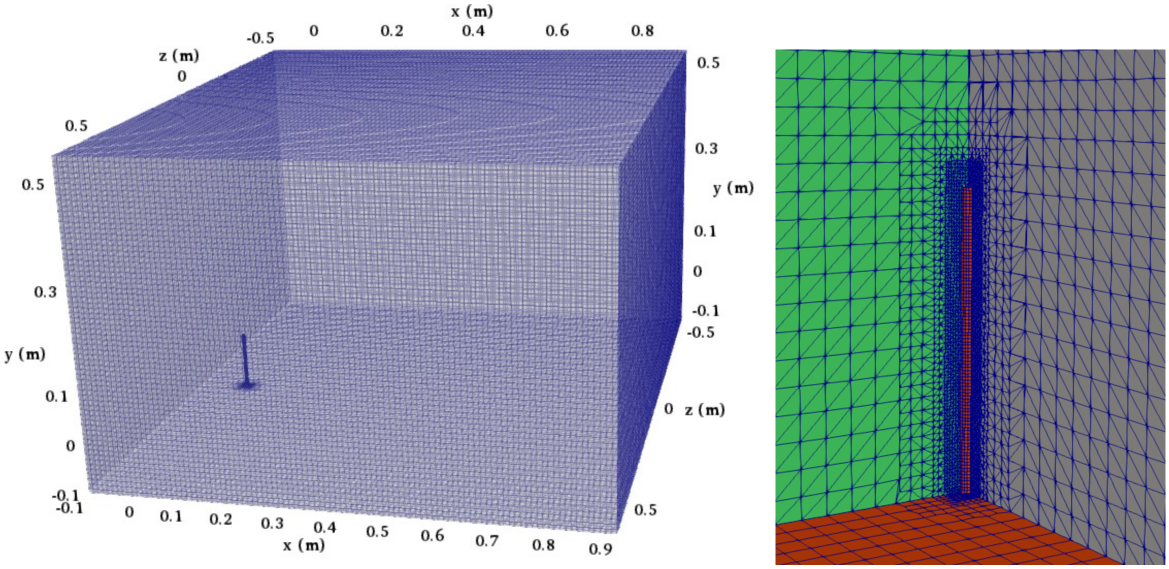

Figure 2-3. Grid configuration for the model: (a) Global grids configuration; and (b) Local grid refinement near the nozzle.

2.4. Results and discussion

2.4.1. Mathematical model calibration and validation

In addition to the calibration of gas void fraction as shown in Figure 2-2, the distribution of bubble velocity was calibrated as it plays an important role in bubbly jets in crossflow. Figure 2-4 shows the comparison between the simulated and measured time-averaged bubble velocities for Case 0.2-3-3 in both the η and z directions, in which the η and z boundaries were defined as $5\%\alpha_{\max}$. It was found that the results by both the RSM and mixture k-ε model agree well with the experimental data (average error level $\bar{e} \leqslant 5.4\%$ for RSM and $\bar{e} \leqslant 6.3\%$ for mixture k-ε model), and the differences between RSM and mixture k-ε model are relatively small. As the distance from the nozzle exit increases, the bubble size distribution tends to be uniform (Zhang and Zhu, 2013), and the predicted bubble velocity matches well with the experimental results.

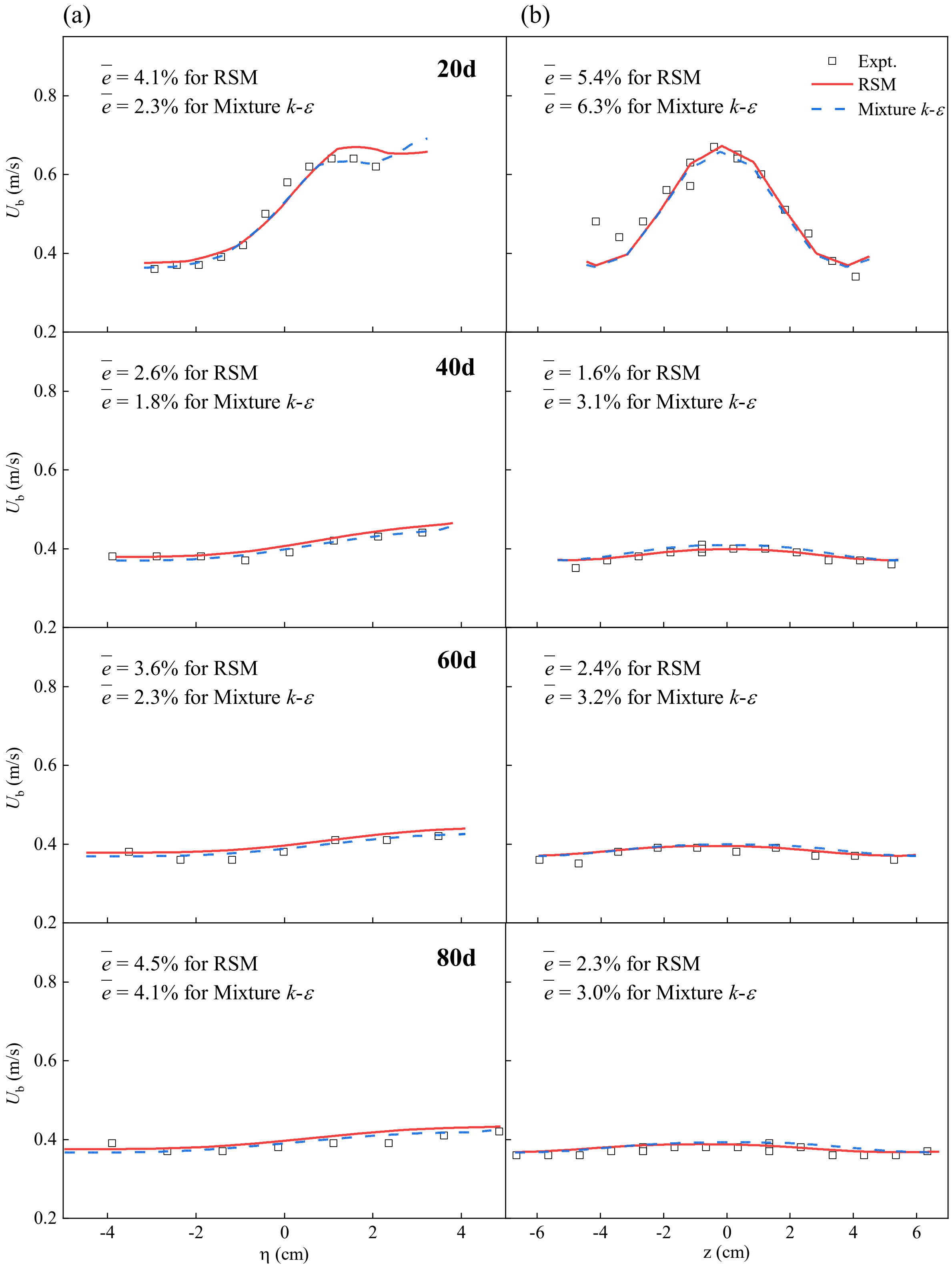

Figure 2-4. Comparison between the simulated and experimental time-averaged bubble velocity at Sections 20-80d for Case 0.2-3-3 in the (a) η direction and (b) z direction. The experimental results

were from Zhang and Zhu (2013), the η and z boundaries were defined by 5%$\alpha_{\max}$, and $\bar{e}$ denotes the average error bar.

The trajectory of water jet centerline was next calibrated for bubbly jets. In the current work, the jet centerline was detected by implementing the scalarTransport function object in OpenFOAM. By using the high speed camera technique, Zhang and Zhu (2014) measured the water jet centerline for both bubbly jets and pure water jets. For pure water jets in crossflow, Lee and Chu (2003) proposed an equation of jet centerline based on experimental and numerical results of advected line puff:

$$\frac{y_c}{L_{mt}} = 2.65\left(\frac{x}{L_{mt}}\right)^{1/2} \qquad \text{for } y_c \le L_{mt} \tag{2-24a}$$

$$\frac{y_c}{L_{mt}} = 1.56\left(\frac{x}{L_{mt}}\right)^{1/3} \qquad \text{for } y_c > L_{mt} \tag{2-24b}$$

where y_c is the centerline location in the y direction, and $L_{mt} = \frac{M_0^{1/2}}{U_a}$ is the momentum length scale for a jet in crossflow. U_a is the ambient crossflow velocity, and the initial specific momentum flux $M_0 = U_0Q_0$, where U_0 and Q_0 are the initial water jet velocity and flow rate, respectively.

Figure 2-5 shows the comparison of the simulated water jet centerlines with the studies of Zhang and Zhu (2014) and Lee and Chu (2003) for Cases 0.2-3-3 (bubbly jet) and 0.2-0-3 (pure water jet). It was shown that both the simulated visual and concentration jet centerlines agree well with the previous studies, and the RSM and mixture k-ε profiles are nearly superimposed by each other. Note that the visual jet centerlines in the numerical simulations were based on the vertical half-width of the iso-volume of $C/C_0 = 0.1\%$, where C is the scalar concentration and C_0 is the initial concentration at the nozzle exit. The concentration centerlines are higher than the visual centerlines, which is typical for jets in crossflow (Lee and Chu, 2003). The vertical locations of the centerlines for the bubbly jet (Case 0.2-3-3) are higher than that for the pure water jet (Case 0.2-0-3) mainly because the bubbly jet has larger initial jet velocity at the nozzle U_{w0} and the lift force of bubbles on the water jet (Zhang and Zhu, 2014).

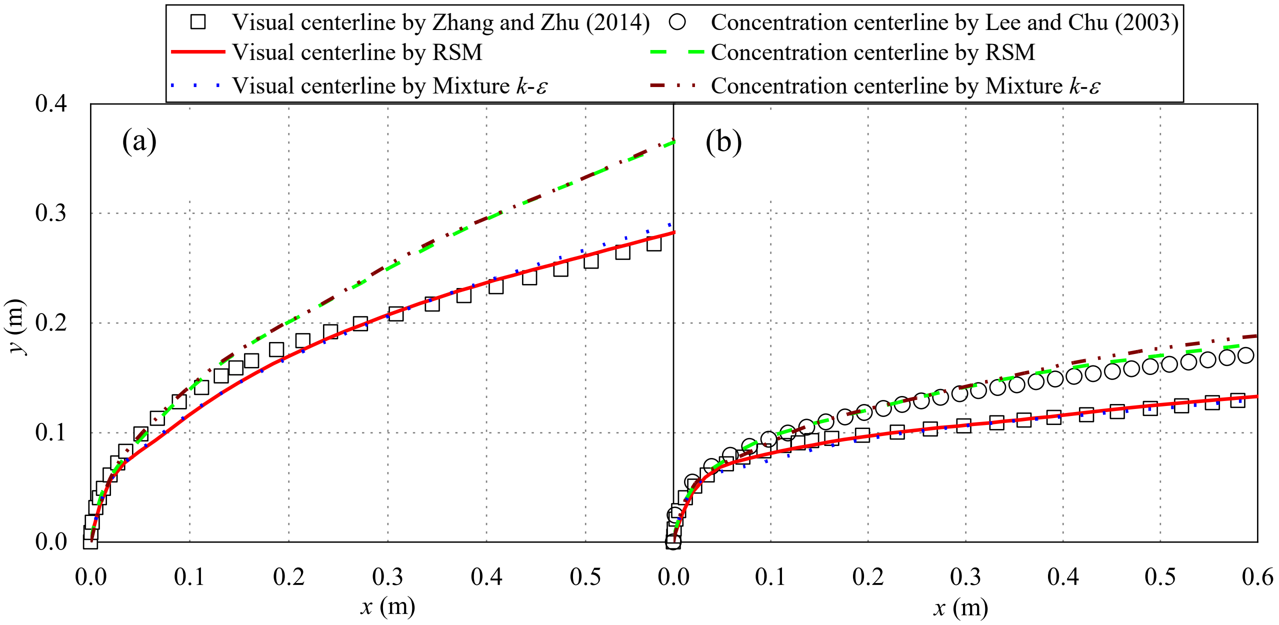

Figure 2-5. Comparison of simulated with experimental/theoretical water jet centerlines for (a) a bubbly jet in crossflow (Case 0.2-3-3), and (b) a pure water jet in crossflow (Case 0.2-0-3). The experimental results were from Zhang and Zhu (2014), and the theoretical results were from Lee and Chu (2003).

The jet expansion (spreading) rate was further calibrated for bubbly jets. For the air phase, Zhang and Zhu (2014) proposed a Gaussian distribution of the gas void fraction as follows,

$$\frac{\alpha}{\alpha_{\max}} = \exp[-0.693(z/b_z)^2] \text{ or } \frac{\alpha}{\alpha_{\max}} = \exp\left[-0.693\left(\eta/b_\eta\right)^2\right] \tag{2-25}$$

where $\alpha_{\max}$ is the maximum gas void fraction, b_z and b_η represent gas-phase half-width in the z and η directions, respectively, and are defined as where $\alpha/\alpha_{\max} = 50\%$.

To investigate the jet expansion simulated by the two turbulence models, Figure 2-6(a) shows that b_z and b_η agree well with the experimental data for both the RSM and mixture k-ε models, and the differences between the two models are small. For the water phase, jet expansion was represented by the visual half-thickness $b_{\mathrm{t,vis}}$ (Zhang and Zhu, 2014). In the simulations, $b_{\mathrm{t,vis}}$ was determined by defining an iso-surface of water-phase with $C = 0.1\%$ (same with that used for determining water jet centerline). Figure 2-6(b) shows that the simulated $b_{\mathrm{t,vis}}$ by both models generally lies well with the experiments, and the maximum differences between the RSM and mixture k-ε models are 4.5% for the bubbly jet, and 6.5% for the pure water jet. For the both jets, small difference between the simulated and experimental $b_{\mathrm{t,vis}}$ occurs near the nozzle, probably because the grid cell size was not fine enough there. Note that the computational time of the RSM is much higher (more than three times) than the mixture k-ε model in this study, owing to the additional transport equations for the Reynolds stresses. Given the similar results predicted by the RSM and mixture k-ε models, which was also illustrated for the flow field in a pure gas jet in crossflow (Le Moullec et al., 2008), the rest of this paper only shows the results of the mixture k-ε model.

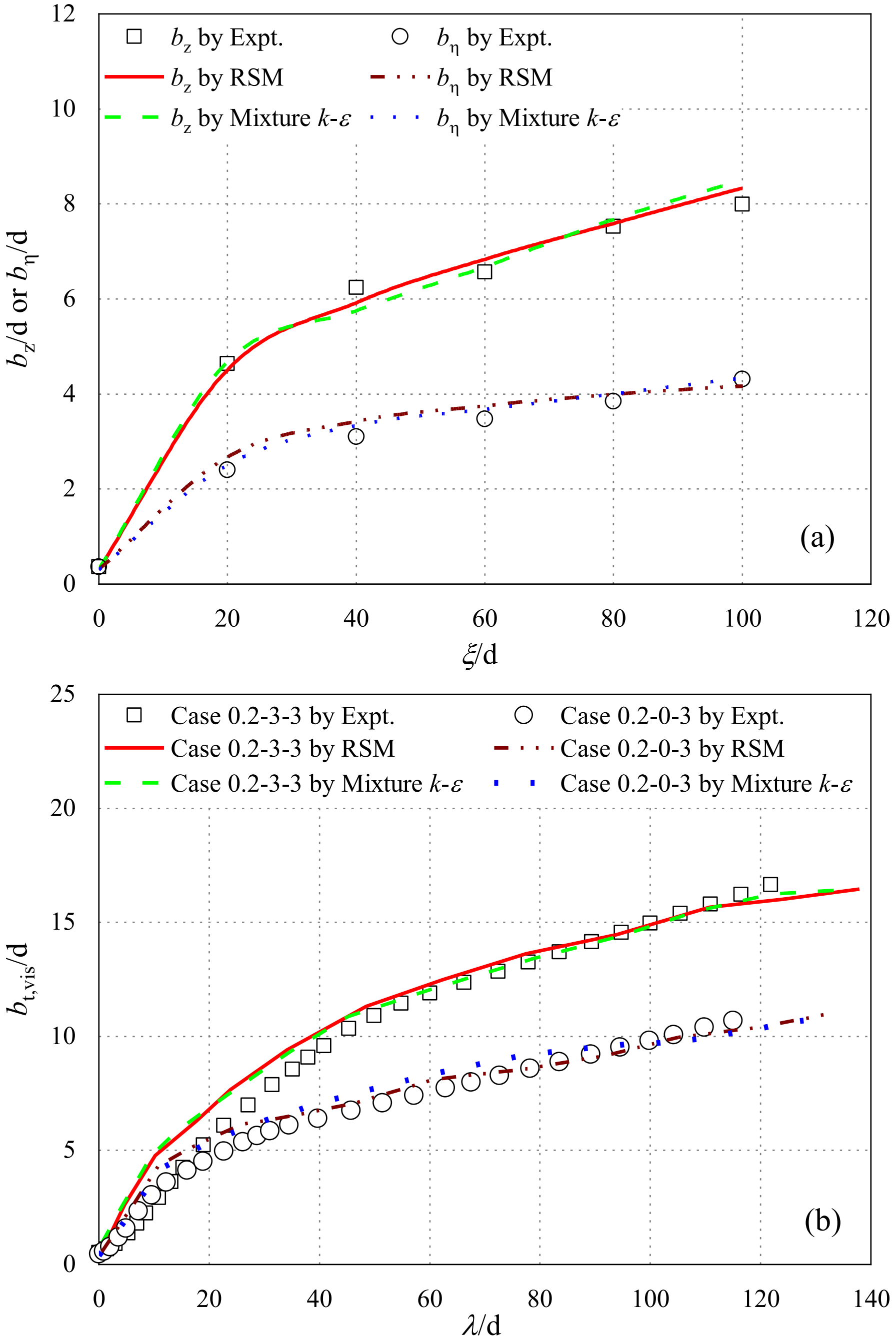

Figure 2-6. Comparison between simulated and experimental (a) half-width of air phase in a bubbly jet (Case 0.2-3-3) and (b) visual half-thickness of water phase in the bubbly jet and a pure water jet (Case 0.2-0-3). The experimental data were from Zhang and Zhu (2014).

The numerical model was validated against the distribution of gas void fraction at Section 80d for Case 0.2-3-3. Figure 2-7 shows the comparison between the predicted and experimental results of Zhang and Zhu (2013), where the simulated cross-section was taken from the iso-volume of gas void fraction $\alpha = 0.05\%$, which was the same as the experiment. As shown in Figure 2-7(a) and (b), the contours of the experimental and simulated gas void fractions resemble each other, either for the kidney shape, range, or the corresponding values. The evolution of gas void fraction at different sections (20-80d) are shown in Figure 2-7(c). It decreases with the increasing distance from the nozzle exit as expected, and the single-peak distribution at Section 20d evolves into two peaks at further distances (60-80d).

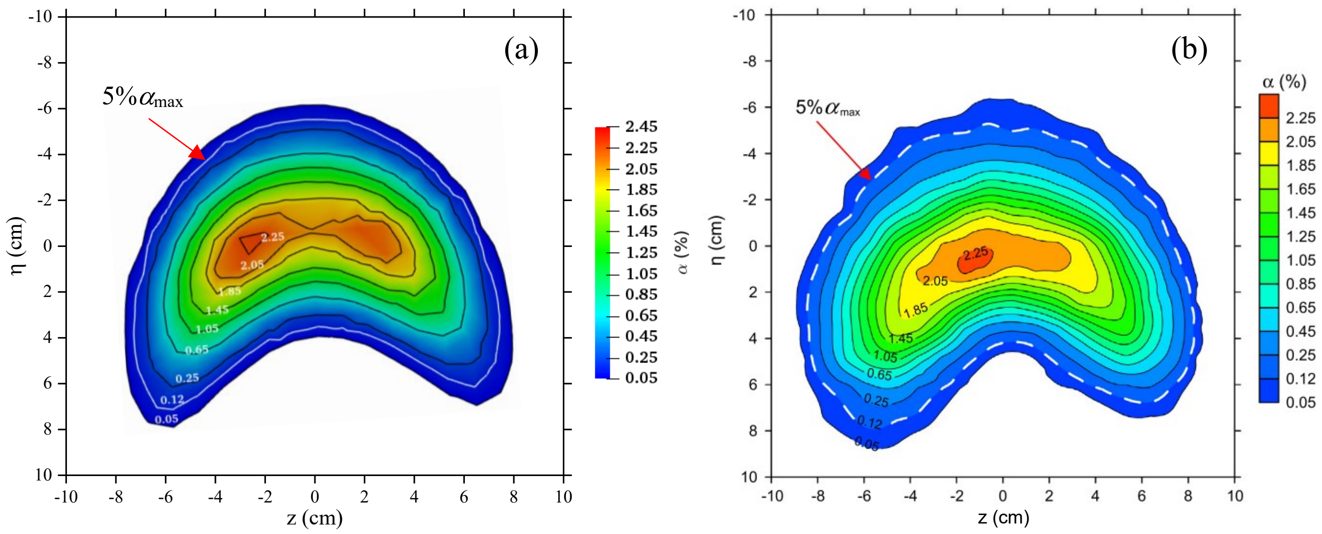

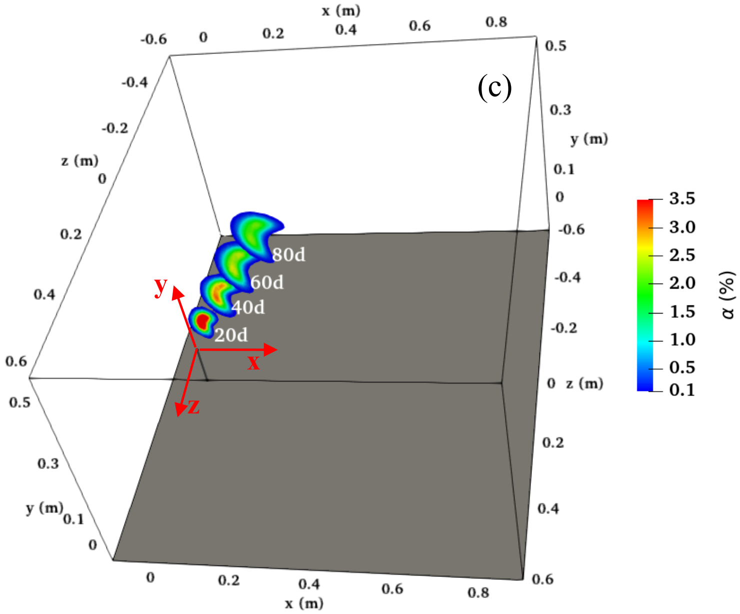

Figure 2-7. Time-averaged gas void fraction distributions for Case 0.2-3-3 at various sections: (a) Section 80d from the URANS model, (b) Section 80d from the experiment of Zhang and Zhu (2013), and (c) Sections 20-80d from the URANS model.

2.4.2. Flow structure and TKE of bubbly jets in crossflow

The instantaneous flow structure of bubbly jets for Case 0.2-3-3 at t = 80 s using the URANS model is shown in Figure 2-8, with the upper part (in red color) representing the air-phase and the lower part (blue color) denoting the water-phase. At the nozzle exit, the two interactive phases (air and water) are injected simultaneously with a volume fraction of $\alpha_0 = 0.5$ for each phase. It was observed that the two phases are initially mixed together after injecting from the nozzle exit, and then the air-phase separates from the water-phase at a certain height, which agree with the experiment of Zhang and Zhu (2013). Figure 2-8 shows that the flow structure simulated by URANS is able to predict the mean flow structure of the bubbly jet, and the turbulence properties were included in the mixture k-ε turbulence model.

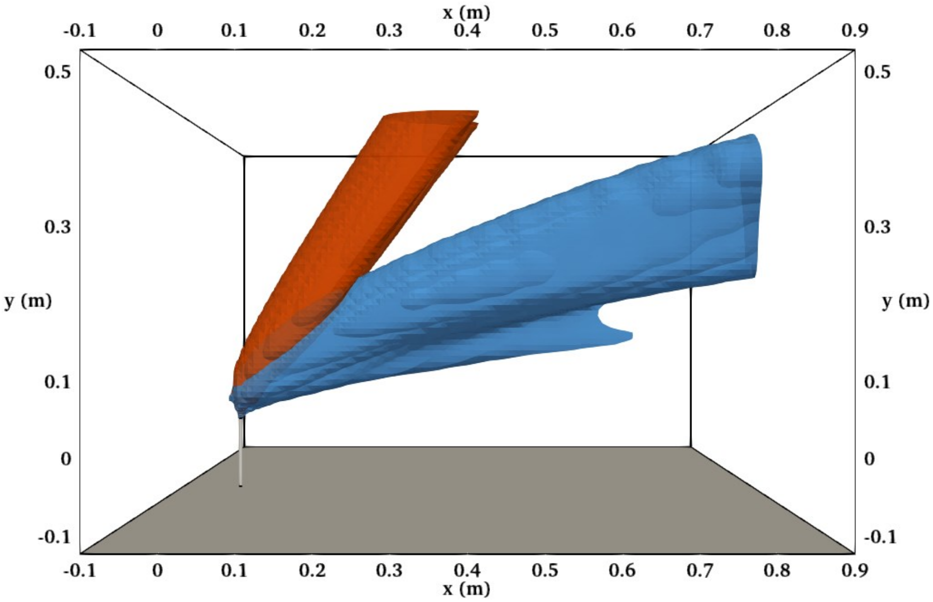

Figure 2-8. Instantaneous flow structures of air-phase (in red color) and water-phase (in blue color) of the bubbly jet of Case 0.2-3-3 at $t = 80$ s. The iso-surfaces of air- and water-phases were defined as $\alpha = 0.05\%$ and $C = 0.05\%$, respectively.

Figure 2-9 shows the vertical distribution of TKE at different sections (Sections x = 4d, 8d, 12d and 16d) in the center-plane (*xy* plane) for both the bubbly jet (Case 0.2-3-3) and pure water jets (Cases 0.2-0-3 and 0.2-0-6). The two pure water jets were selected for the comparison because they have the same initial water jet velocity (Case 0.2-0-6) or the same initial water flow rate (Case 0.2-0-3) as the bubbly jet. It was observed that the location of maximum TKE becomes higher as the jet penetrates farther, and the values of maximum TKE rapidly decrease in the x direction, especially near the nozzle (0.012 – 0.005 m^2/s^2 from 4d to 8d for the bubbly jet). The maximum TKE is larger for the bubbly jet than that for Case 0.2-0-3, mainly because the water velocity at the nozzle is higher for the bubbly jet (twice the Case 0.2-0-3), consistent with that observed in bubbly jet in stagnant water (Wang et al., 2019). However, the maximum TKE of the bubbly jet is smaller than that for Case 0.2-0-6, although the water velocity at the nozzle is the same for both cases. This is probably due to the lower initial water jet momentum for the bubbly jet (half of Case

0.2-0-6) resulted from the lower water jet flow rate, which produces weaker turbulent fluctuations in the flow field.

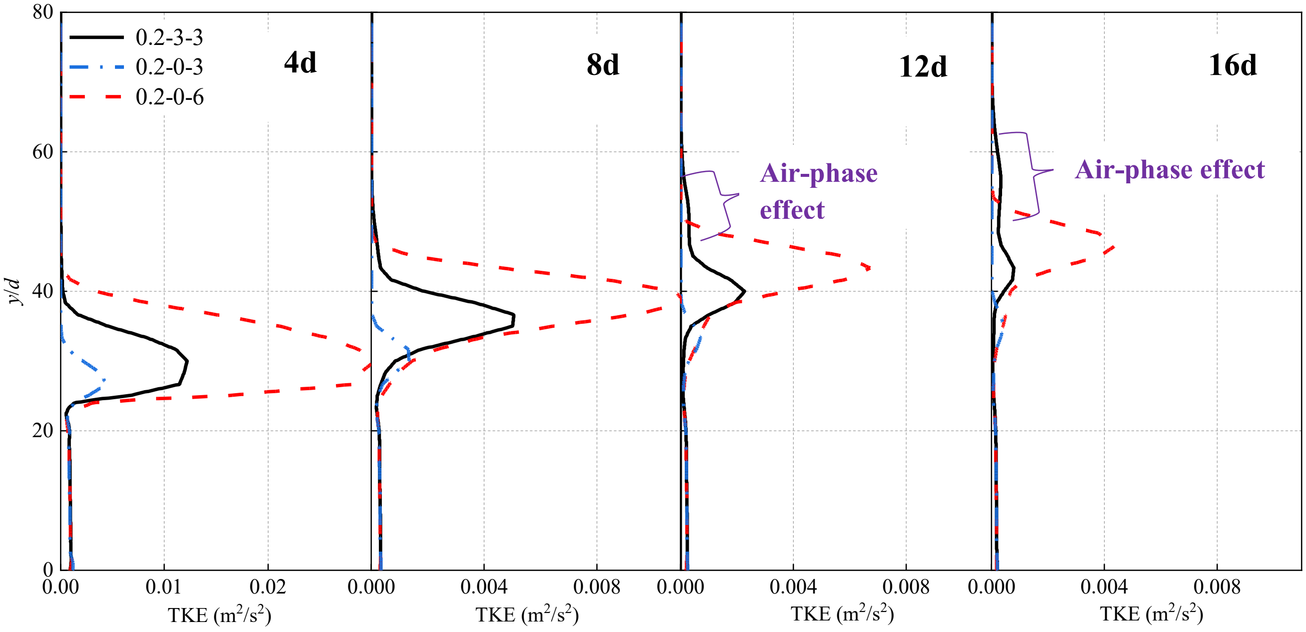

Figure 2-9. Vertical distribution of TKE at different sections (Sections x = 4d, 8d, 12d and 16d) in the center-plane (xy plane) for the bubbly jet and pure water jets.

It is interesting to notice that the TKE distribution evolves from mono-peak to dual-peaks (12d – 16d) as *x* increases for the bubbly jet, where one peak is associated with the water-phase at lower location, and the other is related to the air-phase at higher location. At *x* = 4d – 8d, the mono-peak TKE was mainly dominated by the velocity fluctuations of the air and water jet mixture, since both phases were mixed after injection from the nozzle. However, the air-phase has separated from the water-phase of bubbly jet at *x* = 12d – 16d, and the bubbles appear to increase substantially the turbulence intensity by interacting with the ambient water flow, which has been demonstrated in the bubbly jet in stagnant water (Wang et al., 2019). Therefore, the dual-peak TKE was observed at farther sections, although the maximum value caused by the air-phase of bubbly jet is relatively lower than that by the water-phase. Note that the TKE is relatively smaller ($< 7\times10^{-4}$) in the far-field regions (x > 16d), where the bubbles effect on water jet mixing is also significant and will be illustrated in the following sections.

2.4.3. Water velocity distribution

Figure 2-10 shows the time-averaged in-plane water velocity U_s at different sections of the air-phase in the ξ direction for Case 0.2-3-3, and the cross-section was taken from the iso-volume of α = 0.05%. U_s is the tangential component of U_{yz} at the sections, where $U_{yz} = (U_y \cdot \vec{j} + U_z \cdot \vec{k})$, and U_z is the main contributor to the transverse water movement. U_x was not included in the figure because its absolute value is much larger than U_y or U_z. It was found that water tends to move outwards from the center-plane to form a counter-rotating vortex pair (CVP), and the magnitude of U_s decreases with the increase of distance from the nozzle exit. At Sections 20d and 40d, the water velocity is relatively large (with maximum U_s of 0.18 m/s and 0.08 m/s, respectively), induced by the large initial jet momentum; however, the water velocity varies little at further distances as shown in Sections 60d and 80d, mainly because the water jet separates with the air-phase, and the water in the air-phase region moves under the action of inertia and interaction with bubbles. It is interesting to notice that the water velocity is larger at the bottom and lower at the top of the sections, probably because the water is lifted faster by the bubbles at the bottom region due to the wake of proceeding bubbles, whereas the water is suppressed by the crossflow at the top of the sections.

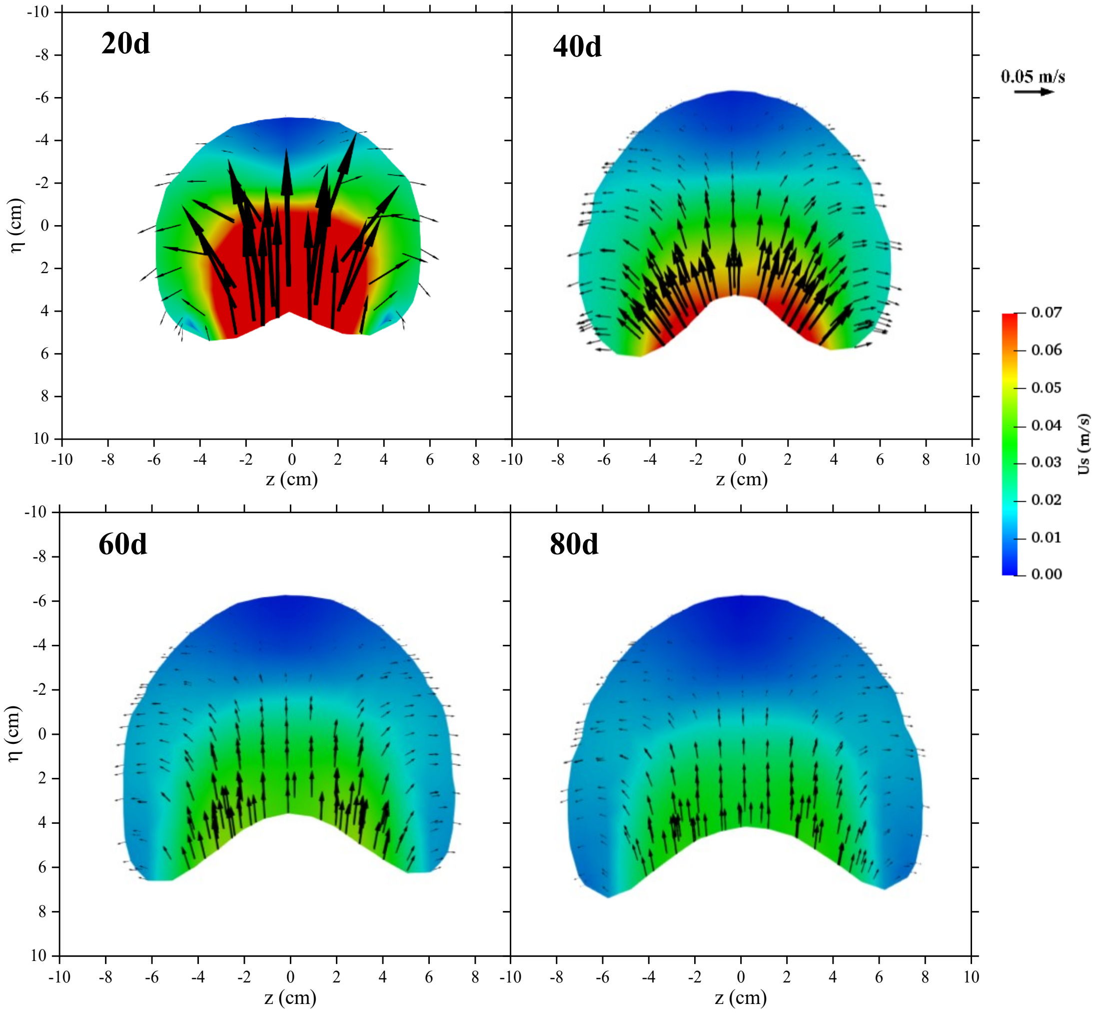

Figure 2-10. Time-averaged in-plane water velocity at different sections (Sections 20-80d) within the air-phase of Case 0.2-3-3.

The bubble effects on the water-phase of a bubbly jet can be better exhibited by comparing the water velocity distributions of the bubbly jet (Case 0.2-3-3) with pure water jets (Cases 0.2-0-6 and Case 0.2-0-3), as shown in Figure 2-11 at the vertical Section *x* = 80d. It was found that the maximum velocity occurs at the center-plane for both the bubbly and pure water jets, consistent with the previous studies for the pure water jet in crossflow (Yuan, 1997; Ziefle and Kleiser, 2009). For the pure water jets, the in-plane velocity is larger for Case 0.2-0-6 than that for Case 0.2-0-3 as expected, because the former has larger initial jet velocity that induces larger and more pronounced CVP (Zhang and Yang, 2017). More importantly, for the bubbly jet, the velocity distribution is both higher and wider than both the pure water jets, with an even more pronounced CVP. Comparison of Case 0.2-3-3 with Case 0.2-0-6 suggests the importance of the lifting and spreading effects of bubbles on the water-phase of a bubbly jet that make the water-phase higher and wider and make the CVP more pronounced and lifted. Comparison of Case 0.2-3-3 with Case 0.2-0-3 suggests the importance of both bubble effects and the effect of the initial water jet velocity.

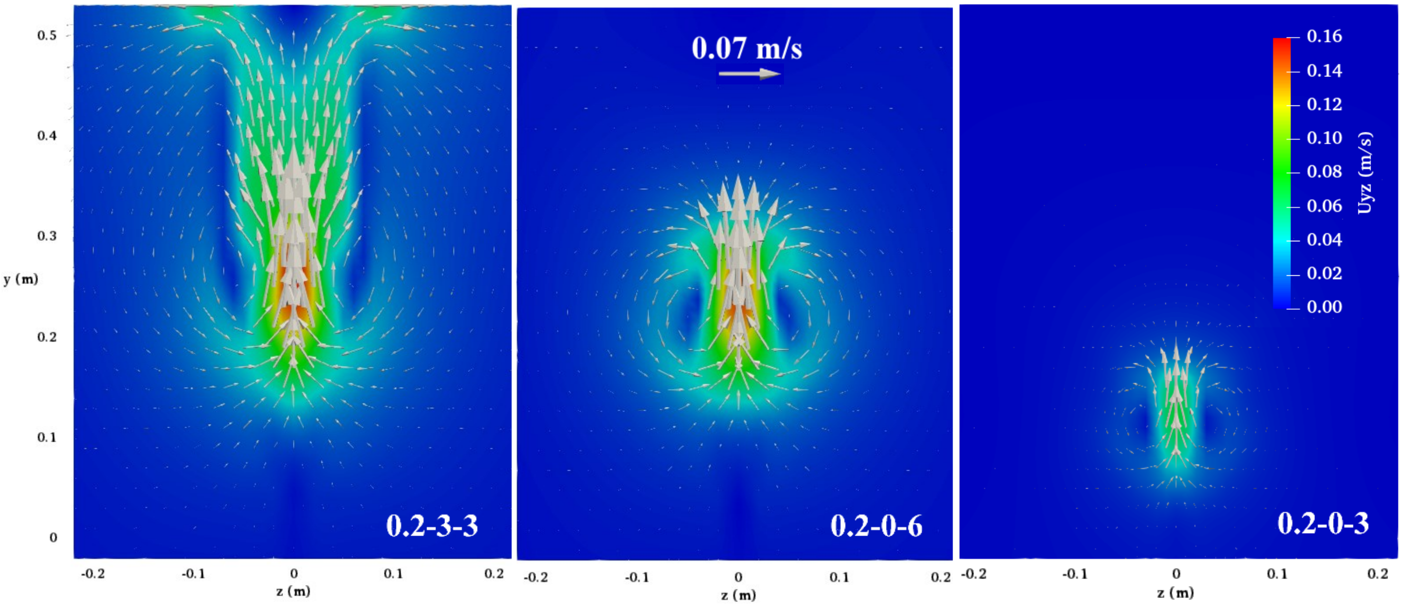

Figure 2-11. Time-averaged in-plane water velocities at the vertical section of x = 80d within the water-phase of the bubbly jet and pure water jets.

2.4.4. Scalar concentration distribution

The injected water of bubbly jets was examined for mixing by introducing a passive scalar with concentration of C_0 = 1.0 at the nozzle exit, where the passive scalar was only implemented into the water phase. Figure 2-12 shows the distribution of normalized concentration C/C_0 at different horizontal sections (xz planes) for the water-phase of Case 0.2-3-3. It was observed that the concentration decreases with the increasing distance from the nozzle, and the spreading area increases correspondingly, both as expected. It is worth mentioning that a “C” shape is formed at Section 15d, and the peak value ($C/C_0 = 0.09$) occurs in the upstream region. The shape evolves into a kidney shape at Section 30d, where the peak value region ($C/C_0 = 0.08$) locates in the two sides of center-plane, and the kidney shape has been elongated at Section 45d due mainly to the transport and mixing of the injected water.

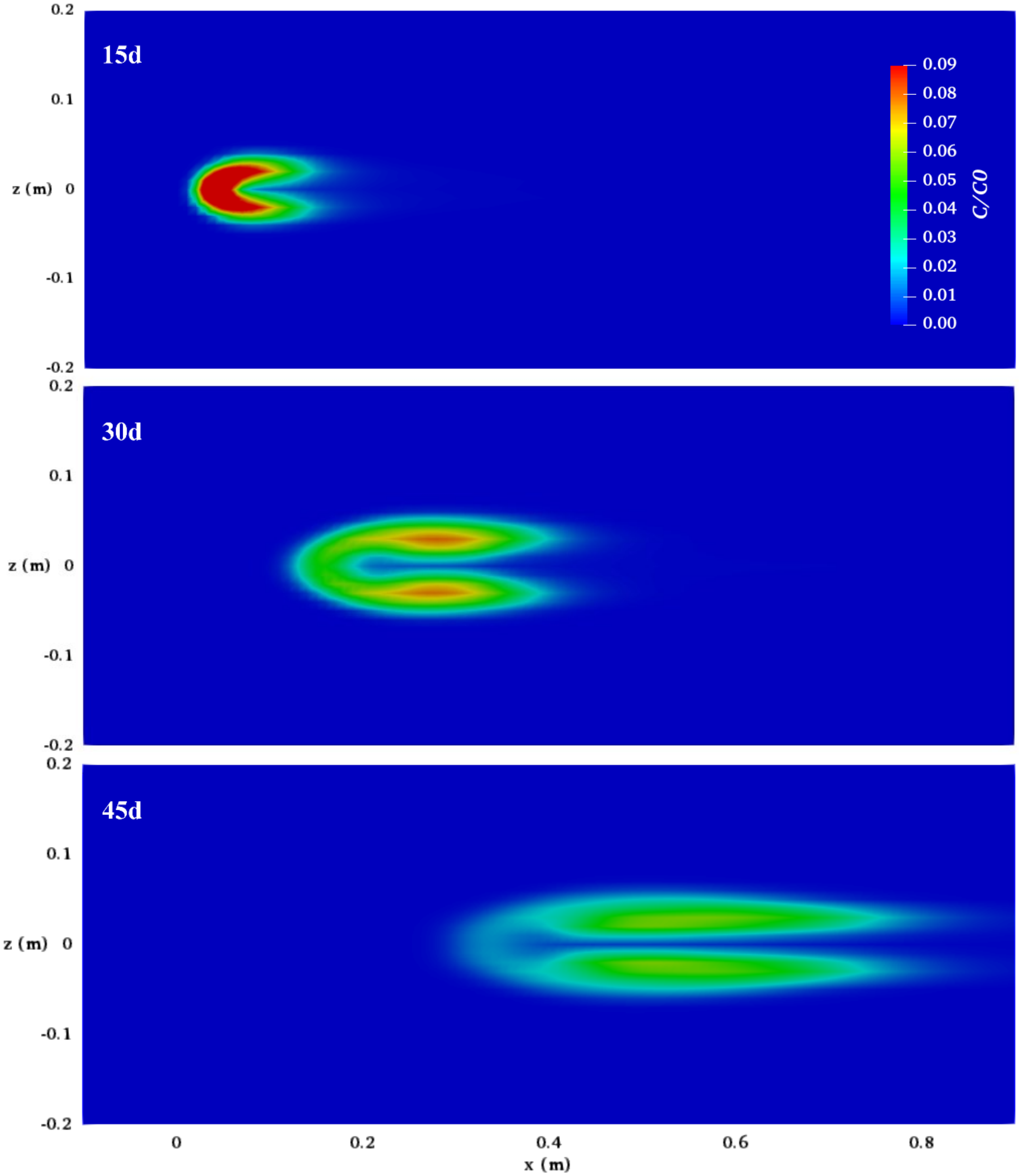

Figure 2-12. Distribution of time-averaged scalar concentration at different horizontal sections (Sections y = 15d, 30d and 45d) for the water-phase of Case 0.2-3-3.

To better illustrate the mixing evolution of water-phase of bubbly jets, as well as to reveal the impact of bubbles on the mixing, the dimensionless center-plane (*xy* plane or $z = 0$ plane) concentration at different vertical sections was plotted in Figure 2-13. It was observed that the concentration increases to its maximum value and then decreases in the vertical (*y*) direction, and the maximum concentration decreases as expected with the increasing distance from the nozzle in the *x* direction. For the pure water jets, compared to Case 0.2-0-3, Case 0.2-0-6 has higher and wider concentration distribution in the *y* direction, and smaller maximum concentration. This can be attributed to the relatively large initial water jet momentum for Case 0.2-0-6 (4 times Case 0.2-0-3), which has been demonstrated to contribute to the spreading and dilution of the water jet in crossflow (Lee and Chu, 2003).

For the bubbly jet of Case 0.2-3-3, the maximum concentration for Case 0.2-3-3 is smaller than that for Case 0.2-0-3, and similar to Case 0.2-0-6. Compared to Case 0.2-0-6, the bubbly jet has larger spreading region, especially at further distances downstream at Sections 64d and 96d, as shown in Figure 2-13. It is interesting to notice that the vertical location of the maximum concentration for the bubbly jet is higher than that for Case 0.2-0-3, but lower than that for Case 0.2-0-6 at Sections 16d and 32d, and it becomes increasingly higher at further distances downstream. This is mainly because that the initial jet momentum for the bubbly jet is twice the Case 0.2-0-3 and half of Case 0.2-0-6, which results in a middle location of the maximum concentration (Lee and Chu, 2003). In addition, at Section 16d where the bubbles have not separated with the water jet, the lift effect of bubbles on the water-phase is weak since the water jet momentum is dominant in this region (Zhang and Zhu, 2013). The water jet is lifted by the bubbles at further distances from the nozzle (Sections 64d and 96d), due mainly to the gas buoyancy effect.

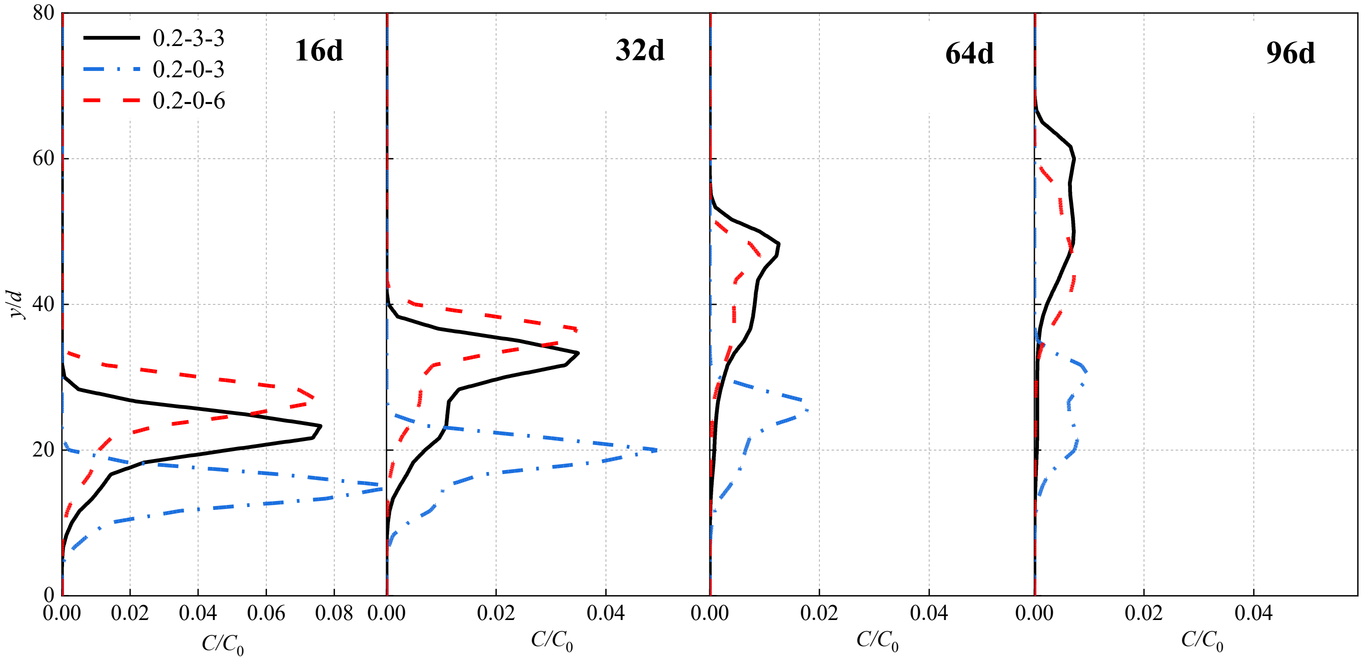

Figure 2-13. Time-averaged center-plane concentration at different sections (Sections x = 16d, 32d, 64d and 96d) for the water-phase of the bubbly jet and pure water jets.

The time-averaged center-plane maximum concentration, C_{max}, in the x direction is compared with the study of Lee and Chu (2003) in Figure 2-14. In the momentum-dominated near- and far-fields, Lee and Chu (Lee and Chu, 2003) proposed:

$$\frac{S_c Q_0}{U_a L_{mt}^2} = 0.16 \frac{y_c}{L_{mt}} \qquad \text{for } y_c \le L_{mt} \qquad (2\text{-}26a)$$

$$S_c = 0.46 \frac{U_a y_c^2}{Q_0} \qquad \text{for } y_c > L_{mt} \qquad (2\text{-}26b)$$

where $S_c = \frac{C_0}{C_{max}}$ represents the jet centerline dilution, and y_c is calculated from Eqs. (2-24a) and (2-24b), respectively.

As shown in Figure 2-14, the maximum concentration decreases sharply to a lower value in a short distance from the nozzle (e.g., C_{max}/C_0 decreased to approximately 0.05 at x/d = 20 for the bubbly jet), and then it decreases slowly with the increasing distances (e.g., C_{max}/C_0 decreased to be higher than 0.005 at x/d = 80 for the bubbly jet). Figure 2-14 shows some differences for the decreasing trends between the present study and the study of pure water jets by Lee and Chu (2003), possibly due to the different domain sizes between the present study and Lee and Chu (2003), as well as the different numerical model setup. However, the center-plane concentrations of Case 0.2-0-3 are larger than that of Case 0.2-0-6 according to both the present and Lee and Chu's studies, which is also consistent with Figure 2-13. The $C_{\max}/C_0$ line of Case 0.2-3-3 overlaps that of Case 0.2-0-6 until $x/d = 40$, after which the bubbly jet profile locates between the two pure water jets. This is probably because the bubbles have already separated from the water phase of the bubbly jet at $x/d = 40$ as presented in Zhang and Zhu (2014), and thus the water-phase acts as a pure water jet afterwards. As described in Eqs. (2-24) and (2-26), a higher initial jet momentum contributes to a higher dilution, and therefore, the maximum concentration profile of the bubbly jet locates between the two pure water jets because its initial jet momentum is between those of the two pure water jets as stated above.

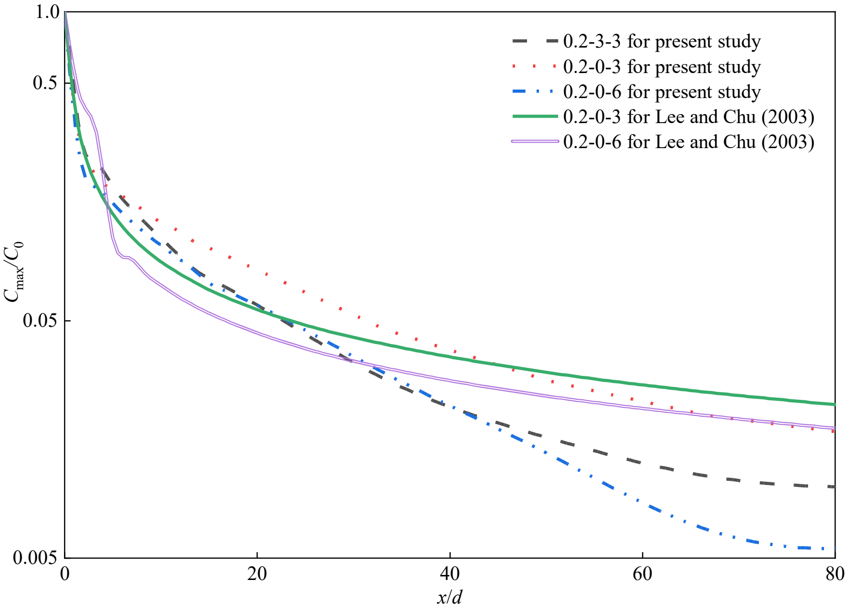

Figure 2-14. Time-averaged maximum concentration at the center-plane (*xy* plane or $z = 0$ plane).

2.4.5. Vorticity distribution

The CVP is the typical, dominant vortex feature for jets in crossflow, which is resulted from the stretching and reorientation of the flow vorticity that originates from the near-field (Yuan et al., 1999). Figure 2-15 shows the positive and negative streamwise vorticities ω_x (calculated by $\frac{\partial U_z}{\partial y} - \frac{\partial U_y}{\partial z}$) at different sections for the water-phase of the bubbly and pure water jets. Overall, the vorticity magnitude decreases with the increasing distance from the nozzle, which can be attributed to the decreasing in-plane velocity U_{yz}. For the pure water jets, it was observed that the positive and negative ω_x distribute at the two sides of the center-plane respectively, with maximum absolute value locating near the centers of CVP, which has been demonstrated by various researches (Yuan et al., 1999; Ziefle and Kleiser, 2009; Du et al., 2019). The maximum vorticity magnitude is larger for Case 0.2-0-6 than that for Case 0.2-0-3 as expected (e.g., 11 for Case 0.2-0-6 and 7 for Case 0.2-0-3 at Section 16d). The location of the maximum vorticity magnitude is higher for Case 0.2-0-6, corresponding with the velocity distribution shown in Figure 2-11.

It was observed that the maximum vorticity magnitude is higher for Case 0.2-3-3 than that for Case 0.2-0-3, but slightly lower than that for Case 0.2-0-6, and the spreading area is much larger for the bubbly jet. Compared to the pure water jets, the evolution of vorticity is much faster for the bubbly jet, especially in the vertical y direction. It is interesting to note that ω_x of the bubbly jet is stretched at the top of the two axisymmetric regions, and the vorticity contour evolves from two vertical “kidney-shapes” at Section 16d to two axisymmetric “thumb-up-shapes” at Section 96d. The two long vortex regions formed in the vertical direction indicate that the water is lifted in the two regions to extend the CVP shown in Figure 2-11.

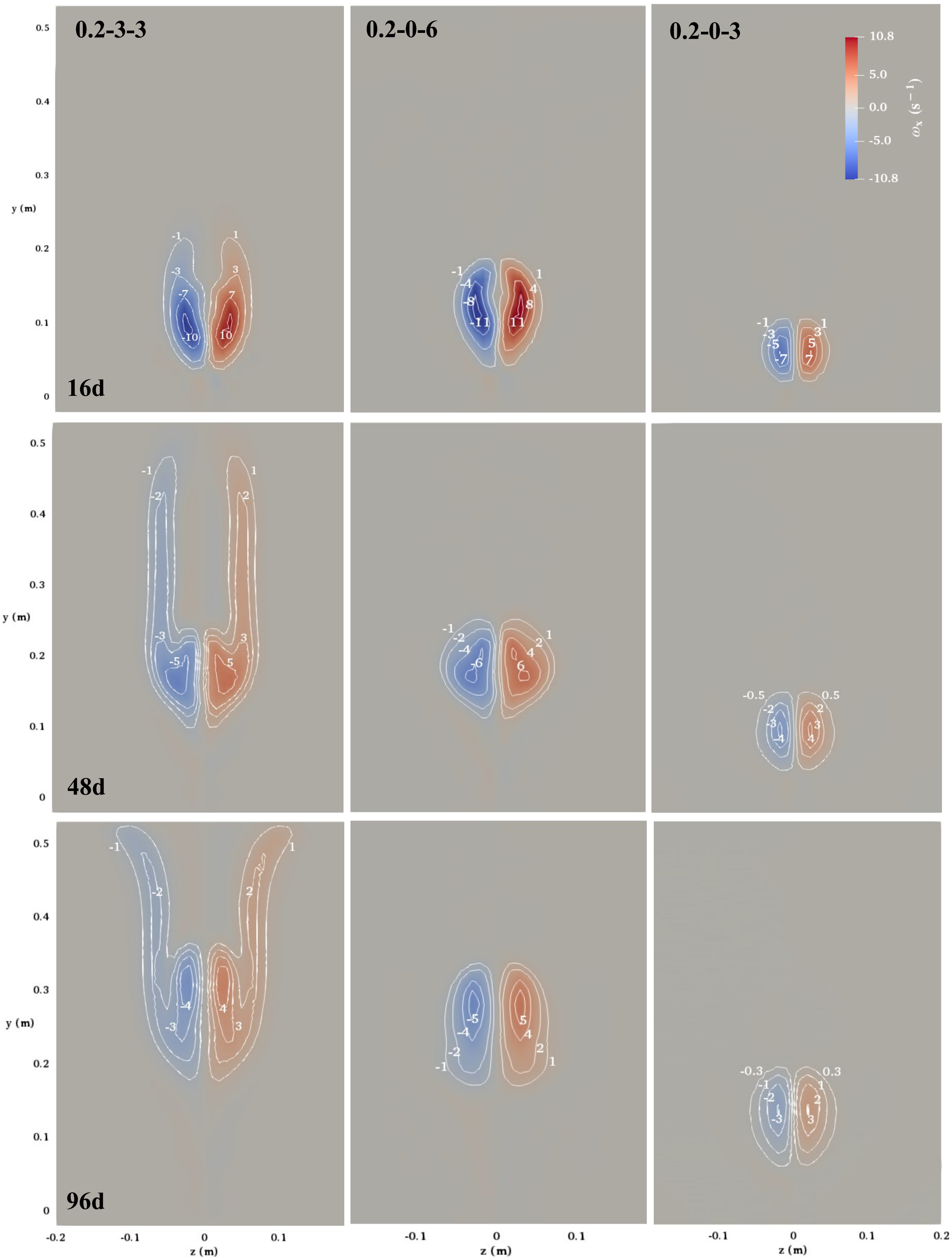

Figure 2-15. Positive and negative streamwise vorticity at different vertical sections (Sections *x* = 16d, 48d and 96d) for the water-phase of the bubbly jet and pure water jets.

To further illustrate the lift phenomenon by bubbles, Figure 2-16(a) and (b) show the iso-surfaces of ω_x = -2 (blue color) and 2 (red color) s^{-1} for both the pure water jet (Case 0.2-0-6) and bubbly jet (Case 0.2-3-3), respectively. For the pure water jet, the vorticity shapes are approximately axisymmetric to form the CVP (Figure 2-16a), similar with that observed in the experiment by Coletti et al. (2013). In addition to the CVP induced by the water injection, two pronounced vortex structures are stretched out at x = 0.2 m (where the bubble plume starts to separate from the water jet as shown in Figure 2-8) in the bubbly jet (Figure 2-16b), which are located at higher positions of both sides of the water-jet-induced CVP. This interesting phenomenon can be related to the lift effect of air bubbles, which enhances water rotation and thus mixing outside of the water-jet-induced CVP.

The bubble effect on water movement can be more clearly demonstrated in Figure 2-16(c) and (d), in which the ω_x contours and water velocity vectors (white color) in the half-plane of Section x = 96d are displayed, accompanying with the streamlines originated from a vertical line (z = 0.05 m) at the crossflow inlet. For the pure water jet (Figure 2-16c), the streamlines under the nozzle and at y > 0.3 m act as free-stream lines, while the streamlines originated from about y = 0 - 0.2 m tend to twist in the clockwise direction, resulting in the formation of CVP caused by the water injection. On the other hand, for the bubbly jet, the behavior of streamlines originated from y < 0.2 m is similar with that for the pure water jet. However, the twist of streamlines at higher positions is also observed in the bubbly jet (Figure 2-16d), although the twist is weaker compared to the water-jet-induced CVP region. This twist of streamlines can be attributed to the upward and outward water movement (indicated by the velocity vectors) induced by the air bubbles, which tend to spread in both y and z directions. Eventually, the water reaches the top surface and moves outwards to tilt the vorticity distribution, resulting in a “thumb-up-shape” at Section 96d.

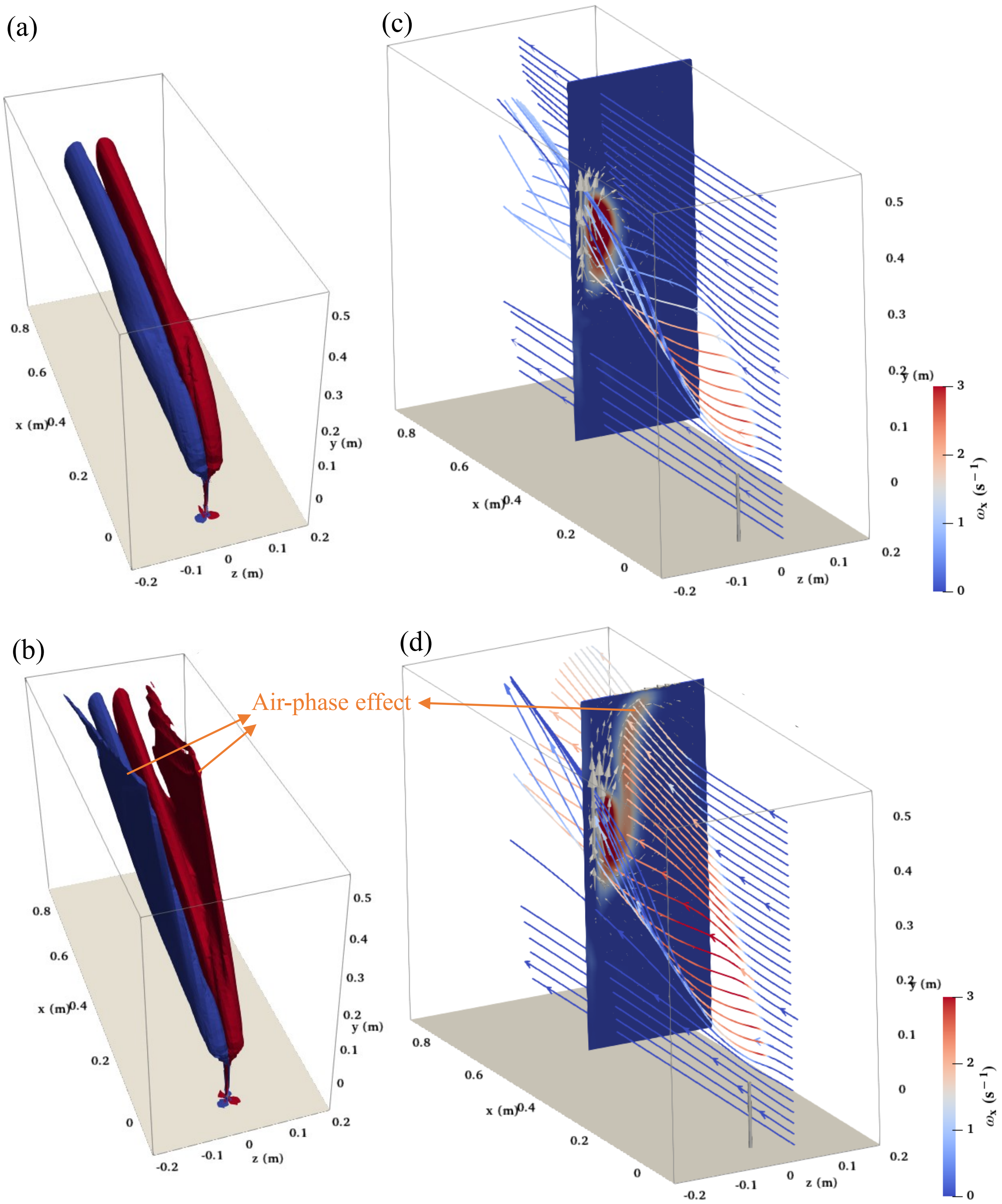

Figure 2-16. Iso-surfaces of ω_x = -2 (blue color) and 2 (red color) s^{-1} for the (a) pure water jet (Case 0.2-0-6) and (b) bubbly jet (Case 0.2-3-3); ω_x contour and water velocity vectors (white color) at Section x = 96d, and streamlines originated from a vertical line (z = 0.05 m) at the crossflow inlet for the (c) pure water jet and (d) bubbly jet.

2.4.6. Effects of crossflow

The ratio of jet exit velocity to crossflow velocity *r* plays a significant role in single-phase jet in crossflow, and the larger value enhances the CVP strength, jet penetration, as well as jet entrainment and mixing (Plesniak and Cusano, 2005). In the present work, three crossflow velocities (0.2, 0.5 and 1.0 m/s, corresponding *r* equal to 17.5, 7.0, and 3.5 respectively) were selected to investigate the hydrodynamics of a bubbly jet. As shown at Section 64d in Figure 2-17, the locations of the maximum concentration, maximum velocity magnitude, maximum vorticity magnitude and water jet centerline all tend to be lower with the increasing crossflow velocity. It was found that the maximum concentration is similar for the three cases in Figure 2-17(a). The concentration configuration in Case 0.2-3-3 shows a kidney shape, whereas it tends to shrink to a circular shape as the crossflow velocity increases. Furthermore, the concentration distribution changes from two peaks to one peak as the crossflow velocity increases, revealing that the crossflow velocity plays a negative role in water jet mixing and spreading.

The velocity and vorticity distributions at Section x = 64d for different crossflow velocities are shown in Figure 2-17(b) and (c), respectively. Both of them show the sharp decreases in the vertical and transverse distributions, illustrating that the bubbles effect on the lifting and spreading of water jet becomes weaker for a larger crossflow velocity. In addition, the maximum velocity magnitude decreases with the increasing crossflow velocity, but the maximum vorticity magnitude varies little, indicating that the rotation of water jet tends to concentrate on a small region for a large crossflow velocity.

Figure 2-17(d) shows the water jet centerline trajectories in different crossflow velocities, and the visual centerline for Case 0.2-3-3 by the present work agrees well with that by Zhang and Zhu (2014). As the crossflow velocity increases, the jet centerline becomes lower, and the deviations between visual and concentration centerlines reduce to a negligible value, mainly because larger crossflow restricts the spreading of the jet as shown in Figure 2-17(a), causing the small difference between the two centerlines.

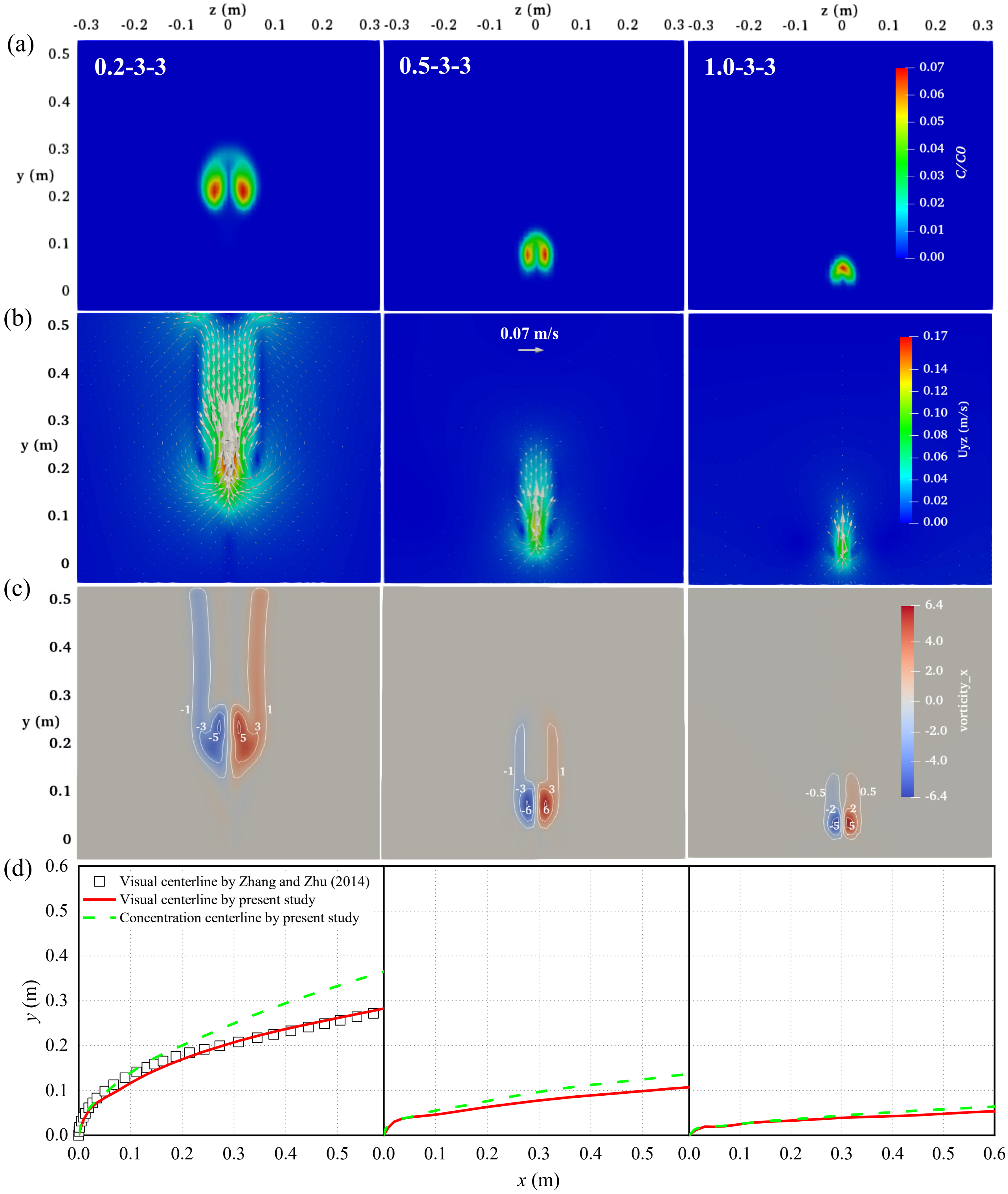

Figure 2-17. Impacts of crossflow velocity to time-averaged properties of bubbly jets: (a) scalar concentrations, (b) in-plane water velocities and (c) vorticities at Section *x* = 64d, as well as (d) water jet centerline trajectories.

2.5. Summary and conclusions

Bubbly jets in crossflow are commonly encountered in many applications, but the numerical simulation on this topic is rare. In this study, a 3-dimensional mathematical model was developed, calibrated and validated to investigate the hydrodynamics that cannot be measured (or measured easily) for both two-phases of air-water bubbly jets in crossflow. By using the open source code OpenFOAM, the Euler-Euler two-fluid model was coupled with the URANS approach. Four different mesh sizes were compared to explore the relationship between grid cell size (Δ) and bubble diameter (d_b), and the mesh size with $\Delta/d_b = 3.3$ provides best agreement with experimental results.

The results showed that the modeled gas void fraction, bubble velocity and water jet centerline trajectories agree well with the experimental data, suggesting its robustness in predicting the mean flow properties of both phases of bubbly jets in crossflow. The main conclusions from this paper are as follows:

(1) The TKE is mainly concentrated in the near-field region (x < 16d). The location of maximum TKE becomes higher as the jet penetrates farther, and the values of maximum TKE rapidly decrease in the x direction, especially near the nozzle. The TKE distribution evolves from mono-peak to dual-peaks as x increases for the bubbly jet due to the interactions between bubbles and ambient water flow.

(2) The in-plane water velocity at the air-phase cross-sections is large near the nozzle, induced by the initial jet momentum, and it decreases sharply from Section 20d to 60d but varies little at larger distances from Section 60d to 80d. Additionally, the water velocity is larger at the bottom and lower at the top of the sections.

(3) The water velocity distribution at the water-phase cross-sections of bubbly jet is higher and wider than the pure water jets with the same initial jet exit velocity and water flow rate, and the maximum water velocity occurs at the center-plane for both bubbly and pure water jets. A pronounced CVP can be well modeled for both the bubbly and pure-water jets.

(4) Generally, the center-plane maximum concentration decreases in the crossflow (x) direction. Compared to pure water jets, the water-phase of bubbly jets is wider in the vertical direction and thus dilution is larger due to the lift of bubbles.

(5) The vorticity contour at the water-phase cross-sections shows a pronounced difference between the bubbly and pure water jets. For bubbly jets, the vorticity is stretched at the top of the two axisymmetric regions, and the vorticity contour evolves from two vertical "kidney-shapes" to two axisymmetric "thumb-up-shapes".

(6) As the crossflow velocity increases, the locations of maximum concentration, maximum velocity magnitude, maximum vorticity magnitude, as well as water jet centerline, all tend to be lower for bubbly jets. With the increase of crossflow velocity, the deviation between the visual and concentration water jet centerlines reduces, and it becomes negligible when the crossflow velocity is large (r = 3.5). In addition, the maximum water velocity magnitude at the water-phase cross-sections of bubbly jets decreases with the increasing crossflow velocity, but the maximum vorticity magnitude varies little.

3. Experiment on bubble characteristics of turbulent bubbly jets in pipe crossflow*

3.1. Introduction

Bubbly jets can be generated by injecting air-water mixtures from submerged nozzles, and bubble behaviors in two-phase jets have attracted considerable interests in many engineering applications including artificial aeration in oceans, lakes and rivers (Asaeda and Imberger, 1989; Schladow, 1993; McGinnis et al., 2004; Wang et al., 2019), exploitation of offshore natural gas (Zheng et al., 2003), subsea blowouts (Milgram, 1983; Swan and Moros, 1993; Yapa et al., 2010), bubble breakwaters (Sun and Faeth, 1986), chemical and nuclear industrial applications (Seol et al., 2007; Zhang et al., 2020), among others. In oceans, lakes and rivers, the existence of bubbles can increase dissolved oxygen concentration by oxygen mass transfer through the air-water interface, and enhance water mixing by entraining ambient water into the bubbly jet. Compared to bubble plumes induced by pure gas injection, the additional water injection at the source (nozzle) promotes the formation of smaller bubbles that have longer residence times, both enhancing interfacial mass transfer (Lima Neto et al., 2008a, b; Zhang and Zhu, 2013).

Crossflowing ambient water is commonly present in oceans, lakes and rivers, which increases the complexity of bubble behaviors in bubbly jets or bubble plumes (Karagozian, 2014; Behera and Saha, 2020; Dong et al., 2021). It has been reported that smaller bubbles can be generated by the crossflowing water (Loubière et al., 2004), and the bubble coalescence tends to be reduced by

---

* The content of this chapter has been published as: Zhang, H., Yin, Z., Chen, M., Zhang, W., 2023. Experiment on bubble characteristics of turbulent bubbly jets in pipe crossflow. Ocean Eng. 271, 113782.

the crossflow, thereby affecting the bubble size distribution (Oguz and Prosperetti, 1993; Tan et al., 2000; Jobehdar et al., 2016). Socolofsky and Adams (2002) conducted physical experiments with various dispersed phases (air, oil, and alcohol) in crossflows, and found that air bubble plumes showed a stronger separation from the entrained ambient water than oil-alcohol plumes as a result of higher slip velocities of bubbles. Zhang and Zhu (2013) investigated the behaviors of air-water bubbly jets in crossflowing water, and the bubble characteristics such as gas void fraction, bubble size distribution and bubble slip velocity were measured using an optical fiber probe. Zhang and Zhu (2014) further investigated the trajectories of bubbly jets in crossflow. The results revealed that bubbles tend to separate from the water jet at a certain distance from the nozzle, and the separation height and centerline trajectories of both the air and water phases were modeled.

A few studies also examined pure gas jets in crossflow (Socolofsky and Adams, 2002; Wang and Socolofsky, 2015; Xu et al., 2018). When a gas jet is injected into crossflowing water, the ambient flow structures and static pressure become unsteady and complicated via the release of a gas jet in the form of bubbles, and bubble behaviors are mainly dependent on the crossflow velocity (Dong et al., 2020). For instance, with the increase of crossflow velocity, bubble breakup occurs and bubble rise velocity will be suppressed; and bubble rise velocity in strong crossflow resembles the terminal velocity of a single bubble in stagnant flow (Wang and Socolofsky, 2015; Xu et al., 2018). Moreover, with the increase of crossflow velocity, the gas-phase trajectories become more curved and fluctuations occur at the gas-liquid interface (Dong et al., 2020). Recently, Dong et al. (2021) experimentally and numerically studied the flow structures of gas jets into crossflow, and a modified integral model was proposed to predict the gas jet evolution, including jet trajectory, inclination angle and penetration length.

Note that all the above-mentioned studies of bubbly jets, air jets or bubble plumes in crossflow were conducted in free-surface crossflow. Relevant studies in crossflow with the top solid boundary effects (e.g., in a pipe/conduit or under ice-cover) are much scarce; yet understanding such effects is important in many applications such as in ocean/river ice prevention (Hussain and Narang, 1984; Cui et al., 2018; Kan et al., 2020; Wang et al., 2020), oil/gas transport in pipelines (Chen et al., 2020; Chen et al., 2022b; Wang et al., 2022), and artificial aeration in ice-covered rivers (Lima Neto et al., 2007). Balzán et al. (2017) studied a gas jet into liquid crossflows in a square conduit, identified three bubble formation regimes near the nozzle (single bubbling, pulse bubbling, and jetting), and determined the effects of dimensionless parameters (e.g., Froude and Reynolds numbers of the gas phase) on the bubble formation. Kang et al. (2019) investigated the bubble characteristics in a closed loop, where the air was injected vertically into flowing water. The trajectory patterns and bubble velocity were investigated under different crossflow velocities, and the relationships between bubble aspect ratio and the Eötvös and Weber numbers were established. Dhar et al. (2021) measured the void fraction, bubble size and velocity of bubble plumes using a fiber optical probe in a pipe. The results indicated that the bubble size increases as the air flow rate increases and the larger bubbles tend to rise to the top side of bubble plumes, both agree with the conclusion of Zhang and Zhu (2014) in free-surface crossflow. Note that these above studies in pipe/conduit crossflow were based on pure gas injection, and thus knowledge gaps still exist on bubbly jets in pipe/conduit crossflow, especially after bubbles reach the top wall boundary.

Regarding measurement techniques of bubbles, various intrusive and non-intrusive methods have been reported. Typical intrusive methods are via needle-type optical fiber probes (Dhar et al., 2021; Behzadipour et al., 2022), conductivity/resistivity probes (Chanson, 2002; Shi et al., 2018;

Dong et al., 2019a), and wire-mesh sensors (Da Silva et al., 2010; Wiedemann et al., 2019). The non-intrusive methods include image processing techniques (Mohagheghian et al., 2020; Cerqueira and Paladino, 2021), Laser Doppler Anemometry (Kulkarni et al., 2001; Gvozdić et al., 2019; Timkin and Gorelik, 2020), particle image velocimetry (Rezvani and Socolofsky, 2012) and particle tracking velocimetry (Seol et al., 2007). Both intrusive and non-intrusive methods have its own pros and cons. The intrusive methods require direct contact between probes and bubbles, which may disturb the surrounding flow field (Cerqueira and Paladino, 2021) or underestimate bubble size (Xu et al., 2018). This limitation can be avoided by using the non-intrusive methods, despite its high requirement of optical access to the flow (De Oliveira et al., 2015).

To the authors' knowledge, this study is probably the first investigation on bubble characteristics of air-water bubbly jets in pipe crossflow. Based on the non-intrusive image-processing method, the bubble characteristics were investigated under different scenarios, and relationships between gas-phase trajectory and flow properties were established. The boundary effects of pipe wall on bubble properties were particularly explored, such as the distributions of gas void fraction, bubble diameter and gas-phase half-width after bubbles reach the top pipe wall. Moreover, bubble mean velocity components in different directions, as well as bubble turbulence characteristics, were studied for the first time in bubbly jets.

3.2. Experimental setup and methodology

3.2.1. Experimental apparatus and procedures

The experiments were conducted in a horizontal pipe with a diameter d_p = 0.25 m and a length l_p = 7.50 m at the University of Alberta (Figure 3-1). At one end of the pipe, tap water at 20 °C was supplied by an underground reservoir through a pump, and a flow straighter was mounted at the inlet of the pipe. At the other end of the pipe, a basin was built to guide the flow into the underground reservoir. To ensure full pipe flow condition and control the flow rate in the pipe, a slide gate was mounted at the outlet of the pipe. The flow was measured via a magnetic flow meter.

As shown in Figure 3-1(a), a circular nozzle of 6 mm was set vertically at 2 cm above the pipe bottom. The air and water were pre-mixed in a Venturi injector (Model 384, Mazzei Injector Corp.) before exiting from the nozzle, as shown in Figure 3-1(b). The air was supplied at a constant pressure of 1 atm from a gas line in the laboratory, and the air and water flow rates were controlled with rotameters. To remove visual distortion of bubbly jets caused by curvature effect of pipe wall, a rectangular transparent box with 3.5 m × 0.5 m × 0.5 m (L × W × H) was built around the pipe and the space between the box and the pipe was filled with water. Similar technique has been adopted by previous studies (Razzaque et al., 2003; do Amaral et al., 2013; Deendarlianto et al., 2019).

As shown in Figure 3-1(b), the origin of the coordinate system was defined at the nozzle exit. x, y, and z represent the longitudinal, transverse, and vertical directions, respectively. ξ indicates the mean trajectory of gas-phase centerline, and η is in the direction perpendicular to ξ and points upwards. The touching distance X_0 is defined as the horizontal distance from nozzle exit to the location where the centerline of bubble plume touches the top pipe wall.

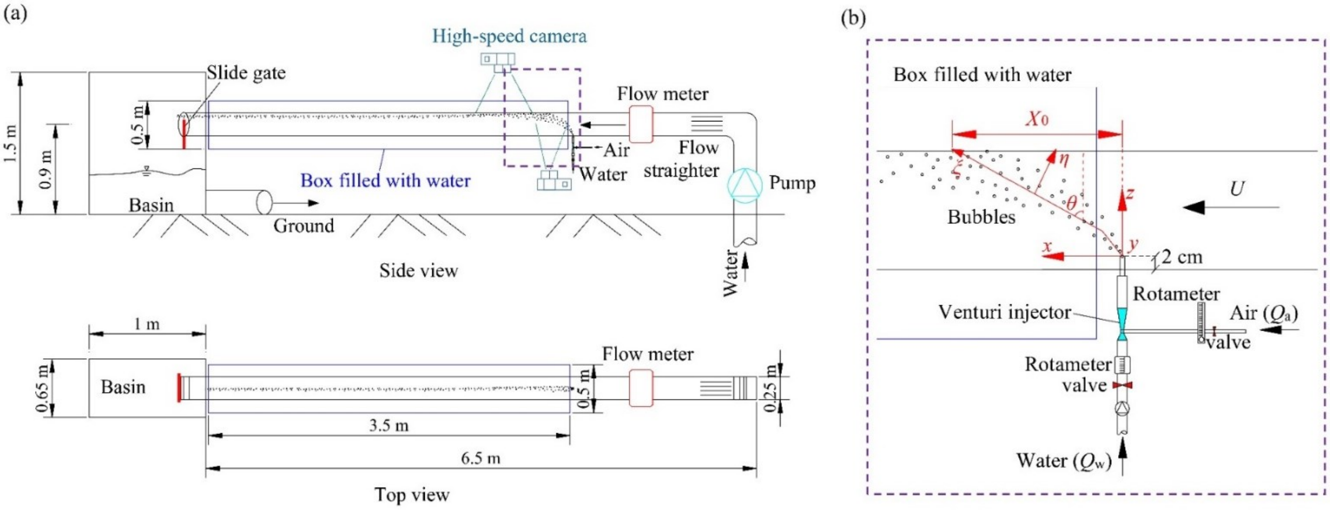

Figure 3-1. Schematics of the experimental setup: (a) side view and top view of the setup; (b) detail near the nozzle and the definition of the coordinate system.

A high-speed camera (Phantom V211, Vision Research Inc.) was used to visualize the bubbles of the bubbly jets. To cover the entire range before and after bubbles reach the top pipe wall, the horizontal measurement range is x = 40 - 465 mm for the side view, and x = 530 - 880 mm for the top view. Images were taken at 200 frame per second with a resolution of 1280 × 800 pixels, and the exposure time was set as 20 μs. A total of 5,477 images were captured for each experimental scenario. The background light source was provided by 2 × 1000 watts halogen lamps and diffused in a softbox.

3.2.2. Experimental scenarios

In this study, a total of 8 experimental scenarios (Table 3-1) were conducted to investigate the bubbly jet behaviors in pipe crossflow. The ambient pipe flow rate Q was set as 20, 30 and 40 L/s (corresponding to ambient flow velocity U = 0.4, 0.6 and 0.8 m/s, respectively); the air flow rate Q_a was 1, 3 and 5 L/min; and the injected water flow rate Q_w was 0, 1.5, 2.3 and 3 L/min. It should be noted that the bubble plume scenario (Q_w = 0) is a special scenario of bubbly jets. The experimental I.D. of each scenario was named after the sequence of U, Q_a and Q_w of the scenario as shown in Table 3-1. The initial gas void fraction at the nozzle exit α_0 was calculated by: $\alpha_0 = Q_a/(Q_a+Q_w)$. All the 8 scenarios were investigated from the side view, and 4 of them (Expt. A-3-0, B-1-1.5, B-3-2.3, C-3-3) were also investigated from the top view.

Table 3-1. Summary of experimental scenarios of bubbly jets in this study. The first character in Experimental I.D. stands for the pipe flow velocity, i.e., A, B, and C = 0.4, 0.6, and 0.8 m/s, respectively; the numbers are the injected air and water flow rates at the nozzle, respectively.

Expt. I.D.	U (m/s)	Q_a (L/min)	Q_w (L/min)	α_0	Re	Re_a	Re_w	We
A-3-0	0.4	3	0	1.00	101,676	717	0	569
B-3-0	0.6	3	0	1.00	152,514	717	0	1,279
A-3-1.5	0.4	3	1.5	0.67	101,676	1,075	15,887	569
B-1-1.5	0.6	1	1.5	0.40	152,514	597	8,826	1,279
B-3-2.3	0.6	3	2.3	0.57	152,514	1,267	18,711	1,279
B-5-3	0.6	5	3	0.63	152,514	1,912	28,243	1,279
C-3-3	0.8	3	3	0.50	203,352	1,434	21,182	2,274
C-5-2.3	0.8	5	2.3	0.68	203,352	1,744	25,770	2,274

In the side view, a total of 5 cross-sections along the gas-phase centerline ξ were measured for each scenario, namely $\xi = 20d$, $35d$, $50d$, $65d$, and $80d$ where d is the nozzle diameter, and 9 points in the η direction were measured at each section. Note that the bubbles have already reached the top wall of the pipe at $80d$ for Expt. A-3-0 and A-3-1.5, and therefore this section was not measured in these two scenarios. Similarly in the top view, 5 sections along the gas-phase centerline were selected for each scenario, $x = 95d$, $105d$, $115d$, $125d$, and $135d$. These sections were selected to examine bubbles characteristics after they have reached the top wall. At each section, 9 points along the y direction were selected for analysis.

3.2.3. Image processing

The raw images captured by the camera were processed in the widely-used software “ImageJ” (Rasband et al., 1997), and Figure 3-2 shows an example of processing the bubbles from the top view of Expt. B-3-2.3. The background of the raw image (Figure 3-2a) was firstly removed by subtracting the image without bubbles (Figure 3-2b). As a result, some regions might be dark (e.g., the left part of Figure 3-2b), and the bubbles cannot be well-captured. Therefore, the 12-bit image was converted to a binary image by applying a grayscale threshold, and the bubbles that were still not well-captured were manually outlined in the image. Afterwards, these bubble outlines were mapped into the threshold images as shown in Figure 3-2(c). The obtained binary image was processed by a series of automatic operations including close, dilate, erode, fill holes and watershed, as well as manual operations (e.g., separate single bubbles that were merged after automatic operations), to make the detection of bubbles more precise (Figure 3-2d). In this study, bubbles smaller than 1 mm^2 were neglected to avoid measurement errors. Figure 3-2(e) shows the detected bubbles, and Figure 3-2(f) depicts the bubble outlines mapped into the raw image. At least 200 images with an interval of 0.13 s (within a total duration of 26 s) were processed for each scenario.

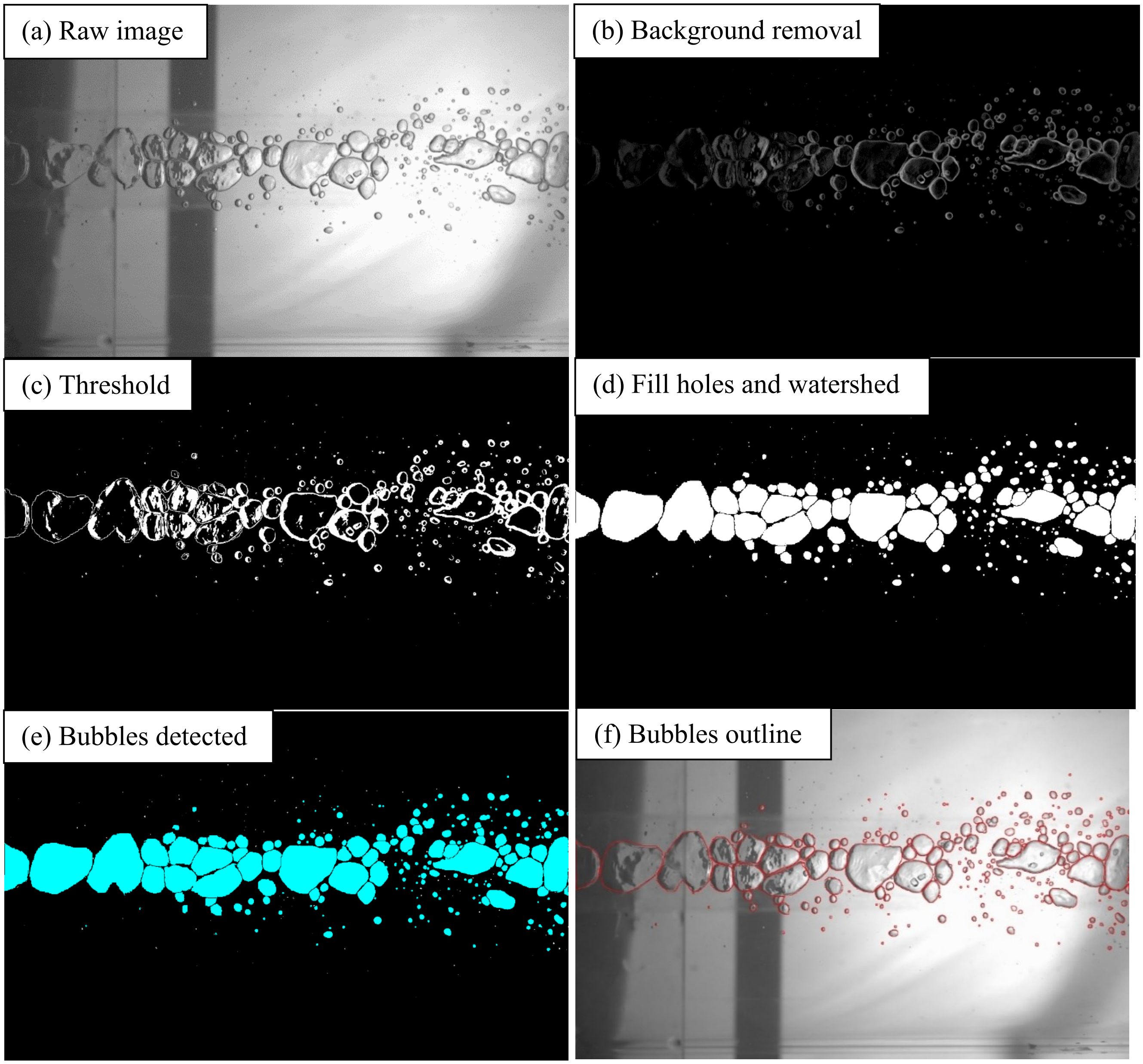
(a) Raw image
(b) Background removal
(c) Threshold
(d) Fill holes and watershed
(e) Bubbles detected
(f) Bubbles outline

Figure 3-2. An example of image processing for bubbles in the top view of Expt. B-3-2.3.

The method of calculating bubble properties is as follows. The gas void fraction α, defined as the ratio of gas volume to the total volume, was determined by calculating the mean gas area fraction at each measuring point surrounded by a small area of 1 mm^2. Bubble diameter was obtained from calculating the area of bubbles passing through each measuring point, assuming circular shape for the bubbles: $d_\mathrm{b} = \sqrt{\frac{4A}{\pi}}$, where A is the bubble area. Bubble velocity was calculated as $U_\mathrm{b} = \frac{P_{t+\Delta t} - P_t}{\Delta t}$, where P_t denotes the current position of the front of each bubble, $P_{t+\Delta t}$ denotes the position of bubble at the next time step, and Δt (0.005 s) is the time interval. The mean bubble diameter and velocity were obtained by averaging all the bubbles passing through each measurement point during the measuring period. Similar methods have been used in Zhang and Zhu (2013), in which the results measured from both image processing and an optical fiber probe were compared and proved to have acceptable differences (of 2.2%, 7.0% and 9.2% for α, d_b and U_b, respectively). Note that these differences do not provide an accurate error estimate. However, comparing the results with an intrusive probe is one of the common approaches for validating image processing techniques (Zhang and Chanson, 2018; Shi et al., 2023). For instance, differences between the two techniques have been reported as ranging from 6% to 14% for α (Kiambi et al., 2003), 10% for d_b (Lima Neto et al., 2008c), and 15% for U_b (Leandro et al., 2014). In this study, the bubble properties computed using image processing are considered acceptably accurate due to the relatively low difference compared to the probe results. To better show the movements of bubbles, U_b was decomposed into two velocity components: U_bx and U_by for the top view; and U_bx and U_bz for the side view.

3.3. Results and analysis

In this Section, most of the results for the side view are included in the Appendix A, since they are similar with those of bubbly jets in free-surface crossflow (Zhang and Zhu, 2013). In the main text, we focus more on the bubble characteristics that has not been reported from the side view (i.e., bubble velocity components and turbulence characteristics), as well as top boundary effect on the bubble behavior (i.e., from the top view).

3.3.1. Photographic observations

Figure 3-3 shows the typical snapshots of the recorded videos (a total duration of at least 26 s) of four scenarios from both the top and side views, with the section positions marked for each scenario. It was observed that most of the bubble shapes are close to round for the top view (Figure 3-3a), except for the bubble plume (Expt. A-3-0), where bubbles coalesce to form large and elongated (slug-like) bubbles. The formation of the slug-like bubbles can be attributed to the absence of initial momentum (no injection of water) that generates large bubbles at the nozzle, the low pipe flow velocity U (0.4 m/s) that makes the large bubbles quickly rise to the top pipe wall, and the pipe wall that retards bubbles and causes the coalescence of bubbles near the wall. For the bubbly jets, the bubble sizes are much smaller and rounded, especially for the higher Q_w and U. This is mainly caused by the turbulence fluctuation (the water jet Reynolds number at the nozzle Re_w varies from 8,826 to 25,770) and shear stress inside the Venturi injector (Risso, 2000; Li et al., 2016; Huang et al., 2020). Furthermore, a higher U in the pipe also increases the turbulence fluctuations (Peixinho et al., 2005), as well as the vertical velocity gradient, which leads to a higher shear stress at the nozzle exit (Papaioannou and Stefanadis, 2005; Kwon and Seo, 2005; Große and Schröder, 2008). For the side view, the bubble shapes are mainly irregular ellipsoids (Figure

3-3b). In addition, compared to pure bubble plume, large quantities of smaller bubbles occur for bubbly jets, and they spread more widely in the η direction.

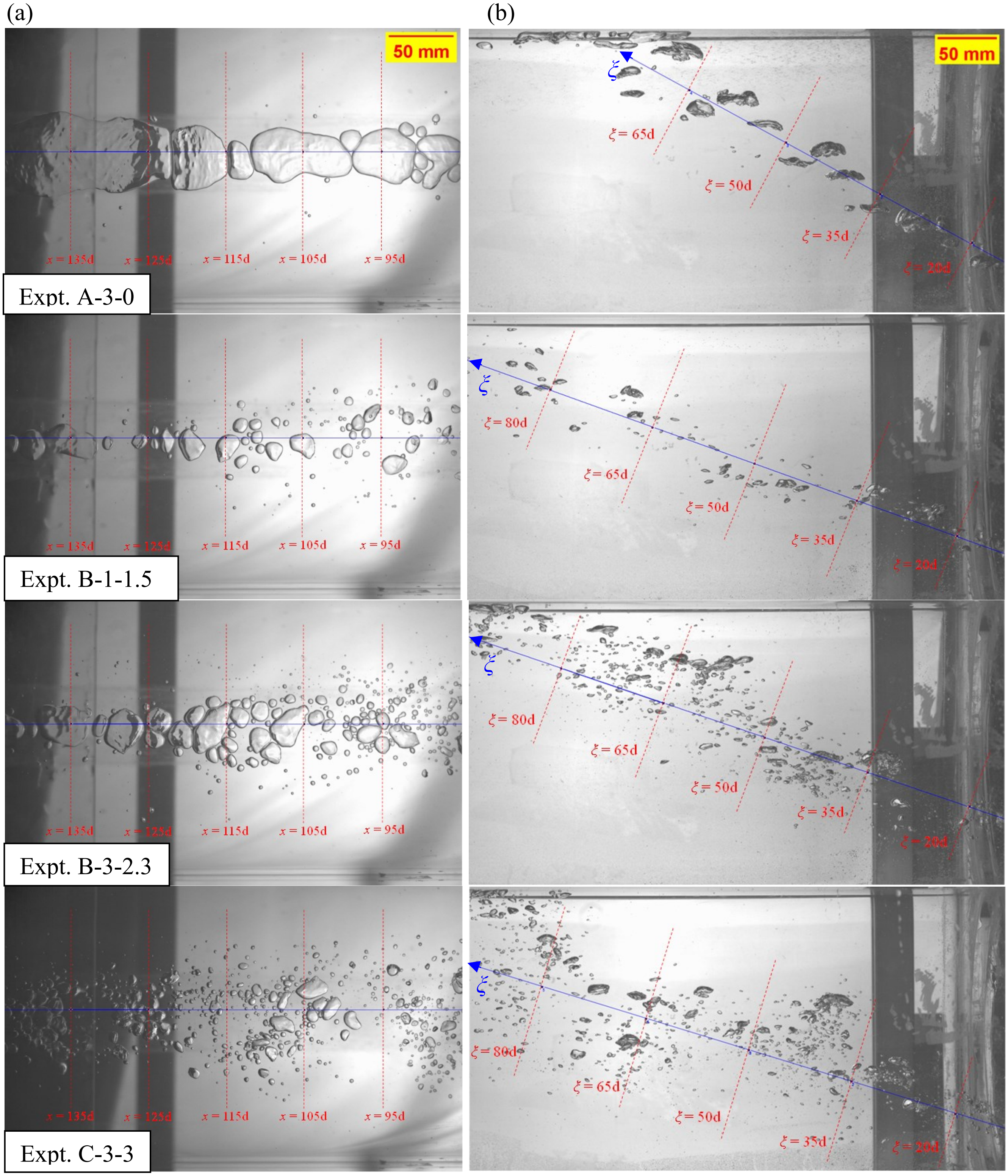

Figure 3-3. Examples of bubbly jets in pipe crossflow: (a) top view and (b) side view. Ambient pipe flow direction: from right to left.

3.3.2. Gas-phase trajectory

The trajectories before bubbles reach the top wall are shown in Figure 3-A1 (Appendix A), where each instantaneous trajectory of the bubble plume (grey line) is fitted by a polynomial curve with a 4th order. The red line is the mean gas-phase centerline trajectory ξ obtained by averaging these instantaneous trajectories, and the blue dashed line represents the virtual centerline from the nozzle to the test section by assuming a straight line (Zhang and Zhu 2013). It is worth mentioning that the trajectories are fitted without considering the bubbles near the top wall, because the trajectories afterwards are simply straight lines (in the streamwise x direction).

To explore the effects of ambient pipe flow velocity, air and water flow rates on the gas-phase trajectory, the relationships between dimensionless touching distance X_0/d and U, Q_a and Q_w need to be established. For a bubbly jet with small Q_w (0 or 1 L/min), Zhang and Zhu (2014) has proposed an equation for predicting the gas-phase inclination angle θ as follows:

$$\theta = tan^{-1}(\vec{U}/\overrightarrow{U_s}) \tag{3-1}$$

where U_s is the bubble slip velocity, which is related to the bubble diameter d_b:

$$\overrightarrow{U_s} = \sqrt{2.14\sigma/(\rho d_b) + 0.505 g d_b} \tag{3-2}$$

where ρ is the water density and σ denotes the surface tension of air-water interface.

For a pure gas jet in free-surface crossflow, Xu et al. (2018) has also derived an equation for predicting θ:

$$\theta = 0.03\frac{Re^{0.63}We^{0.15}}{Re_a^{0.14}} \tag{3-3}$$

where $Re = \frac{\rho_w U d_p}{\mu_w}$ denotes the Reynolds number of the ambient crossflow, $We = \frac{\rho_w U^2 d_p}{\sigma}$ is the Weber number of the ambient crossflow, and $Re_a = \frac{\rho_a u_a d}{\mu_a}$ is the Reynolds number of the air jet at the nozzle.

Zhang and Zhu (2014) figured out that the separation height between the air and water phases increases with an increase in water jet momentum, thereby affecting the trajectory of bubbly jets. Based on Eq. (3-3), for bubbly jets, the Reynolds number of water jet at the nozzle $Re_w = \frac{\rho_w u_w d}{\mu_w}$ should be added to further predict the gas-phase centerline trajectory. Therefore, the following relationship can be constructed for predicting X_0/d:

$$X_0/d = f(Re, We, Re_a, Re_w) = \mathrm{K} Re^{\mathrm{A}} We^{\mathrm{B}} Re_a^{\mathrm{C}} Re_w^{\mathrm{D}} \tag{3-4}$$

where K, A, B, C and D are constants to be determined. After fitting Eq. (3-4) to the current experimental data with the power law curves by using the method of non-linear least square regression, the expression can be written as:

$$X_0/d = 1.8 \frac{Re^{0.73} We^{0.16}}{Re_a^{0.12} (Re_w^{0.15} + 143)} \tag{3-5}$$

The effects of dimensionless parameters on predicted X_0/d using Eq. (3-5) are illustrated by plotting the family of curves (Figure 3-A2). Figure 3-4 shows the relationships between predicted X_0/d by Eq. (3-5) and measured X_0/d, as well as the predicted X_0/d from Eqs. (3-1) and (3-3). It was demonstrated that Eq. (3-5) is able to predict the touching distance in a promising manner, and the maximum deviations between predicted and measured X_0/d are ±8% in this study. The explanations can be divided into two groups: the *Re* and *We* are primarily associated with the pipe flow velocity *U*, and the inclination of gas-phase tends to be enhanced by the higher *U*; meanwhile, increases in Re_a and Re_w produce higher jet momentum, resulting in higher separation heights between air and water phases and smaller inclination angles (Lee and Chu, 2003; Zhang and Zhu, 2014), thereby leading to the shorter touching distances. Additionally, the deviations between predicted X_0/d by Eq. (3-1) for small Q_w in free-surface crossflow and measured values for pipe flow are less than -15%, revealing that the boundary effect on gas-phase trajectory is relatively low for small Q_w. However, larger deviations (50%) are found between the measured and predicted X_0/d by Eq. (3-3), probably due to the absence of water jet properties in Eq. (3-3) as Xu et al. (2018) only examined pure air injection/jets (not bubbly jets).

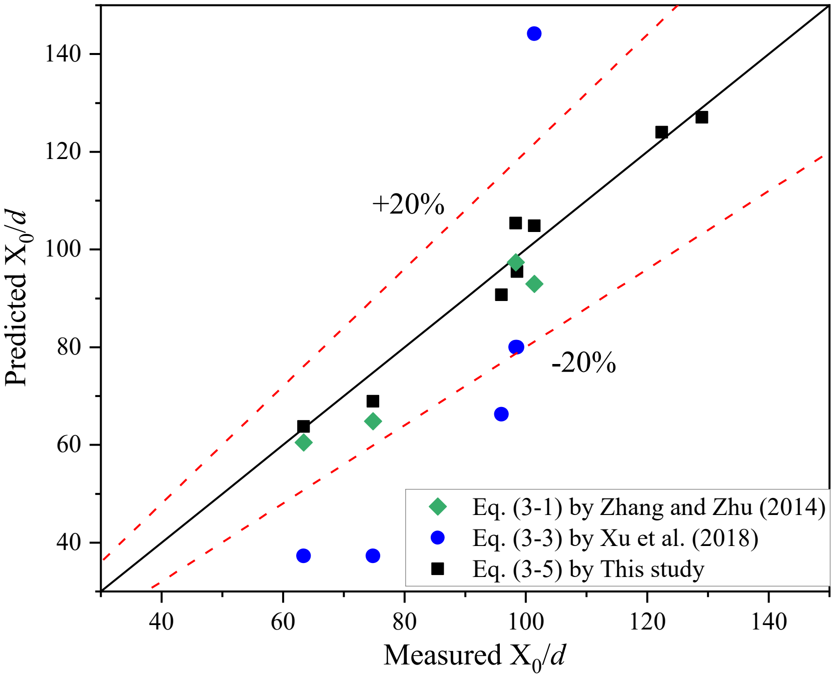

Figure 3-4. Comparison between predicted and measured dimensionless touching distance X_0/d

3.3.3. Distributions of gas void fraction

Figure 3-5(a) shows the distributions of α at different sections from the top view. The peak values typically occur at the centerline ($y = 0$) of gas-phase trajectories, and most of the distributions resemble the Gaussian curves, except for Expt. A-3-0 at $x = 135d$ that shows a top-hat distribution. This is because for the pure bubble plume with a lower U, bubbles move slowly after they reach the top wall, and a slug-like shape is formed at further distances as shown in Figure 3-3(a). Compared to the pure bubble plume, the peak void fractions of the bubbly jets are much lower, due mainly to the generated smaller bubbles by the water jet flow Q_w. As the Q_w increases, the peak void fraction decreases and the distribution of α becomes wider for all the sections (x = 95 - 135d), revealing that higher Q_w delays the gathering of bubbles to the gas-phase centerline.

To better illustrate the distribution of gas void fraction, α is normalized and fitted with the Gaussian distribution by using the method of non-linear least squares regression:

$$\alpha/\alpha_c = \exp\left[-0.693\left(\frac{y-y\prime}{b_w}\right)^2\right] \tag{3-6}$$

where y' is a measurement error of the centerline location, α_c is the centerline gas void fraction, and b_w is the half-width in the y direction for top view. The half-width is defined as the distance from the centerline to where $\alpha/\alpha_c = 0.5$. Figure 3-5(b) shows the fitted results by the Gaussian distribution using the current experimental data in different scenarios. It was found that the normalized void fraction is well fitted with the Gaussian distribution with R^2 = 0.95 - 0.99, which is similar to the distribution of bubbly jets in both stagnant water (Lima Neto et al., 2008a) and free-surface crossflow (Zhang and Zhu, 2013). y' varies from 0 to 3 mm in all the scenarios, which is relatively small and thus can be neglected.

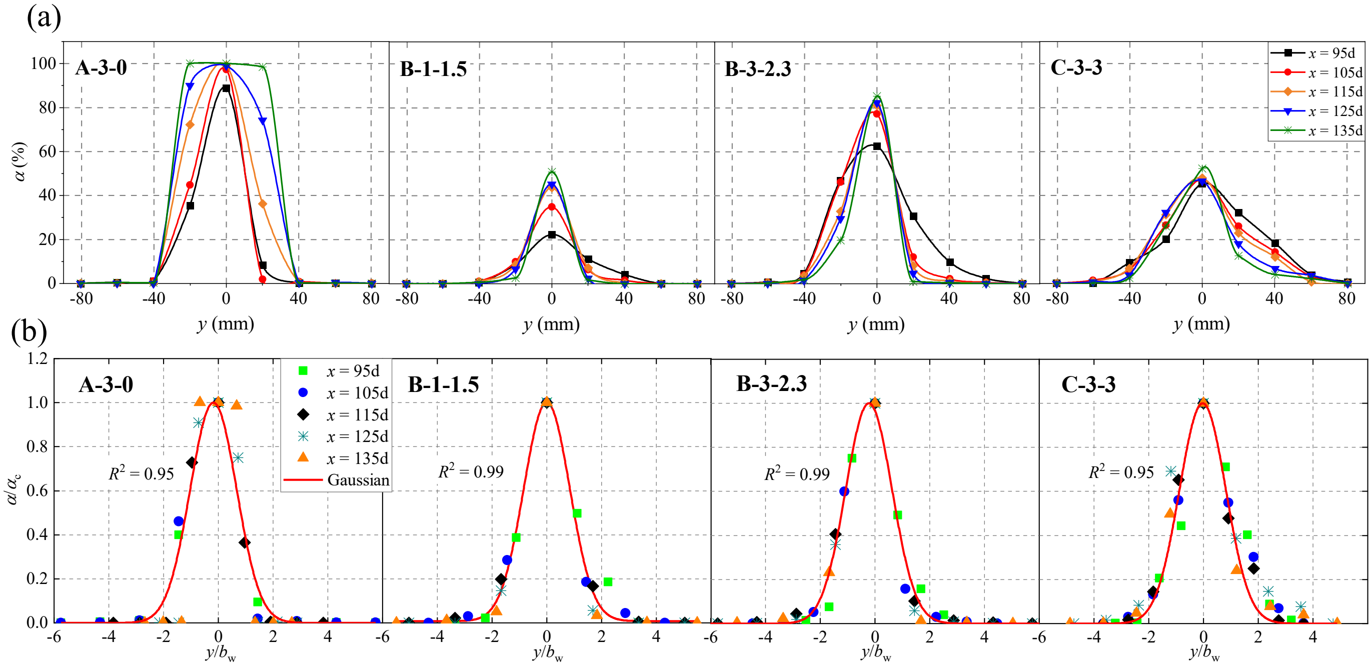

Figure 3-5. Distributions of (a) gas void fraction and (b) normalized gas void fraction at different sections along *y* direction. Both from the top view.

To further investigate the evolution of gas void fraction, Figure 3-6(a) shows the changes of centerline gas void fraction α_c along the *x* direction from the top view. It was found that the values of α_c increases steadily in the *x* direction, which is different with the decreasing trend in the ξ direction for side view in both pipe crossflow (Figure 3-A4) and free-surface crossflow (Zhang and Zhu, 2013). This is mainly because after the bubbles reach the top wall of the pipe, they tend to move towards the centerline of the pipe under the curvature restriction of the pipe shape, leading to an increase in α_c. Note that α_c in Expt. B-1-1.5 is lower than other scenarios, owing to the lower air jet flow rate at the nozzle. The normalized centerline void fraction α_c/α_0 from the top view is also shown in Figure 3-6(b), where α_0 is the initial gas void fraction at the nozzle (Table 3-1). It was observed that the tendencies of α_c/α_0 generally resemble that of α_c. However, some values of α_c/α_0 in Expt. B-1-1.5 and B-3-2.3 are larger than 1.0. This can be ascribed to the relatively larger

α_c than α_0 due to the bubbles moving towards the centerline, and α_0 is relatively smaller for both the scenarios.

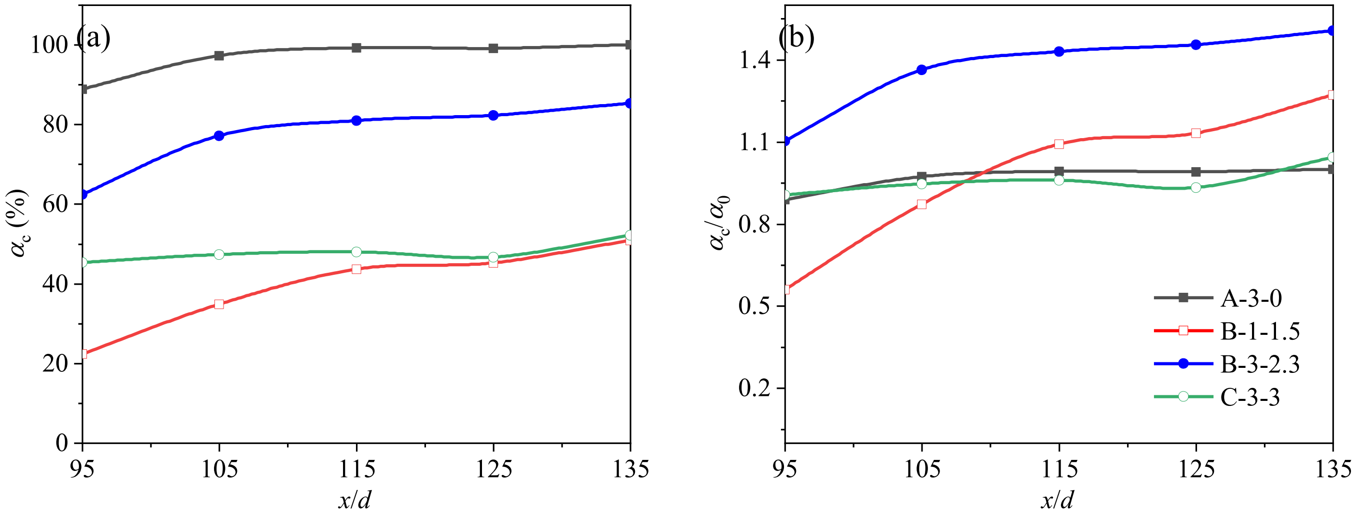

Figure 3-6. Changes of (a) centerline gas void fraction and (b) normalized centerline gas void fraction along the gas-phase trajectories. Both from the top view.

3.3.4. Distributions of bubble size

In this study, the overall bubble size distributions resemble log-normal curves for both the top and side views (see Figure 3-A5 in the Appendix A), similar to the bubble size distribution of bubbly jets measured by fiber-optic probes in stagnant water (Lima Neto, 2008a) and in free-surface crossflow (Zhang and Zhu, 2013). Figure 3-7 shows the mean bubble size distribution at different sections along the *y* direction from the top view. The peak bubble diameter occurs approximately at the gas-phase centerline ($y = 0$), and it decreases to the both sides in the *y* direction. Interestingly, the bubble sizes for the Expt. A-3-0 (bubble plume) are much larger (with maximum d_b of 37.4 mm) than other scenarios at each section, mainly due to the lower pipe flow velocity and the absence of water jet at the nozzle. Furthermore, with the increasing distance from the nozzle, large and elongated slug-like bubbles are formed at the pipe wall as discussed in Section 3.3.1. In comparison, the bubble sizes are relatively smaller (1.6 - 11.2 mm) for bubbly jets with $U = 0.6$

m/s due to the enhanced turbulence fluctuations and shear force exerted on the bubbles by water jet and the higher pipe flow velocity. With the increase of Q_w and U, the bubble sizes tend to be smaller and the distribution of bubble sizes in both the x and y directions are more uniform as shown in Expt. C-3-3.

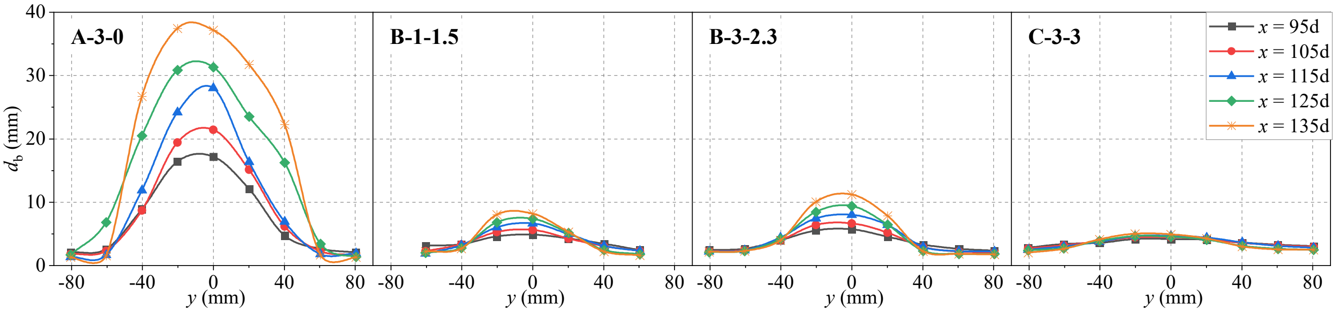

Figure 3-7. Bubble size distribution at different sections along y direction from the top view.

To explore the development of bubble size in bubbly jets, Figure 3-8(a) depicts the changes of centerline bubble size $d_{b,c}$ along the x direction from the top view, where the $d_{b,c}$ was shown in log-scale. In all the measured locations, the standard deviation of mean bubble diameter varies from 15% to 30%, and the deviation at the centerline is denoted in this figure by the error bars. It was observed that $d_{b,c}$ increases steadily (with a slope of 0.02-0.5 mm) with increasing x/d, especially for the scenarios with lower U, mainly due to the curvature and boundary effects of the top wall. Figure 3-8(b) shows the changes of half-width along the x direction from the top view. It was found that b_w/d decreases in the x direction for the bubbly jets, whereas it increases for the bubble plume. The decreasing trend of b_w/d is opposite to the evolution from the side view (Figure 3-A7), because bubbles tend to gather towards the pipe centerline as they travel in the x direction for the bubbly jets. However, large slug-like bubbles are formed at further sections (x/d = 115-135) for the bubble plume (Figure 3-3a), which also develop in the y direction, and therefore b_w/d increases.

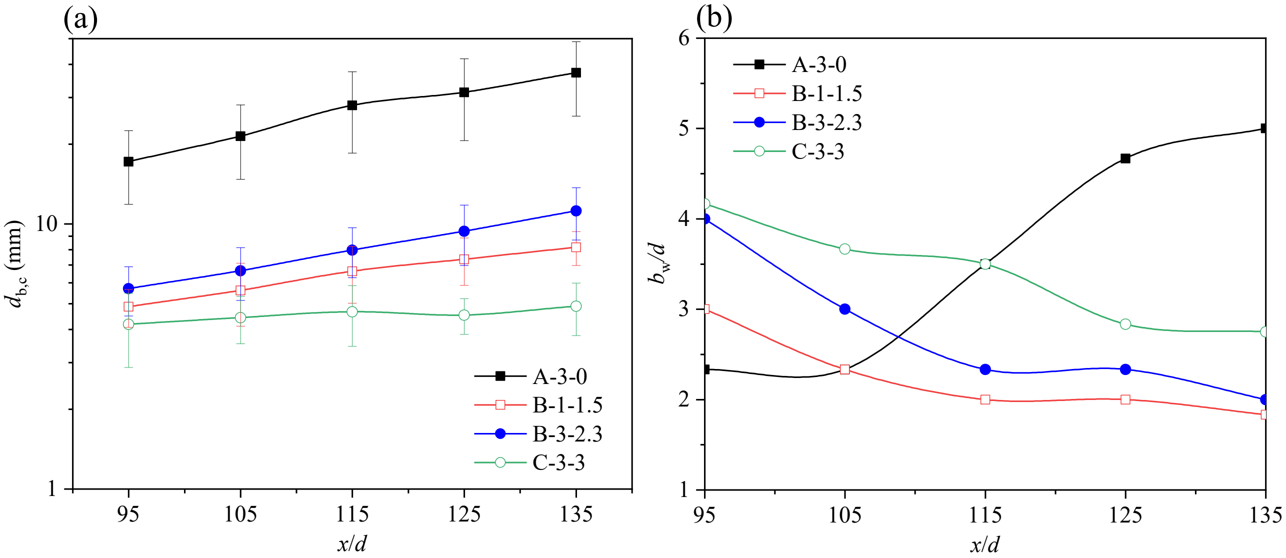

Figure 3-8. (a) Centerline distribution of bubble size. The error bars represent the standard deviation of the measured bubble diameters; and (b) distributions of gas-phase half-width. Both from the top view.

The relationships between $d_{b,c}$ and Re_w, as well as the relationships between $d_{b,c}$ and Weber number were compared and validated with the previous studies of Lima Neto et al. (2008a) and Zhang and Zhu (2013), which can be found in Figure 3-A8 in the Appendix A. They are not included in the main text to make this paper more concise and focused on the more interesting results.

3.3.5. Bubble velocity

Given that the pipe flow velocity U is relatively large in this study, the mean bubble velocity U_b exhibits similar trends with its horizontal component U_{bx}, whereas U_{by} and U_{bz} are also significant in bubble movement. Therefore, it is appropriate to study the bubble velocity components separately.

Figure 3-9 shows the distributions of mean bubble velocity components U_{bx} and U_{by} at different sections from the top view. It was found that U_{bx} increases with an increase in U as expected, and the values of U_{bx} are approximately uniform at each section for most scenarios (Figure 3-9a). Compared to U_{bx}, the differences of the other component of bubble velocity U_{by} are more evident as shown in Figure 3-9(b). A positive value of U_{by} denotes the bubble velocity in the y direction, and a negative value means the reversed direction. The sign of U_{by} and y is opposite to each other, meaning that bubbles tend to travel towards the gas-phase centerline (centerline plane of the pipe) due to the curvature of pipe wall. Furthermore, the peak absolute value of U_{by} (0.05-0.13 m/s) occurs at a certain distance (roughly 20 mm) from the gas-phase centerline, and its distribution is approximately axisymmetric with respect to the centerline. This indicates that U_{by} decreases as the bubbles move to the centerline since the bubbles at the both sides of centerline are moving towards each other.

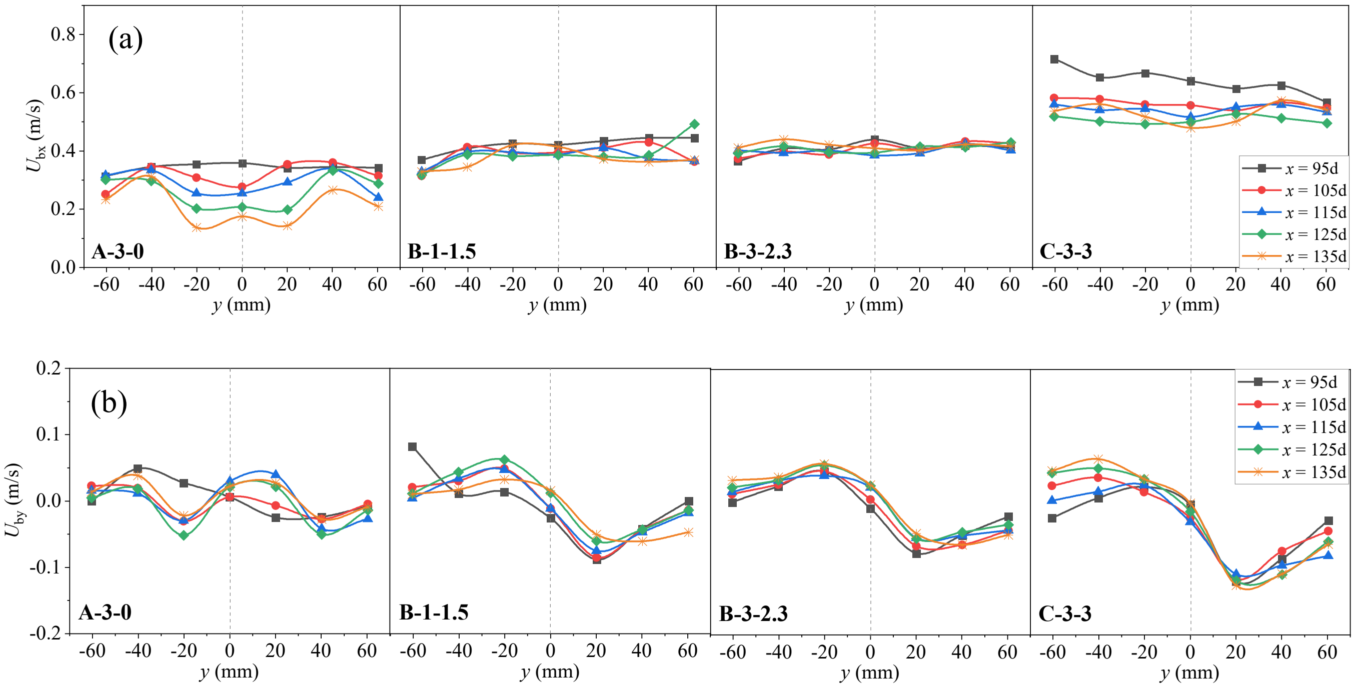

Figure 3-9. Examples of distributions of bubble velocity component along y direction at different sections from the top view. (a) U_{bx} and (b) U_{by}

Compared to the top view, the values of U_{bx} are relatively larger (by 0.2-0.3 m/s for the same scenario) for the side view (Figure 3-10a) owing to the absence of or weakened boundary effect. Rapid decreases occur at the upper side of Sections $\xi = 65d$ in Expt. A-3-0 and $\xi = 80d$ in Expt. B-1-1.5 and C-3-3, because the bubbles are approaching to the top pipe wall at these locations. Figure 3-10(b) shows that U_{bz} generally increases in the η direction for the side view under all the scenarios, except for some locations near the top wall where a decrease is observed. The increase of U_{bz} can be attributed to the increase of buoyancy force exerted on the bubbles (due to the increasing d_b as shown in Figure 3-A6) in the η direction. The decreases of U_{bz} near the top wall indicate the restriction of wall boundary on bubble rising, and U_{bz} will eventually reduce to zero at the top pipe wall.

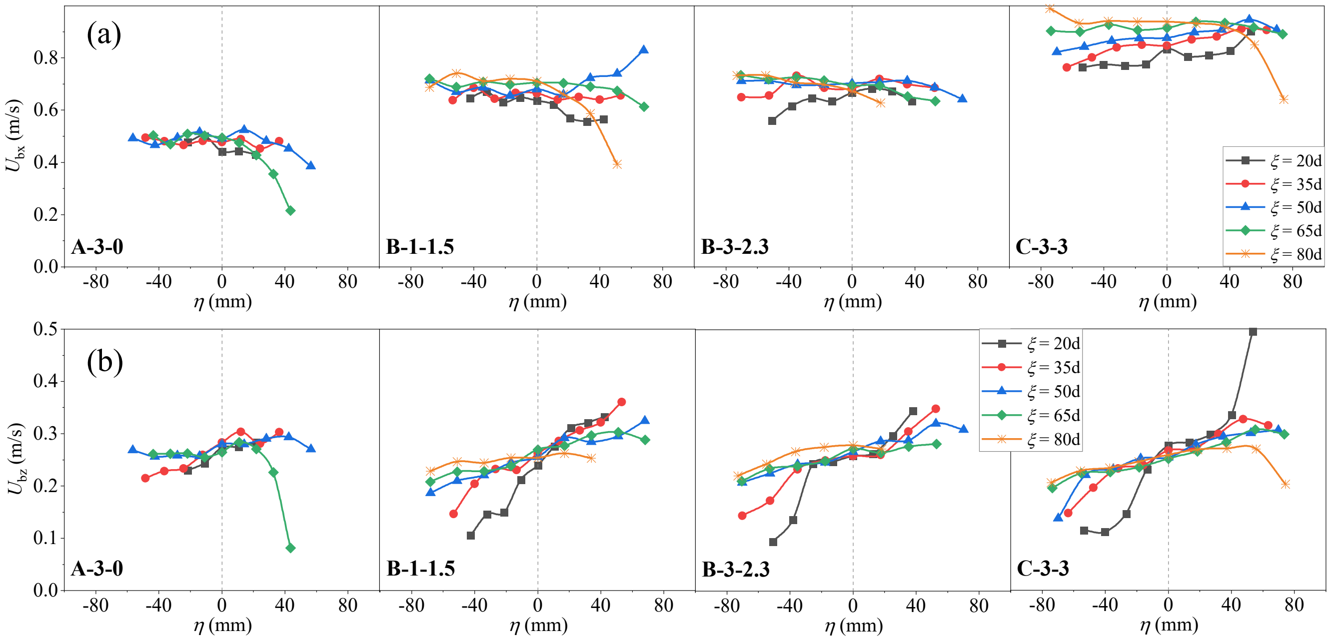

Figure 3-10. Examples of distributions of bubble velocity component along η direction at different sections from the side view. (a) U_{bx} and (b) U_{bz}

Figure 3-11 shows the changes of centerline bubble velocity components $U_{bx,c}$ and $U_{by,c}$ along the x direction from the top view as well as $U_{bx,c}$ and $U_{bz,c}$ along the ξ direction for the side view.

As shown, $U_{bx,c}$ decreases (with a slope of -0.07 to -0.4 cm/s) with an increasing distance from the nozzle for the top view (Figure 3-11a), mainly owing to the resistance on the bubbles by the top wall. However, $U_{bx,c}$ slightly increases or keeps relatively uniform as the bubbles travel further for the side view (Figure 3-11b), due to the absence of the top boundary effect.

As shown in Figure 3-11(a), $U_{by,c}$ tends to fluctuate around zero after bubbles reach the top wall, and the range of $U_{by,c}$ is between -0.026 m/s and 0.029 m/s. This indicates that bubbles move unsteadily near the gas-phase centerline, and bubble collision and coalescence can be visualized at the centerline caused by the relative movement of bubbles from both sides. Figure 3-11(b) shows that $U_{bz,c}$ is approximately uniform along the ξ direction for all the scenarios with an average value of around 0.264 m/s, and the effects of U, Q_a and Q_w on $U_{bz,c}$ are not obvious within their study ranges.

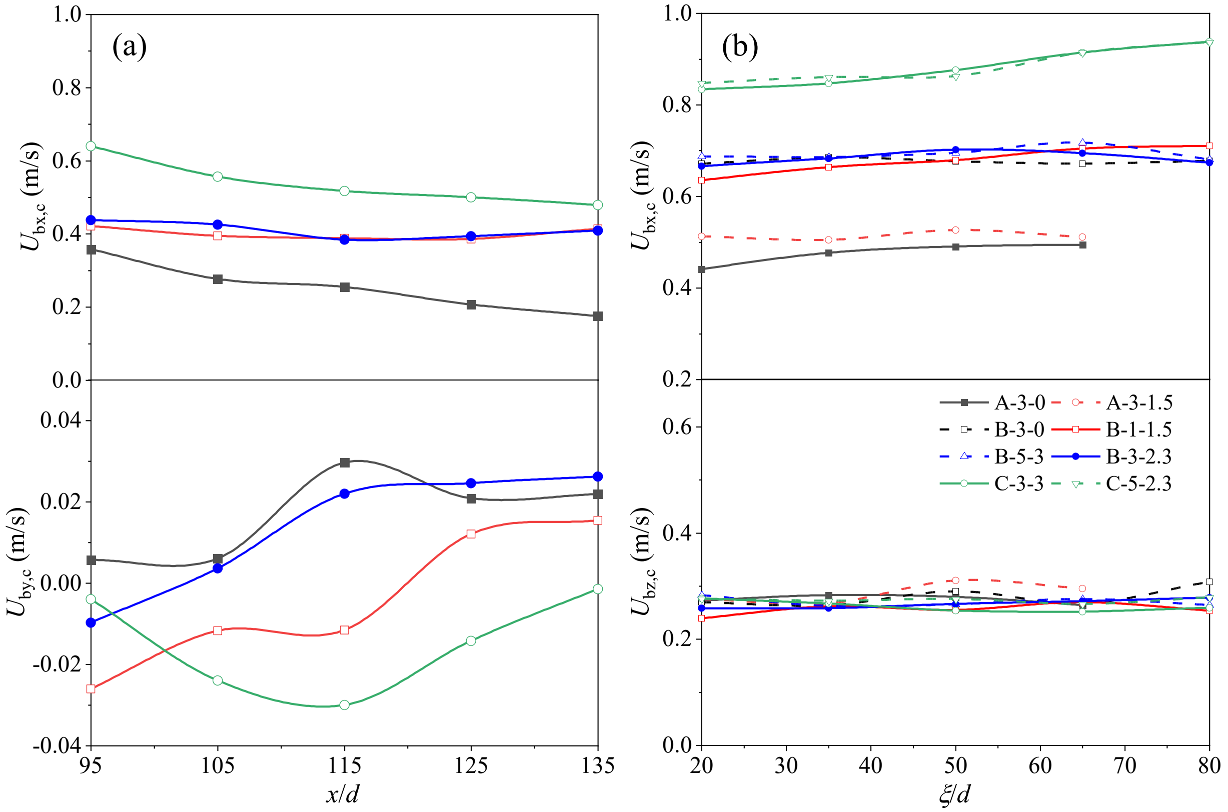

Figure 3-11. Changes of centerline bubble velocity from the (a) top view; and (b) side view.

To further investigate the vertical distribution of horizontal bubble velocity U_{bx}, the U_{bx} values at different sections from both the top and side views were compared with the theoretical water velocity using the well-established 1/7th power law in pipe flow (Schlichting, 1979):

$$\frac{U_{\mathrm{l}}}{U_{\mathrm{m}}} = (\frac{z}{d_{\mathrm{p}}})^{1/7} \tag{3-7}$$

where U_{l} is the local water velocity, and U_{m} is the maximum water velocity, which is theoretically equal to the velocity at the center of the pipe. In this study, to compare with the normalized water velocity, U_{bx} was non-dimensionalized by its maximum value $U_{\mathrm{bx,m}}$, which was assumed at the center of the pipe.

The comparisons between $U_{\mathrm{bx}}/U_{\mathrm{bx,m}}$ and the theoretical 1/7th power law for water velocity are shown in Figure 3-12. All the data points from the side view were used, and only the data points in the gas-phase centerline were selected from the top view because the comparisons focus on the center-plane ($y = 0$) of the pipe. As shown, the $U_{\mathrm{bx}}/U_{\mathrm{bx,m}}$ data points lie well with the 1/7th power law for water velocity, indicating that U_{bx} varies consistently with the water velocity. That is, the bubbles can be deemed as tracers of the water flow field in the pipe. Specifically, the normalized U_{bx} generally decreases from the center of the pipe to the both sides, and much smaller values are obtained near the pipe boundary. Similar conclusions have also been presented for the bubble velocity within boundary layer in the hydraulic jumps (Zhang et al., 2014).

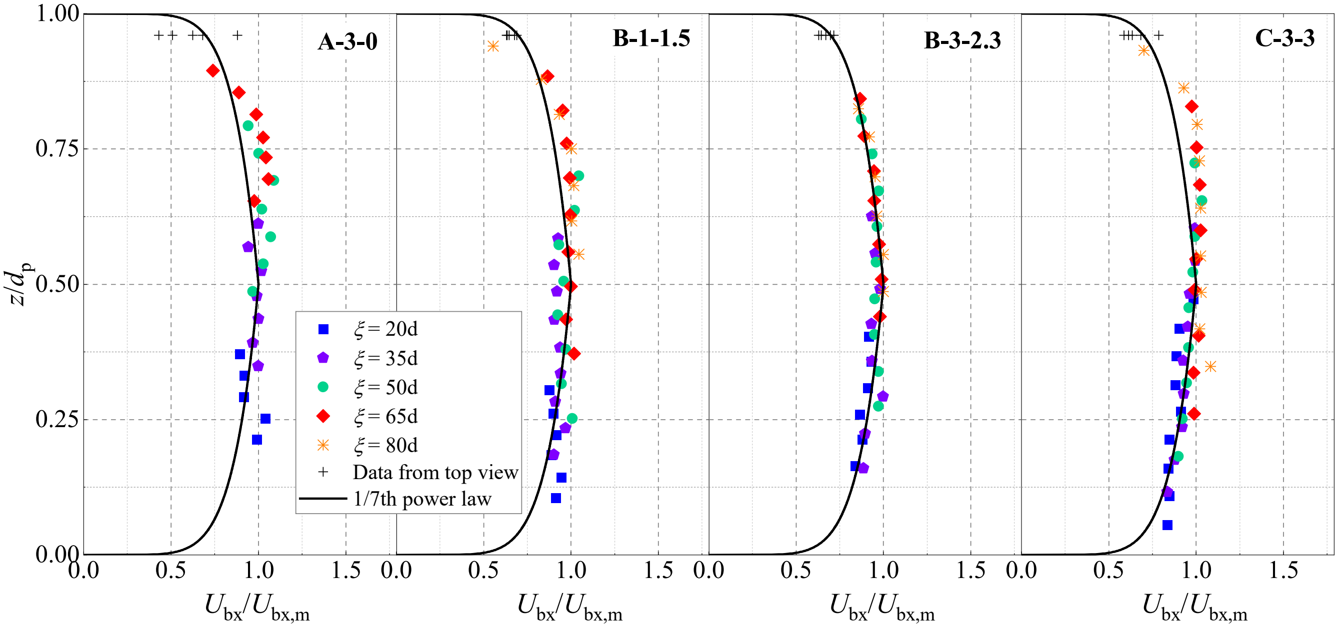

Figure 3-12. Examples of comparison of measured $U_{bx}/U_{bx,m}$ and the 1/7th power law for pipe water velocity.

Bubble rise velocity is an important parameter for bubbly jets in crossflow, which has been studied for pure gas jets in free-surface crossflow (Zhang and Zhu, 2013; Wang and Socolofsky, 2015; Xu et al. 2018). In this study, bubble rise velocity refers to the vertical bubble velocity U_{bz} from the side view, which shows an increasing trend in the η direction (Figure 3-10b). Therefore, U_{bz} was normalized by its centerline value $U_{bz,c}$, and the relationships between $U_{bz}/U_{bz,c}$ and η/b_t for all the scenarios are depicted in Figure 3-A10, where b_t is the half thickness of the bubble plume (defined as the distance from the centerline to where $\alpha/\alpha_c = 0.5$). It was observed that $U_{bz}/U_{bz,c}$ and η/b_t can be described by a linear relationship for all the scenarios. After fitting all the experimental data with the linear relationship, a correlation between $U_{bz}/U_{bz,c}$ and η/b_t can be determined with Eq. (3-8), where $R^2 = 0.81$.

$$\frac{U_{bz}}{U_{bz,c}} = \frac{0.11\eta}{b_t} + 0.98 \tag{3-8}$$

The comparison between the predicted and measured $U_{bz}/U_{bz,c}$ is shown in Figure 3-13. It is demonstrated that Eq. (3-8) is able to satisfactorily predict the normalized bubble rise velocity. Almost all of the data points locate within ±20% of the line, and most (88%) of the predicted data have an error of < 10%. The good prediction of the proposed equation can be attributed to the increasing trend of bubble size in the η direction (Figure 3-A6), since a larger bubble size contributes to a higher rise velocity due to the higher buoyancy force.

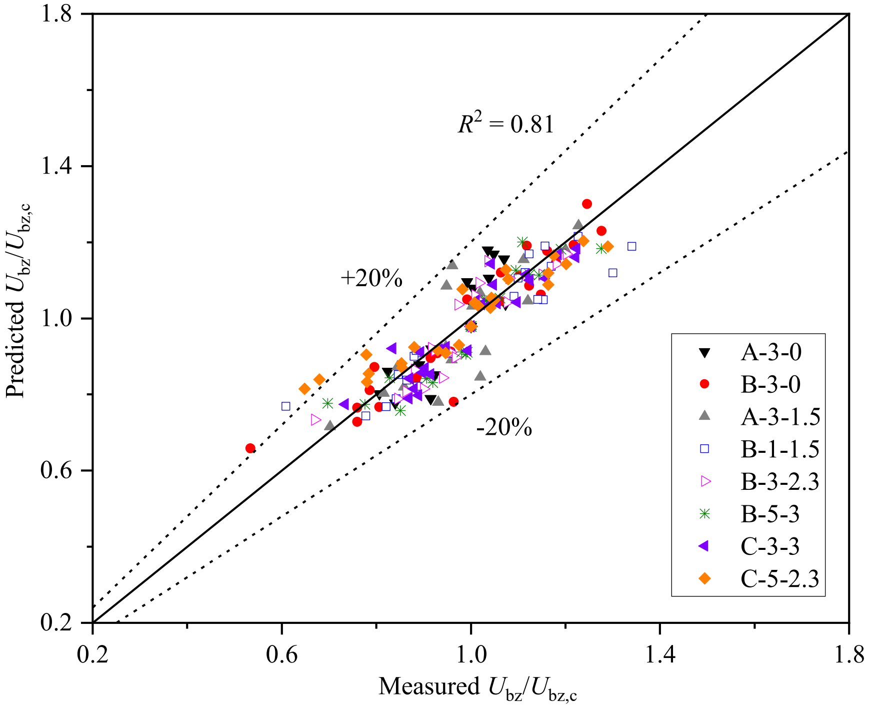

Figure 3-13. Comparison between predicted and measured normalized rise velocity $U_{bz}/U_{bz,c}$

3.3.6. Turbulence characteristics of bubbles

In this study, evident gas-phase oscillation can be observed during bubbles travelling in the pipe, owing to the high Reynolds number of the ambient crossflow (Re = 99,820, 149,730 and 199,640 for U = 0.4, 0.6 and 0.8 m/s, respectively). To further investigate the turbulence characteristics of bubbles, the root-mean-square (*rms*) of bubble fluctuating velocity $(rms)U_b'$ was calculated from both the top and side views. Figure 3-14 depicts a comparison of $(rms)U_b'$ between the bubble plume (Expt. B-3-0) and the bubbly jet (Expt. B-3-2.3) from the side view. In both scenarios, the $(rms)U_b'$ at the downstream side ($\eta < 0$) is slightly higher than that at the upstream side ($\eta > 0$), probably due to the smaller bubble sizes at the downstream side. As reported by many researchers (e.g., Bhole et al., 2008; Laupsien et al., 2022), smaller bubbles tend to be affected by liquid vortices, resulting in a higher *rms* bubble velocity.

Compared to the bubble plume, the values of $(rms)U_b'$ are larger for the bubbly jet, due to that the additional injection of water decreases the bubble size (Figure 3-A6) and thus enhances the bubble velocity fluctuations. The maximum $(rms)U_b'$ occurs near the centerline for the bubble plume, while two peak values exist near the boundary of the bubbly jet. One possible reason for the two peaks is that strong mixing occurs in the mixing (or shear) layer of bubbly region due to the simultaneous water injection for the bubbly jet, and hence the bubbles fluctuate strongly there. These two peaks caused by mixing in the shear lay have also been demonstrated in a pure gas jet in liquid (Dahikar et al., 2010), entrained air bubbles in a plunging jet (Qu et al., 2013) and a confined gas jet (Xiao et al., 2019).

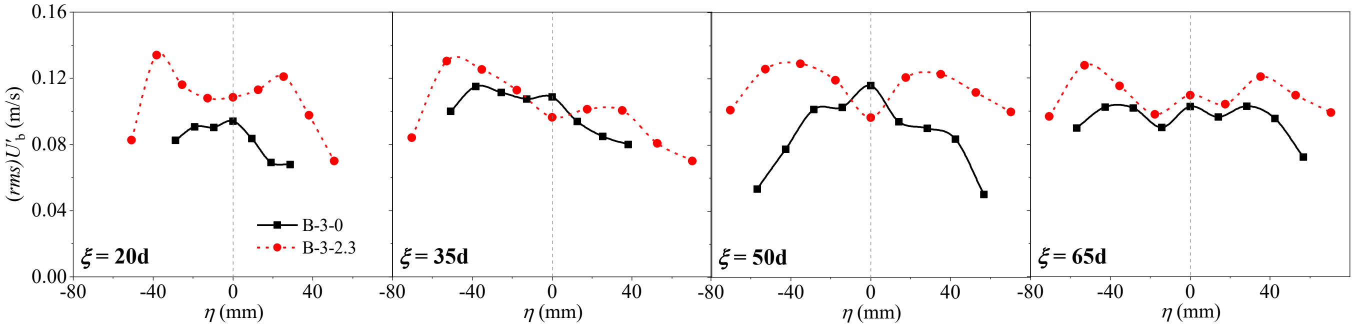

Figure 3-14. Comparison of *rms* bubble velocity fluctuations between bubble plume (Expt. B-3-0) and bubbly jet (Expt. B-3-2.3) from the side view.

The dimensionless turbulence intensity of bubbles, defined as $(rms)U_b'/U$ (Zhang et al., 2014), is further investigated from both the top and side views, as shown in Figure 3-15. For the top view (Figure 3-15a), the maximum $(rms)U_b'/U$ occurs at x = 95d due to the interaction between bubbles and top pipe wall, and then it decreases in the x direction as expected due to the friction effect of top pipe wall. For the side view (Figure 3-15b), the distributions of $(rms)U_b'/U$ varies between different sections for the bubble plume, and the difference decreases as the Q_w and U increases. The bubble turbulence intensity in each scenario generally varies from 0.1 to 0.3 with a mean value of around 0.2, which is comparable with the measured turbulence intensity of pure liquid jets (Kamotani and Greber, 1972; Crabb et al., 1981; Andreopoulos and Rodi, 1984), dense jets (Ben Meftah and Mossa, 2018), or buoyant jets in crossflow (Cintolesi et al., 2019). $(rms)U_b'/U$ has a similar value at different positions for Expt. C-3-3, indicating that higher Q_w and U promote the uniform distribution of bubble turbulence intensity.

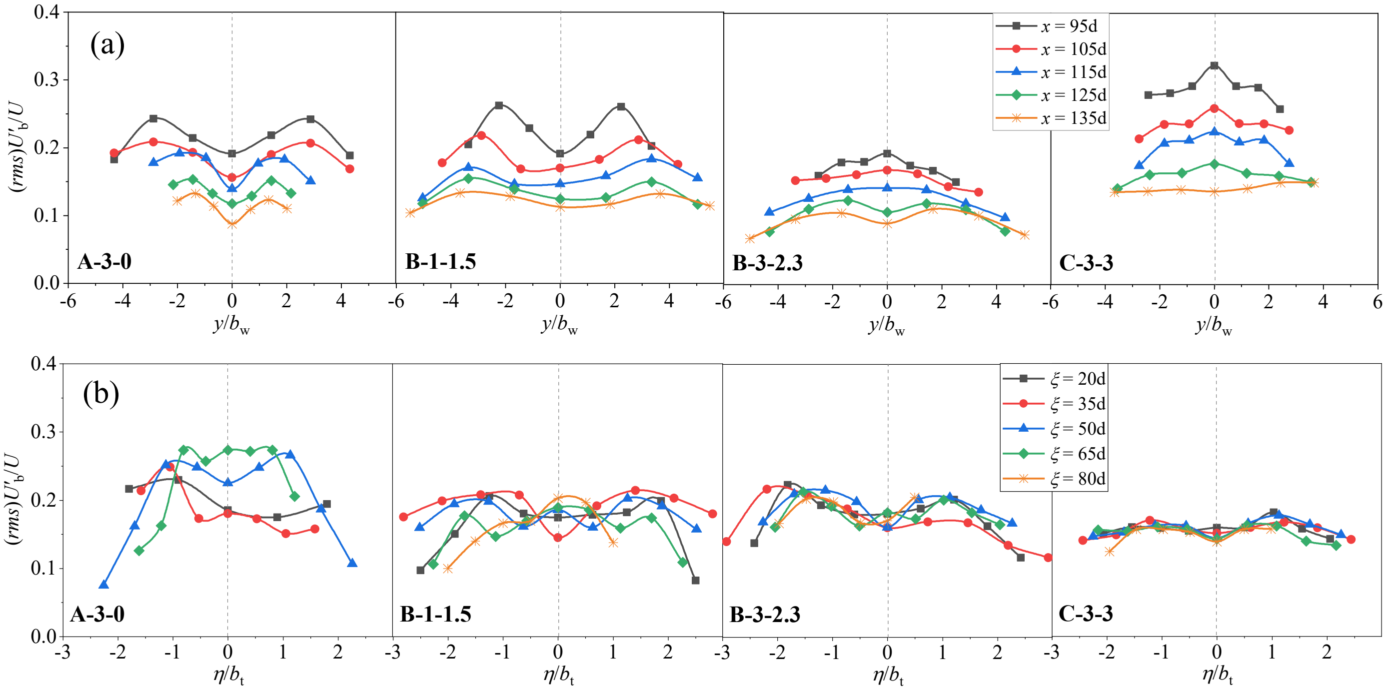

Figure 3-15. Distributions of bubble turbulence intensity $(rms)U_b'/U$ from the (a) top view and (b) side view.

3.4. Summary and conclusions

In this study, a series of physical experiments were conducted on air-water bubbly jets (by injecting air-water mixture) in pipe crossflow. The bubble properties (gas-phase trajectory, gas void fraction, bubble diameter, and bubble velocity) were systematically investigated before and after bubbles touch the top pipe wall, based on image processing techniques. The main conclusions are summarized as follows:

(1) The gas-phase trajectory was related to the Reynolds number and Weber number of the ambient pipe flow, as well as the Reynolds numbers of both the air and water phases of bubbly jets. With these parameters, dimensionless relationship was built with good accuracy (± 8% error) for the horizontal distance that the gas-phase centerline touches the pipe top wall.

(2) Due to the gathering of bubbles towards the pipe center plane under the curvature restriction of the pipe wall, the centerline gas void fraction increases with an increasing distance from the nozzle after touching the pipe wall, and the sign of transverse bubble velocity component U_{by} and y is opposite to each other.

(3) The horizontal bubble velocity U_{bx} increases with an increase in pipe crossflow, and its value is smaller after touching the pipe top wall. The dimensionless $U_{\mathrm{bx}}/U_{\mathrm{bx,m}}$ fits well with the 1/7th power law for water velocity distribution in pipe flow.

(4) Bubble rise velocity generally increases in the η direction due to the increasing bubble size. A dimensionless equation is proposed for predicting bubble rise velocity, and a good agreement with the measured data has been achieved.

(5) The root-mean-square of bubble fluctuating velocity is slightly higher at the downstream side ($\eta < 0$) than that at the upstream side ($\eta > 0$), probably due to the smaller bubble sizes at the downstream side. The additional injection of water enhances the bubble fluctuations, and higher water jet and pipe flow rate promote the uniform distribution of bubble turbulence intensity.

4. A new Eulerian-Eulerian-Lagrangian solver in OpenFOAM and its application in a three-phase bubble column*

4.1. Introduction

Gas-liquid-solid three-phase flows (GLSTPF) exist in a wide range of industrial processes, such as flotation bubble column reactors in chemical engineering (Sarhan et al., 2017a, b, 2018a), three-phase fluidized beds (FB) in biochemical industry (Gruber et al., 2016; Li and Li, 2018), and wastewater treatment in environmental engineering (Chen et al., 2020). Compared to single- or two-phase flows, the presence of three phases substantially increases the complexity of hydrodynamics of a flow field, e.g., bubble breakup and coalescence, bubble induced turbulence, and interaction between different phases (Wen et al., 2005; An et al., 2020). Although a number of experimental studies have been conducted to investigate GLSTPF (Gao et al., 2019; Li et al., 2022b) such as phase holdups, particle size distributions and phase velocities, knowledge gaps (e.g., detailed phase velocity field and vortex structures) still exist on hydrodynamics of GLSTPF due to its complexity nature.

In the last decades, computational fluid dynamics (CFD) has attracted considerable interest in studying GLSTPF (An et al., 2020). Modeling GLSTPF can be typically categorized into five types: pseudo two-fluid (Eulerian-Eulerian, i.e., E-E) approach, three-fluid (E-E-E) approach, Eulerian-Eulerian-Lagrangian (E-E-L) approach, Eulerian-Lagrangian-Lagrangian (E-L-L) approach, and volume of fluid-discrete particle model (VOF-DPM) approach. In the E-E approach, the liquid and

---

* The content of this chapter has been published as: Zhang, H., Yin, Z., Chi, W., Zhang, W., 2023. A new Eulerian-Eulerian-Lagrangian solver in OpenFOAM and its application in a three-phase bubble column. Powder Technol. 426, 118661.

small solid particles are treated as a pseudo-homogeneous phase with varying density and viscosity, whereas the details of particle motion cannot be calculated separately (Gruber et al., 2016). The E-E-E method is frequently applied in dense particle loading systems, where all three phases are separately treated as "fluids" in Eulerian coordinates with interphase interactions included between phases (Sarhan et al., 2016). This method introduces more empirical closures for phase interactions, and individual particle motions cannot be tracked (Zhou et al., 2020).

In the E-E-L approach, gas and liquid are treated as continuous phases in Eulerian coordinates, and solid phase is modeled as dispersed phase in Lagrangian coordinates (Wen et al., 2005; Liu et al., 2019a). On the other hand, the E-L-L approach generally treat liquid as Eulerian continuous phase, while gas and solid are described as Lagrangian dispersed phases (Li and Li, 2018). These two approaches can directly calculate particle motions compared to the pure Eulerian approaches; whereas their drawback is the higher computational requirement due to the use of Lagrangian approach, and thus they are generally applied in low particle loading systems (Liang et al., 2016). In the VOF-DPM approach, interface between gas bubbles and liquid is tracked by the VOF front tracking technique, and solid phase is modeled by the DPM method (Liu and Luo, 2018; Washino et al., 2021). Currently, this approach is only feasible in small scales and dilute systems owing to computational costs (Ji et al., 2018).

As one of the most popular open-source CFD packages, OpenFOAM has inbuilt solvers for various problems, and provides access to source code for developing new solvers (Jasak, 2009). Several CFD studies on GLSTPF have been conducted using the aforementioned E-E (An et al., 2020), E-E-E (Zhu et al., 2023) and VOF-DPM approaches (Chen et al., 2022d), which correspond to the existing solvers in OpenFOAM-v2006, namely *twoPhaseEulerFoam* (or *reactingTwoPhaseEulerFoam*), *multiPhaseEulerFoam* and *MPPICInterFoam*, respectively. By using the E-L-L approach, Gruber et al. (2016) investigated the effect of bubble–particle interaction models on the hydrodynamics of a three-phase bubble column, and the algorithm was developed based on three software packages including OpenFOAM.

Despite of recent progress, existing studies using the E-E-L approach are rather limited, and to the authors' best knowledge, no research and suitable solver have been reported on GLSTPF using the E-E-L approach in OpenFOAM. Wen et al. (2005) investigated flow characteristics of a gas-liquid-solid three-phase fluidized bed using the E-E-L model, and examined the local phase holdup and axial liquid velocity. However, only drag force was considered for the fluid-solid interphase coupling, and selection of bubble size was not described. Sedrez and Shirazi (2021) studied erosion of pipe elbows with GLSTPF using the E-E-L approach in ANSYS FLUENT, but particle effect on fluid behavior and particle-particle collisions were not considered (one-way coupling). To explore the effect of spatial radiation distribution (SRD) on photocatalytic oxidation of methylene blue, Liu et al. (2019a) proposed a SRD model coupling with a reaction kinetic model based on the E-E-L approach in gas-liquid-solid mini-fluidized beds. These previous researches demonstrated the applicability of the E-E-L approach on predicting flow characteristics of GLSTPF, but bubble sizes were fixed in these studies without considering the bubble coalescence and breakup that are however common in GLSTPF (Ghaffarkhah et al., 2018; Pan et al., 2018).

To account for bubble coalescence and breakup, population balance model (PBM), which is based on the population balance equation (PBE), is commonly applied in polydisperse multiphase systems (Sarhan et al., 2018b). Typical methods of solving PBE are the quadrature method of moments (QMOM) proposed by McGraw (1997) and developed by Marchisio et al. (2003), and the fixed pivot technique that belongs to the class method proposed by Kumar and Ramkrishna (Kumar and Ramkrishna, 1996). In PBM, bubble coalescence and breakup are two key terms that influence bubble size distribution (BSD), and various models have been proposed (Prince and Blanch, 1990; Lehr et al., 2002). To couple PBM with CFD models in GLSTPF, the E-E-E approach is the most commonly-used approach in the literature (see the summary in Table 4-1). So far, only one study has been reported on the use of the E-E-L approach, but it had no detailed description on the model formation (Wang et al., 2021a).

Table 4-1. Typical simulation studies coupling PBM with CFD models in GLSTPF.

Studies	Multiphase approaches	Applications	Descriptions
An et al. (2020)	E-E	Slurry bubble column	A correlation of attenuation factor for turbulent dissipation rate in PBM kernel models was proposed, and the gas holdup and BSD were well predicted by combining the Energy-Minimization Multi-Scale approach, PBM and attenuation factor.
Li et al. (2015)	E-E-E	Gas-liquid-slag three-phase flow in ladle metallurgy	The gas, molten steel and slag phases were represented by N_2, water and oil respectively, and the class method was used to solve the PBE and simulate the BSD.
Ge et al. (2018)	E-E-E	Gas-liquid-solid three-phase abrasive flow	A gas-liquid-solid three-phase abrasive flow processing model was proposed based on the Eulerian multiphase model and PBM, and the Luo model was used to describe the aggregation and breakage of bubbles.
Pan et al. (2018)	E-E-E	Gas-liquid-solid three-phase polyethylene FB	The liquid droplet diameter was fixed as a constant value, while the particle size distribution was described by the PBM. The results indicated that the particle growth rate can be enhanced by increasing the condensed liquid content.
Hui et al. (2019)	E-E-E	Gas-liquid-solid three-phase polyethylene FB	A polymerization kinetics model was coupled with the three-fluid model to describe the polymer properties in the FB. The polymerization reaction rate was found to be influenced by the scale-up effect.
Zhou et al. (2020)	E-E-E	Gas-liquid-solid three-phase FB	Good predictions were obtained for the BSD using the CFD-PBM coupled model, and the effects of superficial gas, liquid velocities and particle circulating rate on the BSD were investigated.
Wang et al. (2021a)	E-E-L	Slurry bubble column	The gas and liquid were modeled by E-E approach, the BSD was predicted by PBM, and the solid phase was described by DPM. The results showed that the existence of solid phase can reduce the peak liquid velocity in bubble column, whereas it has no pronounced effect on gas holdup.

Due to the limited studies on GLSTPF using the E-E-L approach, the objective or novelty of this work is: a) to further examine the applicability and reliability of the E-E-L approach on modeling GLSTPF, and in particular, the effects of the PBM model on the accuracy of the E-E-L approach which has not been reported; and b) to reveal the individual particle motions and flow structures (e.g., vortex structures), which have been barely reported in GLSTPF. To achieve these objectives, a new E-E-L solver was developed in OpenFOAM that couples the E-E-L approach and PBM for investigating the characteristics of GLSTPF. In the new solver, gas and liquid phases were described by two-fluid model in Eulerian coordinates, and solid particle motion was solved by DPM in Lagrangian coordinates. Interphase coupling was achieved by considering interfacial forces acting on phases, and particle-particle and particle-wall interactions were resolved by the spring-dashpot-slider method. To solve PBE and model BSD in GLSTPF, the widely-used class method was adopted and coupled with the E-E-L approach. The new solver was tested with and without PBM to examine its impact, and compared with the experimental data in a three-phase bubble column to demonstrate its capability in simulating GLSTPF.

4.2. Mathematical model formation

The framework of the developed solver is demonstrated in Figure 4-1, where our modifications to the existing source code or model are highlighted in red color. Details of the developed mathematical model are described in *Sections 4.2.1* and *4.2.2*.

4.2.1. Eulerian-Eulerian-Lagrangian model

In this Eulerian-Eulerian-Lagrangian approach, liquid and the gas phases were described by the two-fluid model with solid particle effect, and both phases were treated as two interpenetrating continua. The continuity and momentum equations (Liang et al., 2016) were modified (by adding the solid particle terms) and solved for each phase separately:

$$\frac{\partial(\rho_\varphi\alpha_\varphi)}{\partial t}+\nabla\cdot\left(\rho_\varphi\alpha_\varphi\mathbf{U}_\varphi\right)=0 \tag{4-1}$$

$$\frac{\partial(\rho_\varphi\alpha_\varphi\mathbf{U}_\varphi)}{\partial t}+\nabla\cdot\left(\rho_\varphi\alpha_\varphi\mathbf{U}_\varphi\mathbf{U}_\varphi\right)=-\alpha_\varphi\nabla P+\alpha_\varphi\rho_\varphi\mathbf{g}-\nabla\cdot\left(\alpha_\varphi\tau_\varphi^{\text{eff}}\right)+\mathbf{F}_\varphi+\mathbf{F}_{\varphi p} \tag{4-2}$$

where bold letters denote vectors, ρ_φ is the density of fluid phase φ (gas or liquid), $\mathbf{U}_\varphi$ denotes the fluid phase velocity, P is the pressure, $\mathbf{g}$ is the gravitational acceleration vector, $\mathbf{F}_\varphi$ is the interfacial forces between phases of gas and liquid, $\mathbf{F}_{\varphi p}$ is the forces acting on the fluid phases from solid particles, and α_φ represents the fraction of fluid phase. Note that the effect of particle volume fraction α_p was considered in our developed solver, and thus the phase volume fractions satisfy $\alpha_g+\alpha_l+\alpha_p=1$. $\tau_\varphi^{\text{eff}}$ is the effective stress tensor composed of viscous and Reynolds stresses (Yan et al., 2022):

$$\tau_\varphi^{\text{eff}}=-\mu_\varphi^{\text{eff}}\left[\nabla\mathbf{U}_\varphi+\left(\nabla\mathbf{U}_\varphi\right)^T-\frac{2}{3}\left(\nabla\cdot\mathbf{U}_\varphi\right)\mathrm{I}\right] \tag{4-3}$$

In Eq. (4-3), μ_φ^{eff} represents the effective viscosity, which is composed of molecular viscosity μ_φ and turbulent viscosity μ_φ^{T}. For liquid phase, the eddy viscosities induced by bubbles μ_{BI} and by solid particles μ_{PI} are also taken into account. The effective viscosities for both gas and liquid phases can be expressed as follows:

$$\mu_g^{\text{eff}}=\mu_g+\ \mu_g^{\mathrm{T}} \tag{4-4a}$$

$$\mu_l^{\text{eff}}=\mu_l+\ \mu_l^{\mathrm{T}}+\mu_{BI}+\mu_{PI} \tag{4-4b}$$

In this study, turbulent fluctuation of fluid phase was modeled by large eddy simulation (LES) approach. Grid scale large eddies were directly resolved, while isotropic small eddies were modeled by sub-grid scale (SGS) models. The fluid velocity in Eqs. (4-1) and (4-2) can be defined as (Ničeno et al., 2008):

$$\mathbf{U}_\varphi = \widetilde{\mathbf{U}}_\varphi - \mathbf{U}'_\varphi \tag{4-5}$$

where $\mathbf{U}_\varphi$ represents the filtered (resolved) phase velocity, $\widetilde{\mathbf{U}}_\varphi$ is the instantaneous velocity and $\mathbf{U}'_\varphi$ is the unresolved part that needs to be modeled.

The SGS model is the key element in LES and it determines the effect of the unresolved scales of motion on the resolved scales. In the current work, the one-equation SGS model (Ničeno et al., 2008) was adopted for both gas and liquid phases. This model solves a transport equation for the unresolved kinetic energy k_{SGS} as follows:

$$\frac{\partial}{\partial t}(k_{SGS}) + \nabla \cdot \left(k_{SGS}\mathbf{U}_\varphi\right) = \nabla \cdot \left(\frac{\mu_\varphi + \mu_\varphi^{\mathrm{T}}}{\rho_\varphi} \nabla k_{SGS}\right) + G_\varphi - C_e \frac{k_{SGS}^{3/2}}{\Delta} \tag{4-6}$$

where $\Delta = Vol^{1/3}$ is the filtered width, and Vol is the volume of the computational cell. G_φ is the production term, defined as:

$$G_\varphi = \frac{\mu_\varphi^{\mathrm{T}}}{\rho_\varphi}\left|S_{ij}\right| \tag{4-7}$$

where $S_{ij} = \nabla\mathbf{U}_\varphi + \left(\nabla\mathbf{U}_\varphi\right)^{\mathrm{T}}$ is the strain rate of the resolved velocity field. The sub-grid eddy viscosity is calculated from:

$$\mu_\varphi^T = \rho_\varphi C_k \Delta k_{SGS}^{1/2} \tag{4-8}$$

The model constants are $C_e = 1.05$ and $C_k = 0.07$ as suggested by Ničeno et al. (2008). For liquid phase, the bubble and particle induced turbulences are accounted for by increasing the eddy viscosity (Sato and Sekoguchi, 1975):

$$\mu_{BI} = C_\mu \rho_l \alpha_g d_b \left|\mathbf{U}_g - \mathbf{U}_l\right| \tag{4-9a}$$

$$\mu_{PI} = C_\mu \rho_l \alpha_p d_p \left| \mathbf{U}_p - \mathbf{U}_l \right| \tag{4-9b}$$

where the model constant $C_\mu = 0.6$ (Chen et al., 2020), d_p and $\mathbf{U}_p$ are the particle diameter and velocity, respectively.

Based on the DPM approach, the translational particle motion is described in Lagrangian coordinate system, where the origin is set at particle center. The motion of a particle in fluid is governed by integrating a force balance on the particle using Newton's second law of motion:

$$\frac{d\mathbf{x}_p}{dt} = \mathbf{U}_p \tag{4-10}$$

$$\frac{d\mathbf{U}_p}{dt} = \mathbf{F}_{pB} + \mathbf{F}_{pG} + \mathbf{F}_{p\varphi} + \mathbf{F}_{pC} \tag{4-11}$$

where $\mathbf{x}_p$ and $\mathbf{U}_p$ denote the particle position and velocity, $\mathbf{F}_{pB}$ and $\mathbf{F}_{pG}$ are the buoyancy and gravitational forces per unit particle mass, respectively. In this study, the four-way coupling (that considers both fluid-particle and particle-particle interactions) method was applied. $\mathbf{F}_{p\varphi}$ is the interaction force between fluid and solid particle, and $\mathbf{F}_{pC}$ is the contact force induced by particle-particle and particle-wall collisions. $\mathbf{F}_{pC}$ can be calculated based on the soft-sphere model proposed by Cundall and Strack (1980), consisting of a spring, a dashpot and a slider, which has already been implemented in OpenFOAM. Details about the contact force model and determination of parameters are available in Tsuji et al. (1992).

The term $\mathbf{F}_\varphi$ in Eq. (4-2) represents the interphase forces between gas and liquid phases, consisting of four main terms (Ničeno et al., 2008): $\mathbf{F}_\varphi = \mathbf{F}_{lg} = -\mathbf{F}_{gl} = \mathbf{F}_D + \mathbf{F}_L + \mathbf{F}_{VM} + \mathbf{F}_{TD}$, where $\mathbf{F}_{lg}$ refers to the momentum transfer from gas phase to liquid phase and vice versa for $\mathbf{F}_{gl}$, and $\mathbf{F}_D$, $\mathbf{F}_L$, $\mathbf{F}_{VM}$ and $\mathbf{F}_{TD}$ represent the drag force, lift force, virtual mass force and turbulent dispersion force, respectively. The interaction force $\mathbf{F}_{p\varphi}$ between fluid and solid phases includes drag force, shear lift force and virtual mass force: $\mathbf{F}_{p\varphi} = -\mathbf{F}_{\varphi p} = \mathbf{F}_{D,p\varphi} + \mathbf{F}_{L,p\varphi} + \mathbf{F}_{VM,p\varphi}$. The algorithm in the new solver was developed by considering the gas-solid and liquid-solid interaction forces separately, and then all the forces exerted on a solid particle were added together. The corresponding expressions for each force term can be found in the Appendix B.

4.2.2. Population balance model for gas phase

In this study, different bubble sizes were modeled, since bubble breakup and coalescence are important in a two- or three-phase system due to the liquid turbulence (Vieira et al., 2018). The PBM approach is able to simulate BSD and describe the evolution of bubble number density of different bubble sizes, and has been widely applied in gas-liquid two-phase flow simulations (Askari et al., 2018; Sarhan et al., 2018c; Khalil et al., 2021). Note that the comparison of different methods of solving PBE was outside of the scope of this work, and thus the class method implemented in OpenFOAM-v2006 was used, in which BSD were discretized into several classes and the PBE for the i-th bubble class can be expressed as (Kumar and Ramkrishna, 1996):

$$\frac{\partial n_i}{\partial t} + \nabla \cdot (\mathbf{U}_g n_i) = B_{i,co} - D_{i,co} + B_{i,br} - D_{i,br} \tag{4-12}$$

where n_i denotes the bubble number density for class i in each computational cell, and $B_{i,co}$, $D_{i,co}$, $B_{i,br}$, and $D_{i,br}$ represent the birth and death rates due to coalescence and the birth and death rates due to breakage, respectively (see Appendix B).

The bubble number density is related to its gas volume fraction:

$$n_i = \frac{\alpha_i}{V_i} \tag{4-13}$$

where V_i is the volume of a bubble of class i, and

$$\sum \alpha_i = \alpha_g \tag{4-14}$$

where α_g considers the effect of solid holdup ($\alpha_g = 1 - \alpha_l - \alpha_p$) in the new solver. The volume fraction of each bubble class can be normalized by the total gas volume fraction as a scalar f_i:

$$f_i = \frac{\alpha_i}{\alpha_g} \qquad \text{with} \qquad \sum f_i = 1 \tag{4-15}$$

Thus, Eq. (4-12) can be rewritten using f_i as:

$$\frac{\partial \alpha_g f_i}{\partial t} + \nabla \cdot (\alpha_g \mathbf{U}_g f_i) = V_i (B_{i,co} - D_{i,co} + B_{i,br} - D_{i,br}) \tag{4-16}$$

Based on the fixed pivot technique, the discretization scheme of bubble classes can be expressed as (Kumar and Ramkrishna, 1996; Sarhan et al., 2018d): $V_{i+1} = sV_i$, where $s > 1$. The coupling between the PBM and the Eulerian-Eulerian-Lagrangian model was achieved via the Sauter mean diameter d_{32} of bubbles in this study (Figure 4-1), which is defined as the diameter of a sphere that has the same volume to surface area ratio. For the PBM with class method, d_{32} can be determined as follows:

$$d_{32} = \frac{\sum_i f_i}{\sum_i f_i / d_i} \tag{4-17}$$

With Eqns. (12) - (17), bubble number density and hence d_{32} are directly related to the birth and death rates of bubbles. To solve the PBE, closure models for predicting coalescence and breakup of bubbles need to be determined. In this work, the widely-used coalescence model developed by Prince and Blanch (1990) was adopted, which accounts for turbulent and buoyancy-driven collision of bubbles. Two breakage models proposed by Lehr et al. (2002) and Laakkonen et al. (2006) were tested and compared in our study. Both models assume that bubble breakage is caused by the collision between bubbles and turbulent eddies. In Lehr et al.'s model, size distribution of daughter bubbles is derived directly from the breakup rate of bubbles, while Laakkonen et al.'s model requires an additional equation for the size distribution.

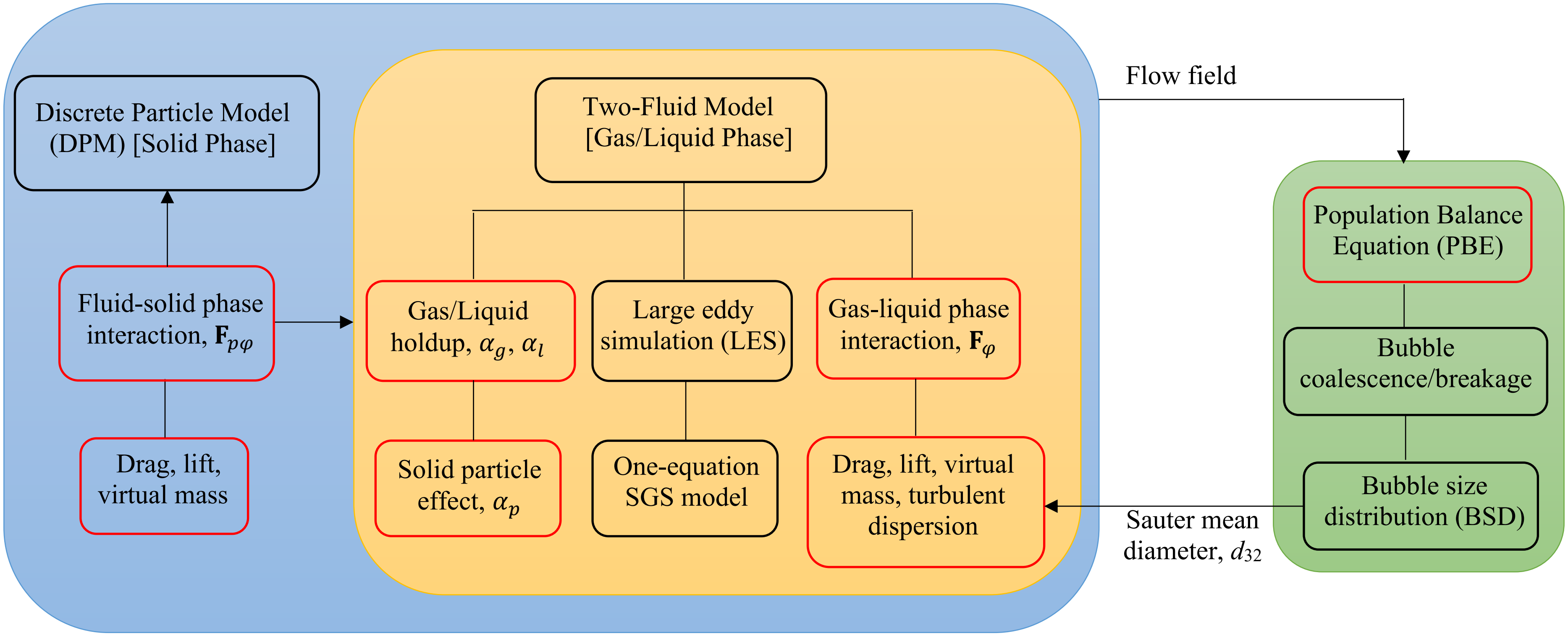

Figure 4-1. Framework of the newly developed solver for GLSTPF, combining the E-E-L approach and PBM. Red color represents our modifications to existing source code or model.

4.3. Numerical methodology

4.3.1. Experiment description

The setup of numerical simulation is based on the experimental setup of a gas-liquid-solid three-phase bubble column reported by Gan (2013). The schematic diagram of the setup is shown in Figure 4-2(a). The bubble column having a radius of r = 0.076 m was filled with a mixture of salty water (the liquid phase; density = 1048.5 kg/m^3), and the water height was 1.050 m. Monosized acrylic beads with a density of 1050 kg/m^3 were used as the solid phase, and a total of 20,000 solid particles were used in the column, resulting in a relatively low particle loading (i.e., the total particle holdup was 1.6%). Dry air was injected into the column with a flow rate of 0.8 L/min via an air stone (sparger) of 0.030 m in diameter and 0.050 m in height, which was placed at the center of the column bottom. Phase Doppler Anemometry technique was used to determine the bubble and solid size distributions, and the generated bubble size was generally within 0.6-2.4 mm. The solid particle diameter was in the small range of 2.75-3.25 mm, and the mean was 3 mm. Figure 4-2(b) shows an example of the size distributions measured at 0.1 m above the gas sparger.

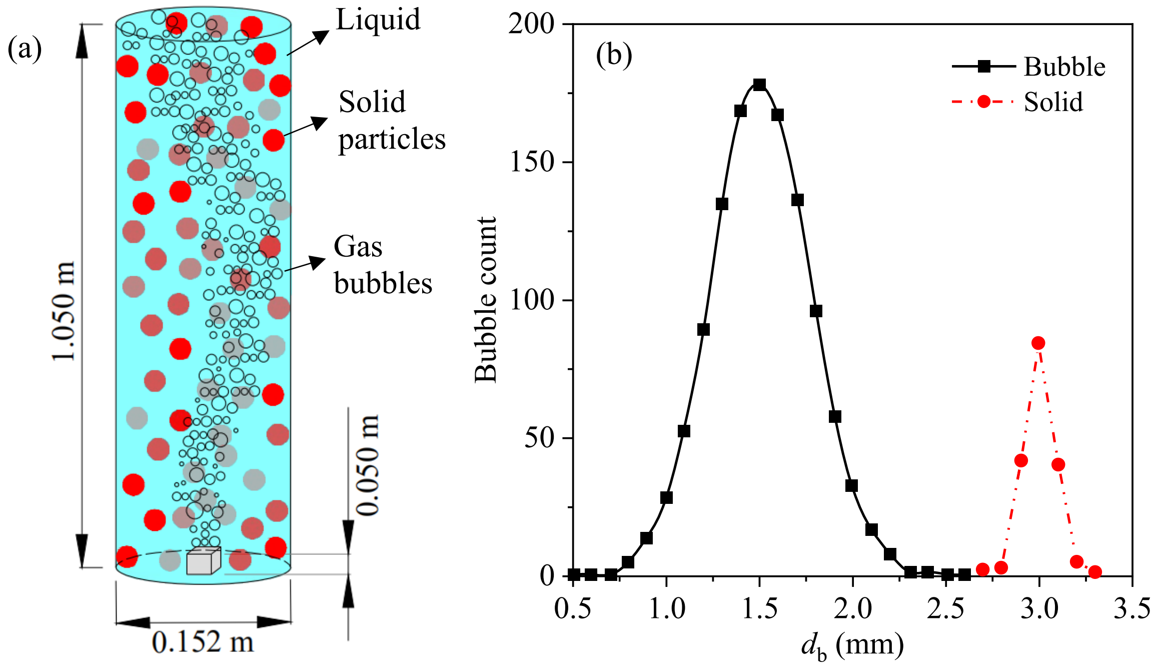

Figure 4-2. (a) Schematic diagram of the three-phase bubble column (not to scale); (b) size distributions at 0.1 m above the gas sparger (adapted from Gan (2013)).

4.3.2. Mesh generation and boundary conditions

In this study, the experimental geometry was discretized into computational grids by the *blockMesh* utility in OpenFOAM. Three grid cell (control volume) sizes were tested, i.e., coarse grid containing 16,860 cells (5.6-10.5 mm edge length), medium grid containing 31,904 cells (4.5-8.8 mm edge length) and fine grid containing 56,056 cells (3.8-7.8 mm edge length). Note that all the three grids adhere to the criterion that their cell sizes are larger than the sizes of bubbles or particles. Figure 4-3(a) and (b) show the configuration of the medium grid for the side and plan views, respectively. Due to that the detailed structure of the gas sparger was not provided in Gan (2013) it was simplified into a rectangular box (3 x 3 x 5 cm^3), and the same treatment was conducted in Gruber et al. (2016). The top surface of the sparger was set as the air inlet with 16 (4 x 4) small faces, as shown in Figure 4-3(b) and (c). Additionally, the top surface of the bubble column was set as outlet, and the remaining surfaces of the column were specified as wall. The coordinate system is defined in Figure 4-3(c), where the origin was set at the inlet center, *y* is the vertical (axial) direction, and *x* and *z* are the radial directions.

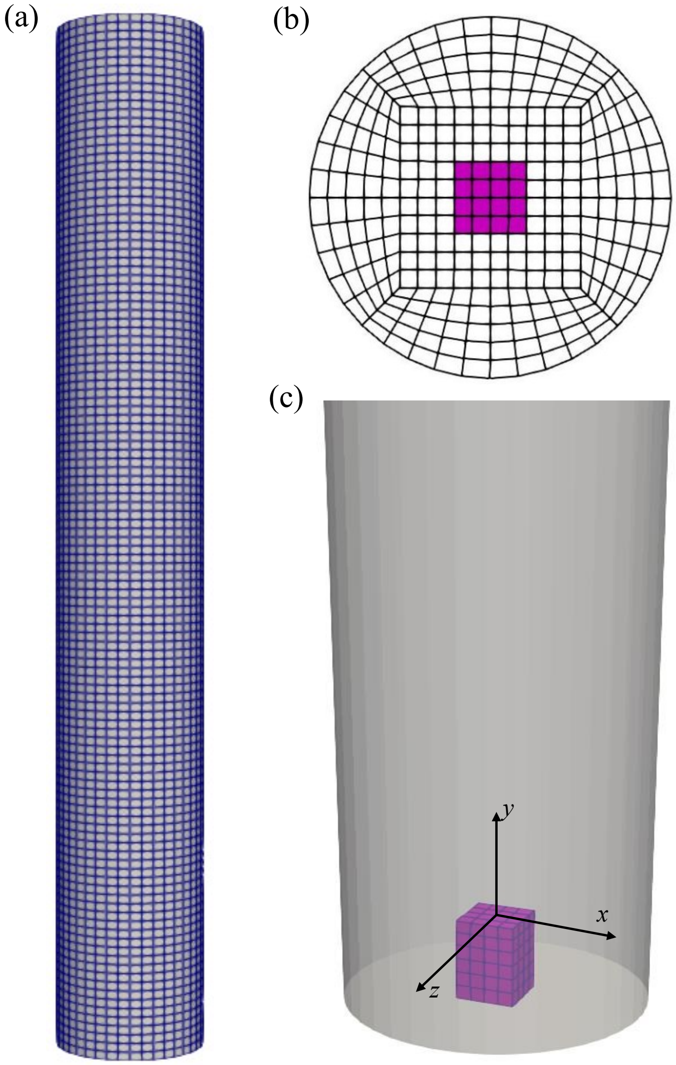

Figure 4-3. Configuration of the medium grid for (a) side view, (b) plan view, and (c) gas sparger and coordinate system.

Using the same phase properties as in Gan's experiment, the bubble column was initially filled with stagnant liquid, and the 20,000 Lagrangian solid particles were randomly distributed in the column, in which the particle positions were determined via MATLAB. No gas exists in the column at the initial time. Gas bubbles consisting of 16 groups (shown in Table 4-2) with $s = 1.26$ were injected from the inlet to drive the flow, and a fixed velocity of 0.015 m/s were specified at the inlet, which was calculated by the ratio of the gas flow rate 0.8 L/min (Gan, 2013) to the inlet area. Therefore, a laminar gas injection is specified at the inlet, yielding a Reynolds number of 30 for the bubble plume. At the outlet, a degassing boundary condition was used for gas-liquid phases, which acts as a free surface for the liquid and allows bubbles to escape. Non-slip boundary condition was imposed at the walls for both the gas and liquid phases. Furthermore, the solid particles bounced back with a restitution coefficient of 0.9 at the walls and 0.1 at the outlet (Gruber et al., 2016). Detailed setup of boundary conditions for each variable is summarized in Table 4-3.

Table 4-2. Bubble classes used in the simulation.

Bubble class index	Bubble diameter (mm)	Bubble class index	Bubble diameter (mm)
1	0.73	9	1.36
2	0.79	10	1.46
3	0.86	11	1.58
4	0.93	12	1.71
5	1.00	13	1.85
6	1.08	14	2.00
7	1.16	15	2.16
8	1.25	16	2.33

Table 4-3. Boundary conditions used in the simulation.

Variable	Inlet	Outlet	Walls
α_g	Dirichlet	inletOutlet	Neumann
$\mathbf{U}_g$	Dirichlet	pressureInletOutletVelocity	noSlip or slip
$\mathbf{U}_l$	Dirichlet	slip	noSlip
p	calculated	calculated	calculated

p_{rgh}	fixedFluxPressure	prghPressure	fixedFluxPressure
k_{SGS}	Dirichlet	inletOutlet	kqRWallFunction
μ_{φ}^{T}	calculated	calculated	nutkWallFunction

4.3.3. Simulation procedure

Same as the basic solvers in OpenFOAM, the newly developed *reactingEulerDPMFoam* is based on the finite volume method to discretize the governing equations. The fluid phase volume fractions were solved by using a modified MULES method (the algorithm was modified to consider the effect of solid particle α_p), and the velocity-pressure was coupled via the PIMPLE algorithm. The first order bounded implicit Euler scheme was used for the time derivative terms in the equations, the second order Gauss linear scheme was adopted for the gradient terms, the limited discretization scheme was used for the divergence terms, and the diffusive terms were interpolated with the Gauss linear uncorrected scheme. The detailed schemes for each term in the governing equations are listed in Table 4-4.

Table 4-4. Numerical schemes used in OpenFOAM: $\emptyset$ is a generic variable, ∇^2 is the Laplacian term, $\nabla^{\perp}$ is the surface-normal gradient term, and $(\emptyset)_f$ is the face interpolation operator.

Term	Scheme
$\partial\emptyset/\partial t$	Euler implicit
$\nabla\emptyset$	Gauss linear
$\nabla \mathrm{p}$	Gauss linear
$\nabla \cdot (\mathbf{U}_{\boldsymbol{\varphi}} \alpha_{\varphi})$	Gauss vanLeer
$\nabla \cdot (\emptyset \mathbf{U}_{\boldsymbol{\varphi}} \mathbf{U}_{\boldsymbol{\varphi}})$	Gauss limitedLinearV 1
$\nabla \cdot (\mathbf{U}_{\boldsymbol{\varphi}} \emptyset)$	Gauss limitedLinear 1
$\nabla \cdot \left(\tau_{\varphi}^{\mathrm{eff}}\right)$	Gauss linear
$\nabla^2\emptyset$	Gauss linear uncorrected
$\nabla^{\perp}\emptyset$	uncorrected

$(\emptyset)_f$	linear

A fixed time step of 0.001 s was adopted to resolve the flow field and the movement of Lagrangian particles, and to ensure the maximum Courant number below 1. Each case was run for more than 300 s real-time, and time averaging was performed after 50 s when the flow reached statistically stationary turbulence (the gas holdup was used to determine the statistical independence of the flow). The numerical simulations were carried out on a cluster (Compute Canada) with 10 processors for each case. A total of 7 numerical cases with different parameters were simulated in this study (see Table 4-5). Cases 1 (with PBM) and 6 (without PBM) were used as the baseline cases.

Table 4-5. Summary of numerical cases of three-phase bubble column in this study: Prince-Laa and Prince-Lehr represent the coalescence model of Prince and Blanch (1990) coupled with the breakage models of Laakkonen et al. (2006) and Lehr et al. (2002), respectively.

Case	Coalescence-breakage models	Mesh grid	Gas slip on walls
1	Prince-Laa	Medium	No
2	Prince-Lehr	Medium	No
3	Prince-Laa	Coarse	No
4	Prince-Laa	Fine	No
5	Prince-Laa	Medium	Yes
6	No PBM	Medium	No
7	No PBM	Medium	Yes

To obtain the solid phase properties in the Eulerian flow field, one challenge was to convert the Lagrangian data to the Eulerian data. The Eulerian particle volume fraction has already been implemented in OpenFOAM-v2006, yet the solid particle velocity still needs to be mapped to the

Eulerian field. Therefore, a *volVectorField* v_{pm} was created in *reactingEulerDPMFoam* to calculate the mean particle velocity in each cell. It should be noted that time-averaging of particle velocity may not be accurate to calculate v_{pm}, since there might not be any particles at a certain time in a specified cell (the particle velocity will be assigned as the default value zero in this case). As a result, v_{pm} is calculated by: $v_{\mathrm{pm}} = \frac{\sum_1^n v_{\mathrm{p}}}{n}$, where v_{p} is the instantaneous velocity for each particle, and *n* denotes the total particle number passing through each cell. v_{pm} was introduced after 50 s real time.

4.4. Results and discussion

4.4.1. Grid independence analysis

A grid sensitivity analysis was conducted on the three grids (coarse, medium, and fine) to investigate the influence of grid resolution on the simulated results. Figure 4-4(a) shows the distribution of mean axial velocity of solid particles, v_{pm}, at *y* = 0.7 m predicted with the three grids, along with the experimental result from Gan (2013). The results show that the simulated v_{pm} by both the medium and fine grids are in good agreement with the experimental data, with only minor differences (up to 0.005 m/s) observed between the two grids. However, the predicted v_{pm} with the coarse grid deviates more from the experimental data, especially for negative values near the wall region. Figure 4-4(b) compares the gas holdup between experimental data and predicted results at *y* = 0.1 m. Again, the predicted results from both the medium and fine grids generally agree well with the experimental data. The deviation between the grids occurs mainly near the centerline, where the maximum deviation is 7% at *x*/r = 0. Large differences (with more than 50% deviations at the centerline) are observed between the results of the coarse grid and the experimental data.

Both the medium and fine grids are capable of providing reliable results, but the simulation time of the fine grid (~ 4.5 days) is approximately 1.5 times longer than that of the medium grid (~ 3 days). Therefore, to balance computational accuracy and cost, the medium grid was selected for the remaining simulation cases.

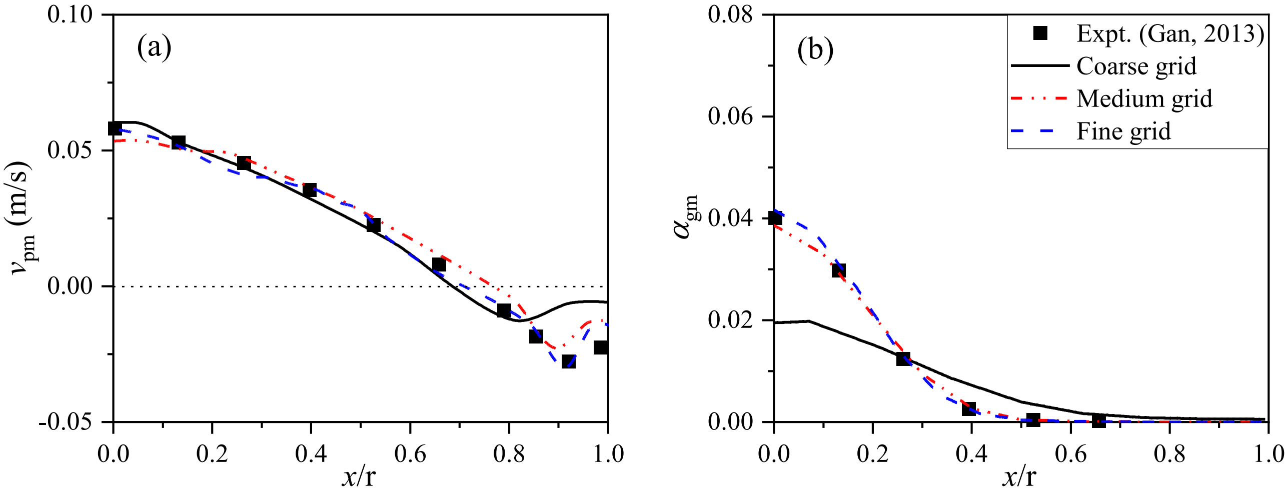

Figure 4-4. Grid effects on the radial distributions of (a) mean axial particle velocity at y = 0.7 m, and (b) mean gas holdup at y = 0.1 m in the center-plane (z = 0 m).

4.4.2. Resolved turbulent kinetic energy

The resolved turbulent kinetic energy $k_{\rm re}$ is a significant criterion in examining the adequacy and feasibility of fluid flow resolved by LES, which can be calculated as: $k_{re} = \frac{1}{2}\left(\overline{(u')^2} + \overline{(v')^2} + \overline{(w')^2}\right)$, where u', v' and w' are the fluctuating velocity components. Figure 4-5 shows the comparison of the resolved axial fluctuating liquid velocity $\overline{(v')^2}$ in the center-plane (z = 0 m) between our study and Gruber et al. (2016) who used the E-L-L approach. The results of both studies showed similar shapes and values of $\overline{(v')^2}$, but the distribution was more stretched in this study, with more axial fluctuations resolved near the gas inlet.

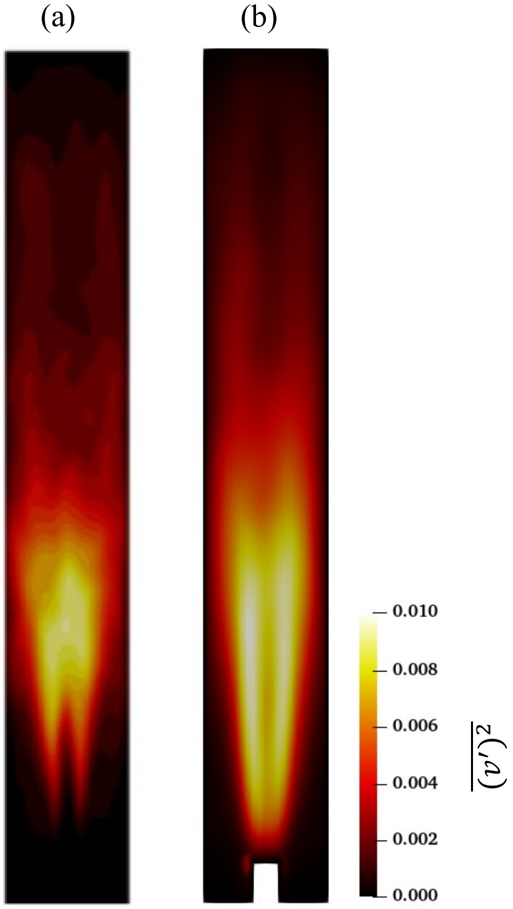

Figure 4-5. Comparison of the resolved fluctuating liquid velocity in the center-plane between (a) Gruber et al. (2016) and (b) current study.

In a well-resolved flow, the ratio of resolved turbulent kinetic energy to the total turbulent kinetic energy, $k' = k_{\text{re}} / (k_{\text{re}} + k_{\text{SGS}})$, is suggested to be greater than 80% (Pope, 2000). Figure 4-6 shows the distribution of k' at the center-plane and different heights along the column. It was observed that k' is higher than 80% at most positions, and all the values are higher than 70% except those near the wall regions, where the turbulent kinetic energy is included in the SGS model.

Therefore, the flow field is considered to be resolved, and the resolution of the LES with the current mesh is acceptable for further analysis.

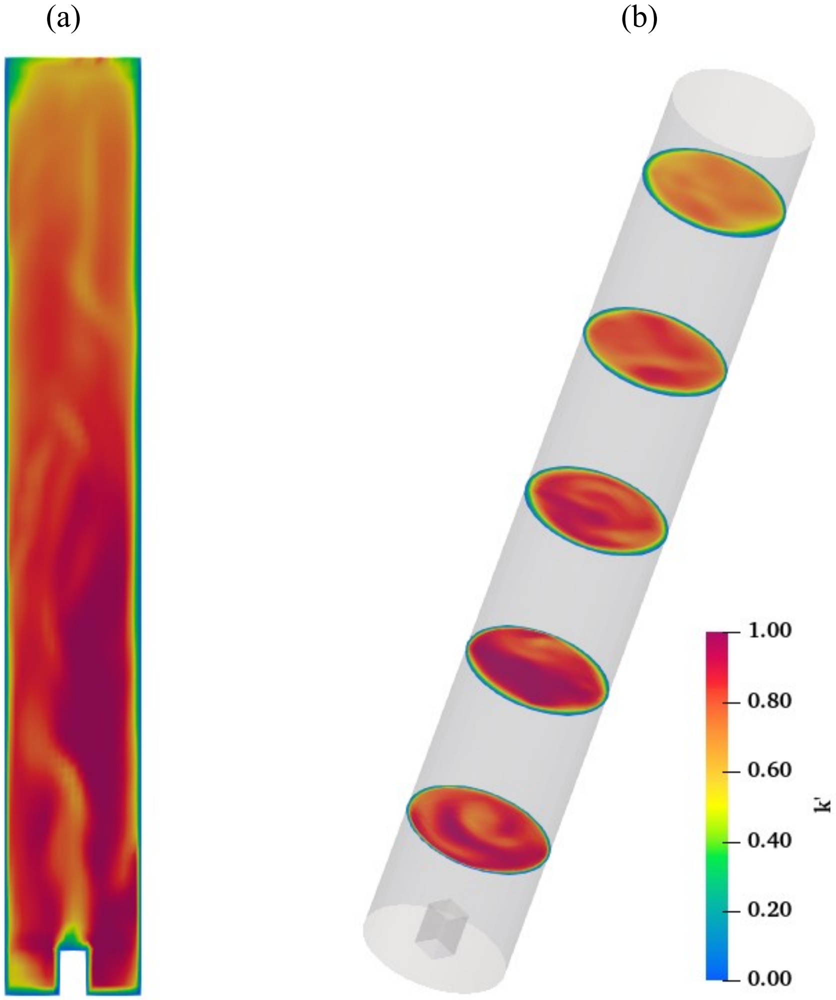

Figure 4-6. The distribution of *k'* at the (a) center-plane and (b) different heights along the bubble column.

4.4.3. Bubble size distribution

Two different methods, namely probability density function (PDF) and cumulative density function (CDF) (Tabib and Schwarz, 2011), were used to evaluate BSD in the bubble column. The relationship between the normalized bubble number and bubble size was used to construct the PDF, and Figure 4-7(a) shows the PDF of each bubble class at $y = 0.1$ m in the center of the column.

The experimental results show that the bubble diameter exhibits a normal distribution with a peak near 1.5 mm. The Prince-Lehr model predicts a lower PDF than the experimental values for d_b < 1.4 mm, and a higher PDF for d_b > 1.4 mm. In comparison, the PDF predicted with the Prince-Laa model is basically consistent with the experimental data for d_b < 1.8 mm. However, the predicted PDF tends to overestimate the experimental data for larger bubbles (d_b > 1.8 mm), probably owing to the larger intervals between adjacent bubble classes as listed in Table 4-2. Therefore, it is necessary to compare the CDF between the experimental and simulated bubble sizes.

Figure 4-7(b) shows the experimental and predicted CDF of bubble classes at $y = 0.1$ m, where the error bar represents the bias within 5% of experimental d_b (Gan, 2013). The predicted CDF profiles from both the Prince-Lehr and Prince-Laa models are consistent with the experimental results. Specifically, the maximum deviation between the Prince-Lehr and experimental results is lower than 5% for d_b < 1.7 mm, whereas it becomes larger (5% - 11%) for d_b > 1.7 mm. On the other hand, the Prince-Laa model shows better agreement with the experiment, and the maximum deviation is generally lower than 5% for all the bubble classes. As a result, the Prince-Laa model was adopted in this work due to its higher accuracy.

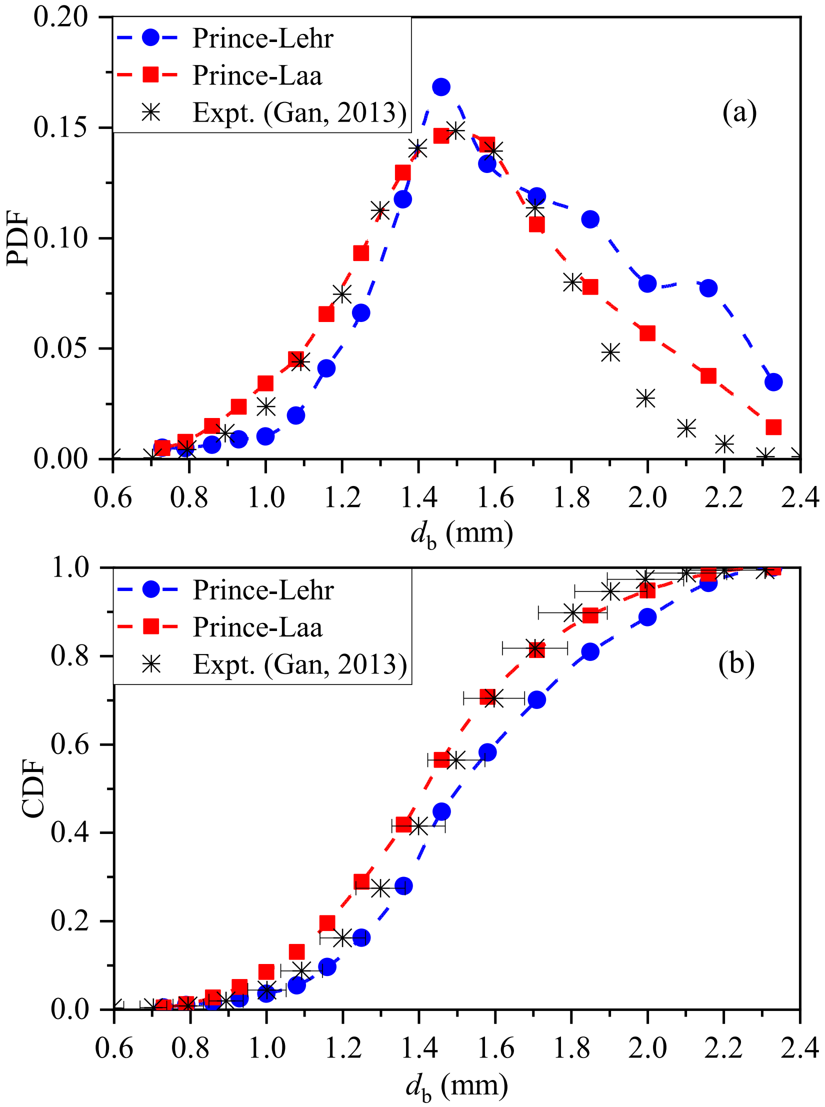

Figure 4-7. Comparison between predicted and experimental (a) PDF and (b) CDF of bubbles at y = 0.1 m in the center of the column.

4.4.4. Phase velocity distribution

To illustrate the effect of PBM on flow characteristics, phase properties (i.e., velocity and holdup) at two different heights (y = 0.1 m and 0.7 m) of the bubble column were investigated and compared with previous studies (Gan, 2013; Gruber et al., 2016) in *Sections 4.4.4 and 4.4.5*. The bubble rise and solid particle velocities were calculated primarily by the momentum/force balances via Eqs. (4-2) and (4-11), respectively. Figure 4-8(a) shows the radial distribution of mean axial bubble velocity v_{gm} at $y = 0.1$ m and $y = 0.7$ m in the center-plane, and both the predicted results with and without PBM are compared with the experimental data (the error bar denotes ±15% deviations of experimental data (Gan, 2013). v_{gm} decreases in the radial direction as expected. At $y = 0.1$ m, the predicted v_{gm} with PBM agrees well (within 15% error level) with the experimental data, except for the near-wall regions where the simulated v_{gm} rapidly decreases to zero. In contrast, larger deviations are observed between the predicted v_{gm} without PBM and measured data. The differences between the predicted v_{gm} with and without PBM decrease at $y = 0.7$ m, but some data points deviate from the measured values (maximum errors of 18% with PBM and 28% without PBM). At both heights, the inaccuracy of modeling near the wall can be attributed to the non-slip conditions of bubble velocity specified at the wall, while the linear interpolation is used in the wall-nearest cell, and thus the interpolated bubble velocity may not be realistic (Gruber et al., 2016). In the experiment, there is a smooth change of v_{gm} in the near wall region, indicating that the individual bubbles are able to slip at the wall as expected.

Thus, the bubble rise velocity with free-slip condition at the wall is further tested in Figure 4-8(b). Compared to the non-slip condition, the predicted rise velocity with the free-slip condition is closer to the measurement values in the near-wall regions. The accuracy of the simulated results is improved to a great extent, and the bias between the predicted v_{gm} with PBM and experimental data is generally smaller than 15% at both heights (0.5% - 10% at $y = 0.1$ m and 0.8% - 14% at $y = 0.7$ m). Compared to the results at $y = 0.1$ m, similar results are predicted with and without PBM at $y = 0.7$ m, indicating that the effects of bubble coalescence and breakup are weaker at higher locations, which is consistent with the experimental observations (Gan, 2013) and one's intuition. Compared to the results without PBM, the predicted bubble rise velocity with PBM is significantly improved with a maximum value of 20% at $y = 0.1$ m and 6% at $y = 0.7$ m.

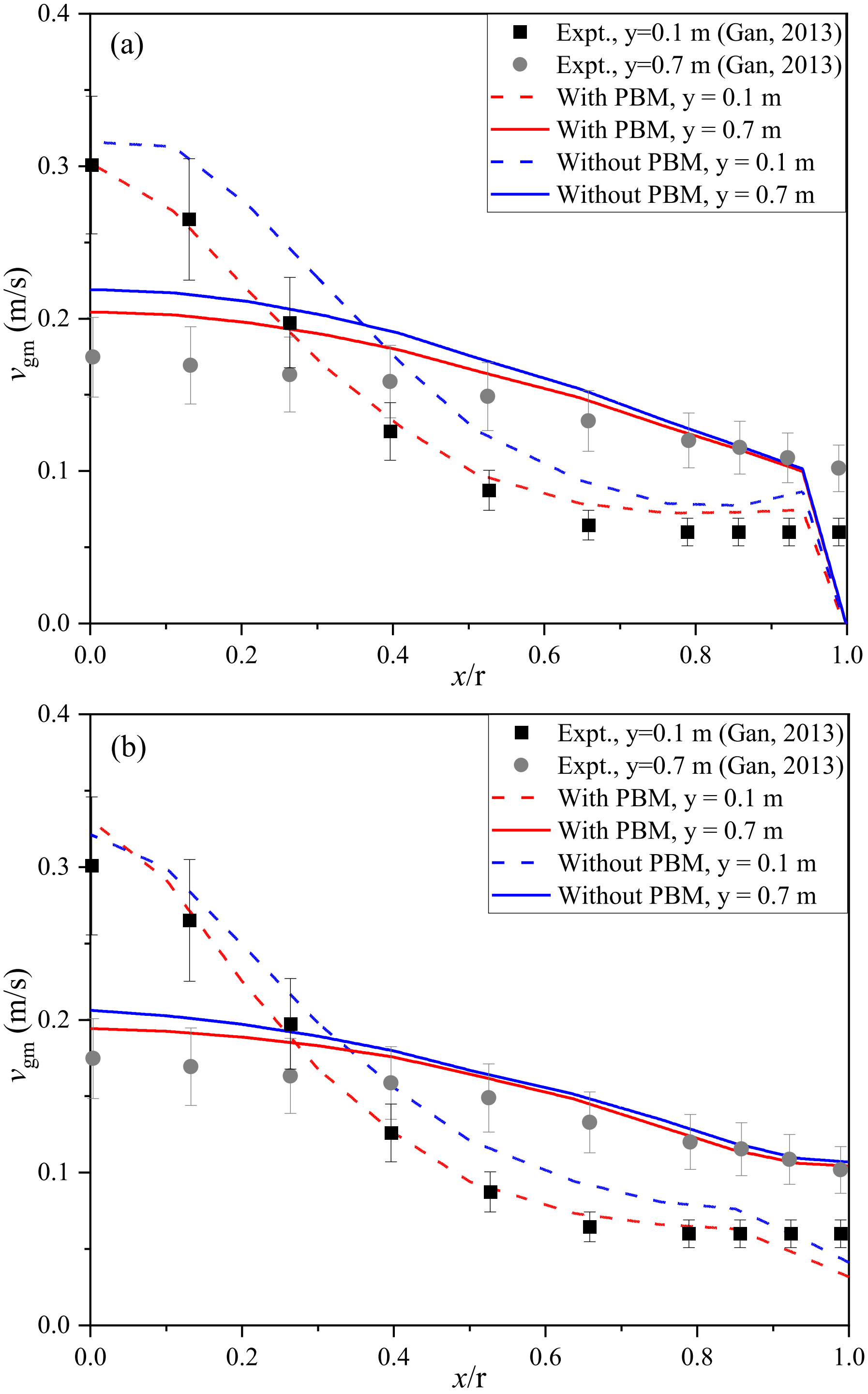

Figure 4-8. The radial distribution of mean axial bubble velocity v_{gm} at $y = 0.1$ m and 0.7 m with (a) non-slip and (b) slip conditions for gas at the wall.

The radial distributions of mean axial particle velocity v_{pm} at $y = 0.1$ m and 0.7 m are shown in Figure 4-9, with error bars indicating ±15% deviations from the experimental data (Gan, 2013). The peak velocity of upward moving particles (positive v_{pm} values) is observed at the center of the column, while the velocity decreases radially and changes to a downward direction near the wall to circulate in the column (Gan, 2013). Good predictions are achieved at $y = 0.7$ m for both the v_{pm} with PBM (maximum difference of 0.005 m/s) and without PBM (maximum difference of 0.010 m/s). At $y = 0.1$ m, the positive values of v_{pm} with PBM agree well with the experimental data, with a maximum deviation of 5.8% at the column center. The positive values without PBM also demonstrate promising results except for the column center (with a deviation of 16%), where bubble coalescence and breakup are significant (Gan, 2013). However, larger deviations occur for the negative values of v_{pm}, although better agreement is achieved with PBM (with a maximum difference of 0.023 m/s). The underestimation of the absolute value of negative v_{pm} is consistent with the findings of Gruber et al. (2016). Possible reasons for this observation will be discussed in the *Section 4.4.5*.

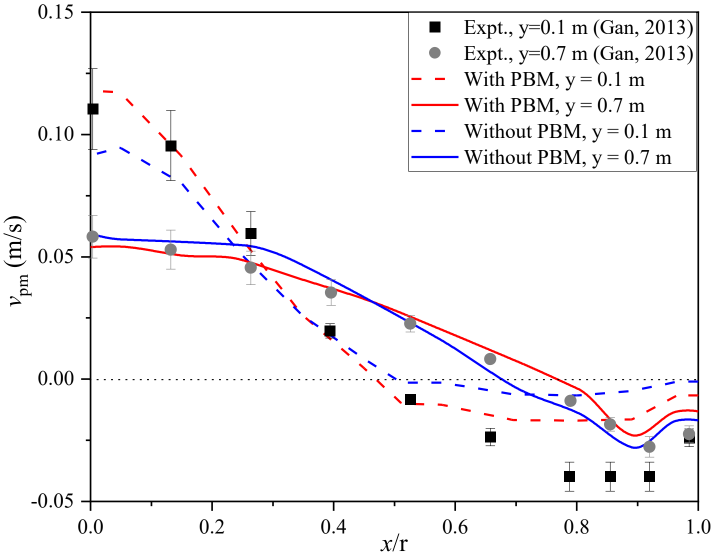

Figure 4-9. The radial distribution of mean axial particle velocity v_{pm} at $y = 0.1$ m and 0.7 m in the center-plane.

To further demonstrate the movement of the three phases in the bubble column, Figure 4-10 displays the velocity fields of all the three phases at the center-plane, where Figure 4-10(a) - (c) are the instantaneous velocity fields at $t = 300$ s, and (d) - (f) present the mean velocity fields. The instantaneous bubble rise velocity v_{g} is irregularly distributed in the bubble column (Figure 4-10a), mainly due to the oscillation of the bubble plume caused by the turbulence effect (Joshi et al., 2002), as well as its interactions with solid particles. The instantaneous liquid velocity v_{l} and solid particle velocity v_{p} generally follow the distribution of gas bubbles, but their maximum magnitudes are significantly lower (25% for v_{l} and 38% for v_{p}) than v_{g} (Figure 4-10b - c). Additionally, the different orientations of liquid velocity vectors indicate the presence of swirling flow in the column (Figure 4-10b), which will be further discussed in *Section 4.4.6*. The mean velocity fields exhibit a symmetric distribution with the highest values at the centerline of the bubble column (Figure 4-10d - f), because the velocities are time-averaged. Similar with the instantaneous distributions, the maximum magnitudes of mean liquid and particle velocities are lower (39% for v_{lm} and 63% for v_{pm}) than v_{gm}. Interestingly, both the liquid and solid phases tend to move outwards and inwards (as depicted by the velocity vectors) in top and bottom regions respectively, to circulate in the column. The minimum mean velocities (moving downwards) for both phases occur in the middle region ($y = 0.3$ - 0.6 m) of the column.

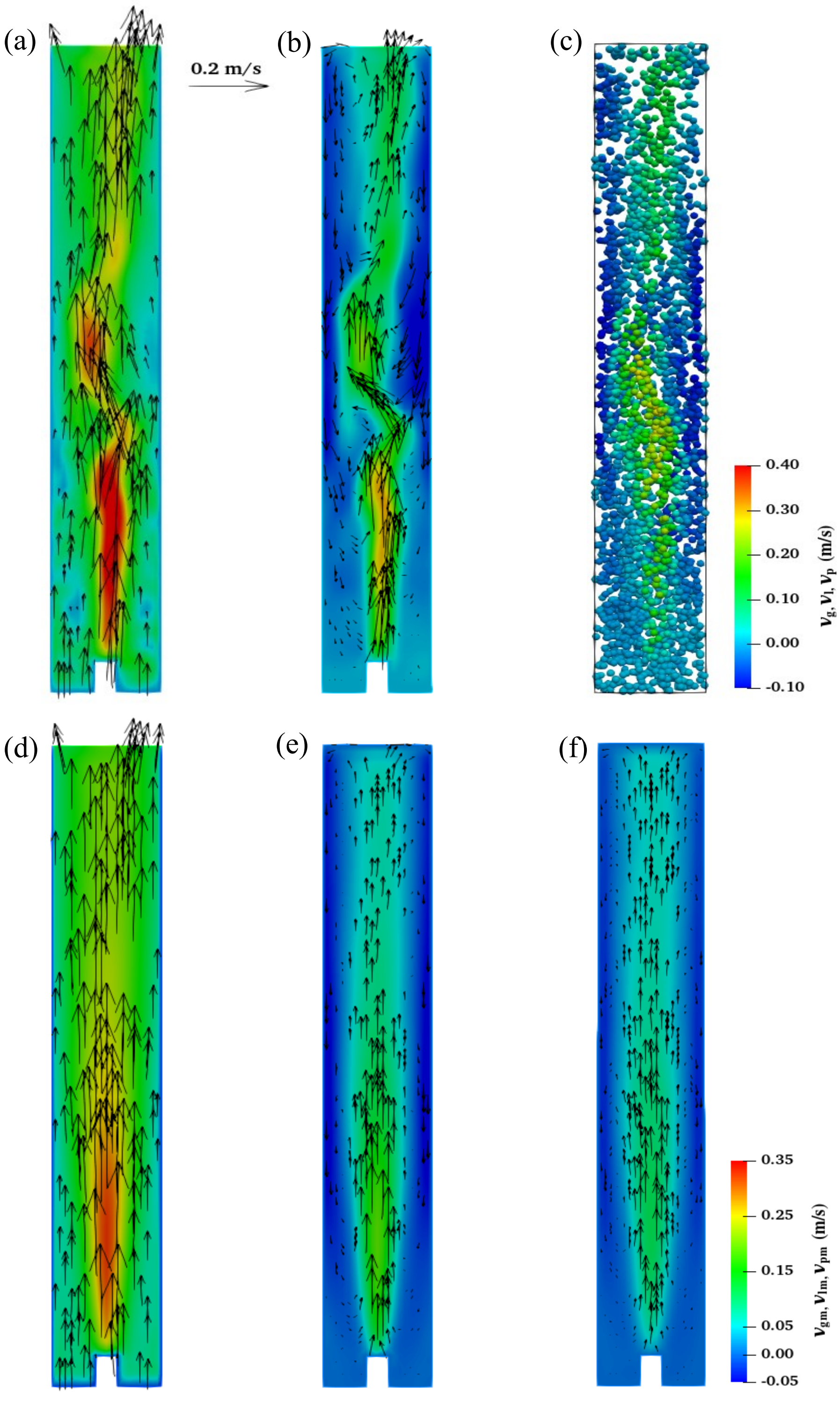
(a)
0.2 m/s
(b)
(c)
0.40
0.30
0.20
0.10
0.00
-0.10
v_g, v_l, v_p (m/s)
(d)
(e)
(f)
0.35
0.25
0.15
0.05
0.00
-0.05
v_{gm}, v_{lm}, v_{pm} (m/s)

Figure 4-10. The instantaneous velocity fields of (a) gas phase, (b) liquid phase and (c) solid phase at $t = 300$ s; and the mean velocity fields of (d) gas phase, (e) liquid phase and (f) solid phase in the center-plane.

4.4.5. Phase holdup distribution

The radial distributions of mean gas holdup α_{gm} at $y = 0.1$ m and 0.7 m are illustrated in Figure 4-11, along with the simulated α_{gm} at $y = 0.7$ m by Gruber et al. (2016) for comparison. At $y = 0.1$ m, the predicted α_{gm} with PBM agrees well with the experimental data, leading to an improvement of 11% at the column center compared to the case without PBM. The difference between the predicted α_{gm} with and without PBM decreases at $y = 0.7$ m. However, both models with and without PBM significantly underpredict the gas holdup at $y = 0.7$ m, with a maximum difference of about 0.01 at $x/\mathrm{r} = 0$, while the predicted values are consistent with those in Gruber et al. (2016). This underprediction could be attributed to the high lift coefficient $C_L = 0.5$ used in the coupling of gas and liquid phases, which leads to a strong lateral spreading in the bubble column. To address this issue, several tests were conducted, and the results suggest that decreasing C_L can resolve the underprediction at $y = 0.7$ m, but this will also increase the gas holdup and velocity at the column center. It is worth noting that after integrating the gas mass flow rate $\dot{m}_g = \int_0^r \rho_g \alpha_{gm} v_{gm} \cdot 2\pi r dr$ at two cross-section ($y = 0.1$ m and 0.7 m) of the column, the gas mass flow rate is conserved in the current simulation. However, in Gan's experiment, $\dot{m}_g$ at $y = 0.7$ m is about twice that at $y = 0.1$ m according to the experimental data. Given the good predictions of v_{gm} and α_{gm} at $y = 0.1$ m, as well as the similar prediction results in Gruber et al. (2016) at $y = 0.7$ m, this underprediction of α_{gm} at $y = 0.7$ m could be related to the experimental errors there.

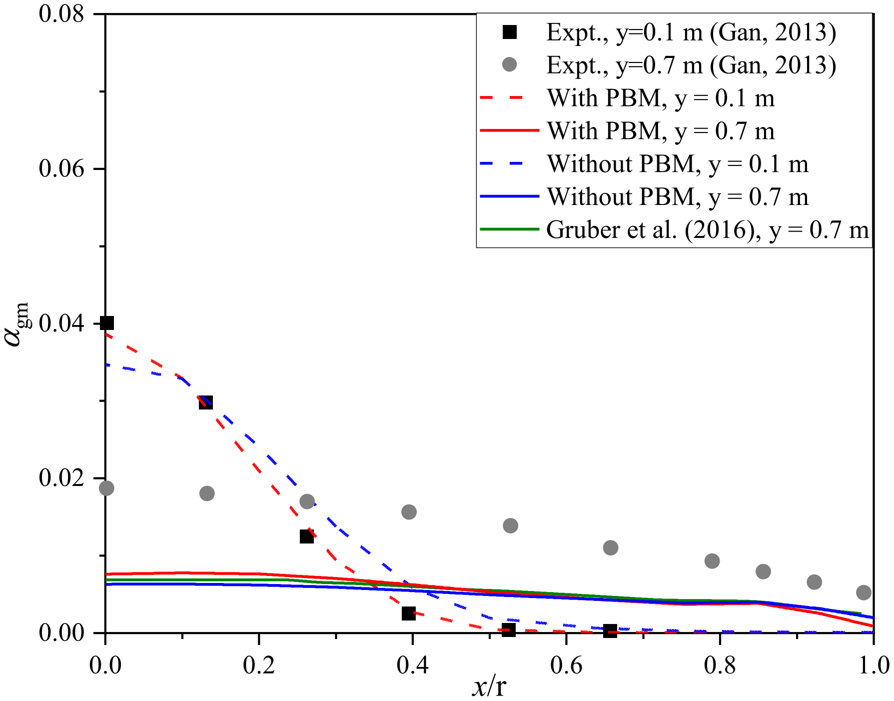

Figure 4-11. The radial distributions of mean gas holdup α_{gm} at $y = 0.1$ m and 0.7 m in the center-plane.

Figure 4-12(a)-(c) shows the isosurface of 0.005 of the instantaneous gas holdup at $t = 50$ s, 150 s, and 300 s, respectively. The gas phase exhibits oscillatory behavior in the bubble column, and the bubbly region widens as it ascends due to plume diffusion in the radial direction. Moreover, the irregular shape of the isosurface signifies the periodic movement and spreading of gas bubbles. To examine the time-averaged diffusion of gas phase, the distribution of mean gas holdup α_{gm} at center-plane is depicted in Figure 4-12(d). The gas bubbles were found to spread widely throughout the column, with the maximum α_{gm} occurring at the centerline. The centerline gas holdup initially decreases rapidly (from 1 to 0.02) near the nozzle and then decreases gradually (from 0.01 to 0.005) from the middle to the top surface.

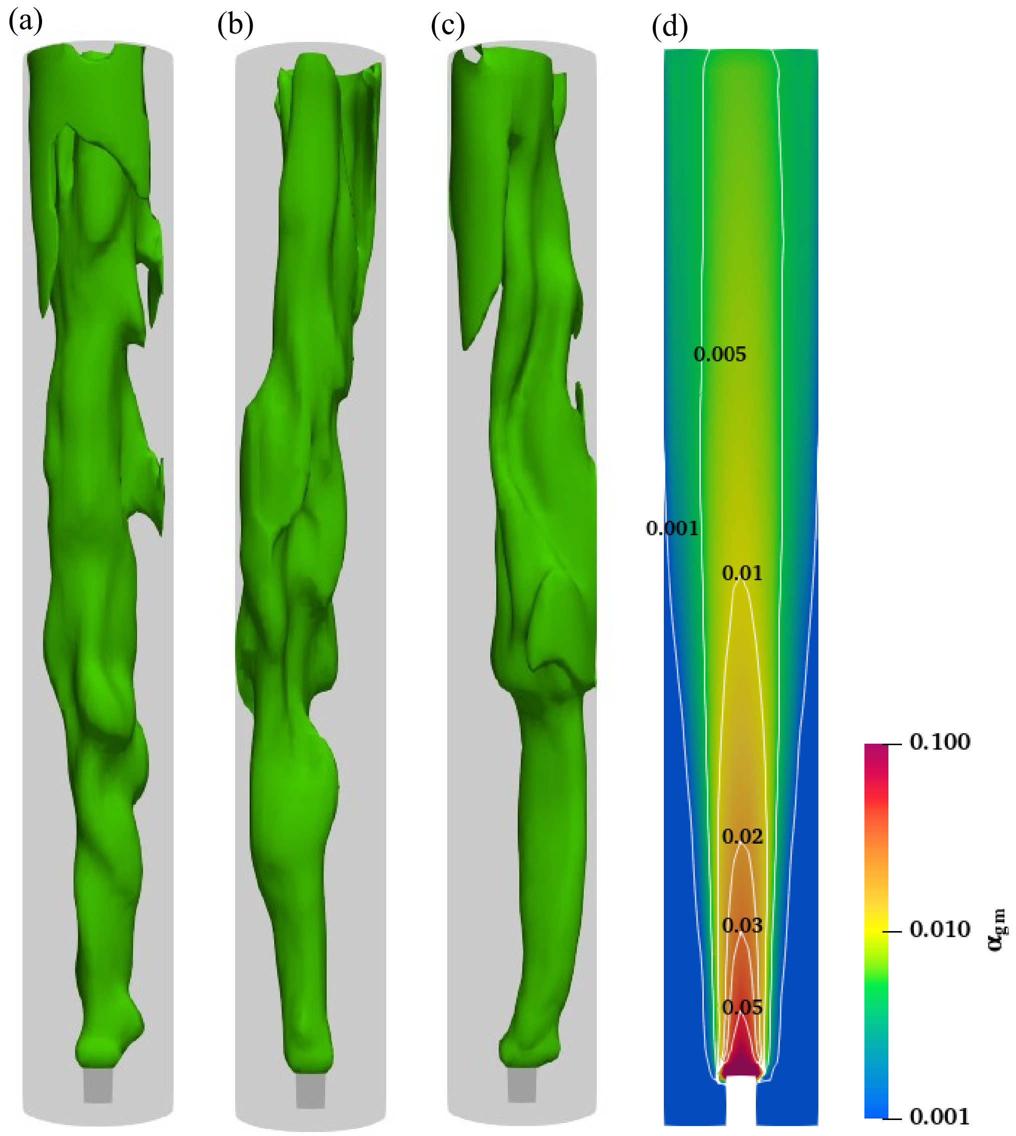

Figure 4-12. The isosurface of the 0.005 instantaneous gas holdups at (a) $t = 50$ s, (b) 150 s, and (c) 300 s; (d) the distribution of mean gas holdup α_{gm} in the center-plane.

The radial distributions of mean particle holdup α_{pm} at $y = 0.1$ m and 0.7 m are shown in Figure 4-13. The predicted α_{pm} with PBM is smaller than that without PBM at $y = 0.1$ m, whereas they are similar at $y = 0.7$ m. The current study improved the predicted α_{pm} at $y = 0.1$ m compared to the results of Gruber et al. (2016). While good agreement is obtained between the predicted α_{pm} with PBM and the experimental results at both heights, the near-wall region presents a challenge for both the present study and Gruber et al. (2016), where α_{pm} is overpredicted. Overall, the introduction of PBM significantly improves the prediction of α_{pm} by up to 30%.

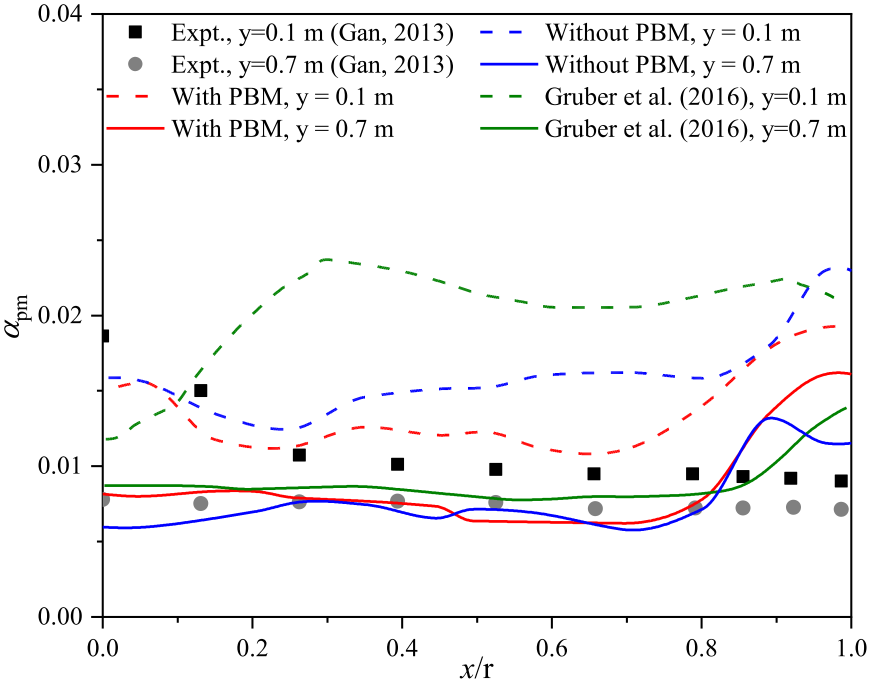

Figure 4-13. The radial distributions of mean particle holdup α_{pm} at y = 0.1 m and 0.7 m in the center-plane.

To further examine the reason of deviation near the wall, the solid particle mass flow rate $\dot{m}_p = \int_0^r \rho_p \alpha_{pm} v_{pm} \cdot 2\pi r dr$ was calculated at both cross-sections (y = 0.1 m and 0.7 m) of the column. It was found that the upward particle mass flow rate equals the downward value at both sections in the current simulation. However, in Gan's experiment, the downward $\dot{m}$ is 47% higher than the upward $\dot{m}$ at y = 0.1 m, while it is opposite (55% lower) at y = 0.7 m. The higher downward $\dot{m}_p$ at y = 0.1 m indicates that either the particle velocity and/or particle holdup was measured higher than their actual values near the wall, and vice versa at y = 0.7 m. Additionally, the increasing trend of particle holdup near the wall has also been observed by many other researchers in three-phase bubble columns (Atta et al., 2009).

Figure 4-14(a) - (c) show the instantaneous distributions of particle holdup α_p at $t = 50$ s, 150 s, and 300 s, respectively. The distribution of α_p is discontinuous, because it is obtained by mapping the Lagrangian data to the Eulerian field. At $t = 50$ s, the solid particles are non-uniformly distributed in the column (Figure 4-14a). As time progresses, the particles tend to settle more in the lower region of the bubble column due to the slightly larger density of the particles than the liquid (Figure 4-14b and c), which is consistent with the experiment observations (Gan, 2013).

The time-averaged distribution of particle holdup α_{pm} is shown in Figure 4-14(d), revealing that the solid particles tend to accumulate at the bottom of the column (near the sparger wall) and the top corner of the column. Near the top of the column, the particles move towards both sides and flow downwards along the wall to circulate in the bubble column (Figure 4-10f). In the lower region of the column, the downward solid particles can only be drifted up by the bubbles near the sparger, whereas they settle down at other radial positions (Gan, 2013). In other regions, the solid particles are primarily concentrated near the centerline and the walls, indicating that their movement follows the fluid circulation in the column.

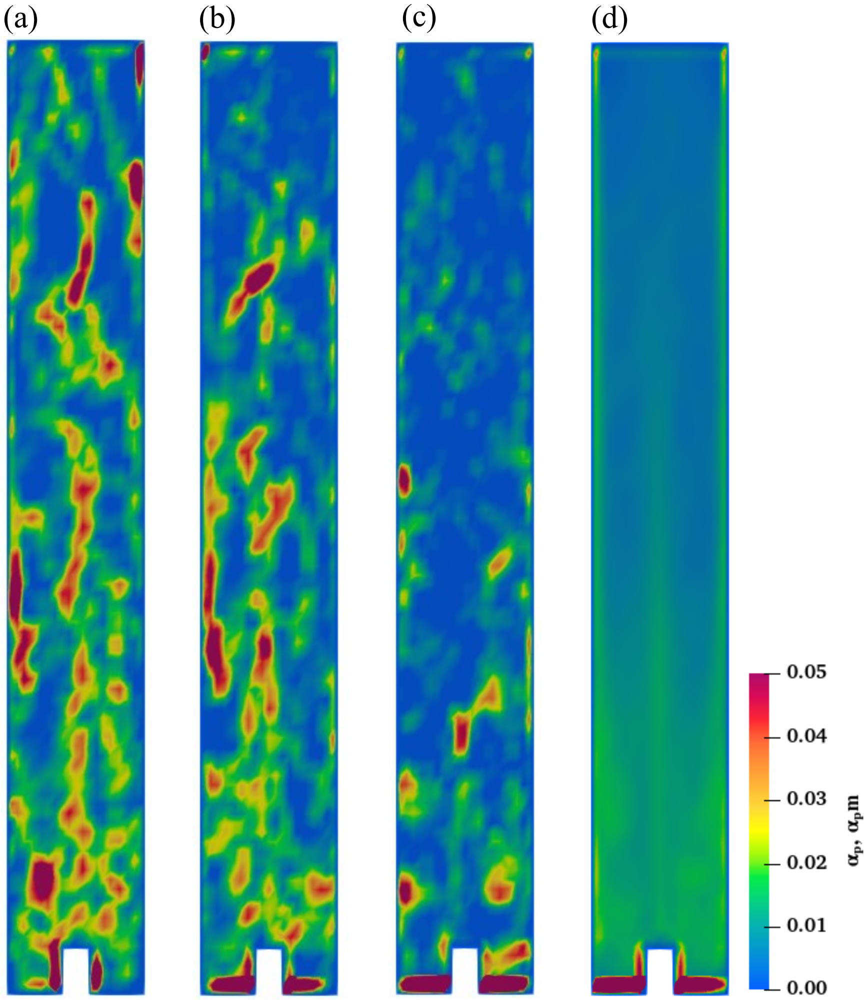

Figure 4-14. The distributions of instantaneous particle holdups α_{p} at (a) t = 50 s, (b) 150 s, and (c) 300 s; (d) the distribution of mean particle holdup α_{pm} in the center-plane.

4.4.6. Vorticity distribution

It is well known that swirling flow exists in two-phase bubble columns, which triggers flow instabilities (Liu and Li, 2018; Liu et al., 2020). The orientation and angular speed of local spinning motion can be represented by vorticity, which is often used to determine the existence of vortices, as well as describing the formation, transformation, and extinction of vortex rings (Liu and Li, 2018). Vorticity $\boldsymbol{\omega}$ is defined as the curl of flow velocity (Liu et al., 2020):

$$\boldsymbol{\omega} = \nabla \times \mathbf{U}_l \tag{4-18a}$$

$$\omega_{\mathrm{x}} = \frac{\partial w}{\partial y} - \frac{\partial v}{\partial z},\ \omega_{\mathrm{y}} = \frac{\partial u}{\partial z} - \frac{\partial w}{\partial x},\ \omega_{\mathrm{z}} = \frac{\partial v}{\partial x} - \frac{\partial u}{\partial y} \tag{4-18b}$$

where $\mathbf{U}_{\mathrm{l}}$ is the liquid velocity vector, ω_{x}, ω_{y}, and ω_{z} are the vorticity components, and $|\boldsymbol{\omega}| = \sqrt{\omega_{\mathrm{x}}^2 + \omega_{\mathrm{y}}^2 + \omega_{\mathrm{z}}^2}$.

To better understand the characteristics of swirling and oscillating flow in the three-phase bubble column, the instantaneous distributions of vorticity components ω_{y} and ω_{z} at $t = 300$ s are demonstrated in Figure 4-15, in which ω_{x} is not shown due to the similar results as ω_{z}. Figure 4-15(a) shows the distributions of ω_{z} at the center-plane, as well as the 2D streamlines obtained from the instantaneous liquid velocity. It was found that ω_{z} is randomly distributed in the plane, and the positive and negative values indicate that the local flow is rotating in the opposite directions, respectively. The rotation and vortices can be more clearly observed through the streamlines, where the vortices are smaller and denser in the top half of the column at $t = 300$ s. The isosurfaces of $\omega_{\mathrm{z}} = 3$ s^{-1} and -3 s^{-1} are shown in Figure 4-15(b). The positive and negative ω_{z} originate from the gas sparger, and irregular shapes of ω_{z} develop along the column axis, which is consistent with the development of instantaneous liquid velocity field (Figure 4-10a and b).

Figure 4-15(c) shows the distributions of ω_{y} at different heights along the column axis at $t = 300$ s. The maximum magnitude of ω_{y} (4 s^{-1}) is much lower than ω_{z} (10 s^{-1}), owing to the higher liquid velocity in the *y* direction induced by the bubble plume. The peak of ω_{y} occurs at around half height of the bubble column, indicating that horizontal oscillation and rotation of the flow are stronger in that region. This phenomenon can be further demonstrated in Figure 4-15(d), where the isosurfaces of $\omega_{\mathrm{y}} = 2$ s^{-1} and -2 s^{-1} are depicted. The isosurface distributions are discontinuous in the column, and different scales of vortex structures can be observed. Specifically, the horizontal vortex structure is mainly in the middle region of the column, and both the positive and negative ω_{y} intersect with each other, illustrating the existence of complex swirling flow in the column.

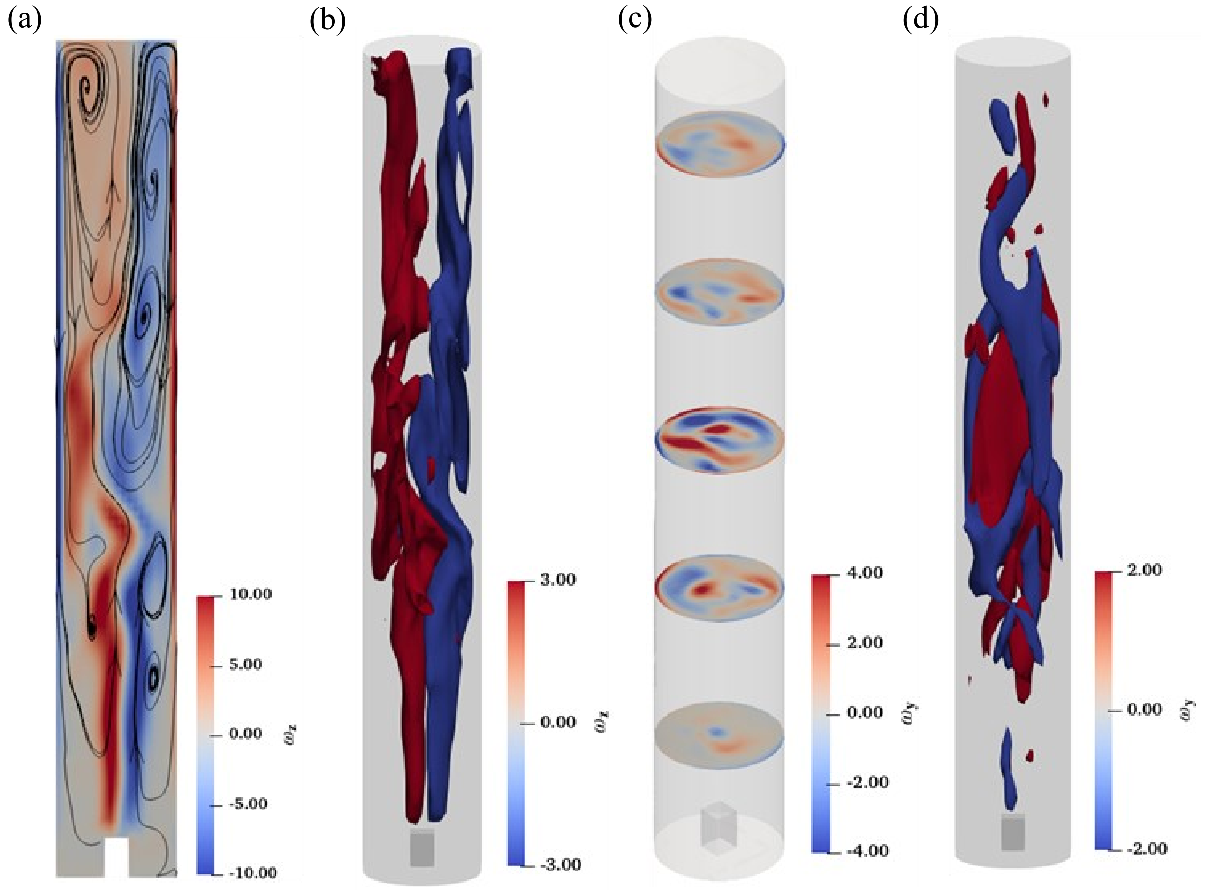

Figure 4-15. The instantaneous distributions of vorticity components at t = 300 s: (a) ω_z in the center-plane, (b) the isosurfaces of $\omega_z = 3\ \mathrm{s}^{-1}$ and $-3\ \mathrm{s}^{-1}$, (c) ω_y at different heights along the column axis and (d) the isosurfaces of $\omega_y = 2\ \mathrm{s}^{-1}$ and $-2\ \mathrm{s}^{-1}$.

4.4.7. Discussion about collision models

In this study, the particle-particle collision was directly detected (deterministic treatment) by using the discrete particle model in OpenFOAM (Zhang et al., 2021), and the particle-bubble collision was not included because the subsequent particle-bubble agglomeration was not considered due to the larger size of particles than bubbles and the challenge of applying agglomeration models to an Eulerian-Eulerian-Lagrangian approach. To make the proposed solver more feasible in various applications, the particle-bubble collision is suggested to be included, and a brief discussion regarding particle-bubble and particle-particle collision models is provided here for future reference.

Considering the particle-bubble collision, the collision frequency is an important parameter related to particle-bubble relative velocity, which originates from the flow turbulence and gravitational motion of particles and bubbles (Kostoglou et al., 2020). It has been demonstrated that flow turbulence contributes significantly to the collision frequency (Ngo-Cong et al., 2018; Hassanzadeh et al., 2018). Darabi et al. (2019) found that the collision frequency in the turbulent zone is 10-12 times higher than that in the quiescent zone, but they did not develop a general expression for predicting the collision frequency in both zones. Most collision frequency models are valid only in turbulent flows (Koh et al., 2006), but there are some regions (e.g., far from the impeller/stator-rotor region) where the gravitational collision dominates in a practical flotation device (Kostoglou et al., 2020). Recently, a few studies have proposed equations for the collision frequency including the effects of both turbulence and gravity (Ngo-Cong et al., 2018; Kostoglou et al., 2020). A suitable collision model needs to be selected and implemented in the proposed solver for predicting particle-bubble collisions.

In terms of particle-particle collisions, there are mainly three different mechanisms for the collision frequency in different flow regimes (Jeldres et al., 2018): Brownian motion (laminar), differential sedimentation (laminar), and flow shear (laminar or turbulent). It has been reported that each collision mechanism should be independent of each other, and the actual collision frequency of particles can be calculated by the sum of the contributions from each mechanism (Jeldres et al., 2018; Song et al., 2019). For the collisions caused by flow shear, although different forms of collision frequency models have been proposed for laminar or turbulent flows (Meyer and Deglon, 2011), few general expressions were applicable in both flow regimes. Alternatively, most researchers used or combined the previous particle collision models for different flow conditions using either Eulerian or Lagrangian approaches (Sun and Cao, 2021; Dodds et al., 2022; Su et al., 2023; Gao et al., 2023). Therefore, a more fundamental particle-particle collision model is suggested to be developed in the future.

4.5. Summary and conclusions

In this study, a new E-E-L coupled solver was developed within the OpenFOAM framework to simulate gas-liquid-solid three-phase flow (GLSTPF). Gas and liquid phases were described in Eulerian coordinates, while the solid phase was treated as discrete particles. Interphase coupling was achieved by the interfacial forces, and particle-particle or particle-wall interactions were resolved by the spring-dashpot-slider method. The turbulence of fluid phase was modeled by the LES approach. The developed solver was tested in a three-phase bubble column, and validated with the experimental results.

The main conclusions from this paper are as follows:

(1) The predicted bubble size distribution and phase velocities agree well with the experimental data, suggesting the robustness of the proposed solver for GLSTPF.

(2) The introduction of PBM in the solver significantly improves the predictions of gas/solid phase velocities and holdups, especially at lower region of the bubble column where the bubble coalescence and breakup are significant.

(3) The instantaneous bubble rise velocity is irregularly distributed in the bubble column, mainly due to the oscillation of bubble plume. The instantaneous liquid and solid particle velocities generally follow the distribution of gas bubbles, but the magnitudes are significantly lower than bubble velocity.

(4) The gas holdup decreases in the radial direction due to the lateral spreading of gas bubbles, and the solid particles are accumulated at the bottom and the top corner of the bubble column. Both the liquid and solid phases tend to move outwards and inwards in top and bottom regions respectively, to circulate in the column.

(5) Swirling and oscillating flow exists in the column. The vorticity exhibits irregular shapes over the column, and different scales of vortex structure were observed. The maximum magnitude of ω_y (4 s^{-1}) is much lower than ω_z (10 s^{-1}), owing to the higher axial liquid velocity induced by bubble plume.

5. Distributions of bubble size, gas void fraction, and sand concentration in air-water-sand three-phase jets in crossflow*

5.1. Introduction

Multi-phase jet in crossflow (MJC) garnered significant attention across a range of applications, including artificial aeration in oceans, lakes, and rivers (McGinnis et al., 2004; Wang et al., 2019; Dhar et al., 2021), offshore gas/oil exploitation (Dong et al. 2021; Chen et al., 2022a; Wang et al., 2022), and subsea blowouts (Dissanayake et al., 2018; Mitrou et al., 2018; Li et al., 2022c), among others. Regarding the injection method at the source (nozzle), multi-phase jets can be categorized into pure gas or sand jets, two-phase bubbly jets (air-water) or slurry jets (water-sand), and three-phase jets (air-water-sand). In environments such as oceans, crossflowing ambient water is typically present, which adds complexity to the jet behaviors including mixing characteristics (Dong et al., 2020; Zhang and Zhang, 2022), bubble size distributions (Jobehdar et al., 2016; Kang et al., 2019), and the velocities of dispersed phases (Xu et al., 2018; Newland and Woods, 2023).

Compared to pure gas jets, the concurrent injection of water and gas in bubbly jets can generate smaller bubbles with extended residence times, thereby enhancing gas-liquid interfacial mass transfer (Lima Neto et al., 2008a; Zhang and Zhu, 2013). Various experiments have been conducted to explore the characteristics of bubbly jets in crossflow, focusing on bubble properties (e.g., gas void fraction, bubble size distribution, and bubble velocity), jet trajectories, and mixing or dilution characteristics. Under the influence of crossflow, the dispersed phase (e.g., air, oil, and

---

* The content of this chapter has been submitted as a journal manuscript: Zhang, H., Yin, Z., Zhu, D. Z., and Zhang, W., 2023. Distributions of bubble size, gas void fraction, and sand concentration in air-water-sand three-phase jets in crossflow. Ocean Engineering, Under Review.

alcohol) tends to separate from the liquid phase at a specific height due to buoyancy effects. Notably, air bubble plumes exhibit more pronounced separation compared to oil or alcohol plumes, primarily because of the higher slip velocities of the bubbles (Socolofsky and Adams, 2002).

Zhang and Zhu (2014) investigated the trajectories of both gas and liquid phases of air-water bubbly jets, observing that the gas-phase spreading rate exhibited a linear relationship with bubble diameter. As reported by Zhang and Zhu (2013), the radial distribution of gas void fraction exhibited a Gaussian shape, similar to that observed in stagnant water (Lima Neto et al., 2008a). Due to the diminished wake effect induced by crossflow, the bubble slip velocity resembled the terminal velocity of a single bubble in stagnant water. In a recent numerical simulation of bubbly jets in crossflow by Zhang and Zhang (2022), it was found that the liquid phase extended more widely in the vertical direction due to the lift of bubbles, resulting in greater dilution compared to pure water jets. Additionally, in a pipe crossflow scenario, Zhang et al. (2023a) reported that bubble fluctuations could be intensified through the additional injection of water. Furthermore, the distribution of bubble turbulence intensity tended to become more uniform as water jet and pipe flow rates increased.

In addition to the study of air-water bubbly jets, significant attention has been directed towards the investigation of pure sand or slurry jets, owing to their relevance in diverse applications such as wastewater discharge, mining operations, and marine bed capping (Azimi et al., 2011; Chen et al., 2022b). Concerning pure sand or slurry jets in stagnant water, extensive experimental and numerical investigations have aimed to elucidate the characteristics of these jets, encompassing aspects such as particle concentration, velocity, mixing, spreading patterns, and deposition behavior. For instance, in vertically downward slurry jets in stagnant water, it has been consistently observed that the distribution of sand velocity and concentration closely adheres to the Gaussian profile (Singamsetti, 1966; Hall et al., 2010; Huai et al., 2013), mirroring the behavior of bubbles in vertically upward bubbly jets in stagnant water (Lima Neto et al., 2008a). Mingotti and Woods (2020) have further underscored the substantial influence of particle sedimentation on altering fluid buoyancy in both upward and downward particle-laden plumes in stagnant water, leading to shifts in the intrusion height of the fluid. Furthermore, Manzouri and Azimi (2019) delved into the intricacies of sand deposition patterns by releasing sand particles from oblique pipes into stagnant water, and they emphasized the predominant role of nozzle size in mound formation, while release angle and height played secondary roles. Conversely, in the examination of deposition behavior involving an upward-inclined sediment-laden jet originating from the bottom of a water tank, Chen et al. (2023) identified that the discharge angle primarily governed the sediment velocity profile.

In the realm of pure sand or slurry jets in crossflow, most existing research has concentrated on the scenario of downward injection above a flowing channel. For instance, Bhuiyan et al. (2010) conducted experiments examining mounds formed by sediment release into a crossflow, analyzing mound height, longitudinal profiles, and areal extent under varying flow conditions. Employing large eddy simulation, Decrop et al. (2015) undertook a numerical investigation of the evolution of turbidity plumes in crossflow, exploring parameters like particle concentration, velocity, plume trajectory, and different turbulent structures. Expanding the scope to encompass both stratified and unstratified ambient fluids, Mingotti and Woods (2022) conducted a series of experiments, shedding light on the dynamics of positively or negatively buoyant particle-laden plumes in crossflow. Additionally, James et al. (2022) explored particle separation behavior within turbulent particle plumes in crossflow, revealing a critical separation threshold where particles exhibited separation behavior when their Stokes settling speed exceeded 0.92 times the vertical plume speed.

While extensive research has been dedicated to air-water or water-sand two-phase jets, the investigation of more complex three-phase (e.g., air-water-sand) jets has received limited attention, despite their practical relevance in scenarios such as subsea blowouts that typically involve a mixture of gas, liquid (oil/water), and sand (Brooks et al., 1978; Jernelöv, 2010; Bogoyavlensky et al., 2020; Chen et al., 2020). Nonetheless, various studies have been conducted in different domains, such as fluidized beds and wastewater treatment (Kang et al., 2018; Xie et al., 2022), to investigate three-phase flow phenomena. In the realm of measuring phase properties within three-phase flow, a variety of intrusive and non-intrusive methods have been developed. Intrusive techniques include the use of ultrasonic probes (Bouillard et al., 2001), electrical conductivity probes (Liu et al., 2007), and optical fiber probes (Mokhtari and Chaouki, 2019; Li et al., 2022a). On the other hand, typical non-intrusive methods encompass image processing techniques (Götz et al., 2016; Dong et al., 2019b), electrical resistance tomography (Razzak et al., 2009; Hansen et al., 2019), and phase Doppler anemometry (Gan, 2013). Compared to intrusive methods that are constrained to measuring specific locations at one time, non-intrusive methods offer the advantage of faster data acquisition without perturbing the flow field (Jin et al., 2010). However, it is important to note that non-intrusive methods tend to have high requirements for optical operations (De Oliveira et al., 2015).

This research represents, to the best of the authors' knowledge, one of the pioneering studies on air-water-sand three-phase jets in crossflow. The research leveraged image processing techniques to extract bubbles and sand particles from primary images, and subsequently conducted measurements of their respective properties under varying flow conditions. In this study, the focus is on the distributions of bubble size, gas void fraction (bubble concentration), and sand concentration, under the impacts of different key flow parameters at the nozzle (i.e., initial sand concentration, air and slurry flow rates). Moreover, different pertinent models were proposed to predict the gas void fraction and sedimentation behavior of sand particles under different scenarios.

5.2. Experimental setup and methodology

5.2.1. Apparatus and procedures

Experiments were carried out in a large horizontal water flume of 25 × 1.2 × 0.8 m^3 (L × W × H) in the T. Blench Hydraulics Laboratory at the University of Alberta. The side walls are made of transparent glass. Honeycomb flow straighteners in the feed plenum are used to distribute uniform flow in the flume, and a tailgate at the downstream end of the flume is used to control the water depth. In this study, the crossflow discharge was kept at 158 L/s and the water depth was 0.65 m, resulting in an average longitudinal crossflow velocity of 0.2 m/s. This led to a turbulent crossflow with a Reynolds number of 249,600.

Figure 5-1(a) shows the experimental setup, where a nozzle with 0.012 m diameters was built vertically upwards at about 11 m downstream of the flume entrance. To eliminate the effects of the bottom wall and ensure a more uniform distribution of crossflow velocity in the measurement region, the nozzle exit was situated at 0.12 m higher than the flume bed (Zhang and Zhu, 2013). In this study, the nozzle height was determined by measuring the mean longitudinal water velocity U_x using an Acoustic Doppler Velocimeter (ADV) (Nortek Vectrino Plus) at 0.25 m upstream from the nozzle. The distribution of U_x along the water depth H is shown in Figure 5-C1 (Appendix C). U_x remains approximately uniform above 0.12 m, especially for the water depth between 0.12 m and 0.3 m. This observation illustrates that the boundary layer thickness was approximately 0.12 m, and thus the nozzle exit was established at that location. Minor oscillations are observed at $H >$ 0.3 m with a maximum variation of about 0.03 m/s, which is probably caused by the surface waves generated at the entrance of the water flume. The sand particles (Sil Industrial Minerals Inc., Edmonton, Canada) used in this study were carefully sieved to an average diameter of $d_s = 1.3$ mm (between 1.2-1.4 mm) with a density of $\rho_s = 2630$ kg/m^3. Prior to injection from the nozzle, a slurry tank was employed to premix water and sand, which were subsequently supplied to the nozzle using a centrifugal pump with a maximum capacity of 0.9 L/s. Specifically, the water depth in the slurry tank was kept at a constant level through controlled inflow and outflow, while sand particles were meticulously weighed and distributed within the tank to achieve the desired concentrations. To ensure a uniform sand distribution in the tank, sand particles and water were strongly mixed by a stirrer.

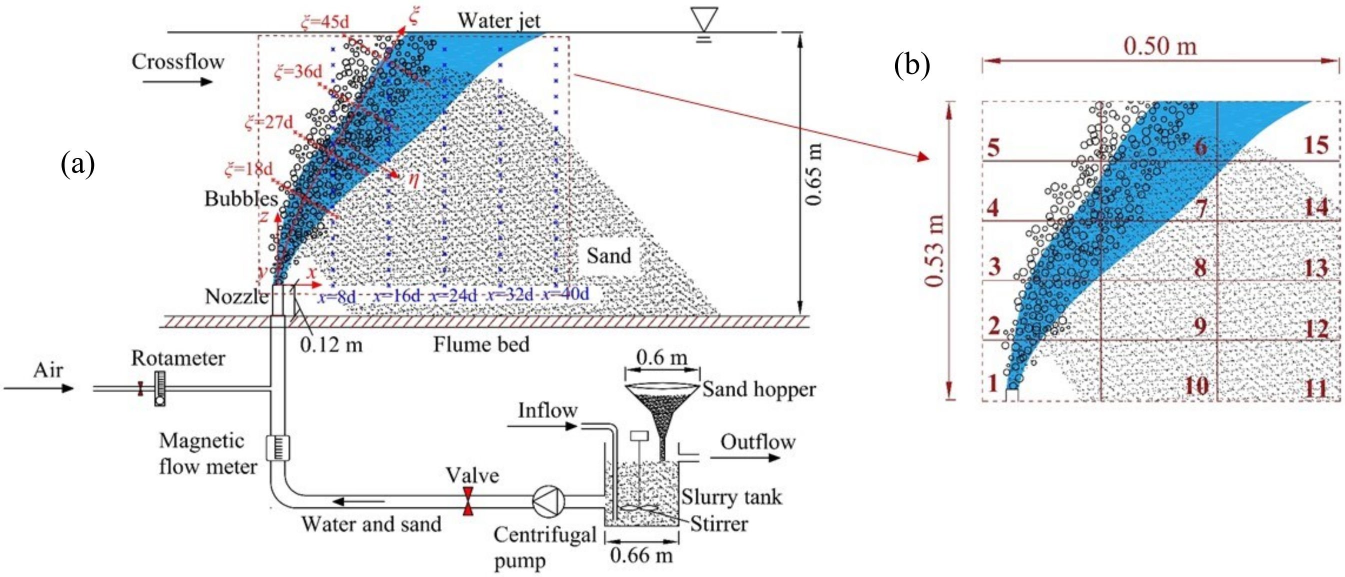

Figure 5-1. (a) Schematic of the experimental setup and measurement points; and (b) Test section and measurement sub-windows.

The slurry (water-sand mixture) flow rate was regulated using a valve and monitored by a magnetic flow transmitter (FoxBoro, IMT25). To keep a constant sand concentration, sand particles were added into the slurry tank at a constant rate via a funnel-shaped sand hopper. The slurry was conveyed through a pipeline and further mixed with air supplied from a laboratory gas line. Air pressure was controlled at 1 atm using a pressure-regulating valve, and constant air flow rates were monitored and controlled with a rotameter. The coordinate systems are illustrated in Figure 5-1(a), with the origin located at the nozzle exit. x, y, and z represent the longitudinal, transverse, and vertical directions, respectively. ξ denotes the direction of gas-phase centerline, and η is the direction perpendicular to ξ, pointing towards the downstream side.

To visualize the behavior of bubbles and sand in the three-phase jets, a high-speed camera (Phantom V211, Vision Research Inc.) with a sensor size of 1280 × 800 pixels was employed. The camera was equipped with a Nikon lens with a focal length of $f = 60$ mm and an aperture of $f / 2.8$. The depth of field (DOF), defined as the distance within which objects captured by the camera are well-focused, was estimated to be approximately 20 mm (see Appendix D) in our study, where the working distance (the distance between the front of the lens and the measurement plane) was 640 mm. The background illumination was provided by 2 × 1000 watts halogen lamps and diffused in a softbox. The entire measurement region (L × H = 0.50 m × 0.53 m) was divided into 15 sub-windows (Figure 5-1b). Images were captured at 500 frames per second with a field of view of 220×138 mm^2 for each sub-window, corresponding to a spatial resolution of 5.8 pixels per millimeter. The exposure time was set to 100 μs. A total of 9,130 images (equivalent to a total duration of 18.26 s) were captured for each sub-window under each experimental scenario, which was shown to be sufficient to obtain reliable results (see Figure 5-C2 in Appendix C).

In this work, a total of 18 scenarios (Table 5-1) were conducted to investigate the bubble and sand behaviors in the three-phase jet in crossflow. The initial volumetric sand concentration C_0 was set to 0, 0.25%, 0.5%, and 1%; the slurry flow rate Q_{sl} was 18, 24, and 30 L/min; and the air flow rate Q_g was 0.2, 0.4, and 0.6 L/min. It is worth noting that Q_{sl} was relatively high compared to Q_g due to the necessity for a substantial water velocity to transport and inject sand particles from the nozzle during the experiments. The experimental I.D. of each scenario was named after the sequence of C_0, Q_{sl}, and Q_g of the scenario as shown in Table 5-1. The initial gas void fraction at the nozzle exit α_{g0} was calculated by: $\alpha_{g0} = Q_g/(Q_g+Q_{sl})$. Table 5-1 also shows the initial densimetric Froude number $Fr_0 = \frac{u_l}{\sqrt{dg(\rho_l-\rho_g)/\rho_l}}$ (Lima Neto et al., 2008c), Reynolds number and Weber number for both liquid and gas phases $Re_l = \frac{\rho_l u_l d}{\mu_l}, We_l = \frac{\rho_l u_l^2 d}{\sigma}, Re_g = \frac{\rho_g u_g d}{\mu_g}, We_g = \frac{\rho_g u_g^2 d}{\sigma}$, and the Stokes number for the sand particles $St_s = \frac{(\rho_s-\rho_l)d_s^2 u_l}{18\mu_l d}$ (Azimi et al., 2012), where u_l and u_g are the initial liquid and gas velocities, which are calculated as $u_l = u_g = \frac{4Q_{sl}}{(1-\alpha_{g0})\pi d^2}$.

Table 5-1. Summary of experimental scenarios of air-water-sand three-phase jets in this study. The first character in Experimental I.D. stands for the initial sand concentration, i.e., A, B, C, and D = 0, 0.25%, 0.5%, and 1%, respectively; the numbers are the injected slurry and gas flow rates at the nozzle, respectively.

Expt. I.D.	α_{s0} (%)	Q_{sl} (L/min)	Q_g (L/min)	α_{g0} (%)	Fr_0	Re_l	Re_g	We_l	We_g	St_s
A-24-0.2	0	24	0.2	0.8	10.4	42,718	2,892	2,090	2.57	/
A-24-0.4	0	24	0.4	1.6	10.5	43,071	2,915	2,125	2.61	/
A-24-0.6	0	24	0.6	2.4	10.6	43,424	2,939	2,160	2.65	/
B-24-0.2	0.25	24	0.2	0.8	10.4	42,718	2,892	2,090	2.57	45.5
B-24-0.4	0.25	24	0.4	1.6	10.5	43,071	2,915	2,125	2.61	45.9
B-24-0.6	0.25	24	0.6	2.4	10.6	43,424	2,939	2,160	2.65	46.2
C-18-0.2	0.5	18	0.2	1.0	7.8	32,127	2,175	1,182	1.45	34.2
C-18-0.4	0.5	18	0.4	2.2	7.9	32,480	2,199	1,209	1.48	34.6
C-18-0.6	0.5	18	0.6	3.2	8.0	32,833	2,222	1,235	1.52	35.0
C-24-0.2	0.5	24	0.2	0.8	10.4	42,718	2,892	2,090	2.57	45.5
C-24-0.4	0.5	24	0.4	1.6	10.5	43,071	2,915	2,125	2.61	45.9
C-24-0.6	0.5	24	0.6	2.4	10.6	43,424	2,939	2,160	2.65	46.2
C-30-0.2	0.5	30	0.2	0.7	13.0	53,309	3,608	3,256	4.00	56.8

C-30-0.4	0.5	30	0.4	1.3	13.1	53,662	3,632	3,299	4.05	57.1
C-30-0.6	0.5	30	0.6	2.0	13.2	54,015	3,656	3,342	4.10	57.5
D-24-0.2	1	24	0.2	0.8	10.4	42,718	2,892	2,090	2.57	45.5
D-24-0.4	1	24	0.4	1.6	10.5	43,071	2,915	2,125	2.61	45.9
D-24-0.6	1	24	0.6	2.4	10.6	43,424	2,939	2,160	2.65	46.2

In each scenario, a total of 4 cross-sections along the gas-phase centerline ξ were measured for both bubbles and sand, namely ξ = 18d, 27d, 36d, and 45d (where d represents the nozzle diameter), and 15 points in the η direction were measured at each section. Moreover, additional 5 cross-sections in the x direction were selected to measure sand characteristics, namely x = 8d, 16d, 24d, 32d, and 40d, and 16 points in the z direction were selected for analysis at each section (Figure 5-1a).

5.2.2. Image processing

The images captured by the camera were processed in the widely-used open-source software "ImageJ" (Rasband et al., 1997), and Figure 5-2 shows an example of image processing for bubbles and sand using the sub-window "3" of Expt. C-24-0.4. To separate bubbles and sand particles from the raw image (Figure 5-2a), the 8-bit image was first converted into a binary image. Then, a high grayscale threshold and a series of filters, including size and circularity selections, were applied to identify and isolate the in-focus sand particles (Figure 5-2b). The sand particles extracted from the raw image are depicted in Figure 5-2(c), while the remaining content is shown in Figure 5-2(d). To improve the processing efficiency and automatically separate bubbles and sand particles, these image processing steps were encapsulated into a macro within ImageJ (an example of the program can be found in Appendix E).

Subsequently, the image containing only bubbles was obtained by applying a relatively lower threshold to further remove the out-of-focus sand particles in Figure 5-2(d), and the in-focus bubbles were sharpened (Figure 5-2e). The sharpened bubbles were extracted by applying another threshold and a series of filters including close, dilate, erode, fill holes, and watershed (Figure 5-2f). Detailed information about these processes can be found in our previous study (Zhang et al., 2023a). In this study, bubbles smaller than 0.3 mm^2 were neglected to avoid measurement errors. Figure 5-2(g) shows the in-focus bubbles after extraction from the raw image. Finally, Figure 5-2(h) depicts the outlines of bubbles (red color) and sand particles (green color) superimposed onto the raw image. For each sub-window, a total of 4,565 images (by selecting every other images from the total of 9,130 images) with an interval of 0.004 s were processed to obtain reliable and accurate results. All the images were carefully reviewed to ensure that at least 85% in-focus bubbles and sand particles had been successfully extracted for each image.

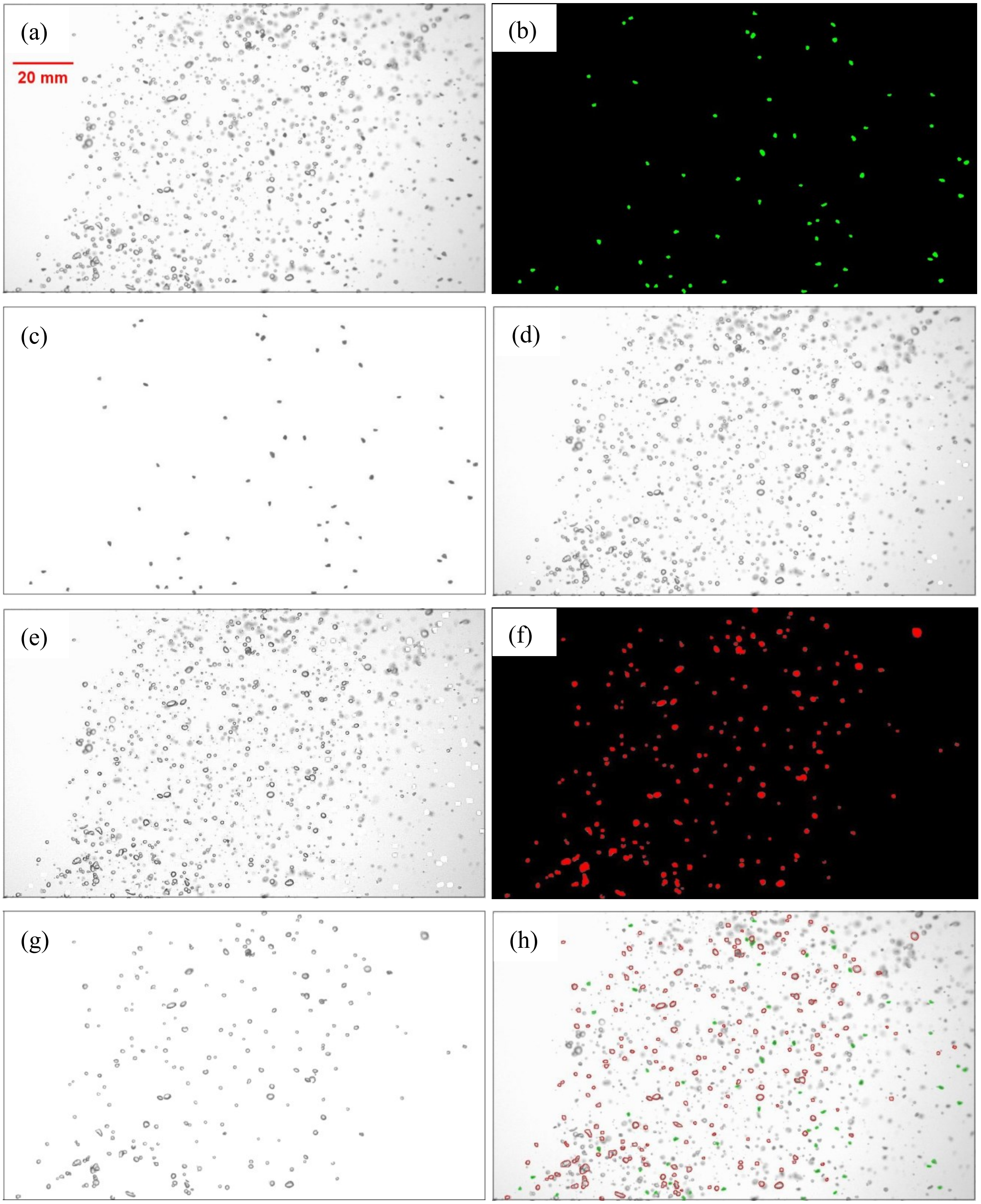

Figure 5-2. An example of image processing for bubbles and sand using the sub-window “3” of Expt. C-24-0.4. (a) Raw image; (b) Threshold and filters; (c) Sand extraction; (d) Subtraction from the raw

image; (e) Sharpened in-focus bubbles; (f) Threshold and filters; (g) Bubbles extraction; and (h) Outlines of sand and bubbles.

The methods of calculating bubble and sand properties are as follows. Firstly, a circular region with 15 mm diameter was defined at each measuring point to represent a flow sample. This diameter was determined from a preliminary measurement using different diameters (10, 15, and 20 mm) at 18d from the nozzle exit along the gas-phase centerline in Expt. C-24-0.4, and all the relative errors for different properties (e.g., bubble size, bubble and sand concentrations) are less than 3.2%. The equivalent bubble diameter was obtained by calculating the area of each bubble passing through the circle, assuming a circular shape for the bubbles: $d_{\mathrm{b}} = \sqrt{\frac{4A}{\pi}}$, where A is the bubble area. The Sauter mean diameter (SMD) d_{32}, expressed as a ratio of volume to surface, is used to evaluate the BSD at different measurement points, $d_{32} = \left(\sum_{i=1}^{n} d_{b,i}^{3}\right)/\left(\sum_{i=1}^{n} d_{b,i}^{2}\right)$, where $d_{b,i}$ is the diameter of the ith bubble (Zhou et al., 2022).

The gas void fraction α_{g}, defined as the ratio of the gas volume to the total volume, was calculated by dividing the sum of the bubble volumes within the defined flow sample by the total volume of the sample: $\alpha_g = \sum_{1}^{N}(\sum_{i=1}^{n} \forall_{b,i} /\forall_f) /N$, where $\forall_{b,i}$, $\forall_f$, n and N denote the volume of the i^{th} bubble, the volume of the flow sample, bubble number in the sample, and the total number of images (4,565 in this study), respectively. $\forall_{b,i}$ is calculated using the equivalent bubble diameter, and $\forall_f = A_f \times \mathrm{DOF}$, where A_f is the area of the circular region of the flow sample. Similar approaches for calculating gas void fraction have been employed in various studies (Al-Yahia et al., 2020; Serra et al., 2020; Cheng et al., 2023). The same method was used to calculate sand concentration α_s, defined as the ratio of the sand particles' volume to the total volume of the flow sample.

To assess the accuracy of the proposed image processing method, the gas void fraction α_g was calibrated by comparing it with results obtained using an optical fiber probe (RBI Instruments Inc., 2010). Generally, the optical probe is considered accurate in terms of gas void fraction (Besagni et al., 2016). The uncertainties associated with an optical probe are mainly due to (Vejražka et al., 2010): improper dewetting at the probe tip (the blinding effect), alteration of bubble trajectory prior to or during the piercing process (the drifting effect), and bubble deformation and deceleration at the probe tip (the crawling effect). It has been reported that the uncertainties caused by intrusion of the probe can be counteracted when measuring the cumulative time-averaged gas void fraction (Vejražka et al., 2010; Le Corre et al., 2018). Typical methods of evaluating the uncertainties of an optical probe include calibration with other measurement techniques (e.g., high-speed camera) (Gui et al., 2019; Wang et al., 2021b) or calculating the statistical errors (e.g., standard deviation of several measurements) (Estrada Perez, 2014; Behzadipour and Azimi, 2023). The same RBI probe used in this study had been carefully calibrated with measurements conducted in a bubble column in a previous study (Zhang and Zhu, 2013), showing a 2.2% difference for gas void fraction. In this section, the gas void fraction was measured three times at each measurement point using the probe, with a three-minutes duration for each time. The mean value was employed for comparison with that measured by the image processing method, and the standard deviation was used to represent uncertainties of the probe measurement. Figure 5-3 illustrates the comparison between the two techniques for four scenarios (with and without the sand injection), showing that the maximum difference between the two methods is as small as 10%. Therefore, the image processing method is deemed reliable for subsequent analysis. Additionally, the measurement errors associated with bubble size are estimated to be within 3% caused by the depth of field.

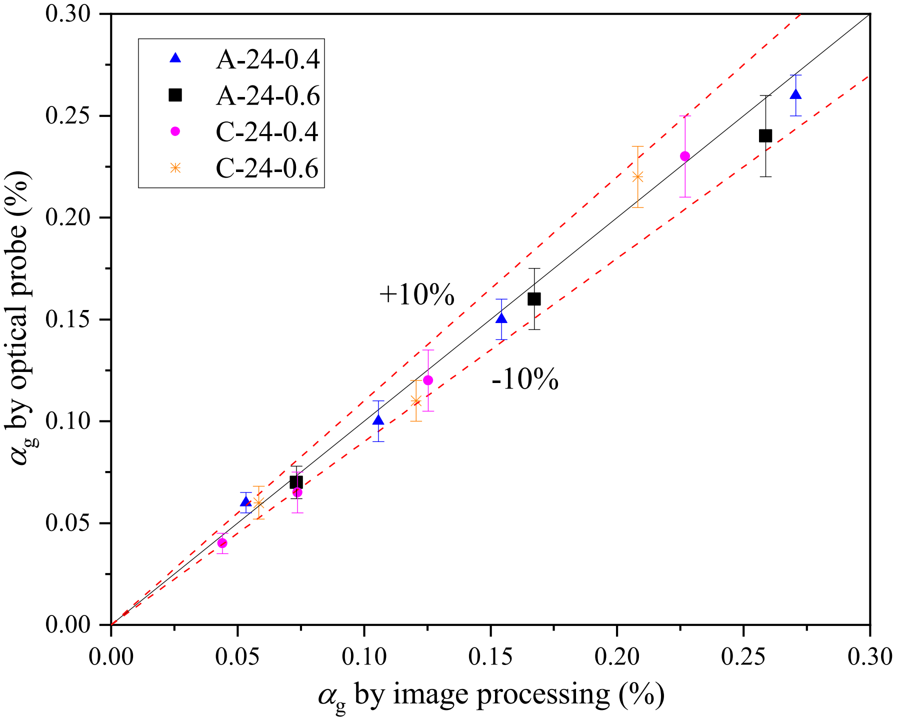

Figure 5-3. Comparison of gas void fraction α_g measured by an optical fiber probe and the image processing technique. The error bars denote the standard deviations of the probe.

5.3. Results and analysis

5.3.1. Bubble size distribution

The bubble size distribution (BSD) was examined using two different methods: the probability density function (PDF) and the cumulative density function (CDF). Figure 5-4 provides an example of the PDF and CDF of bubble diameter at 45d from the nozzle exit along the gas-phase centerline (ξ

= 45d and $\eta = 0$), with the effects of three parameters (initial sand concentration α_{s0}, gas flow rate Q_g, and slurry flow rate Q_{sl}) evaluated separately. The results indicate that bubble diameters range from 0.6 mm to 3.0 mm for all scenarios (the cutoff of 0.6 mm is due to the removal of smaller bubbles to avoid measurement errors), indicating that the slurry flow rate in this study is sufficient to generate small bubbles (Zhang et al., 2023a). Figure 5-4(a) displays the fitted lines of the BSD using the log-normal profile, with raw data from Expt. D-24-0.4 as an example. The peak values of PDF represent the most frequent bubble diameters, which range from 0.85 mm to 1.15 mm for the scenarios studied. Larger Q_g and smaller α_{s0} and Q_{sl} tend to result in peak PDFs occurring at larger bubble diameters, and the PDF distributions become more uniform.

The effects of the three parameters can be further observed by the CDF in Figure 5-4(b). It was found that the gas flow rate plays a dominant role in affecting bubble diameter, with a maximum CDF difference (actual difference) of 20% for Q_g ranging from 0.2 to 0.6 L/min. The maximum CDF difference (actual difference) is 12% for α_{s0} between 0 and 1%, and it is 9% for Q_{sl} between 18 and 30 L/min. The injection of sand particles tends to generate smaller bubbles, yet a comparison between Expts. C-24-0.4 and D-24-0.4 suggests that further increasing α_{s0} may not have a significant effect on bubble breakup. Moreover, the CDF profiles tend to overlap between Expts. C-24-0.6 and C-30-0.6, indicating that a slurry flow rate of 24 L/min is sufficient to breakup bubbles, and further increasing Q_{sl} may have a reduced effect on the BSD at this location.

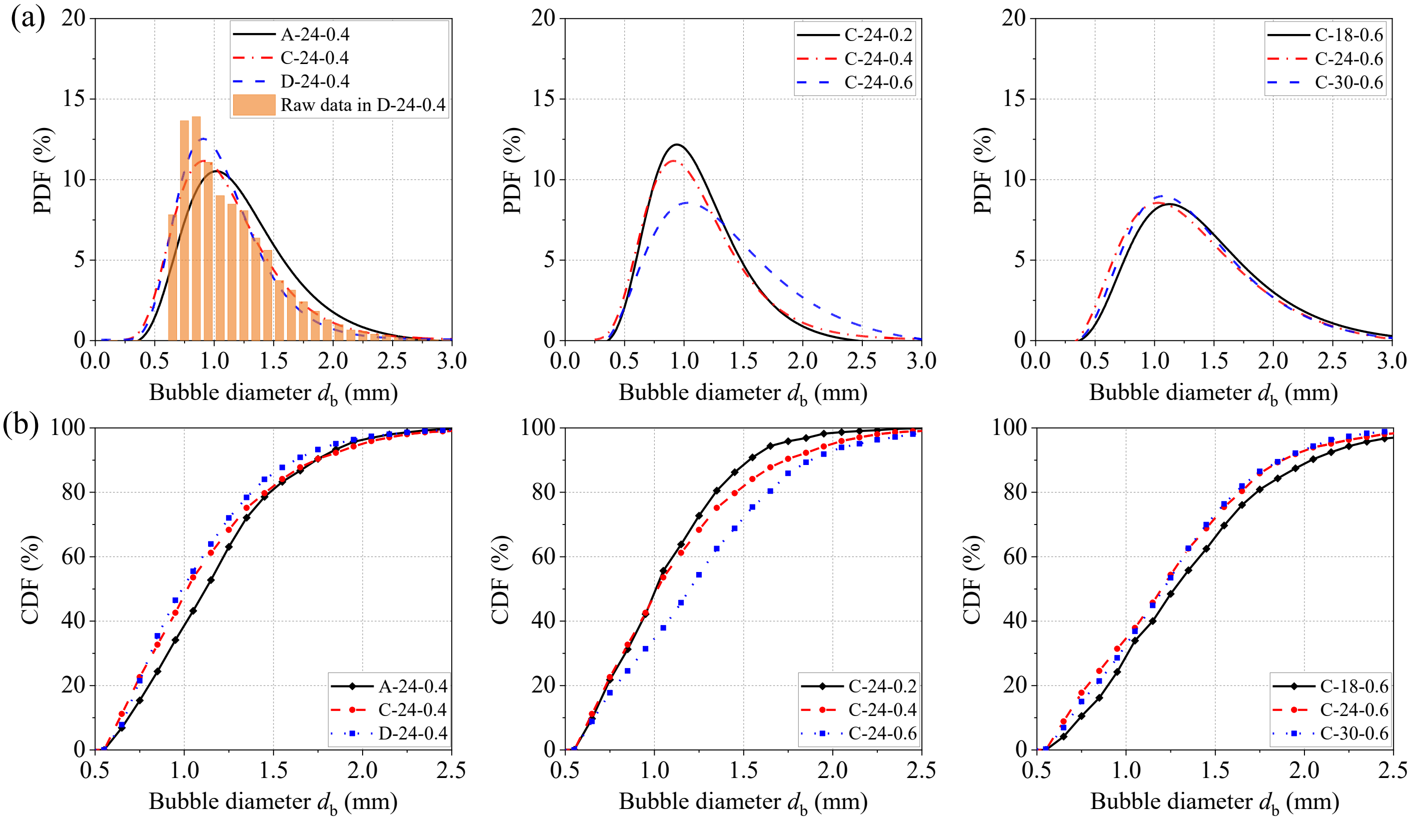

Figure 5-4. Examples of (a) PDF and (b) CDF of bubble diameter at 45d from the nozzle exit along the gas-phase centerline (ξ = 45d and η = 0).

Figure 5-5(a) and (b) illustrate examples of d_{32} distribution in the η direction for Q_{sl} = 24 L/min and α_{s0} = 0.5%, respectively. At all the measurement points, the standard deviation of BSD varies from 21% to 28% of SMD, and it was not drawn for better figure clarity. In general, the SMD falls within the range of 1.0 - 2.0 mm for the studied scenarios. The peak value of d_{32} occurs at the gas-phase centerline (η = 0), and the SMD is typically higher at the upstream side (η < 0) than the downstream side due to the higher buoyancy force (Zhang et al., 2023a). Figure 5-5(a) shows that the maximum SMD increases by 25% as the gas flow rate rises from 0.2 L/min to 0.6 L/min, whereas the impact of the initial sand concentration is relatively small (less than 10%). On the other hand, Figure

5-5(b) demonstrates that the maximum SMD is also susceptible to the slurry flow rate, especially for a smaller gas flow rate (e.g., it reduced by 26% from Expt. C-18-0.2 to C-30-0.2). Furthermore, it can be observed that the distribution of SMD at a specific section tends to be more uniform as the slurry flow rate increases, which aligns with observations on air-water bubbly jets in Zhang and Zhu (2013).

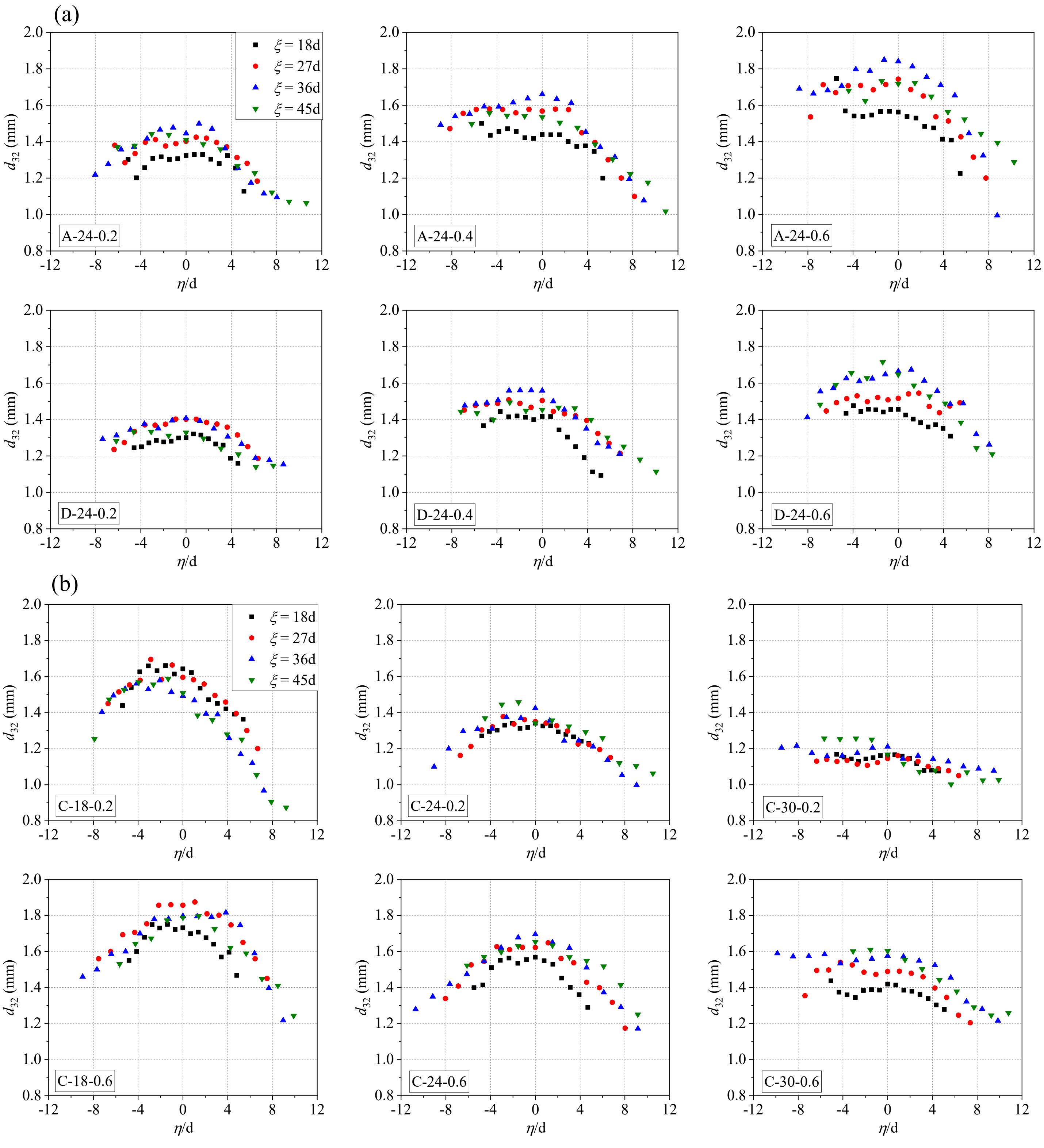

Figure 5-5. Examples of distributions of Sauter mean bubble diameter in the η direction for (a) Q_{sl} = 24 L/min and (b) α_{s0} = 0.5%.

5.3.2. Typical measurement results of gas void fraction

To investigate the effects of flow parameters, particularly the initial sand concentration, on gas void fraction (α_g), Figure 5-6(a) presents typical distributions of α_g non-dimensionalized by α_{g0} in the η direction for Q_{sl} = 24 L/min. As expected, the gas void fraction decreases as the bubbles move further in the ξ direction, and the distributions of α_g/α_{g0} become wider in the η direction. An increase in the gas flow rate results in a larger α_g/α_{g0}, whereas it tends to be lower with an increase in the initial sand concentration, indicating that the additional injection of sand particles promotes the spreading of bubbles.

According to Zhang and Zhu (2013), the normalized void fraction α_g/α_{gc} in two-phase bubbly jets can be described by a Gaussian distribution, where α_{gc} is the void fraction at the gas-phase centerline:

$$\alpha_g/\alpha_{gc} = \exp\left[-0.693(\eta/b_t)^2\right] \tag{5-1}$$

where b_t is the half-thickness in the η direction, defined as the distance from the centerline to where $\alpha_g/\alpha_{gc} = 0.5$. Using the method of non-linear least squares regression, Figure 5-6(b) displays the fitted experimental data with the Gaussian distribution for both two-phase and three-phase jets. It can be observed that α_g/α_{gc} fits well with the Gaussian profile for the bubbly jets (Expts. A-24-0.4 and A-24-0.6), similar to the findings reported in Zhang and Zhu (2013) and Zhang et al. (2023a). However, the experimental data are slightly higher near the downstream boundary of the bubbly region ($\eta/b_t > 1.5$) for the three-phase jets, especially for the scenarios with higher initial sand concentration (maximum deviation of $\alpha_g/\alpha_{gc} \approx 0.2$ for Expt. D-24-0.4), whereas the upstream boundary does not have this phenomenon. This can be attributed to that as the bubbles rise, a large number of sand particles tend to separate from the bubbly region and reverse their directions to settle down to the flume bed. These particles interact with bubbles and drive the bubbles to spread further downstream, resulting in a wider distribution compared to the bubbly jets.

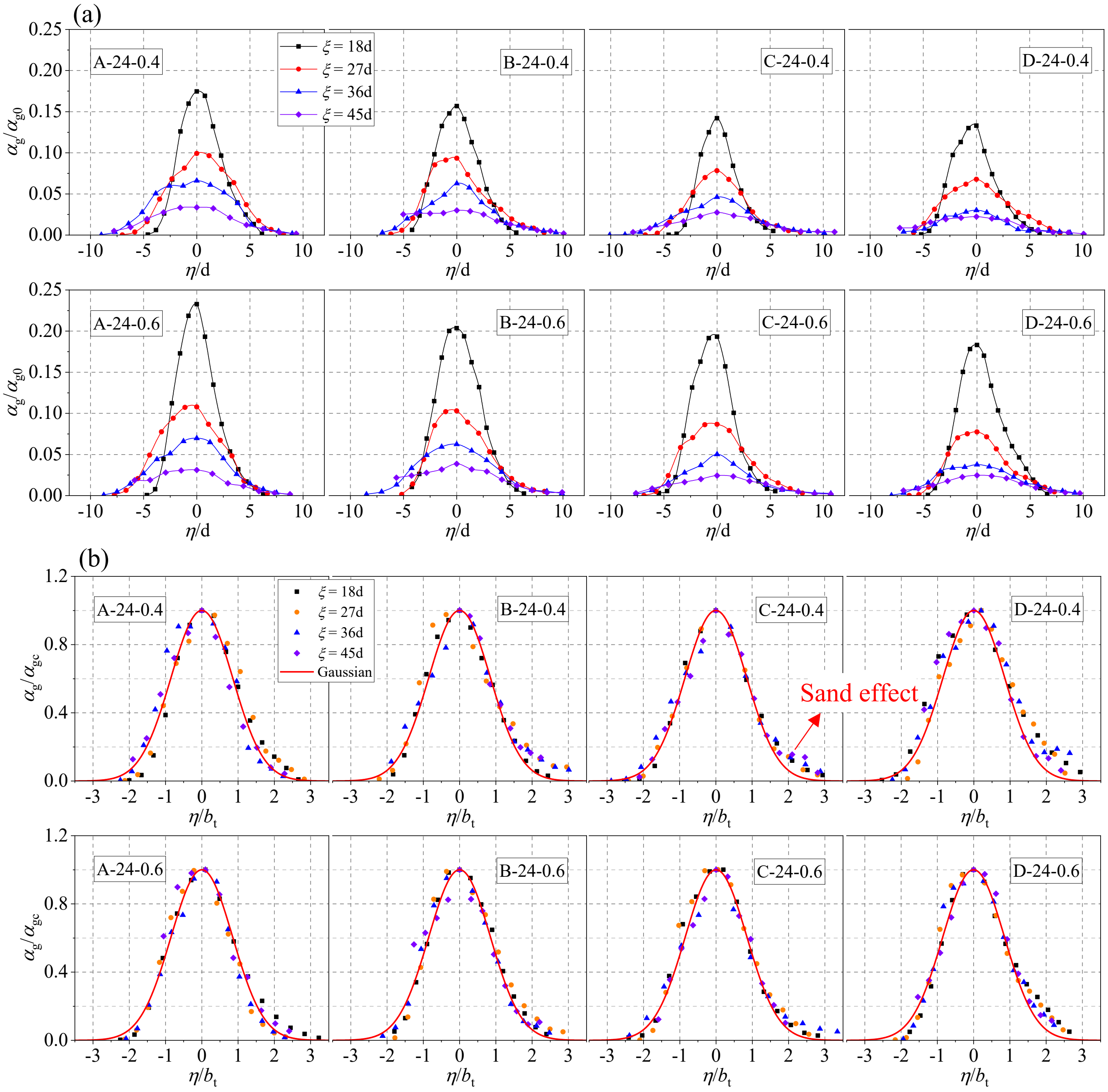

Figure 5-6. Examples of distributions of gas void fraction α_g non-dimensionalized by (a) initial void fraction α_{g0} and (b) centerline void fraction α_{gc} in the η direction for Q_{sl} = 24 L/min.

5.3.3. Distributions of centerline gas void fraction

Figure 5-7 illustrates the distributions of dimensionless void fraction α_{gc}/α_{g0} along the gas-phase centerline (in the ξ direction) for all the 18 scenarios, exhibiting a decreasing trend as bubbles move further. The value of α_{gc}/α_{g0} generally increases with the gas and slurry flow rates (Q_g and Q_{sl}), and decreases with the initial sand concentration (α_{s0}). Therefore, the centerline gas void fraction α_{gc} can be expressed as a function of α_{g0}, α_{s0}, Q_g, Q_{sl}, and other variables. In this work, the experimental observations led to consider 10 main variables to predict α_{gc}:

$$\alpha_{gc} = f\left(\alpha_{g0}, \alpha_{s0}, \xi, d, u_g, u_l, \rho_g, \rho_l, \mu_g, \mu_l\right) \tag{5-2}$$

where $u_g, u_l, \rho_g, \rho_l, \mu_g, \mu_l$ are the velocities at the nozzle, densities, and viscosities of the gas- and liquid-phases, respectively. The Buckingham's Pi theorem allows us to determine 7 dimensionless (or Π) groups by subtracting 3 fundamental dimensions of mass, length, and time. Three mutually independent variables, $u_{l0}, \rho_l,$ and d are selected as the repeating variables, the other seven non-repeating variables are distributed to construct the seven Π-groups as follows:

π_1: $u_l, \rho_l, d, \alpha_{g0}$
π_2: $u_l, \rho_l, d, \alpha_{s0}$
π_3: u_l, ρ_l, d, ξ
π_4: u_l, ρ_l, d, u_g
π_5: u_l, ρ_l, d, ρ_g
π_6: u_l, ρ_l, d, μ_g
π_7: u_l, ρ_l, d, μ_l

Using dimensional analysis, the dimensionless numbers for each group can be constructed as follows: $\pi_1 = \alpha_{g0}$, $\pi_2 = \alpha_{s0}$, $\pi_3 = \frac{\xi}{d}$, $\pi_4 = \frac{u_g}{u_l}$, $\pi_5 = \frac{\rho_g}{\rho_l}$, $\pi_6 = \frac{\rho_l u_l d}{\mu_g} = Re_*$, $\pi_7 = \frac{\rho_l u_l d}{\mu_l} = Re_l$.

Note that π_7 is the liquid Reynolds number at the nozzle, whereas π_6 is a characteristic Reynolds number which contains both gas and liquid variables. Therefore, π_6 is multiplied by π_4 and π_5, and $\pi_6' = \frac{\rho_g u_g d}{\mu_g} = Re_g$ is obtained, which represents the gas Reynolds number at the nozzle. Based on the aforementioned dimensionless numbers, the following relationship can be established:

$$\alpha_{gc} = f(\pi_1, \pi_2, \pi_3, \pi_6', \pi_7) = f(\alpha_{g0}, \alpha_{s0}, \frac{\xi}{d}, Re_g, Re_l) \tag{5-3}$$

then we get:

$$\frac{\alpha_{gc}}{\alpha_{g0}} = f(\alpha_{s0}, \frac{\xi}{d}, Re_g, Re_l) \tag{5-4}$$

Given the positive effects of Q_g and Q_{sl} on α_{gc}/α_{g0}, as well as the negative effects of ξ/d and α_{s0} as shown in Figure 5-7, the following equation is used to best describe the trend using the method of non-linear least squares regression:

$$\frac{\alpha_{gc}}{\alpha_{g0}} = \frac{0.002 Re_g^{0.68} Re_l^{0.02}}{\exp\,(30\alpha_{s0} + 0.06\xi/d)} \text{ with } R^2 = 0.94 \tag{5-5}$$

Figure 5-8 shows the comparison between measured and predicted centerline void fraction α_{gc}/α_{g0}, where almost all the data points fall within ±15% error lines, and most (82%) of the predicted data have an error of less than 10%, demonstrating a satisfactory prediction of the proposed equation.

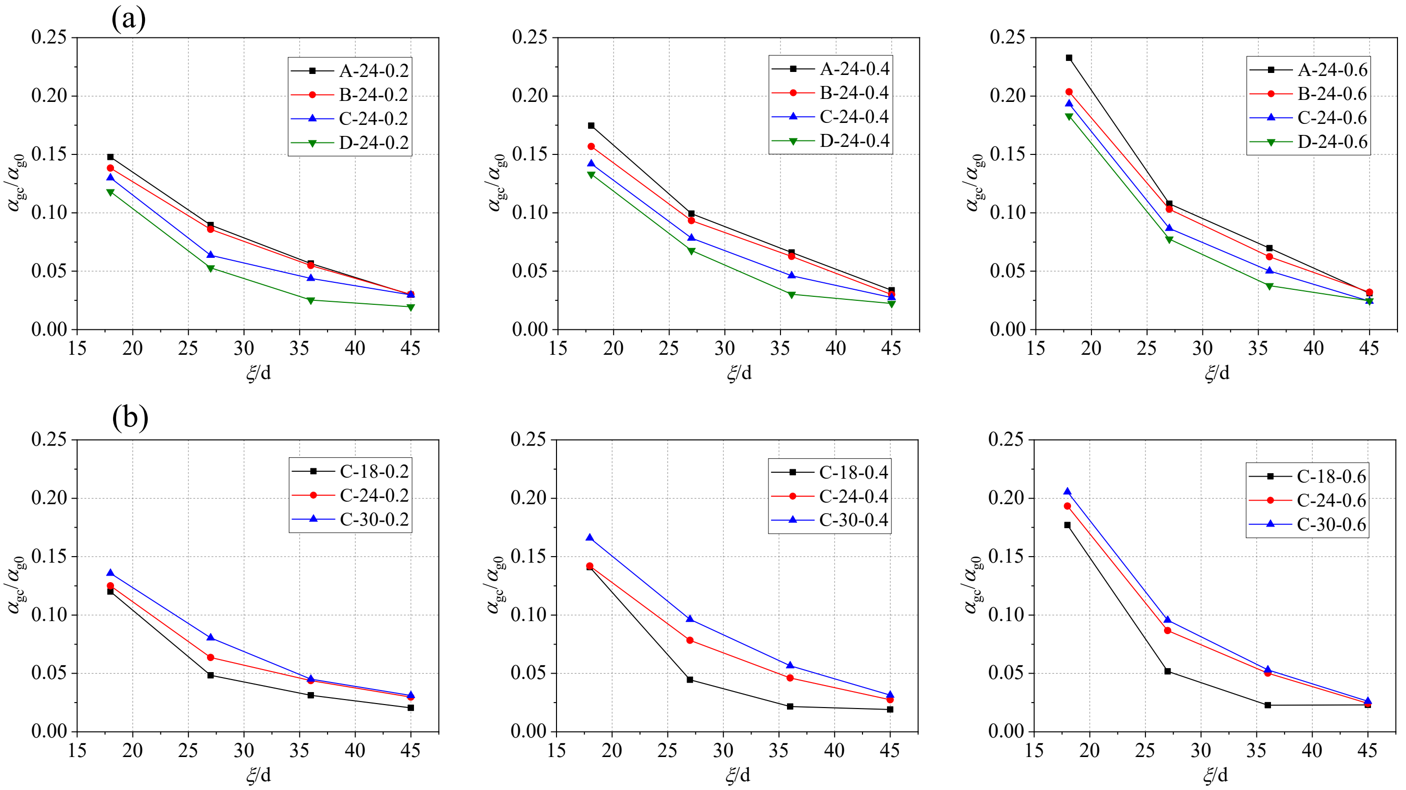

Figure 5-7. Distributions of void fraction along gas-phase centerline (in the ξ direction) for (a) Q_{sl} = 24 L/min and (b) $\alpha_{s0} = 0.5\%$.

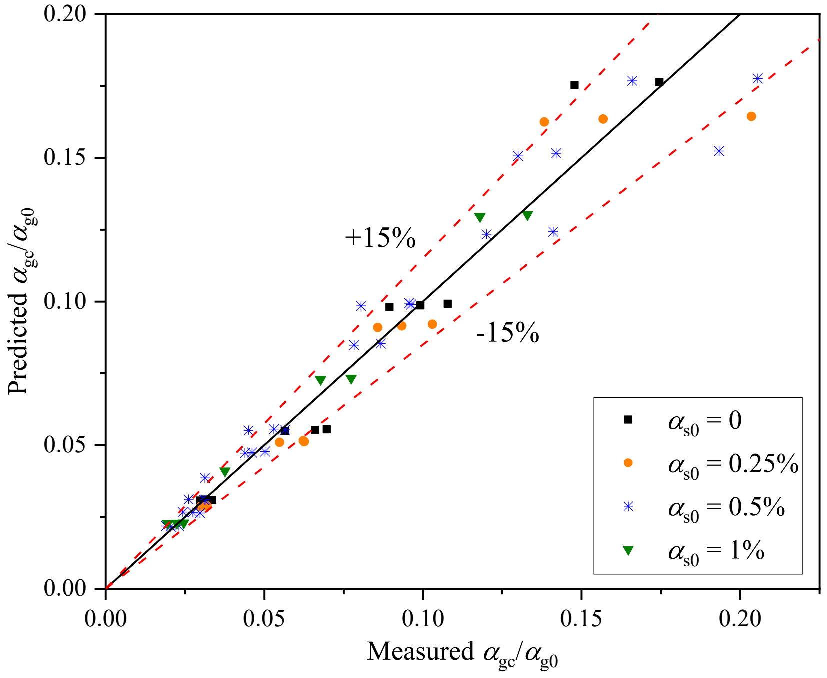

Figure 5-8. Comparison between measured and predicted centerline void fraction α_{gc}/α_{g0}

It is interesting to note that α_{gc}/α_{g0} varies little from ξ = 36d to 45d for the scenarios (Expts. C-18-0.2, C-24-0.2, C-30-0.2, C-18-0.4, C-18-0.6 D-24-0.2, D-24-0.4, and D-24-0.6) with a relatively large initial sand concentration α_{s0} = 1%, small air flow rate Q_g = 0.2 L/min, and small slurry flow rate Q_{sl} = 18 L/min (Figure 5-7), indicating that the centerline void fractions approximately achieve their terminal values at ξ = 45d in these scenarios. Therefore, α_{gc} was further non-dimensionalized by its terminal value $\alpha_{gc,t}$ for these scenarios, and related to the non-dimensional centerline location $\xi/b_{t,t}$, where $b_{t,t}$ is the terminal half-thickness at ξ = 45d. The following relationship is established to best describe the trend:

$$\frac{\alpha_{gc}}{\alpha_{gc,t}} = 148.7\left(\frac{\xi}{b_{t,t}}\right)^{-2.2} \tag{5-6}$$

Figure 5-9(a) shows the change of $\alpha_{gc}/\alpha_{gc,t}$ along the gas-phase centerlines for the aforementioned 8 scenarios and the fitting curve by Eq. (5-6). It was found that $\alpha_{gc}/\alpha_{gc,t}$ decreases as $\xi/b_{t,t}$ increases until reaching its terminal value at $\xi/b_{t,t} \approx 10$, and this decreasing trend can be well predicted by Eq. (5-6) with a R^2 of 0.93. The comparison between measured and predicted $\alpha_{gc}/\alpha_{gc,t}$ is shown in Figure 5-9(b), where most (70%) of the predicted $\alpha_{gc}/\alpha_{gc,t}$ have an error of less than 15% compared to the measured data. Note that there are some data points ($\alpha_{gc}/\alpha_{gc,t} < 2$) that fall outside the ±15% error lines, mainly due to their relative small values ($\alpha_{gc}/\alpha_{g0} < 0.05$), which might be more prone to the measurement error. Nevertheless, all the predicted data yield an error of less than 25% in Figure 5-9(b), demonstrating the reliability of the proposed equation.

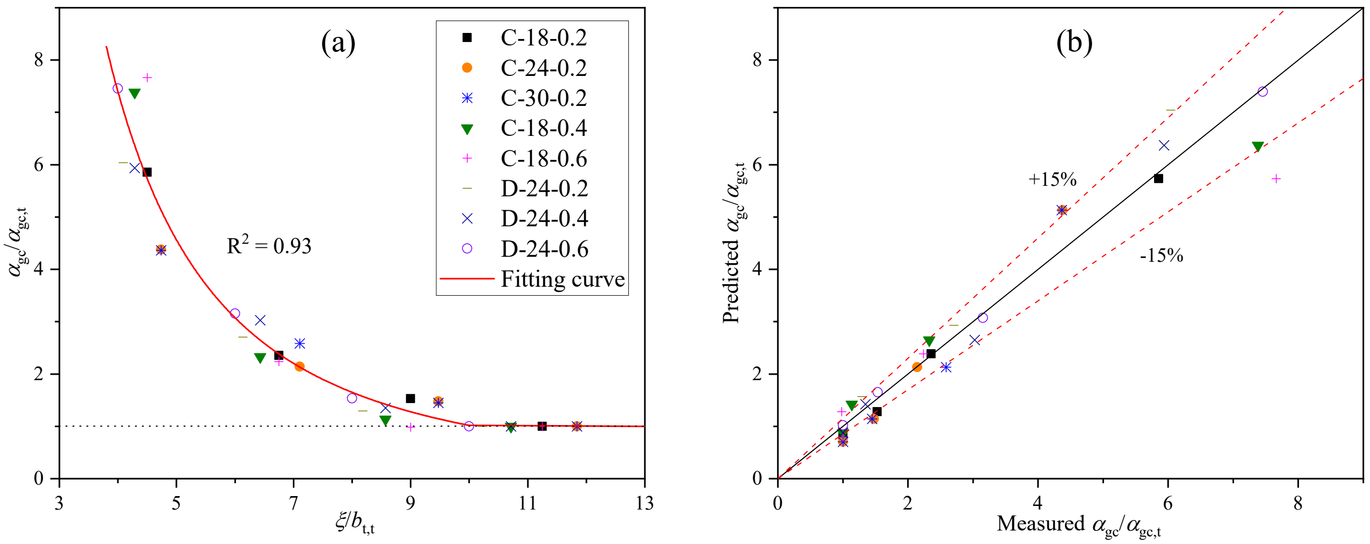

Figure 5-9. (a) Change of dimensionless void fraction $\alpha_{gc}/\alpha_{gc,t}$ along the gas-phase centerlines; and (b) Comparison between measured and predicted $\alpha_{gc}/\alpha_{gc,t}$

5.3.4. Distributions of sand concentration within bubbly region

Due to the differences in density and buoyancy characteristics, sand particles tend to separate from the bubbly region and settle down to the flume bed after rising to a certain distance from the nozzle. As a result, the particles exist both inside and outside the bubbly region in this study. To illustrate the different behaviors of sand particles in these different regions, the analysis of sand concentration is separately conducted within the bubbly region and in the vertical direction (mostly outside the bubbly region).

Figure 5-10 shows the typical examples of the distributions of sand concentration α_s in the η direction within the bubbly region for Q_{sl} = 24 L/min. The distribution of α_s is similar to that of gas void fraction at ξ = 18d, with the peak value occurring at the gas-phase centerline (η = 0). However, α_s exhibits significantly larger values downstream than upstream, due to the downward movement of particles as presented in *Section 5.3.2*. This leads to a general increase in sand concentration at higher sections (ξ = 27d and 36d) in the η direction. It is worth noting that α_s drops significantly (< 0.04%) at $\xi = 36$d, suggesting that most sand particles have separated from bubbles at this section.

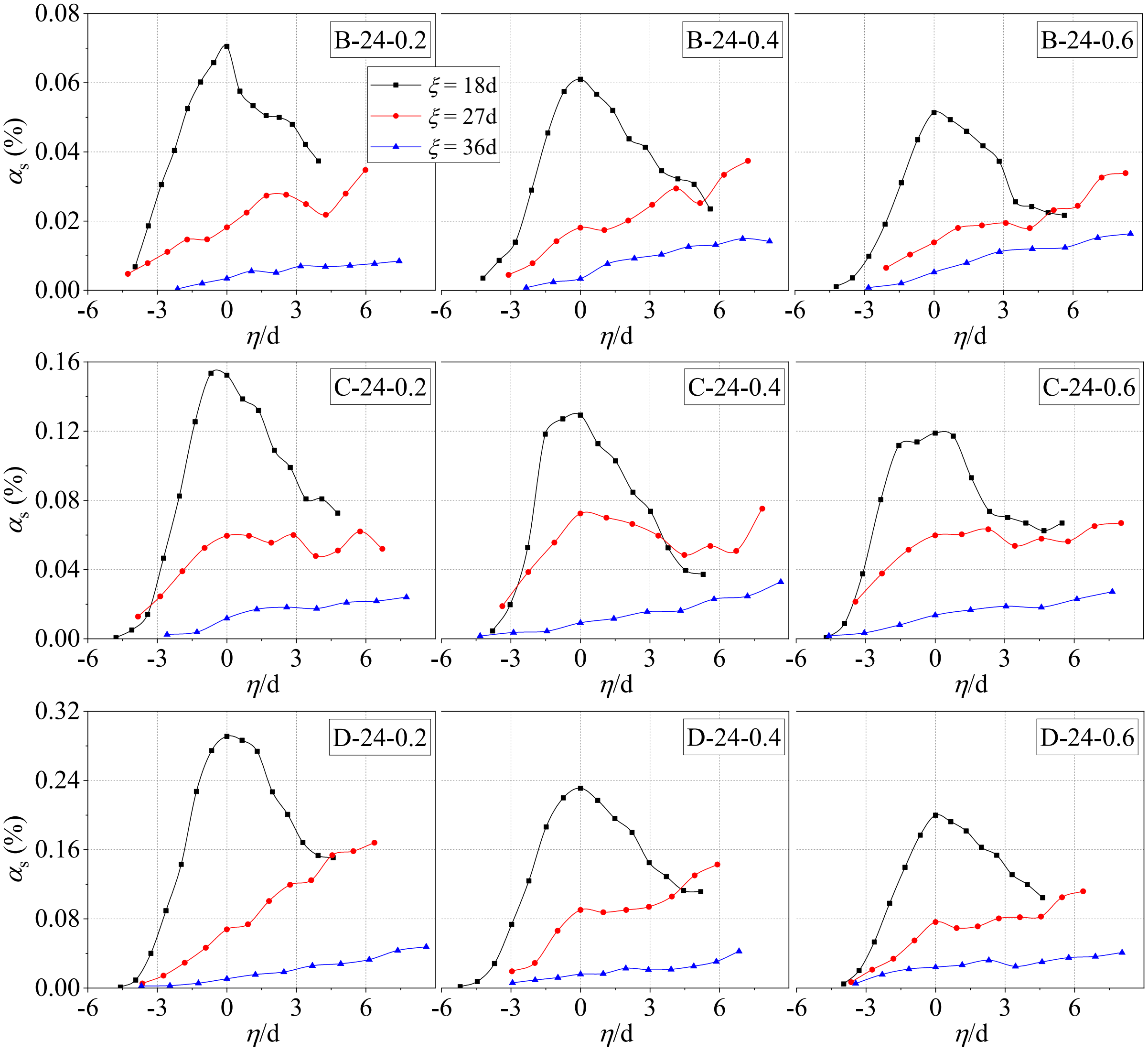

Figure 5-10. Distributions of sand concentration in the η direction within the bubbly region for Q_{sl} = 24 L/min.

The three columns of the figure show that α_s increases with increasing initial sand concentration α_{s0} as expected. The maximum α_s for α_{s0} = 1% (denoted by Expt. "D" series) is approximately four times that for α_{s0} = 0.25% (denoted by "B"). Furthermore, the three rows reveal that α_s tends to decrease as the gas flow rate Q_g becomes larger, especially at $\xi = 18$d. Increasing

Q_g from 0.2 to 0.6 L/min results in a decrease in maximum α_s by 25% to 31%. This negative effect of the gas flow rate may be due to the enhanced ambient flow turbulence by higher gas flow rates, resulting in intensified bubble-particle and particle-particle collisions (Ngo-Cong et al., 2018; Lain et al., 2020). These collisions may lead to the energy dissipation of rising sand particles, causing more to settle from the bubbly region and thus decreasing the sand concentration. Another possible explanation is that a higher gas flow rate generates more bubbles, which are likely to induce an increased upward movement and dispersion of particles in the bubbly region, resulting in a wider distribution of particles and a lower sand concentration.

To explore the effects of slurry flow rate Q_{sl} on sand concentration, $\xi = 18d$ is further explored, where most sand particles may have already separated from the bubbly region for a lower Q_{sl}. Figure 5-11 shows the distributions of α_s at $\xi = 18d$ in the η direction within the bubbly region. The maximum sand concentration increases as the slurry flow rate increases, probably because the particle momentum is enhanced by the higher Q_{sl} due to the higher velocity at the nozzle. More particles tend to rise to a higher position ($\xi = 18d$) before they separate from the bubbly region, thereby increasing the sand concentration there. It is interesting to note that, as the gas flow rate becomes larger, the maximum α_s at section $\xi = 18d$ decreases from 0.15% to 0.04% for $Q_{sl} = 18$ L/min, indicating that the sand concentration is susceptible to the gas flow rates for a lower slurry flow rate.

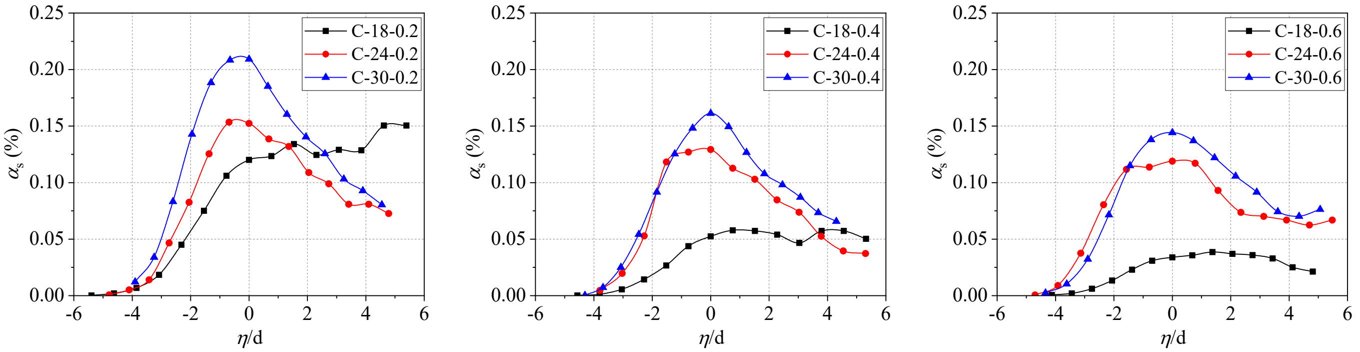

Figure 5-11. Distributions of sand concentration at ξ = 18d in the η direction within the bubbly region for α_{s0} = 0.5%.

5.3.5. Vertical sand distribution at different streamwise locations

The vertical distribution of sand concentration is important to evaluate the evolution of sand particles. Figure 5-12 (a) shows an example of the vertical distribution of sand concentration for Expt. C-24-0.4. The upper boundary of sand region can be observed by the vertical position where α_s approaches 0. The peak concentration occurs at a certain height and generally decreases in the streamwise (x) direction. However, it is noteworthy that the position of peak values initially rises from x = 8d to x = 16d, and then migrates downwards at further streamwise locations. The rising of the peak position from x = 8d to x = 16d is primarily due to the dominance of jet momentum in this region, where the sand particles are lifted to higher positions. Beyond x = 16d, particle gravity takes over, leading to the downward movement of sand particles towards the bed.

The distribution of α_s shows a similar trend as the initial sand concentration increases from 0.5% to 1% as shown in Figure 5-12(b) for Expt. D-24-0.4, in which the peak values are approximately twice as high as those for Expt. C-24-0.4. It is interesting to note that the sand concentration varies more intensely in the vertical direction for Expt. D-24-0.4. This phenomenon is probably due to the enhanced flow turbulence and particle collisions induced by additional particles (Lain et al., 2020), thereby contributing to the instability of the sand distribution.

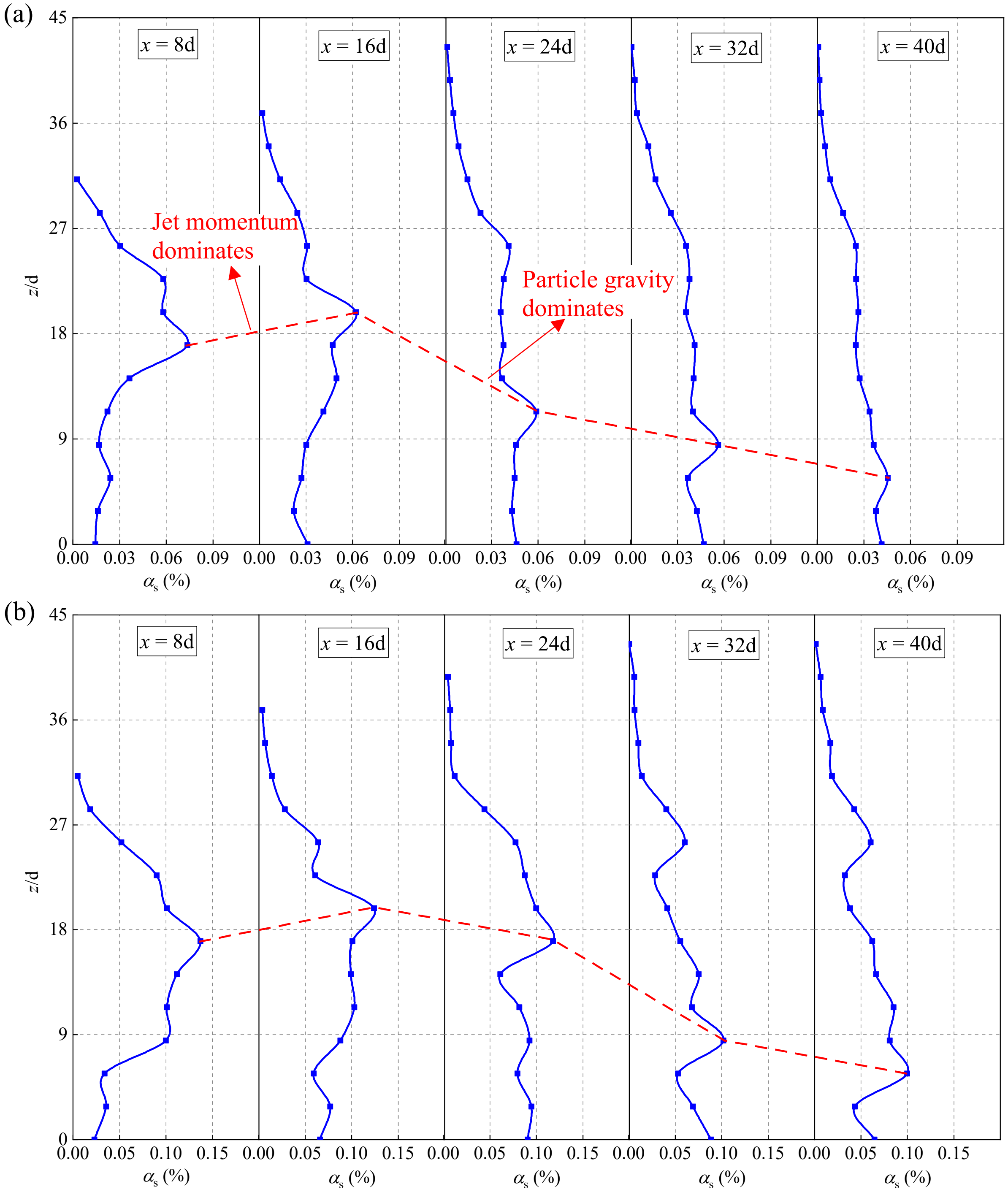

Figure 5-12. Examples of distributions of sand concentration in the vertical direction for (a) Expt. C-24-0.4 and (b) Expt. D-24-0.4. The red lines indicate the variations in vertical positions of peak concentrations along the streamwise direction.

Typically, the amount of sediment delivered to the flume bed is related to the near-bed suspended sand concentration (Mooneyham and Strom, 2018), which can be deemed as a representative of the deposition rate of sand particles (Ouillon et al., 2022a; Liu et al., 2023). Therefore, the sand concentration at $z = 0$ (at the same level as the nozzle exit) is selected to represent the sedimentation (or deposition) behavior in this study. To denote this concentration, the term "sedimentation concentration (α_{ss})" is introduced in this study for conciseness. The distributions of normalized sedimentation concentration α_{ss}/α_{s0} in the streamwise direction is shown in Figure 5-13. Generally, α_{ss}/α_{s0} resembles a parabolic distribution, with its peak value occurring at a specific streamwise distance from the nozzle. The lowest value of α_{ss}/α_{s0} in the test region is found at x = 8d, where it is as small as $\leqslant 0.04$, indicating that this position is close to the upstream boundary ($\alpha_{ss}/\alpha_{s0} = 0$) of the sand region.

Figure 5-13(a) shows that increasing the gas flow rate tends to shift the position of maximum α_{ss}/α_{s0} from x = 32d to 24d. This shift may be attributed to the enhanced bubble-particle and particle-particle collisions induced by higher gas flow rates (as stated in *Section 5.3.4*), causing more particles to reverse their direction at a lower height and descend to the flume bed over a shorter streamwise distance. On the other hand, the initial sand concentration has a maximum effect of 15% on the peak value of α_{ss}/α_{s0}, but it does not significantly impact its peak position. Decreasing the slurry flow rate also shifts the position of maximum α_{ss}/α_{s0} to a shorter streamwise distance (Figure 5-13b). This shift is primarily due to the reduction in initial jet momentum, which allows particles to separate from the bubbly region at an earlier stage. Furthermore, the peak value of α_{ss}/α_{s0} decreases (e.g., 29% from Expt. C-18-0.4 to C-30-0.4) as the slurry flow rate increases, demonstrating that Q_{sl} plays a significant role in particle spreading and sediment deposition behavior.

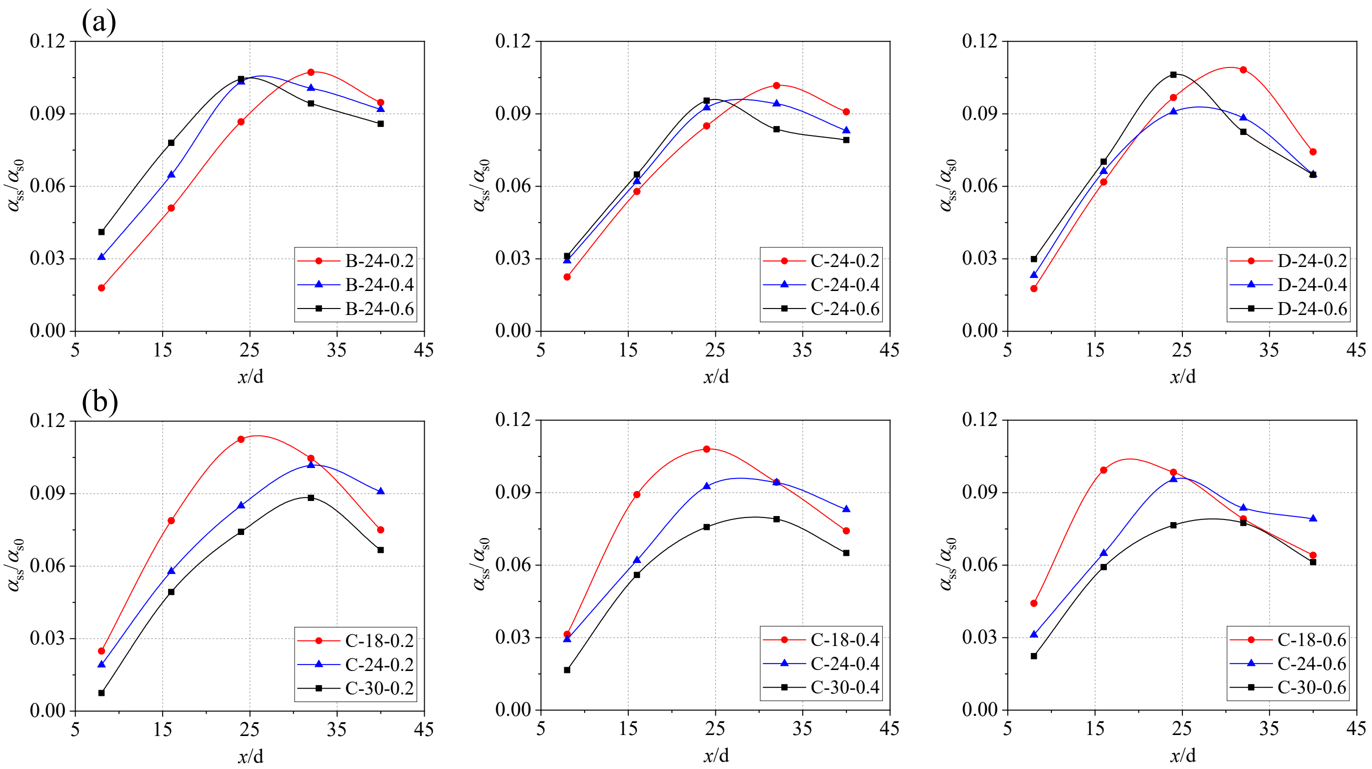

Figure 5-13. Distributions of normalized sedimentation concentration α_{ss}/α_{s0} in the streamwise direction for (a) Q_{sl} = 24 L/min and (b) α_{s0} = 0.5%.

To predict the sedimentation concentration of air-water-sand three-phase jets in crossflow, a relationship is constructed considering the dominant parameters observed in Figure 5-13:

$$\alpha_{ss} = f\left(\alpha_{g0}, \alpha_{s0}, x, d, u_g, u_l, \rho_g, \rho_l, \mu_g, \mu_l\right) \tag{5-7}$$

Applying similar steps of dimensional analysis as outlined in Section 5.3.3, the following relationship can be established:

$$\frac{\alpha_{ss}}{\alpha_{s0}} = f(\alpha_{g0}, \frac{x}{d}, Re_g, Re_l) \tag{5-8}$$

As shown in Figure 5-13, α_{ss}/α_{s0} is mainly determined by the approximately parabolic distribution with x/d, and the slurry flow rate could affect the peak value and its streamwise position, whereas the gas flow rate primarily influences the peak position. To account for these factors, Q_{sl} is represented by its Reynolds number (Re_l) to dominate the peak values, while the effect of both Q_{sl} and Q_g on the peak position is considered by their non-dimensional parameter α_{g0}. During the fitting of the experimental data, Re_g was found to play a minor role and was consequently neglected, probably due to that the gas effects on the peak position have already been accounted for in α_{g0}. Therefore, Eq. (5-8) may be expressed in the following form:

$$\frac{\alpha_{ss}}{\alpha_{s0}} = p\left(\frac{x}{d} + q\alpha_{g0} - m\right)^2 + n \times Re_l^k \tag{5-9}$$

where p, q, m, n, and k are model constants to be determined. After fitting Eq. (5-9) to the experimental data using the method of non-linear least squares regression, the final expression yielding a R^2 of 0.91 is as follows:

$$\frac{\alpha_{ss}}{\alpha_{s0}} = -0.016\left(0.1\frac{x}{d} + 17.4\alpha_{g0} - 3.2\right)^2 + 3.3 \times Re_l^{-0.3} \tag{5-10}$$

Figure 5-14 shows the validation of the predicted α_{ss}/α_{s0} using Eq. (5-10) with all the measured data at different streamwise locations. It is evident that most data points (approximately 90%) fall within the ±15% error lines, and all the measured and predicted data generally have a difference of less than 20%, demonstrating the reliability of the proposed equation. The maximum α_{ss}/α_{s0} in this study is lower than 0.12 and typically occurs at x = 24d or x = 32d for different scenarios. It is worth noting that the small values (< 0.05) of α_{ss}/α_{s0} are only observed at x = 8d, whereas the values at x = 40d are relatively larger (> 0.06). This is mainly because the measurement region is not able to cover the entire sand region due to the wide spreading of particles in the streamwise direction. If the measurement region were elongated, the smallest value of α_{ss}/α_{s0} would be expected to occur at further streamwise locations.

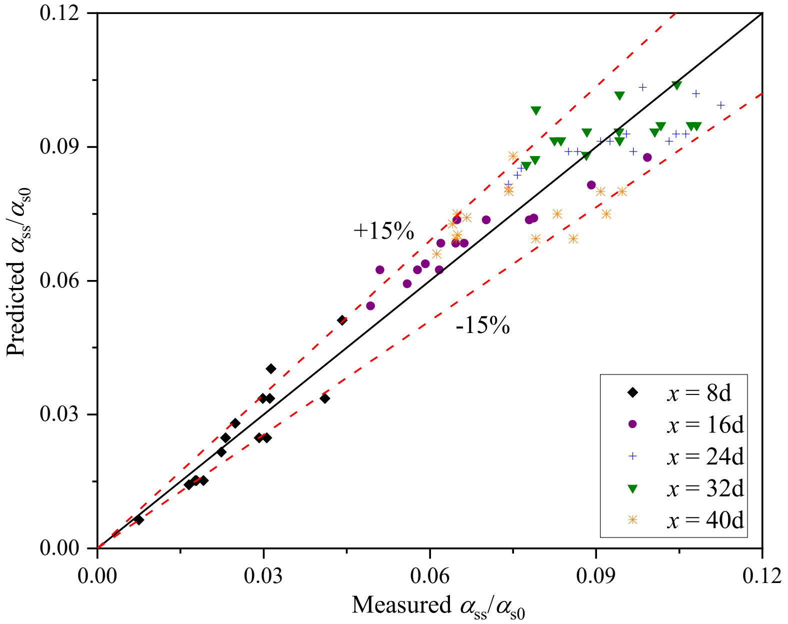

Figure 5-14. Comparison between measured and predicted sedimentation concentration α_{ss}/α_{s0} at different streamwise locations.

5.4. Summary and conclusions

In this paper, a series of physical experiments were conducted to investigate air-water-sand three-phase jets in crossflow. The bubble size, gas void fraction, and sand concentration were systematically investigated based on image processing techniques. The key conclusions drawn from this research are summarized as follows:

(1) The initial gas and slurry (liquid-solid-mixture) flow rates play significant roles in influencing the Sauter mean diameter of bubbles, whereas the initial sand concentration has a relatively minor effect on the bubble size distribution.

(2) Sand particles exhibit a tendency to separate from the bubbly region, driving bubbles to spread further downstream. This leads to a broader distribution of gas void fraction compared to two-phase bubbly jets in crossflow.

(3) The non-dimensional centerline gas void fraction α_{gc}/α_{g0} generally increases with the gas and slurry flow rates, and decreases with the initial sand concentration. The terminal void fraction is achieved at ξ = 45d for scenarios characterized by relatively high initial sand concentration and low air and slurry flow rates. Two relationships were proposed to predict the gas void fraction.

(4) In the bubbly region, sand concentration increases with higher initial sand concentration and slurry flow rates, but decreases with increasing gas flow rates. Higher gas flow rates contribute to a more uniform distribution of sand concentration.

(5) Sedimentation concentration typically follows a parabolic distribution in the streamwise direction. Increasing gas flow rates and decreasing slurry flow rates result in a shift of the peak sedimentation concentration position to a shorter streamwise distance. A relationship was proposed to predict the sedimentation concentration.

6. Large eddy simulation of air-water-sand three-phase jets in crossflow[*]

6.1. Introduction

The phenomenon of multi-phase jets in crossflow (MJC) has garnered significant attention in various applications, ranging from artificial aeration in oceans, lakes, and rivers (McGinnis et al., 2004; Wang et al., 2019; Dhar et al., 2021) to offshore gas/oil exploitation (Dong et al., 2021; Chen et al., 2022a; Wang et al., 2022) and subsea blowouts (Dissanayake et al., 2018; Mitrou et al., 2018; Li et al., 2022c). Multi-phase jets can be classified based on the injection method at the source (nozzle) into pure gas/oil or sand jets, two-phase bubbly jets (air-water) or slurry jets (water-sand), and three-phase jets (air-water-sand). In environments such as oceans, where crossflowing ambient water is prevalent, the complexities of jet behaviors, including mixing characteristics (Dong et al., 2020; Zhang and Zhang, 2022), bubble size distributions (Jobehdar et al., 2016; Kang et al., 2019), and the velocities of dispersed phases (Xu et al., 2018; Newland and Woods, 2023), are further amplified.

Extensive experimental studies have been conducted on the pure gas injection into liquid crossflow, mainly focusing on bubble/gas-phase behaviors including bubble size, rising velocity, gas void fraction, bubble jet penetration and trajectory. (Socolofsky and Adams, 2002; Dong et al., 2021). On the other hand, CFD modelling has also attracted interest in studying pure gas jets in crossflow. Le Moullec et al. (2008) delved into the study of a wastewater treatment reactor where air was injected into water crossflow. They applied the Euler-Euler two-fluid model, coupled with

---

[*] The content of this chapter is being prepared and will be submitted as a journal manuscript.

two turbulence models: k-ε and Reynolds Stress Model (RSM). Rek et al. (2017) conducted numerical modeling of an air jet in crossflowing water using the CFD code OpenFOAM, employing the Volume of Fraction (VOF) method to simulate the interface between bubbles and water. Mitrou et al. (2018) performed an Eulerian-Lagrangian simulation of a gas jet in water crossflow, investigating vortex structures induced by the interaction between the two phases. Dong et al. (2021) conducted experimental and numerical studies on the flow structures of gas jets into crossflow, proposing a modified integral model to predict gas jet evolution, including trajectory, inclination angle, and penetration length. Utilizing large eddy simulations and the population balance model (PBM), a few studies have explored the characteristics of oil jets in crossflow, encompassing the size of oil droplets, dilution characteristics, and turbulence structures (Aiyer et al., 2019; Daskiran et al., 2021, 2022).

Compared to bubble plumes induced by pure gas injection, the concurrent injection of water in bubbly jets can generate smaller bubbles with high initial momentum, thereby enhancing gas-liquid interfacial mass transfer and mixing efficiency (Lima Neto et al., 2008a; Seo and Kim, 2021; Kim et al., 2022). Under the influence of crossflow, the dispersed phase (e.g., air, oil, and alcohol) tends to separate from the liquid phase at a specific height due to buoyancy effects (Socolofsky and Adams, 2002; Zhang and Zhu, 2013, 2014). The radial distribution of gas void fraction exhibited a Gaussian shape, similar to that observed in stagnant water (Lima Neto et al., 2008a; Seo et al., 2022). Attempts have been made to develop numerical models for bubbly jets in crossflow. For instance, Lagrangian integral models have been developed for gas-oil bubbly jet/plumes in coastal currents under deepwater conditions (Zheng et al., 2003; Chen and Yapa, 2003, 2004; Dissanayake et al., 2018). These numerical models can predict well the jet/plume geometries, trajectories, and gas dissolution. However, the detailed hydrodynamics (e.g., gas/liquid velocity distribution, vorticity) and mixing characteristics were not reported. Based on an Euler-Euler two-fluid approach, one recent study (Zhang and Zhang, 2022) investigated the two-phase properties and vortex structures of bubbly jets in crossflow, and found that the liquid phase extended more widely in the vertical direction due to the lift of bubbles, resulting in greater dilution compared to pure water jets.

The slurry (sediment-laden) jets in crossflow have also attracted considerable interest due to the relevance of deep-sea mining, volcanic eruption, and subsea blowout (Bordoloi et al., 2020; Peacock and Ouillon, 2023). In contrast to the rising bubbles in bubbly jets, the sediment is likely to separate from the liquid phase and fallout for sediment-laden jets in crossflow due to the negative buoyancy of particles (Mingotti and Woods, 2022; Newland and Woods, 2023). For instance, James et al. (2022) revealed that particles exhibited separation behavior when their Stokes settling speed exceeded 0.92 times the vertical plume speed. Employing a mixture model for the sediment and water phases, Decrop et al. (2015) undertook a LES to investigate the evolution of turbidity plumes in crossflow, exploring parameters like particle concentration, velocity, plume trajectory, and different turbulent structures. For two types of sediment plumes (midwater plume and collector plume) associated with deep-sea mining, Ouillon et al. (2022a, b) developed an advection-diffusion-settling model to explore the evolution and deposition characteristics in the plumes. Considering the slurry (mixture of water and sediment) as a single continuous phase, Chen et al. (2022c) conducted a LES of a slurry jet in crossflow, and investigated the slurry concentration and turbulence characteristics under different conditions.

While extensive numerical studies have been dedicated to air-water or water-sand two-phase jets in crossflow, limited attention has been paid to the more complex three-phase jets, despite their practical relevance in scenarios such as subsea blowouts and dredging process (Decrop et al., 2018; Bogoyavlensky et al., 2020; Chen et al., 2020). Nonetheless, three-phase CFD studies have been extensively conducted in other areas, such as slurry bubble columns and fluidized beds. Three-phase flow modelling can be typically categorized into five types: pseudo two-fluid (Eulerian-Eulerian, i.e., E-E) approach, three-fluid (E-E-E) approach, Eulerian-Eulerian-Lagrangian (E-E-L) approach, Eulerian-Lagrangian-Lagrangian (E-L-L) approach, and volume of fluid-discrete particle model (VOF-DPM) approach. The pros and cons of each method were systematically summarized in Zhang et al. (2023b). Decrop et al. (2018) conducted a LES to investigate the sediment dilution of the overflow in dredging work, where the water-sediment mixture was released into crossflow including the effect of entrained air bubbles. In their study, the water-sediment mixture was solved using a mixture model, while air bubbles were tracked using a Lagrangian discrete phase model. Their model can be deemed as a special form of E-E-L approach, yet only one set of momentum equation is solved for the liquid-solid mixture with relative slip velocities included, and the liquid-solid interactions such as drag force were not considered.

To the best of the authors' knowledge, this work is the first study on numerical simulation of air-water-sand three-phase jets in crossflow. Based on an Eulerian-Eulerian-Lagrangian three-phase model, the flow field and particle movement are comprehensively investigated. The remainder of this paper is organized as follows: *Section 6.2* presents the velocity measurements and uncertainty analysis; the mathematical model and setup details are introduced in *Section 6.3*; *Section 6.4* presents the numerical results, including model validation, distributions of phase concentration and velocity, turbulent kinetic energy and vortical structures; finally, a brief conclusion is provided in *Section 6.5*.

6.2. Experimental methodology

6.2.1. Velocity measurements of gas and sand

The scenario C-24-0.4 in Chapter 5 was selected as a typical case for the calibration of the current model, and further investigation on the characteristics of air-water-sand three-phase jets in crossflow. After the separation of bubbles and sand (as presented in Section 5.2.2), the obtained binary images were employed to analyze the velocities of gas bubbles and sand particles using the bubble image velocimetry (BIV) and particle tracking velocimetry (PTV) techniques, respectively. The BIV method introduced by Ryu et al. (2005) combines the shadowgraph images obtained from using the background light and the particle image velocimetry (PIV) technique that correlates the consecutive images to determine the velocity by treating bubbles as tracers. This technique has been successfully used in several studies of air-water two-phase flows (Shuai et al., 2019; Amin et al., 2023). Given that the sand concentration is relatively low (0.5% at the nozzle) in this study, the individual sand particle's movement can be determined by using the PTV technique and transformed to the Eulerian field.

The gas velocity was analyzed using a free MATLAB plug-in, PIVlab (Thielicke and Sonntag, 2021). Cross-correlation of consecutive images with a three-pass algorithm and a 50% overlap was applied to obtain the instantaneous gas velocity vectors. In the three-pass approach, the first interrogation window size of 128 × 128 pixels (22 × 22 mm^2) was adopted to ensure it is at least four times larger than the peak bubble displacement (Keane and Adrian, 1990); and the second and third window sizes were 64 × 64 and 32 × 32 pixels, respectively. Furthermore, the cross-correlation function between windows was computed using the discrete Fourier transform, the deformation linear window, and the Gaussian subpixel estimator in PIVlab.

Correlation-based PTV for sand particle movement was executed using another MATLAB plug-in, PTVlab (Brevis et al., 2011). Two main steps in the PTV algorithm are the particle detection and particle tracking. The particle centroid detection was performed using a Gaussian mask algorithm, which searches for particles in the image that match a defined mask with cross-correlation (Takehara and Etoh, 1998). The parameters for the detection algorithm in this study include an intensity threshold of 70, a standard deviation of 10 pixels, and a correlation threshold of 0.5. Moreover, in the particle tracking algorithm, the image pairs were cross-correlated by an interrogation area of 20 pixels, a minimum correlation of 0.7, and a similarity neighbor of 25%.

After processing a total of 4,565 images for each sub-window, the scale of the velocity vector was calibrated with the spatial resolution of 5.8 pixels/mm and the time step of 0.004 s between consecutive images. Finally, the instantaneous velocity data of gas and sand at specific points in PIVlab and PTVlab were extracted to calculate arithmetic mean velocities.

6.2.2. Uncertainty analysis

According to the measurement method of concentrations of air and sand as shown in *Section 5.2.2*, the main uncertainties for their concentrations were mainly induced by the circular area and depth of field (DOF). The errors caused by the circular area have already been figured out as 3.2% in *Section 5.2.2*, so the next step is to evaluate the uncertainty of DOF.

The DOF and its uncertainty were determined through the following methods or steps:

(a) The DOF was initially estimated by observing a ruler physically using the high-speed camera. By adjusting the ruler position forward and backward with respect to the focal plane ($y = 0$), the image became blurred at round $y = \pm 25$ mm. As a result, the preliminary estimation of the DOF suggested it to be within 50 mm.

(b) Subsequently, the DOF was calculated using Eq. 5-D1 (Appendix D), providing an estimated value of 20 mm.

(c) Finally, the DOF used in image processing was calibrated using the gas void fraction measured by the RBI probe. In image processing, a lower grayscale threshold could result in more identified bubbles, corresponding to a larger estimated DOF. The current image processing algorithm identifies approximately 80%-85% in-focus bubbles (based on visual inspection of the images) by applying an appropriate grayscale threshold (varying from case to case). If the threshold is further reduced, out-of-focus (blurred) bubbles will be inevitably detected. Assuming and using the mean probe values as a reference (Figure 5-3), the DOF in image processing varies between 17.8 and 22.7 mm using the equation in *Section 5.2.2*: $\alpha_g = \sum_1^N (\sum_{i=1}^n \forall_{b,i} / \forall_f) / N$.

Consequently, the DOF of 20 mm, estimated by Eq. 5-A1 in Method (b), was used for the calculations of gas void fraction in this study. The maximum DOF uncertainty caused by the threshold was estimated as (22.7-20)/20 = 13.5%. Based on the values of the two previously listed sources of uncertainty, the total uncertainty in measurements of concentration was estimated to be their root sum squared value (Warwaruk and Ghaemi, 2023), which was approximately 13.9%.

Sources of uncertainty in the measurement of gas velocity include errors due to (a) the DOF; (b) the measurement in PIVlab; and (c) the statistical convergence of velocity. The details for each source of uncertainties are listed below.

(a) In most studies using the BIV technique, the DOF has been considered as a primary source of uncertainty (Na et al., 2020; Kong et al., 2023). All bubbles within the DOF appear sharp in the images, while those outside the focal plane can introduce bias to velocity vectors. The error due to the thickness of the DOF, ε_{D}, is estimated as (Ryu et al., 2005):

$\varepsilon_{\mathrm{D}} = \mathrm{DOF}/2L$, where L is the working distance. For a DOF of 20 mm and L of 640 mm used in this study, ε_{D} is estimated as 1.6%. After considering the DOF uncertainty (17.8 - 22.7 mm), the estimated ε_{D} is 1.8%.

(b) Compared to the uncertainty in a standard PIV measurement (e.g., estimated as approximately 0.1 pixels in Raffel et al. (2018)), the BIV measurement may induce higher uncertainty due to different bubble sizes, shapes, and dispersive characteristics (Lim et al., 2015; Zhang and Chanson, 2018; Ma et al., 2020), leading to challenges to directly estimate it. Alternatively, the errors can be assessed by comparing it with another simultaneous measurement system that has significantly lower uncertainty (Neal et al., 2015; Scharnowski and Kähler, 2020). Comparisons have been made between the BIV and other techniques (e.g., fiber optic reflectometry) in highly aerated flows to estimate the uncertainties (Ryu et al., 2005; Bung and Valero, 2015). In this study, the gas void fraction is relatively low (1.6% at the nozzle) and each in-focus bubble can be clearly identified. Therefore, the velocity magnitude measured by PIVlab was compared with the values measured by manual tracking plug-in in ImageJ. The manual tracking is essentially a Lagrangian method by carefully selecting the front of each bubble in two consecutive images, which serves as a reference velocity in this study for evaluating the uncertainty in PIVlab measurement. Figure 6-F1 (see Appendix F) shows the comparison of these two methods for the mean gas velocity around the gas-phase centerline for the current scenario C-24-0.4. The uncertainty associated with measurements in PIVlab is estimated to be within 7.5%.

(c) The random noise of the BIV measurements was evaluated using the statistical convergence of the gas velocity. Figure 6-F2 shows an example of the statistical convergence of mean gas velocity at the centerline of ξ = 18d and 27d, where the horizontal axis denotes the number of data points (n) normalized with the total number of data points (N). The total number of data points decreases from the gas-phase centerline (around $N = 2500$) to boundary ($N = 0$) due to the decreasing gas void fractions, and only the measurement points with $N > 150$ were selected to calculate the mean gas velocity. The results showed that the arithmetic mean generally converged after $n/N = 0.6$, and the maximum variation of the mean gas velocity was approximately 1% from $n/N = 0.8$-1.0 for all the measurement points in the current scenario.

Accordingly, the total uncertainty of the three sources in measurements of mean gas velocity was estimated to be their root sum squared value of 7.8%. Uncertainty analysis was also conducted for the sand velocity based on the errors due to DOF, measurement in PTVlab, and statistical convergence. The results indicated similar uncertainty values for each source as the gas velocity. Consequently, the total uncertainty in measurements of mean sand velocity was estimated to be 8.0% in this study.

6.3. Mathematical model and numerical methodology

In this study, the Eulerian-Eulerian-Lagrangian three-phase solver developed in Chapter 4 was used, and coupled with the LES to model the sub-grid turbulence. The gas and liquid phases are modeled in the Eulerian coordinates, and the sand particles were modeled in the Lagrangian coordinates. The interphase forces between the gas and liquid phases include drag force, virtual mass force and turbulent dispersion force, while the interphase forces between the fluid and solid phases are buoyancy force and drag force. In the current LES, the one-equation SGS model (Niceno et al., 2008) was adopted for the liquid phase. To model different sizes of bubbles, 14 classes were selected as shown in Table 6-1. The widely-used coalescence model developed by Prince and Blanch (1990), and breakage model proposed by Laakkonen et al. (2006) were adopted.

Table 6-1. Bubble classes used in the simulation.

Bubble class index	Bubble diameter (mm)	Bubble class index	Bubble diameter (mm)
1	0.30	8	1.04
2	0.36	9	1.24
3	0.43	10	1.47
4	0.51	11	1.76
5	0.61	12	2.10
6	0.73	13	2.51
7	0.87	14	3.00

6.3.1. Grid configuration and boundary conditions

In this study, the experimental geometry was discretized into computational grids by the *blockMesh* utility in OpenFOAM. Four grid cell (control volume) sizes were tested, i.e., Grid 1 containing 6,371,490 cells (1.0-16.4 mm edge length), Grid 2 containing 9,069,666 cells (1.0-15.3 mm edge length), Grid 3 containing 11,727,098 cells (0.9-14.4 mm edge length), and Grid 4 containing 13,420,072 cells (0.8-12.8 mm edge length). It should be noted that the grid cell size is much smaller than that used in Chapter 2, mainly because the bubble or sand particle sizes are much smaller (around 3 times) than that in Chapter 2. As discussed in Chapter 2, the grid cell size should generally be larger than the sizes of bubbles/particles when employing the Eulerian-Eulerian or Eulerian-Lagrangian approach. In this simulation, the average bubble size is approximately 1.0 mm, allowing for the exploration of smaller grid cell sizes in the LES grid sensitivity analysis. Figure 6-1(a) shows an example of grid configuration for the three-phase jet model using Grid 3, where the local refinement was implemented near the nozzle, and the grid cell size increases smoothly from the nozzle exit to each side of the computational domain. To validate the mathematical model and examine 3D hydrodynamics, the same configurations as the experiments were used in the simulations. The computational domain was reduced to 1.2 m in length to save the computational time. The nozzle was set at 0.1 m downstream of the crossflow inlet, and the coordinate origin was set at the nozzle exit where the mixture of gas, liquid, and sand was injected. It should be noted that *x*, *y*, *z* are the longitudinal, vertical, transverse directions, respectively. An example of instantaneous flow structures of gas-phase (in red color), liquid-phase (in cyan color), and sand-phase (in yellow color) at *t* = 40 s is shown in Figure 6-1(b).

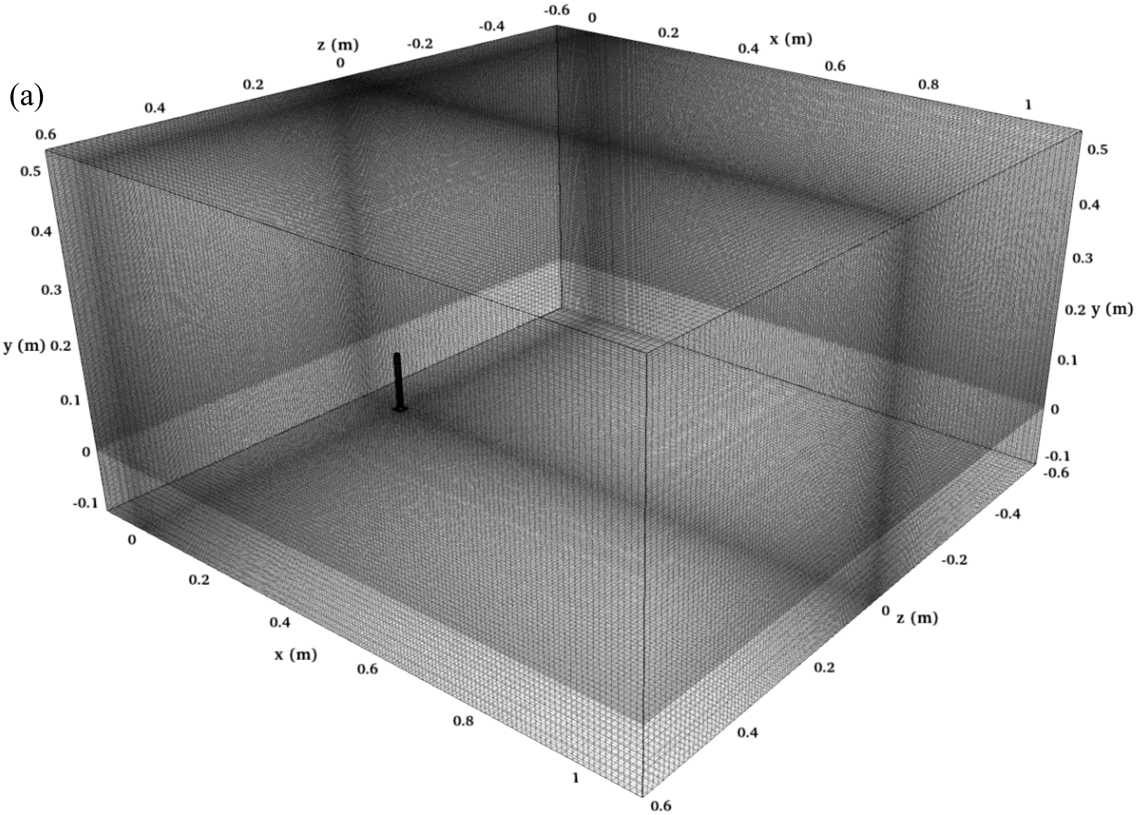

(b)

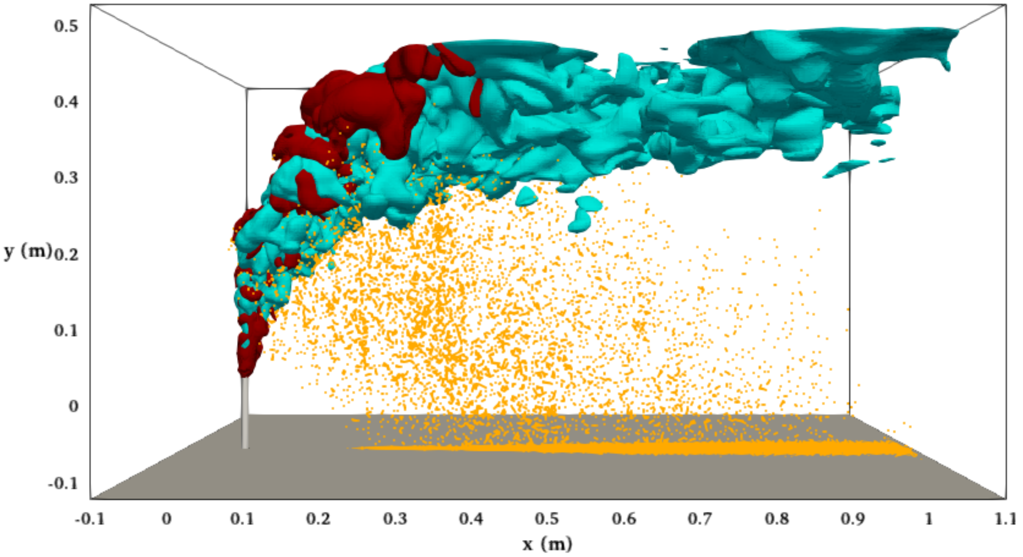

Figure 6-1. (a) Grid configuration for the three-phase jet model; and (b) instantaneous flow structures of gas-phase (in red color), liquid-phase (in cyan color), and sand-phase (in yellow color) at *t* = 40 s. The iso-surfaces of gas and liquid phases were 3% of their initial concentrations.

The boundary conditions were specified as follows. Given the approximately uniform water velocity above the nozzle exit (Figure 5-B1), a constant value of cross-sectional average velocity, 0.2 m/s, was assigned at the crossflow inlet. Its maximum deviation from the actual velocity in the region of interest (above the nozzle exit) is about 0.03 m/s, which is assumed to have minor effects on the simulation results. At the crossflow outlet, the velocity was set to inletOutlet, typically equivalent to zero gradient, though it switches to a fixed value (zero in this study) if there is backward flow at the outlet. At the nozzle exit boundary, a mean vertically upward velocity of 3.5 m/s was prescribed for all three phases, with a fluctuation scale (i.e., turbulence intensity) of 10%. The initial gas volume fraction was calculated by $\alpha_0 = Q_g/(Q_g + Q_l)$, where Q_g and Q_l were gas and liquid flow rates, respectively. Slip and zero-gradient boundary conditions were imposed at the top surface of the domain for liquid and gas, respectively. The rest surfaces were specified as wall boundaries, and the no-slip boundary conditions were adopted. Furthermore, the solid particles bounced back with a restitution coefficient of 0.9 at the walls and 0.1 at the top boundary.

Initially, the water was flowing from crossflow inlet to outlet with the same velocity at crossflow inlet, and the hydrostatic pressure distribution at time $t = 0$ was defined in the vertical y direction. No gas and sand particles exist in the channel flow at the initial time, and the scalar concentration is zero in the domain. Gas bubbles consisting of 14 groups (shown in Table 6-1) with $s = 1.7$ were predefined at the nozzle exit.

6.3.2. Simulation procedure

The governing equations were solved using the developed Eulerian-Eulerian-Lagrangian solver in Zhang et al. (2023b) in the open source CFD package OpenFOAM v2006. This solver is based on the finite volume method to discretize the governing equations. The fluid phase volume fractions were solved by using a modified MULES method with considering the effect of sand concentration α_s, and the velocity-pressure was coupled via the PIMPLE algorithm. The first-order bounded implicit Euler scheme was employed for the time derivative terms in the equations, while the second-order Gauss linear scheme was adopted for the gradient terms. The limited discretization scheme was applied to the divergence terms, and the diffusive terms were interpolated using the Gauss linear uncorrected scheme. The detailed schemes for each term in the governing equations are listed in Table 6-2.

Table 6-2. Numerical schemes used in OpenFOAM: $\emptyset$ is a generic variable, ∇^2 is the Laplacian term, $\nabla^{\perp}$ is the surface-normal gradient term, and $(\emptyset)_f$ is the face interpolation operator.

Term	Scheme
$\partial\emptyset/\partial t$	Euler implicit
$\nabla\emptyset$	Gauss linear

$\nabla \mathrm{p}$	Gauss linear
$\nabla \cdot (\mathbf{U}_{\boldsymbol{\varphi}} \alpha_{\varphi})$	Gauss vanLeer
$\nabla \cdot (\emptyset \mathbf{U}_{\boldsymbol{\varphi}} \mathbf{U}_{\boldsymbol{\varphi}})$	Gauss limitedLinearV 1
$\nabla \cdot (\mathbf{U}_{\boldsymbol{\varphi}} \emptyset)$	Gauss limitedLinear 1
$\nabla \cdot \left(\tau_{\varphi}^{\mathrm{eff}}\right)$	Gauss linear
$\nabla^2 \emptyset$	Gauss linear uncorrected
$\nabla^{\perp} \emptyset$	uncorrected
$(\emptyset)_f$	linear

The adjustable time step with a maximum value of 0.0001 s was adopted to resolve the flow field and the movement of Lagrangian particles, and to satisfy the Courant number requirement $C_o = \Delta t \frac{U_{\max}}{\Delta x_{\min}} < 1$, in which $\Delta x_{\min}$ represents the shortest distances between the computational points. The simulation was run for more than 40 s real-time, and time averaging was performed after 20 s when the flow reached statistically stationary turbulence (the gas void fraction was used to determine the statistical independence of the flow). In the three-phase solver, the Lagrangian particle (sand-phase) concentration and velocity were converted to the Eulerian field to evaluate the time-averaged properties, and the detailed procedure can be found in Zhang et al. (2023b). The numerical simulations were carried out on a cluster (Compute Canada) with 192 processors.

6.4. Results and discussion

6.4.1. Grid sensitivity analysis and model validation

Before the grid sensitivity analysis of the LES model, a preliminary simulation using the mixture *k*-*ε* turbulence model was conducted for comparison. Figure 6-F3 (see Appendix F) shows the instantaneous flow structures of the liquid-phase at $t = 15$ s with the LES and mixture *k*-*ε* model using the same grid (Grid 3). The iso-surface of the LES appears highly contorted, indicating a high level of resolved turbulence. However, it is evident that the resolved fluctuation level is significantly lower in the mixture k-ε model, and the iso-surface is more indicative of the mean flow structure. Hence, the use of LES is essential for capturing turbulent fluctuations in three-phase jets in crossflow, as compared to the mixture k-ε model.

A grid sensitivity analysis was conducted on the four grids to investigate the influence of grid resolution on the simulated results. Figure 6-2(a) shows the distributions of mean gas void fraction α_{gm} at ξ = 18d predicted with the four grids, along with the experimental result. The results shows that the predicted α_{gm} generally agree with the experimental data by all the grids. However, the peak α_{gm} at the gas-phase centerline (η = 0) predicted by Grids 1 and 2 are much higher (e.g., 25% for Grid 1) than the experimental data, whereas the predicted values by finer Grids 3 and 4 lie well with the experiment. Similar prediction can be observed by the distributions of mean gas velocity U_{gm} in Figure 6-2(b), where the distribution of U_{gm} becomes wider as the grid becomes finer. Given the similar results predicted by Grids 3 and 4, Grid 3 is selected for the following computations considering the balance of accuracy and computation time.

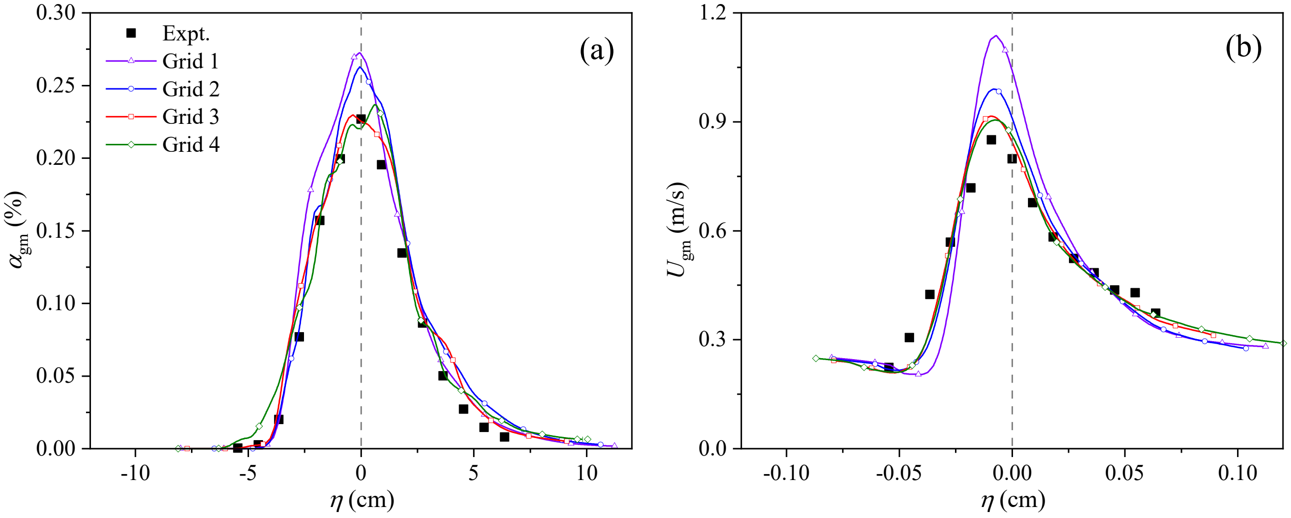

Figure 6-2. Comparison between the simulated and experimental results at ξ = 18d using four different grid cell sizes for (a) mean gas void fraction α_{gm}; and (b) mean gas velocity U_{gm}.

The concentration and velocity of both gas and sand phases are utilized for comparison and validation against the experiments conducted in this study. Figure 6-3 shows the comparison between the simulated and experimental distributions of mean gas void fraction α_{gm} and mean gas velocity U_{gm} at sections ξ = 18d - 36d in the η direction. Figure 6-3(a) shows that α_{gm} agree well with the experimental data at sections ξ = 18d and 27d with a relative error lower than 13.9%. The relative error at some points of ξ = 36d is higher than 13.9%, yet the actual difference of α_{gm} is within 0.03%, which can be easily caused by the numerical error (e.g., induced by grid resolution and discretization schemes), as well as the velocity deviation between the realistic (Figure 5-B1) and simplified inlet boundary condition. The predicted U_{gm} also agrees well with the experiments at sections ξ = 18d and 27d (Figure 6-3b), as well as the values at the downstream side of ξ = 36d. The relative difference at the upstream side of ξ = 36d is larger (e.g., with maximum relative error of 35% at the upstream boundary η = -7 cm), which is deemed acceptable in this study, taking into account the influence of numerical error and the simplified inlet condition.

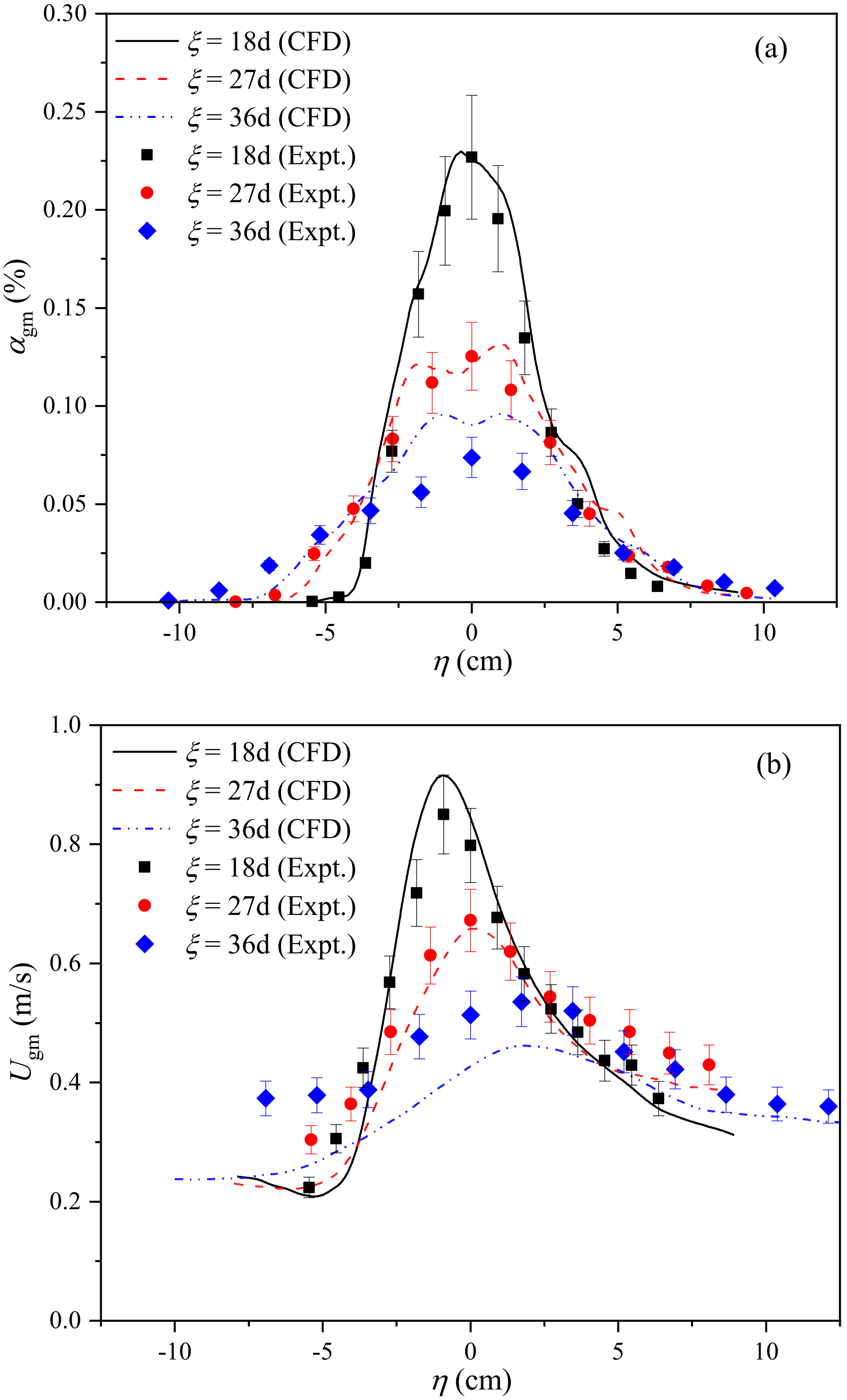

Figure 6-3. Comparison between the simulated and experimental distributions at sections $\xi = 18d$ - $36d$ in the η direction for (a) mean gas void fraction α_{gm}; and (b) mean gas velocity U_{gm}. The error bars represent a 13.9% uncertainty in the measured α_{gm} and a 7.8% uncertainty in the measured U_{gm}.

Figure 6-4 shows the comparison between the simulated and experimental distributions of mean sand concentration α_{sm} and mean sand velocity U_{sm} at sections x = 8d - 40d in the vertical direction. The results show that the predicted α_{sm} and U_{sm} generally agree well with the experiments, with the relative errors lower than 10% at most positions. In the CFD simulations, the α_{sm} and U_{sm} vary more intensely in the vertical direction, probably due to the small grid cell size (e.g., average cell volume 0.08 cm^3) used for LES. Given the method of transforming the Lagrangian particles into Eulerian field, the time-average of sand property is calculated based on each small cell, which may lead to the fluctuating distributions in the vertical direction. However, in the experiment, each water sample has a volume of 3.53 cm^3, which is able to mitigate substantial fluctuations and thus yield smoother measurements compared to the CFD simulation. Nevertheless, the overall trend predicted by the CFD resembles the experimental results with acceptable relative errors, and thus the model validation is deemed successful in this study.

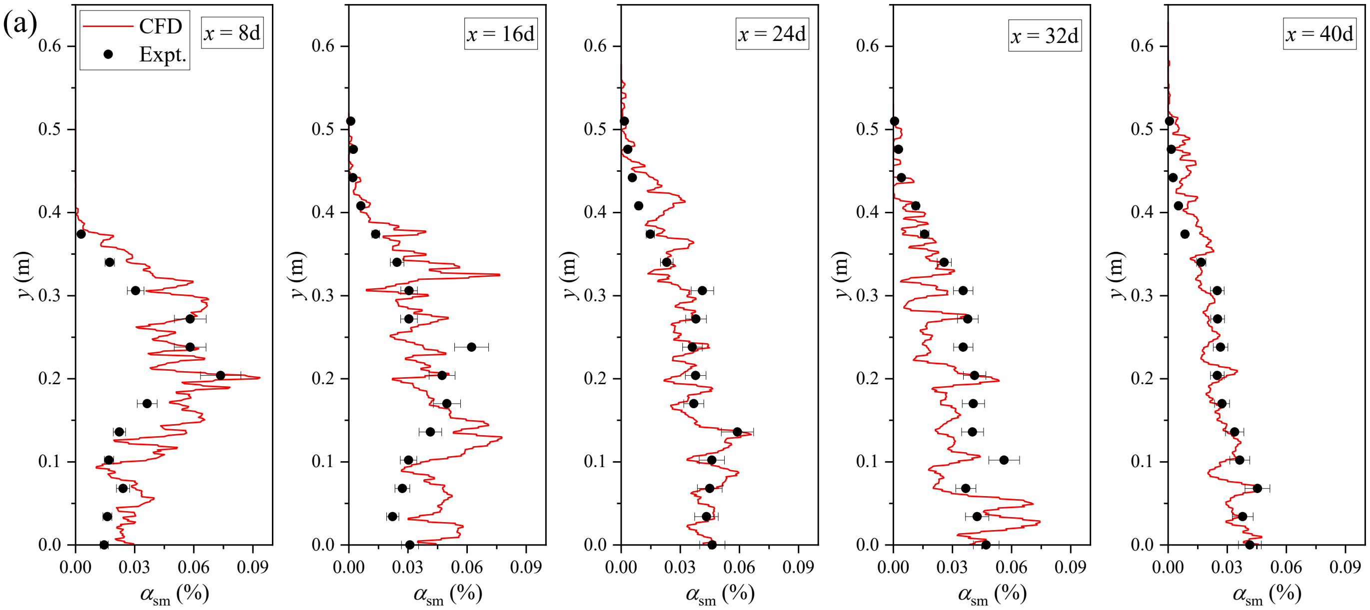

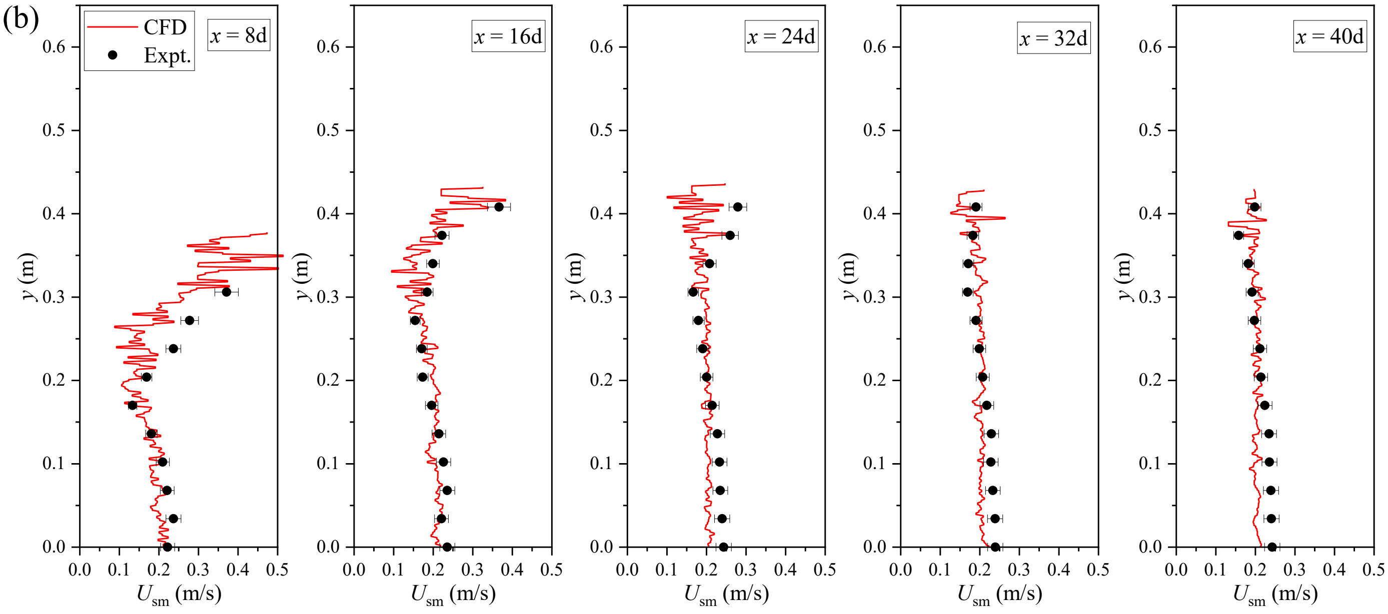

Figure 6-4. Comparison between the simulated and experimental distributions at sections x = 8d - 40d in the vertical direction for (a) mean sand concentration α_{sm}; and (b) mean sand velocity U_{sm}. The error bars represent a 13.9% uncertainty in the measured α_{sm} and an 8.0% uncertainty in the measured U_{sm}.

6.4.2. Phase concentration distribution

The distribution of mean gas void fraction at sections ξ = 9d - 45d of the bubbly region is shown in Figure 6-5(a), where the boundary of each section is defined as 2% of the initial value at the nozzle. As expected, the peak α_{gm} decreases and the section area increases with the increasing distance from the nozzle. The distribution of α_{gm} evolves from an ellipse to a kidney shape, similar to the air-water bubbly jet in crossflow where a counter-rotating vortex pair (CVP) was observed in the bubbly region (Zhang and Zhang, 2022). The distributions of instantaneous and mean gas void fractions at the center-plane are shown in Figure 6-5(b) and (c), respectively. The gas bubbles move approximately vertically before y/d = 15, mainly due to the high initial momentum of the three-phase jet and their strong mixing with the liquid-phase. Under the crossflow effect, the mean gas void fraction is slightly diluted to the downstream side (e.g., the angle is ≈17.7° from the vertical direction for the 0.05% contour line in Figure 6-5c). Beyond *y*/d = 15, the distribution of α_{gm} is bent over in the crossflow direction continuously until *y*/d = 25, where the angle between downstream 0.05% contour line and the vertical direction starts to be approximately constant as 40°.

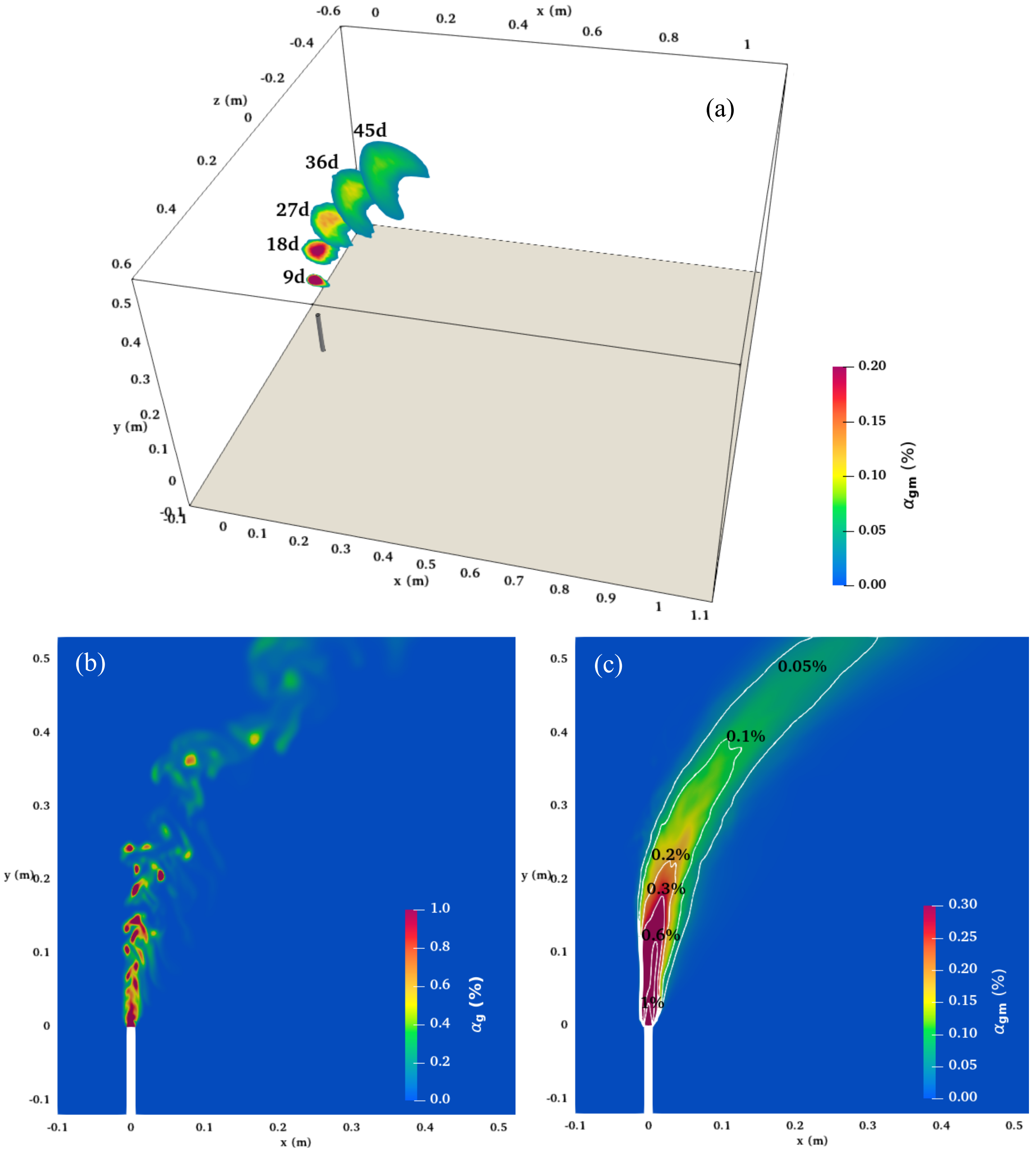

Figure 6-5. Gas void fraction distributions of (a) the mean values at sections $\xi = 9\mathrm{d} - 45\mathrm{d}$; (b) the instantaneous value at the center-plane; and (c) the mean value at the center-plane.

For the liquid-phase, a passive scalar was implemented to examine its mixing characteristics with concentration of $C_0 = 1.0$ at the nozzle exit. The distribution of instantaneous and mean scalar concentrations at the center-plane are shown in Figure 6-6(a) and (b), respectively. The instantaneous concentration shows that the liquid-phase oscillates slightly after injection until $y/\mathrm{d} \approx 6$. Beyond $y/\mathrm{d} \approx 6$, the oscillation becomes more intense and the liquid-phase spread widely in the direction perpendicular to the jet trajectory. This pronounced jet expansion has been found to be associated with the increased turbulent kinetic energy (TKE) in the jet core of a single-phase jet in crossflow (Esmaeili et al., 2015), which will be further discussed in Section *6.3.4*. The overall dilution of the liquid-phase can be observed by the mean concentration C_m in Figure 6-6(b). After injection from the nozzle exit, the centerline C_m decreases smoothly from 1.0 to 0.9 at around $y/\mathrm{d} = 6$, and then decreases rapidly (e.g., 0.5 at around $y/\mathrm{d} = 10$) and spread widely with the increasing distance from the nozzle.

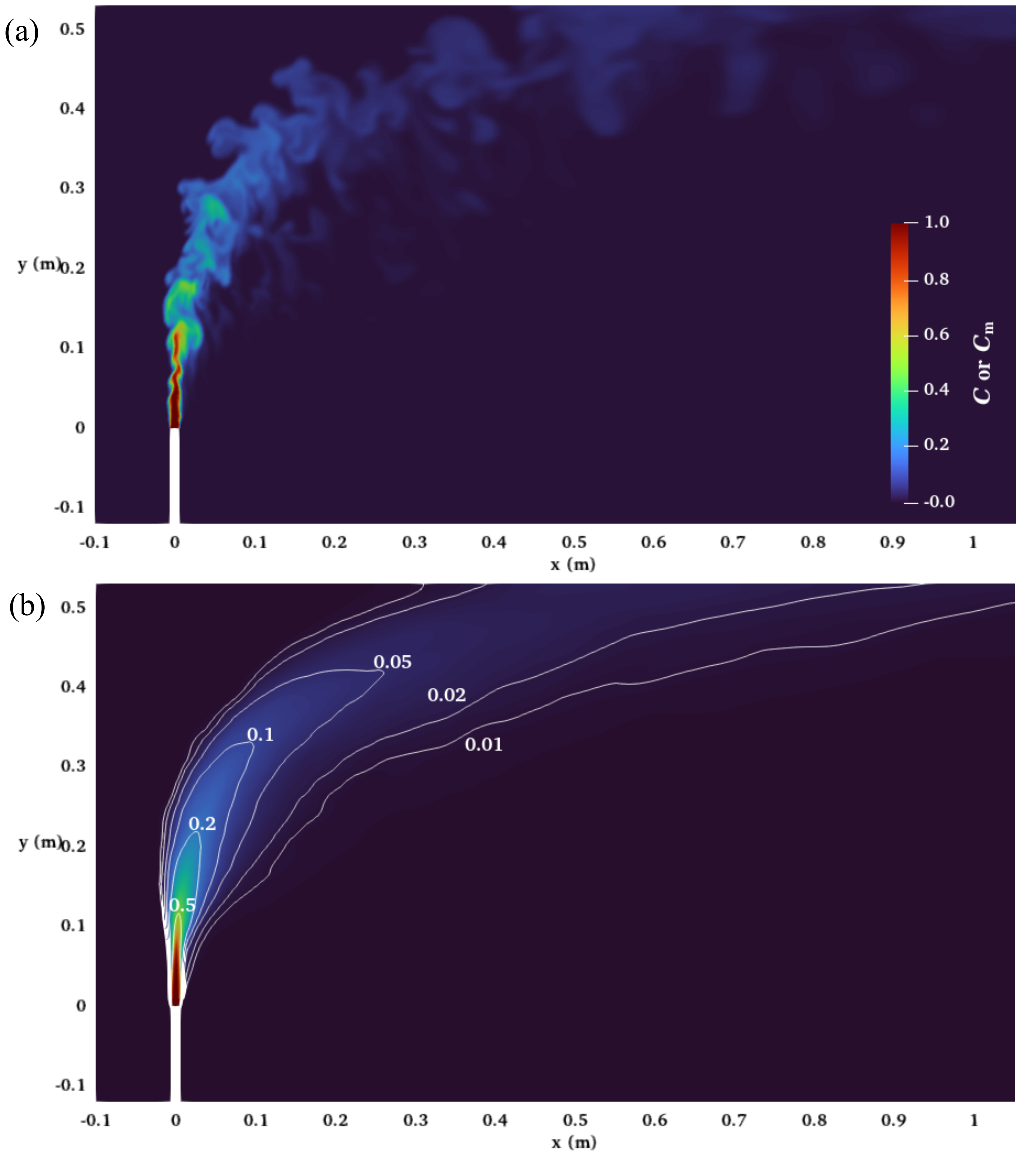

Figure 6-6. Distributions of center-plane concentration for the liquid-phase of the three-phase jet. (a) instantaneous value C; and (b) mean value C_{m}.

For a single-phase jet in crossflow, Hodgson and Rajaratnam (1992) conducted comprehensive laboratory experiments on circular jets at right angles to crossflow and proposed:

$$S_c = 1.09\left(\frac{\alpha x}{d}\right)^{1/3} \tag{6-1}$$

where $S_c = \frac{C_0}{C_{max}}$ represents the jet centerline dilution, and $\alpha = U_0/U_a$ is the relative strength of the jet compared to the crossflow, where U_0 is the initial liquid jet velocity and U_a is the ambient crossflow velocity. Furthermore, in the momentum-dominated near- and far-fields of a single-phase jet in crossflow, Lee and Chu (2003) proposed the following equations to predict the centerline concentration:

for $y_c \leq L_{mt}$,
$$\frac{y_c}{L_{mt}} = 2.65\left(\frac{x}{L_{mt}}\right)^{1/2} \tag{6-2}$$

$$\frac{S_c Q_0}{U_a L_{mt}^2} = 0.16\frac{y_c}{L_{mt}} \tag{6-3}$$

for $y_c > L_{mt}$,
$$\frac{y_c}{L_{mt}} = 1.56\left(\frac{x}{L_{mt}}\right)^{1/3} \tag{6-4}$$

$$S_c = 0.46\frac{U_a y_c^2}{Q_0} \tag{6-5}$$

where y_c is the centerline location in the y direction, and $L_{mt} = \frac{M_0^{1/2}}{U_a}$ is the momentum length scale for a jet in crossflow. The initial specific momentum flux $M_0 = U_0 Q_0$, where Q_0 is the initial liquid jet velocity and flow rate, respectively.

Figure 6-7 shows the comparison between the present and previous studies for evolution of the scalar concentration C_c along the centerline. Compared to the equation proposed by Lee and Chu (2003), C_c/C_0 predicted in this study agrees better with the equation proposed by Hodgson and Rajaratnam (1992). The maximum difference occurs at around x/d = 2.5 with an actual value of 0.18, which is reasonable because the current grid cell size is not enough to resolve the turbulence that near to the nozzle. Additional test suggests that the difference of predicted C_c/C_0 between this study and Eq. (6-1) can be narrowed after applying a finer grid.

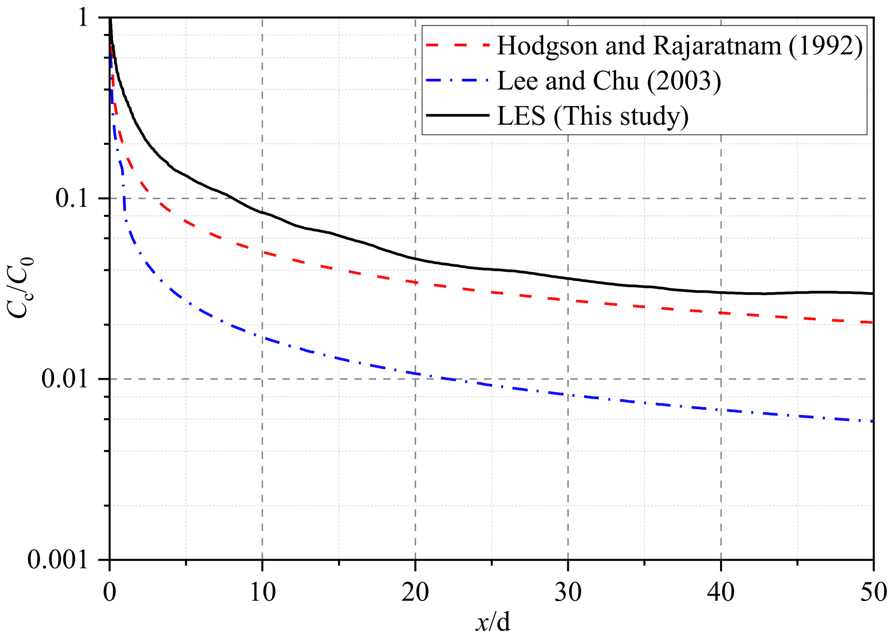

Figure 6-7. Evolution of the scalar concentration for the liquid-phase along the centerline.

For the sand-phase, the distribution of mean sand concentration is not continuous, as shown in Figure 6-8 at the center-plane. This is because the Eulerian field of sand-phase is mapped by the modeled Lagrangian particles, instead of a continuous phase. The sand particles penetrate to a certain height and then move downwards under gravity. Interestingly, some particles reverse their direction and move downwards right after the injection from the nozzle (around y/d = 2), probably due to the effects of turbulence and particle collisions. It should be noted that the deposited particles at the bed is not enough to form a certain height due to their small size during the 40 s simulation, and the higher values than 0.1% only occur in one layer of grids.

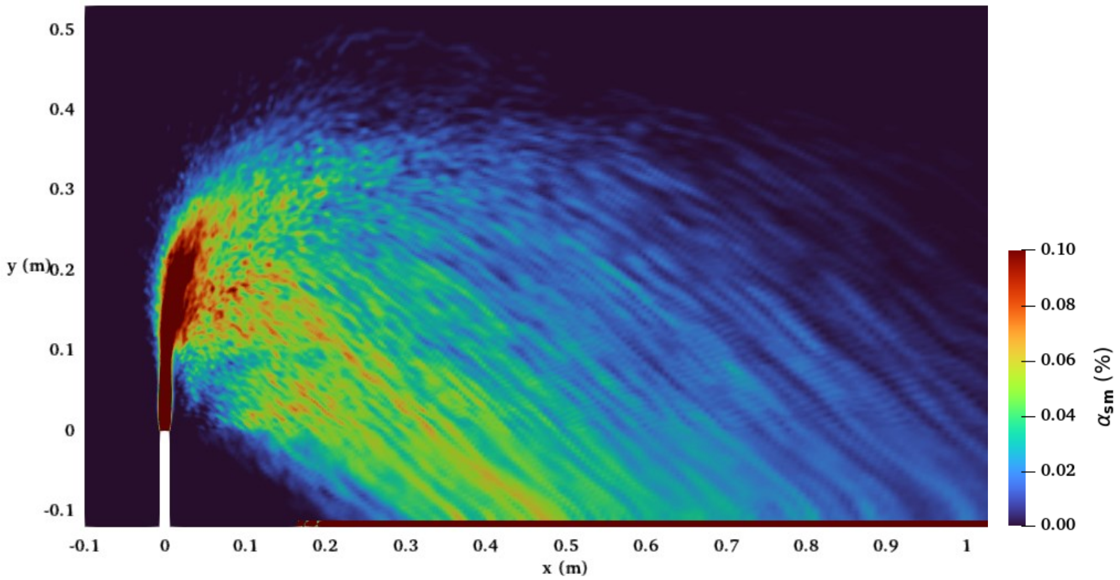

Figure 6-8. The mean sand concentration distribution at the center-plane.

6.4.3. Phase velocity distribution

Figure 6-9 shows the mean velocity distributions at sections ξ = 9d - 45d in the bubbly region for the three phases. At section ξ = 9d, the maximum velocities for gas, liquid and sand phases are as large as 2.1, 2.0, and 1.9 m/s, since the initial jet momentum dominates there. The velocities decrease along the gas-phase trajectory as expected, and the location of maximum velocity migrate from the center to the downstream side of the bubbly region. This is probably because the bubble velocity is suppressed by the crossflow at the upstream side of the bubbly region, while the liquid and sand phases tend to separate from the bubbly region with a lower position. The overall velocity is the highest for the gas-phase and lowest for the sand-phase due to the buoyancy effects.

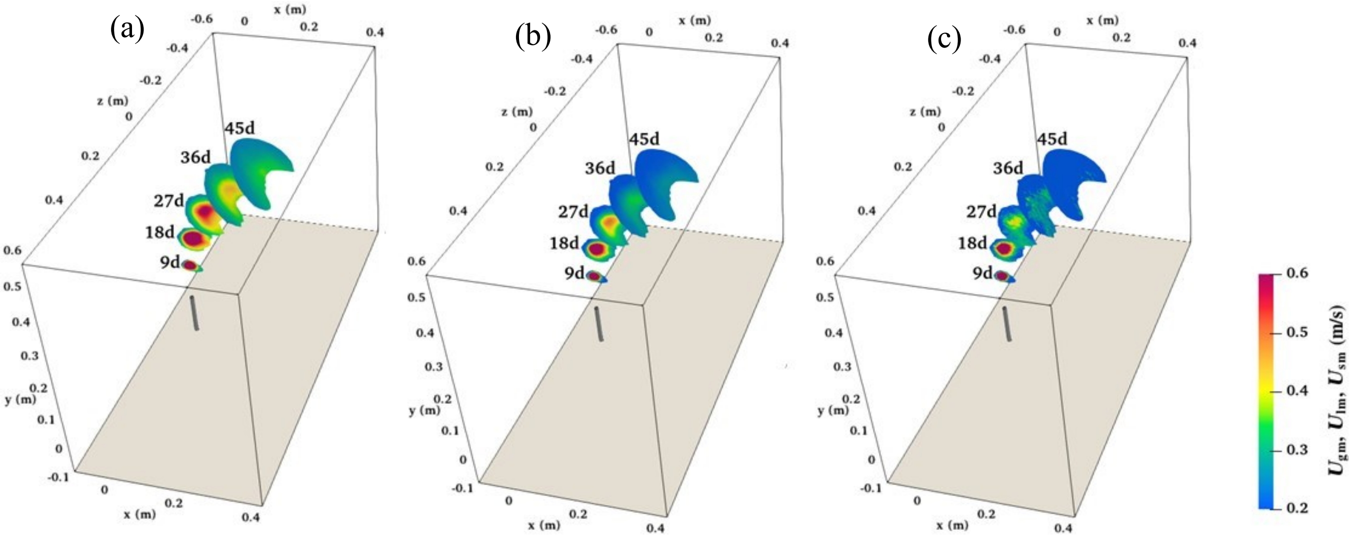

Figure 6-9. Mean velocity distributions at sections ξ = 9d - 45d in the bubbly region for the (a) gas-phase; (b) liquid-phase; and (c) sand-phase.

Figure 6-10(a) shows the distributions of instantaneous and mean horizontal velocities of the liquid-phase at the center-plane. As is observed, strong disturbance of the instantaneous horizontal velocity U_{lx} occurs, and both positive and negative U_{lx} exist in the jet region. This can be attributed to the strong turbulence induced by the jet, and the spreading of the liquid-phase to both the upstream and downstream sides of the jet under the high velocity ratio of jet to crossflow (i.e., 17.5). The mean horizontal velocity U_{lmx} reveals that the negative values occur mainly near the downstream side of nozzle wall and the near-field region of the jet due to wake effects. As the jet develops along its trajectory, the horizontal velocity increases and reach its maximum value of 0.3 m/s at around y/d = 17. It should be noted that U_{lmx} at the downstream side rapidly decreases from 0.22 to 0.1 m/s, mainly due to the CVP effect which tends to entrain the ambient flow to the jet.

For the vertical velocity in Figure 6-10(b), the positive U_{ly} generally decreases along the jet trajectory as expected. However, negative U_{ly} (maximum absolute value of 0.2 m/s) is observed in some regions upstream of the jet, which is caused by the shear-layer vortices (Daskiran et al., 2020). The negative values are not obvious in the mean distributions because the shear-layer vortices are highly unsteady and cannot be exhibited through the time-average. It is interesting that a slight separation starts to develop for the distribution of U_{lmy} at around $x/\mathrm{d} = 12$, and therefore a secondary flow in the upper region is formed that is mainly induced by the lift of bubbles.

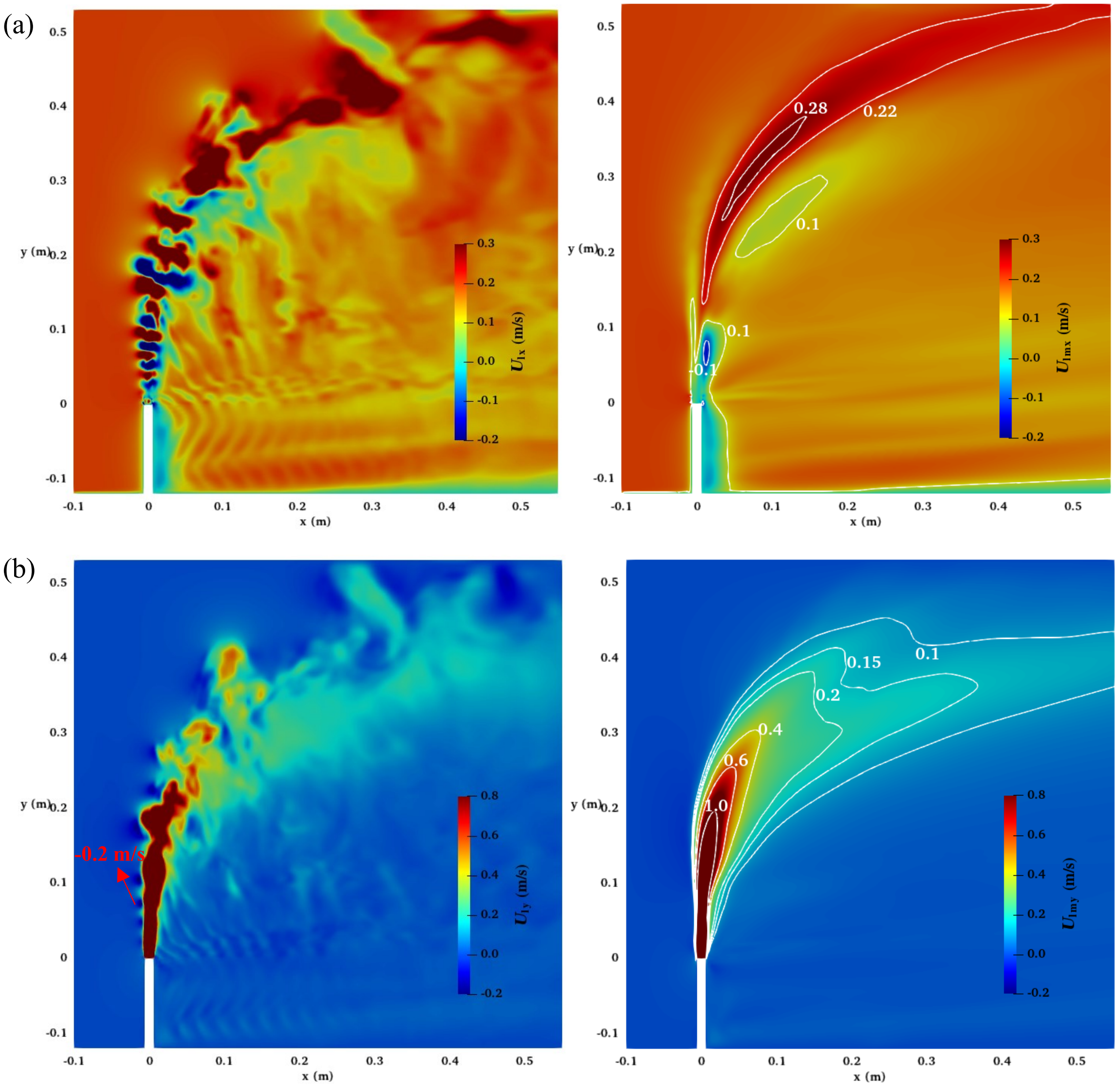

Figure 6-10. Instantaneous and mean velocity distributions of the liquid-phase at the center-plane: (a) horizontal velocity U_{lx} and U_{lmx}; and (b) vertical velocity U_{ly} and U_{lmy}

For the sand-phase, Figure 6-11 depicts the distributions of instantaneous particle velocity and mean velocity mapped to the Eulerian field at the center-plane. As shown in Figure 6-11(a), the total velocity generally decreases along the jet trajectory. Under the effects of crossflow and particle collisions, a number of sand particles start to escape from the jet region at an early stage ($y/\mathrm{d} \approx 2$). The random collisions between particles result in the formation of a wide falling region. It is interesting that a sharp decrease (down to < 0.12 m/s in the black dot region) of the mean velocity U_{sm} is observed under the downstream boundary of jet, and then U_{sm} smoothly increases as the particles falling to the bed. The sharp decrease may be attributed to the energy dissipation of particles through collisions, leading to the decrease of momentum and thus escape from the jet region with a lower velocity. The distribution of positive horizontal velocity is similar to the total velocity (Figure 6-11b). Negative values are present in the upstream side of the jet due to the shear-layer vortices and spreading of particles, especially in the near-field ($y/\mathrm{d} < 15$) where the initial jet momentum dominates. Similar to the horizontal velocity in the liquid-phase, U_{smx} decreases rapidly in the downstream side of the jet, which is probably due to the CVP effect.

The mean vertical velocity U_{smy} of sand-phase exhibits similar decreasing trend as the total velocity within the jet region (Figure 6-11c). Both the instantaneous and mean vertical velocities demonstrate that the particles escape from the jet region with a low rising velocity (<0.1 m/s), and they decrease rapidly to the negative value (e.g., the dot line with -0.01 m/s) in the sand spreading region. Subsequently, the negative velocity increases sharply to reach a relatively large value (e.g., the dash line with -0.1 m/s), and then fall to the bed with a relatively uniform settling velocity, probably due to the increased drag force exerted on particles. Furthermore, the transverse velocity shows a chaotic distribution due to the transverse spreading and turbulence effect, with both positive and negative values occurring randomly. Nevertheless, the strong perturbance mainly exist around the jet region, whereas sand particles tend to keep falling within the center-plane (e.g., $U_{\mathrm{smz}} \approx 0$) after reaching a relatively uniform settling velocity (e.g., $U_{\mathrm{smy}} = -0.1$ m/s).

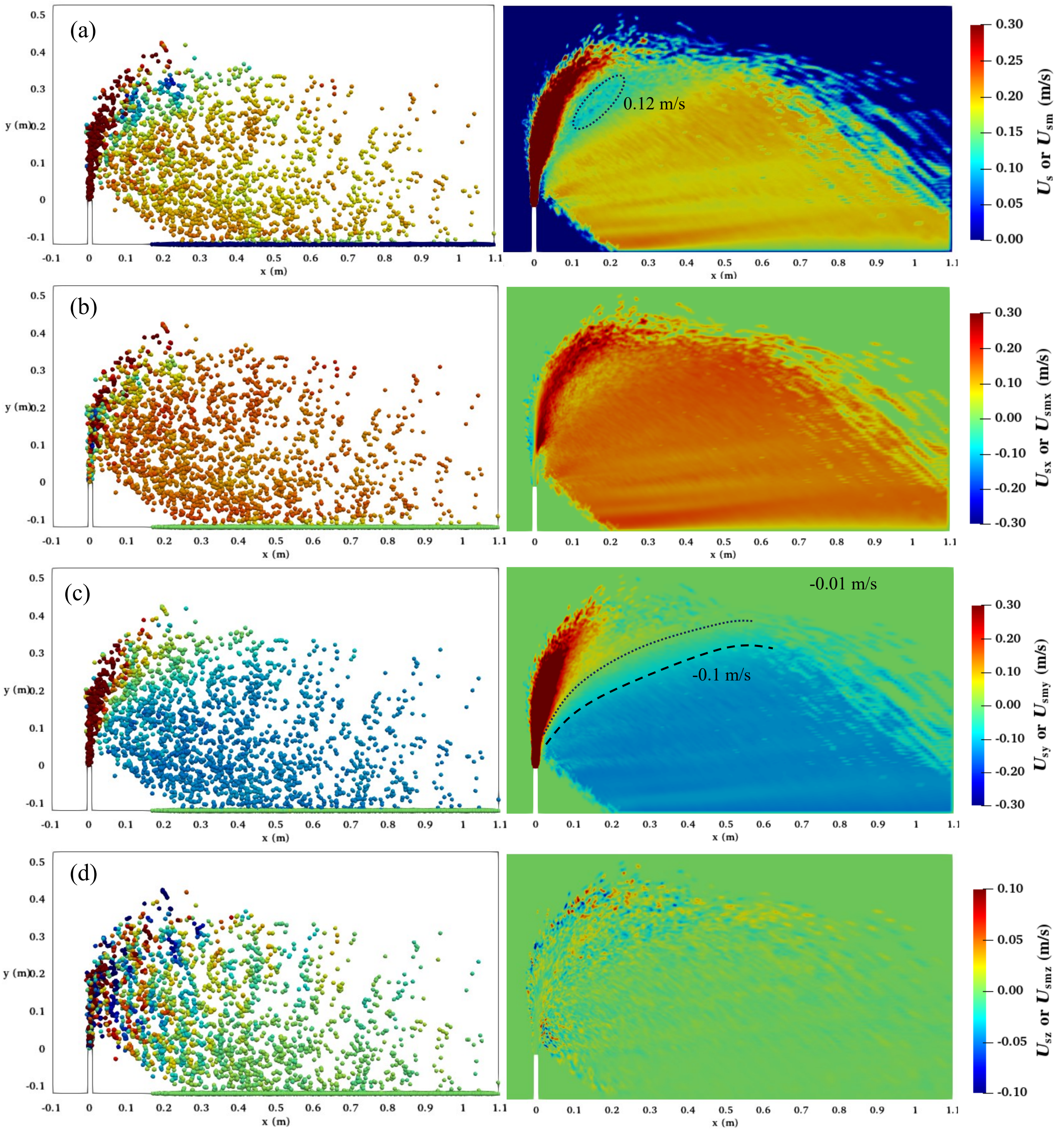

Figure 6-11. Instantaneous and mean velocity distributions of the sand-phase at the center-plane for the (a) total velocity; (b) horizontal velocity; (c) vertical velocity; and (d) transverse velocity.

6.4.4. Turbulent kinetic energy and vortical structures

The resolved turbulent kinetic energy k_{re} is a significant criterion in examining the adequacy and feasibility of fluid flow resolved by LES, which can be calculated as: $k_{re} = \frac{1}{2}\left(\overline{(u')^2} + \overline{(v')^2} + \overline{(w')^2}\right)$, where u', v' and w' are the fluctuating velocity components. In a well-resolved flow, the ratio of resolved turbulent kinetic energy to the total turbulent kinetic energy, $k' = k_{\mathrm{re}} / (k_{\mathrm{re}} + k_{\mathrm{sgs}})$, is suggested to be greater than 80% (Pope, 2000). Figure 6-12(a) shows the distribution of k' at the center-plane. It was observed that k' is well resolved with higher than 90% at most positions in the jet and sand spreading regions, except the region near the nozzle ($y/\mathrm{d} < 8$) where the more than 20% TKE is included in the SGS model.

Figure 6-12(b) shows the distribution of resolved TKE k_{re} at the center-plane, along with a streamline originated from the nozzle exit. k_{re} is around 0.08 $\mathrm{m^2/s^2}$ at the jet exit induced by the perturbance boundary condition. Past the jet exit, the peak k_{re} is observed at the leading and trailing edges of the jet and increases with the distance from the nozzle until $y/\mathrm{d} \approx 7$, where the leading and the trailing edges collapse into one single peak near the centerline and the k_{re} started to increase rapidly. This phenomenon of k_{re} is probably the reason of the pronounced jet expansion of liquid-phase at the same location (Figure 6-6), and similar results have also been observed in Esmaeili et al. (2015). Figure 6-12(c) shows the variations of TKE represented by the k_{re}, k_{sgs}, and k_{total} ($= k_{\mathrm{re}} + k_{\mathrm{sgs}}$) along the center streamline. It can be observed that k_{re} and k_{total} are much larger than k_{sgs} beyond the location of $l_{\mathrm{s}}/\mathrm{d} \approx 6$, where the k_{re} started to increase linearly (with a slope of 0.07) until it reaches the peak value at $l_{\mathrm{s}}/\mathrm{d} = 9$. The resolved TKE decreases rapidly from 0.08 $\mathrm{m^2/s^2}$ at the jet exit to 0.01 $\mathrm{m^2/s^2}$ at $l_{\mathrm{s}}/\mathrm{d} = 1.5$, and then increases smoothly until the k_{re} in leading and the trailing edges collapse. A similar variation of k_{re} has also been observed in a recent LES study on single-phase turbulent jets (Ren et al., 2023).

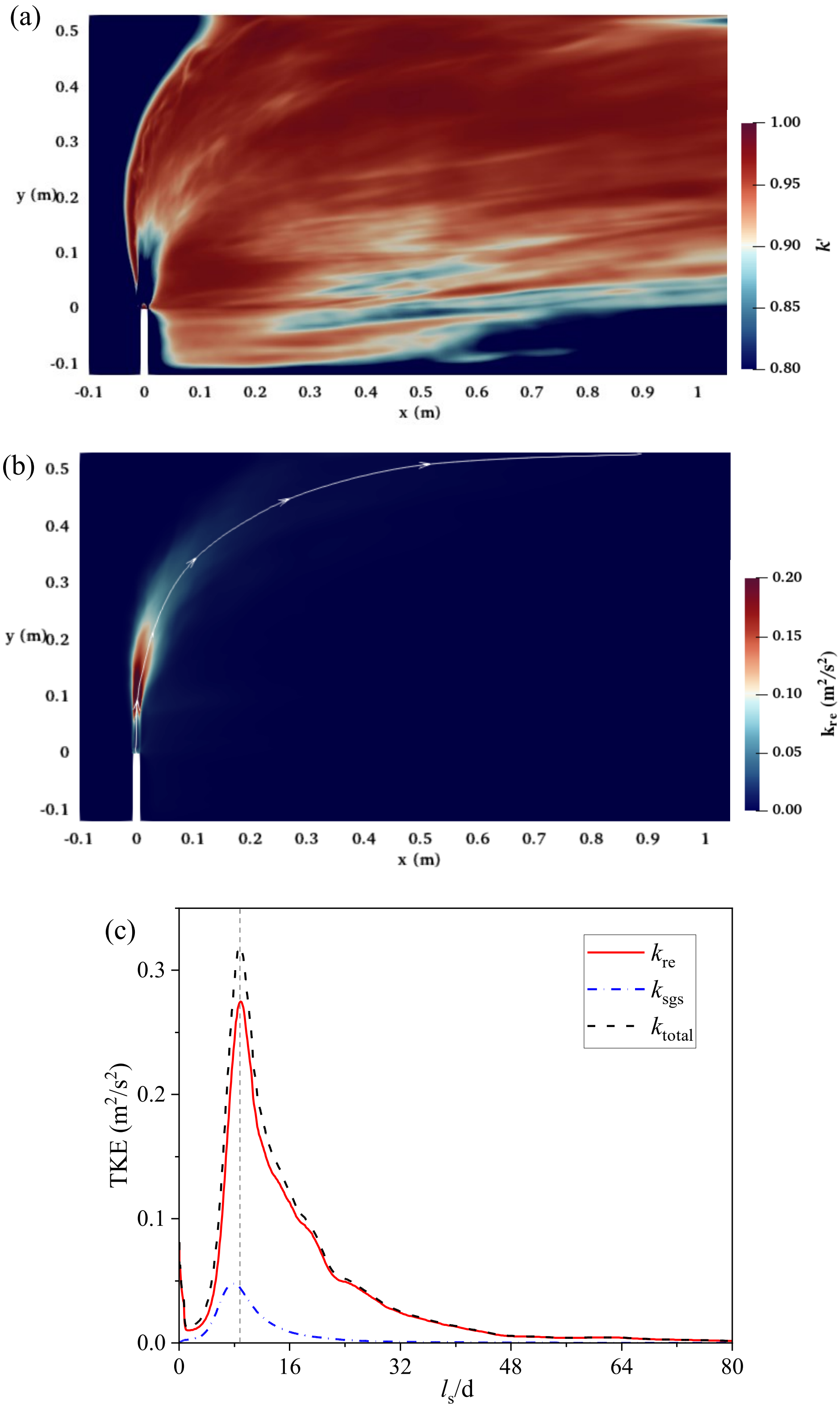

Figure 6-12. The distributions of (a) *k*’ at the center-plane; (b) resolved TKE at the center-plane and a streamline originated from the nozzle exit; and (c) resolved, modeled, and total TKE along the streamline (l_s is the length along the streamline).

Figure 6-13 shows the distributions of mean streamwise vorticity ω_x (calculated by $\frac{\partial U_z}{\partial y} - \frac{\partial U_y}{\partial z}$), along with the streamlines originated from a vertical line (z = 0.02 m) at the crossflow inlet. The two vortical structures denote the iso-surfaces of ω_x of 10 (red color) and -10 (blue color), which are approximately symmetric with respect to the center-plane. Additionally, two vertical half-planes at sections x = 0.1 m and 0.4 m are selected to illustrate the distribution of ω_x and the in-plane vectors. It is observed that the streamlines act as free-stream lines downstream of the crossflow inlet, until they encounter the vortical structures at y/d > 10, where they tend to rise with the jet and twist in the clockwise direction, resulting in the formation of CVP. However, the lower streamlines bypass the jet region and then slightly rise and twist due to the small values of ω_x, which can be observed in the vertical planes. These small ω_x are probably caused by the strong CVP formed by the high initial jet velocity. As the jet travels further downstream, ω_x in the lower region decreases (e.g., from 8 s^{-1} at x = 0.1 m to 3 s^{-1} at x = 0.4 m) due to the weakened CVP.

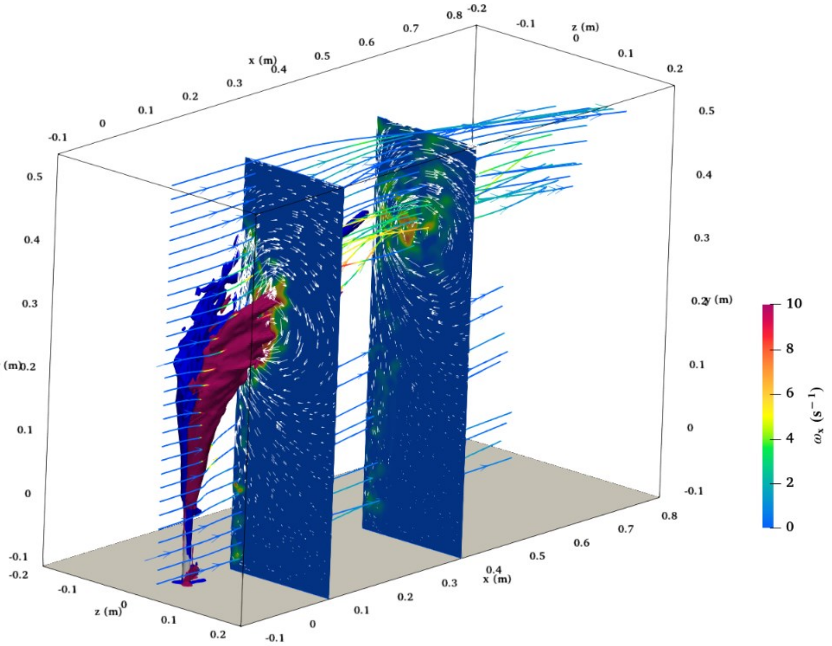

Figure 6-13. Distributions of mean streamwise vorticity ω_x at sections x = 0.1 m and 0.4 m, along with the streamlines originated from a vertical line (z = 0.02 m) at the crossflow inlet. The two vortical structures denote the iso-surfaces of ω_x of 10 (red color) and -10 (blue color).

The Q-criterion is further used to depict the vortical structures of the liquid-phase with the iso-surface of $Q = 50$ (Figure 6-14). In the near-field, Figure 6-14(a) shows that the shear layer vortices induced by Kelvin-Helmholtz instabilities start to occur after the injection, and can be clearly observed at the upstream side of the jet. The column-like wake vortices are generated below the jet region and are elongated to the region near the bottom wall. The positive ω_y (red color) indicates the wake vortices rotating in the counterclockwise direction, and the negative value (blue color) represents the clockwise rotation. The wake vortices decrease in the streamwise direction, accompanying with the weakened vorticity ω_y as shown in the plane. This can be attributed to the jet rise and the blending of the jet with the crossflow (Daskiran et al. 2020). As the jet penetrates further downstream, Figure 6-14(b) shows that the strength of vorticity ω decreases, and the distribution of $Q = 50$ iso-surface becomes wider and sparse, indicating that the impact of the jet weakens as it continues to mix with the ambient fluid.

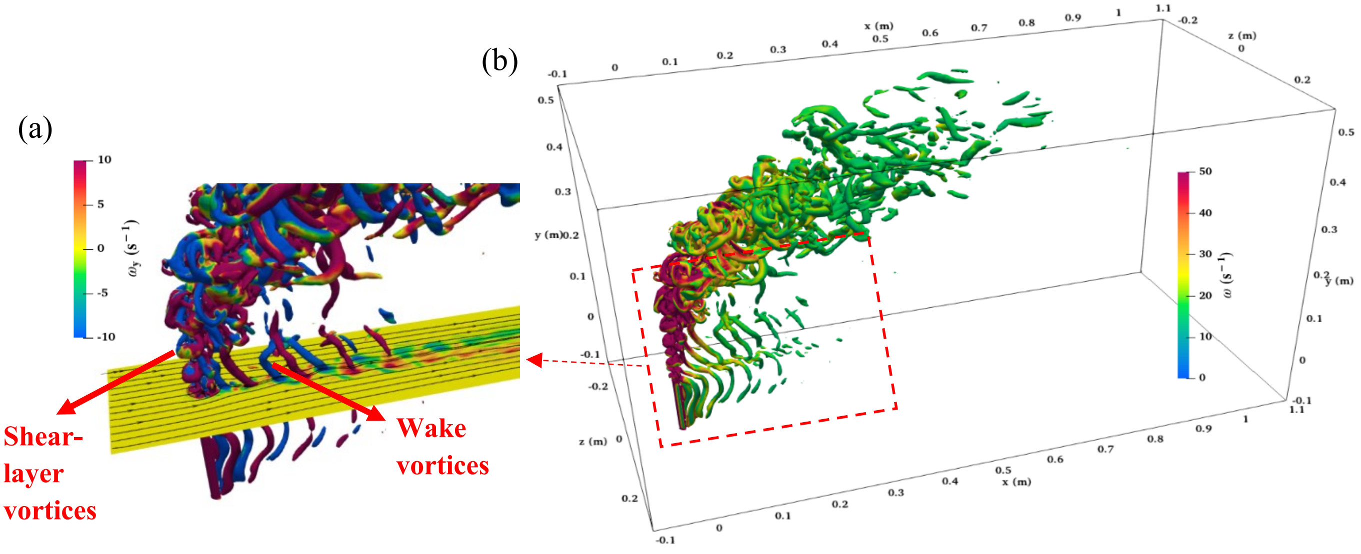

Figure 6-14. Vortical structures of the three-phase jet using the iso-surface of 50 of the Q-criterion colored by (a) vertical vorticity ω_y. The horizontal plane at section $y/d = 5$ along with surface streamlines; and (b) total vorticity ω.

6.5. Summary and conclusions

In this study, the flow field and particle movement are comprehensively investigated for the air-water-sand three-phase jets in crossflow, based on a LES coupling with an Eulerian-Eulerian-Lagrangian three-phase model. The results showed that the predicted concentration and velocity of both gas and sand agree well with the experimental data. The main conclusions from this paper are as follows:

(1) A pronounced jet expansion of the scalar concentration for the liquid-phase was observed at the location where the leading and the trailing edges of resolved turbulent kinetic energy collapse into one single peak.

(2) In the bubbly region, the overall velocity is the highest for the gas-phase and lowest for the sand-phase due to the buoyancy effects.

(3) Under wake effects, negative values of the mean horizontal velocity occur near the downstream side of nozzle wall and the near-field region of the jet. Due to the lift of bubbles, the mean vertical velocity reveals a secondary flow in the upper jet region.

(4) Sand particles escape from the jet region with a low rising velocity, and then turn downwards and accelerate rapidly to ultimately achieve a relatively uniform settling velocity as they descend to the bed.

(5) Typical vortical structures were observed for the three-phase jets in crossflow, including shear-layer vortices, wake vortices, and counter-rotating vortex pair. The strength of vorticity decreases as the jet penetrates further downstream.

7. General conclusions and recommendations

7.1. Conclusions

In this thesis, the characteristics of multi-phase jets in crossflow is studied on two major aspects: (a) the flow field and vortex structures of two-phase bubbly jets in crossflow through numerical simulation, as well as the effects of top boundary on bubble properties of bubbly jets in pipe crossflow through experiments; and (b) the distributions of bubble size, bubble and sand concentrations in air-water-sand three-phase jets in crossflow through experiments, as well as the phase properties and vortical structures by a developed three-phase numerical model.

The general conclusions are listed below:

1) For bubbly jets in free-surface crossflow, the vertical distribution of turbulent kinetic energy (TKE) evolves from mono-peak to dual-peaks as the jet penetrates farther for the bubbly jet due to the interactions between bubbles and ambient water flow. Counter-rotating vortex pairs can be clearly observed for both phases. Compared to pure water jets, bubbly jets are stretched wider in the vertical direction due to the lift of bubbles and thus dilution is larger. Interestingly, the vorticity at water jet cross-sections of bubbly jets evolves from two vertical "kidney-shapes" to two axisymmetric "thumb-up-shapes". Moreover, as the crossflow velocity increases, the locations of maximum concentration, maximum velocity magnitude, maximum vorticity magnitude, as well as water jet centerline, all tend to be lower for bubbly jets.
2) For bubbly jets in pipe crossflow, the horizontal distance from nozzle exit to where bubble centerline touches the top pipe wall can be expressed as a function of the Reynolds and

Weber numbers of the ambient pipe flow, and the Reynolds numbers of both the air and water phases of bubbly jets. The centerline gas void fraction and bubble size increase with distances after bubbles touch the top wall, mainly because bubbles are prone to gathering to the centerline to form larger bubbles. Afterwards, the (horizontal) bubble velocity decreases mainly due to the resistance force from the top wall. Good agreement has been achieved between horizontal bubble velocity and the 1/7th power law for water velocity in the pipe, and a correlation was proposed for predicting bubble rise velocity. Furthermore, the additional injection of water enhances the bubble fluctuations, and higher water jet and pipe flow rate promote the uniform distribution of bubble turbulence intensity.

3) Gas-liquid-solid three-phase flow has been accurately predicted utilizing a newly developed Eulerian-Eulerian-Lagrangian (E-E-L) solver within OpenFOAM, demonstrating excellent agreement between the predicted phase properties and experimental data. The introduction of PBM in the solver significantly improves the predictions of gas/solid phase velocities and holdups, especially at lower region of the bubble column where the bubble coalescence and breakup are significant. The instantaneous liquid and solid particle velocities generally follow the distribution of gas bubbles, but the magnitudes are significantly lower than bubble velocity. Moreover, the vorticity exhibits irregular shapes over the column, and different scales of vortex structure were observed.
4) For air-water-sand three-phase jets in crossflow, the initial gas and slurry (liquid-solid-mixture) flow rates play significant roles in influencing the Sauter mean diameter of bubbles in the studied scenarios. Sand particles that tend to separate from the bubbly region drive bubbles to spread further downstream, which leads to a broader distribution

of gas void fraction compared to two-phase bubbly jets in crossflow. In the bubbly region, sand concentration increases with higher initial sand concentration and slurry flow rates, but decreases with increasing gas flow rates. Additionally, the sand concentration at the same level as the nozzle exit typically follows a parabolic distribution in the streamwise direction, and the peak position shifts closer to the source with an increased gas flow rate or reduced slurry flow rate. Furthermore, dimensionless prediction equations are proposed for the gas void fraction and sand concentration, which agree well with the experimental data ($R^2 = 0.91 - 0.94$).

5) Coupled with large eddy simulation, the newly developed E-E-L three-phase solver has been successfully applied to study air-water-sand three-phase jets in crossflow. The results show that a pronounced jet expansion of the scalar concentration for the liquid-phase is observed at the location where the leading and the trailing edges of resolved turbulent kinetic energy collapse into one single peak. In the bubbly region, the overall velocity is the highest for the gas-phase and lowest for the sand-phase due to the buoyancy effects. Under the lift of bubbles, the mean vertical velocity reveals a secondary flow in the upper jet region. Sand particles escape from the jet region with a low rising velocity, and then turn downwards and accelerate rapidly to ultimately achieve a relatively uniform settling velocity as they descend to the bed. Typical vortical structures were observed for the three-phase jets in crossflow, including shear-layer vortices, wake vortices, and counter-rotating vortex pair.

This thesis will improve the knowledge in four primary aspects: (1) the detailed flow field and vortical structures in both two- and three-phase jets in crossflow; (2) bubble characteristics of bubbly jets in crossflow with the effect of top solid boundary; (3) the applicability and reliability of the E-E-L approach on modeling gas-liquid-solid three-phase flow; and (4) The mutual influence between air bubbles and sand particles on their concentrations in air-water-sand three-phase jets in crossflow. Furthermore, the developed solver couples the Eulerian-Eulerian-Lagrangian approach with the PBM, allowing for the simulation of various bubble sizes and individual particle movements in gas-liquid-solid three-phase flows. Based on the validation work in this thesis, the developed solver is considered to be at least 85% reliable in modeling three-phase bubble columns and air-water-sand three-phase jets in crossflow, with the solid phase treated as the Lagrangian phase.

This thesis complements the existing works on multi-phase jets in crossflow, and provides detailed measurement and modeling methods for the investigation of two-phase bubbly jets and air-water-sand three-phase jets in crossflow. The current results advance the practical applications such as artificial aeration, wastewater treatment, oil/gas transportation in pipelines, subsea blowouts, etc. For instance, in the event of a subsea blowout, the findings from air-water-sand three-phase jets can be utilized to estimate gas concentration along the gas-phase trajectory, using the terminal concentration as a reference. Appropriate precautions can be implemented considering the sand spreading region and corresponding concentrations. Additionally, the transport and fate of pollutants in the liquid phase can be estimated based on the results of scalar concentration evolution presented in this thesis.

7.2. Future research

Based on laboratory experiments and numerical simulations, this research covers the gas/liquid/solid phase behaviors in two- and three-phase jets in crossflow. However, there are still aspects left for further studies. General recommendations on further research are suggested: (a) to add oil to the jet and to study the pollutant transport and fate in both experiments and numerical simulations. Additionally, exploring the influence of ocean waves and stratification in crossflow is a valuable avenue for future research; (b) to consider modeling gas bubbles as Lagrangian particles, employing the E-L approach in bubbly jets or the E-L-L approach in three-phase jets in crossflow. Despite the high computational costs of the Lagrangian approach, the individual bubble movements are worth investigating, especially for the three-phase jets, where particle interactions (e.g., bubble-sand collisions) can be more directly studied.

Based on each study conducted in this thesis, the detailed recommendations on further studies are listed as follows:

1) To investigate the small-scale turbulent properties that need to be resolved for bubbly jets in crossflow, and to compare the near-field vortex structures with the pure water jets. To achieve this, different multi-phase models or approaches with smaller mesh grids are expected to be developed and compared.
2) To investigate the bubbly jet characteristics using different nozzle heights, and in particular, to explore the effects of pipe wall on bubble behaviors (e.g., bubble deformation and breakup near the nozzle, bubble trajectories, etc.) after the injection from the nozzle.
3) To include the particle effects on bubble breakage and coalescence in the developed E-E-L solver, and further evaluate its performance in higher particle loading systems. Additionally, the particle-bubble agglomeration is suggested to be investigated and implemented in the current solver for practical applications such as flotation process.
4) To investigate the velocity distributions and turbulence characteristics of both bubbles and sand in air-water-sand three-phase jets in crossflow, as well as the deposition behavior of sand particles.

5) To investigate and compare the phase properties under different flow conditions (e.g., Reynolds number and jet-to-crossflow velocity ratios) for the three-phase jets, as well as injecting higher concentrations of bubbles and sand. To achieve this, it is crucial to overcome the limitations of the experiment, such as the high initial water flow rate in this study. This is essential to provide benchmark data for the model validation.

Bibliography

Aiyer, A.K., Yang, D., Chamecki, M., Meneveau, C., 2019. A population balance model for large eddy simulation of polydisperse droplet evolution. J. Fluid Mech. 878, 700-739.

Al-Yahia, O.S., Yoon, H.J., Jo, D., 2020. Experimental study of bubble flow behavior during flow instability under uniform and non-uniform transverse heat distribution. Nucl. Eng. Technol. 52(12), 2771-2788.

Amin, M.R., Zhu, D.Z., Rajaratnam, N., 2023. Air-bubble entrainment by translating turbulent jets in stagnant water. Phys. Fluids 35(7).

An, M., Guan, X., Yang, N., 2020. Modeling the effects of solid particles in CFD-PBM simulation of slurry bubble columns. Chem. Eng. Sci. 223, 115743.

Andreopoulos, J., Rodi, W., 1984. Experimental investigation of jets in a crossflow. J. Fluid Mech. 138, 93-127.

Asaeda, T., Imberger, J., 1989. Structure of bubble plumes in linearly stratified environments. 249, 35–57.

Askari, E., Proulx, P., Passalacqua, A., 2018. Modelling of bubbly flow using CFD-PBM solver in openfoam: Study of local population balance models and extended quadrature method of moments applications. ChemEngineering 2 (1), 1-23.

Atta, A., Razzak, S.A., Nigam, K.D.P., Zhu, J.X., 2009. (Gas) - Liquid - Solid circulating fluidized bed reactors: Characteristics and applications. Ind. Eng. Chem. Res. 48 (17), 7876-7892.

Azimi, A.H., Zhu, D.Z., Rajaratnam, N., 2011. Effect of particle size on the characteristics of sand jets in water. J. Eng. Mech. 137(12), 822-834.

Azimi, A.H., Zhu, D.Z., Rajaratnam, N., 2012. Computational investigation of vertical slurry jets in water. Int. J. Multiph. Flow 47, 94-114.

Balzán, M.A., Sanders, R.S., Fleck, B.A., 2017. Bubble formation regimes during gas injection into a liquid cross flow in a conduit. Can. J. Chem. Eng. 95 (2), 372-385.

Behera, S., Saha, A.K., 2020. Evolution of the flow structures in an elevated jet in crossflow. Phys. Fluids 32(1), 015102.

Behzadi, A., Issa, R.I., Rusche, H., 2004. Modelling of dispersed bubble and droplet flow at high phase fractions. Chem. Eng. Sci. 59 (4), 759-770.

Behzadipour, A., Azimi, A.H., 2023. Hydrodynamic modifications in vertical bubble plumes by a grid-screen. Chem. Eng. Sci. 282, 119307.

Behzadipour, A., Azimi, A.H., Lima Neto, I.E., 2022. Effect of grid-screen on bubble characteristics of vertically discharged bubble plumes. Chem. Eng. Sci. 253, 117545.

Ben Meftah, M., Mossa, M., 2018. Turbulence measurement of vertical dense jets in crossflow. Water 10(3), 286.

Besagni, G., Brazzale, P., Fiocca, A., Inzoli, F., 2016. Estimation of bubble size distributions and shapes in two-phase bubble column using image analysis and optical probes. Flow Meas. Instrum. 52, 190-207.

Bhole, M.R., Joshi, J.B., Ramkrishna, D., 2008. CFD simulation of bubble columns incorporating population balance modeling. Chem. Eng. Sci. 63(8), 2267-2282.

Bhuiyan, F., Rajaratnam, N., Zhu, D.Z., 2010. An experimental study of mounds formed by dumping coarse sediment in channel flow. J. Hydraul. Res. 48(3), 283-291.

Bhusare, V.H., Dhiman, M.K., Kalaga, D.V., Roy, S., Joshi, J.B., 2017. CFD simulations of a bubble column with and without internals by using OpenFOAM. Chem. Eng. J. 317, 157-174.

Bogoyavlensky, V., Nikonov, R., Erokhin, G., Bryskin, V., 2020. Passive seismic monitoring study of the Earth degassing in the Arctic. Geomodel 2020, 2020(1), 1-5.

Bordoloi, A.D., Lai, C.C., Clark, L., Carrillo, G.V., Variano, E., 2020. Turbulence statistics in a negatively buoyant multiphase plume. J. Fluid Mech. 896, A19.

Bouillard, J., Alban, B., Jacques, P., Xuereb, C., 2001. Liquid flow velocity measurements in stirred tanks by ultra-sound Doppler velocimetry. Chem. Eng. Sci. 56(3), 747-754.

Brevis, W., Niño, Y., Jirka, G.H., 2011. Integrating cross-correlation and relaxation algorithms for particle tracking velocimetry. Exp. Fluids 50, 135-147.

Brooks, J.M., Bernard, B.B., Sauer Jr, T.C., Abdel-Reheim, H., 1978. Environmental aspects of a well blowout in the Gulf of Mexico. Environ. Sci. Technol. 12(6), 695-703.

Bung, D.B., Valero, D., 2015, June. Image processing for bubble image velocimetry in self-aerated flows. In 36th IAHR World Congress (Vol. 28).

Buwa, V.V., Ranade, V.V., 2002. Dynamics of gas-liquid flow in a rectangular bubble column: experiments and single/multi-group CFD simulations. Chem. Eng. Sci. 57, 4715-4736.

Cerqueira, R.F.L., Paladino, E.E., 2021. Development of a deep learning-based image processing technique for bubble pattern recognition and shape reconstruction in dense bubbly flows. Chem. Eng. Sci. 230, 116163.

Chanson, H., 2002. Air-Water Flow Measurements with Intrusive, Phase-Detection Probes: Can We Improve Their Interpretation? J. Hydraul. Eng. 128(3), 252–255.

Chen, F., Yapa, P.D., 2003. A model for simulating deep water oil and gas blowouts-Part II: Comparison of numerical simulations with “Deepspill” field experiments. J. Hydraul. Res. 41 (4), 353-365.

Chen, F., Yapa, P.D., 2004. Modeling gas separation from a bent deepwater oil and gas jet/plume. J. Marine Syst. 45, 189-203.

Chen H., Li Y., Xiong Y., Wei H., Saxén H., Yu Y., 2022d. Effect of particle holdup on bubble formation in suspension medium by VOF–DPM simulation. Granul. Matter 24 (4) 120.

Chen, J., Yao, Z., Jiang, C.B., Wu, Z.Y., Deng, B., Long, Y.N., Bian, C., 2022b. Experiment study of the evolution of coral sand particle clouds in water. China Ocean Eng. 36(5), 720-733.

Chen, Q.Y., He, Y.P., Xiong, T., Li, M.Z. Liu, W.H., 2022c. Study on the dynamic characteristics of the overflow advection and diffusion of trailing suction hopper dredgers based on CFD. Ocean Eng. 252, 111263.

Chen, S., Zhang, Y., Wang, X., Teng, K., Gong, Y., Qu, Y., 2022a. Numerical simulation and experiment of the gas-liquid two-phase flow in the pigging process based on bypass state. Ocean Eng. 252, 111184.

Chen, W., Xu, H.L., Kong, W.Y., Yang, F.Q., 2020. Study on three-phase flow characteristics of natural gas hydrate pipeline transmission. Ocean Eng. 214, 107727.

Chen, Y., Otoo, E., Chen, Y., Xu, Z., Li, X., Zhou, Y., 2023. Deposition behaviour of inclined momentum sediment-laden jet. Ocean Eng. 278, 114399.

Cheng, L., Gu, H., Zhang, J., Zhu, F., Yu, X., Meng, Z., 2023. An experimental study on interfacial parameters in a narrow rectangular channel under different flow regimes. Prog. Nucl. Energy 159, 104644.

Cintolesi, C., Petronio, A., Armenio, V., 2019. Turbulent structures of buoyant jet in cross-flow studied through large-eddy simulation. Environ. Fluid Mech. 19 (2), 401-433.

Clift, R., Grace, J.R., Weber, M.E., 1978. Bubbles, Drops and Particles. Academic Press, New York, USA.

Coletti, F., Benson, M.J., Ling, J., Elkins, C. J., Eaton, J.K., 2013. Turbulent trans- port in an inclined jet in crossflow. Int. J. Heat Fluid Flow 43, 149–160.

Crabb, D., Durao, D.F.G., Whitelaw, J.H., 1981. A round jet normal to a crossflow. Trans. ASME I: J. Fluids Eng. 103, 142-153.

Cui, P., Zhang, A.M., Wang, S., Khoo, B.C., 2018. Ice breaking by a collapsing bubble. J. Fluid Mech. 841, 287-309.

Cundall, P.A., Strack, O.D., 1980. A discrete numerical model for granular assemblies. Geotechnique 30 (3), 331-336.

Da Silva, M.J., Thiele, S., Abdulkareem, L., Azzopardi, B.J., Hampel, U., 2010. High-resolution gas-oil two-phase flow visualization with a capacitance wire-mesh sensor. Flow Meas. Instrum. 21(3), 191–197.

Dahikar, S.K., Joshi, J.B., Shah, M.S., Kalsi, A.S., RamaPrasad, C.S., Shukla, D.S., 2010. Experimental and computational fluid dynamic study of reacting gas jet in liquid: Flow pattern and heat transfer. Chem. Eng. Sci. 65(2), 827-849.

Darabi, H., Koleini, S.J., Deglon, D., Rezai, B., Abdollahy, M., 2019. Investigation of bubble- particle interactions in a mechanical flotation cell, part 1: collision frequencies and efficiencies. Miner. Eng. 134 54–64.

Daskiran, C., Cui, F., Boufadel, M.C., Socolofsky, S.A., Katz, J., Zhao, L., Ozgokmen, T., Robinson, B., King, T., 2021. Transport of oil droplets from a jet in crossflow: Dispersion coefficients and Vortex trapping. Ocean Model. 158, 101736.

Daskiran, C., Cui, F., Boufadel, M.C., Zhao, L., Socolofsky, S.A., Ozgokmen, T., Robinson, B., King, T., 2020. Hydrodynamics and dilution of an oil jet in crossflow: The role of small-scale motions from laboratory experiment and large eddy simulations. Int. J. Heat Fluid Flow 85, 108634.

Daskiran, C., Liu, R., Lee, K., Katz, J., Boufadel, M.C., 2022. Estimation of overall droplet size distribution from a local droplet size distribution for a jet in crossflow: Experiment and multiphase large eddy simulations. Int. J. Multiph. Flow 156, 104205.

De Oliveira, W.R., De Paula, I.B., Martins, F.J.W.A., Farias, P.S.C., Azevedo, L.F.A., 2015. Bubble characterization in horizontal air-water intermittent flow. Int. J. Multiph. Flow 69, 18-30.

Decrop, B., De Mulder, T., Toorman, E., Sas, M., 2015. Large-eddy simulations of turbidity plumes in crossflow. Eur. J. Mech. B/Fluids 53, 68-84.

Deendarlianto, Rahmandhika, A., Widyatama, A., Dinaryanto, O., Widyaparaga, A., Indarto, 2019. Experimental study on the hydrodynamic behavior of gas-liquid air-water two-phase flow near the transition to slug flow in horizontal pipes. Int. J. Heat Mass Transf. 130, 187–203.

Deshpande, S.S., Anumolu, L., Trujillo, M. F, 2012. Evaluating the performance of the two-phase flow solver interFoam. Comput. Sci. Discovery 5(1), 014016.

Dhar, L., Anne, F., Recchia, G., Etienne, S., Béguin, C., Scott, D., Bornard, L., 2021. Bubble characteristics from injected air sheet through slots in a water cross-flow. Int. J. Multiph. Flow 142, 103693.

Dhotre, M.T., Niceno, B., Smith, B.L., 2008. Large eddy simulation of a bubble column using dynamic sub-grid scale model. Chem. Eng. J. 136, 337-348.

Diaz, M.E., Iranzo, A., Cuadra, D., Barbero, R., Montes, F.J., Galán, M.A., 2008. Numerical simulation of the gas–liquid flow in a laboratory scale bubble column: influence of bubble size distribution and non-drag forces. Chem. Eng. J. 139 (2), 363-379.

Dissanayake, A.L., Gros, J., Socolofsky, S.A., 2018. Integral models for bubble, droplet, and multiphase plume dynamics in stratification and crossflow. Environ. Fluid Mech. 18 (5), 1167-1202.

do Amaral, C.E.F., Alves, R.F., Da Silva, M.J., Arruda, L.V.R., Dorini, L., Morales, R.E.M., Pipa, D.R., 2013. Image processing techniques for high-speed videometry in horizontal two-phase slug flows. Flow Meas. Instrum. 33, 257–264.

Dodds, D., Sarhan, A.A.R., Naser, J., 2022. CFD investigation into the effects of surrounding particle location on the drag coefficient. Fluids 7 (10) 331.

Dong, C., Lu, L., Wang, X., 2019a. Experimental investigation on non-boiling heat transfer of two-component air-oil and air-water slug flow in horizontal pipes. Int. J. Multiph. Flow 119, 28–41.

Dong, P., Lu, B., Gong, S., Cheng, D., 2020. Experimental study of submerged gas jets in liquid cross flow. Exp. Therm. Fluid Sci. 112, 109998.

Dong, P., Wang, K., Cheng, D., Lu, B., 2021. Submerged gas jet in liquid cross flow: Modeling and flow structures analysis. Ocean Eng. 242, 110128.

Dong, T., Liu, M., Li, X., Zahid, S., 2019b. Catalytic oxidation of crotonaldehyde to crotonic acid in a gas-liquid-solid mini-fluidized bed. Powder Technol. 352, 32-41.

Drew, D.A., Lahey, R.T., 1987. The virtual mass and lift force on a sphere in a rotating and straining flow. Int. J. Multiph. Flow 13, 113-121.

Du, Z.B., Huang, W., Yan, L., Li, L.Q., Chen, Z., Li, S.B., 2019. RANS study of steady and pulsed gaseous jets into a supersonic crossflow. Int. J. Heat Mass Tran. 136, 157-169.

Esmaeili, M., Afshari, A., Jaberi, F.A., 2015. Turbulent mixing in non-isothermal jet in crossflow. Int. J. Heat Mass Tran. 89, 1239-1257.

Estrada Perez, C.E., 2014. Multi-Scale Experiments in Turbulent Subcooled Boiling Flow Through a Square Channel with a Single Heated Wall (Doctoral dissertation).

Fard, M.G., Vernet, A., Stiriba, Y., Grau, X., 2020. Transient large-scale two-phase flow structures in a 3D bubble column reactor. Int. J. Multiphase Flow 127, 103236.

Gan, Z.W., 2013. Holdup and velocity profiles of monosized spherical solids in a three-phase bubble column. Chem. Eng. Sci. 94, 291-301.

Gao, Y., Gao, X., Hong, D., Cheng, Y., Wang, L., Li, X., 2019. Experimental investigation on multiscale hydrodynamics in a novel gas–Liquid–Solid three phase jet-Loop reactor. AIChE J. 65 (5), e16537.

Gao, Y., Xu, Y., Song, K., Li, Q., Yao, H., Chen, H., Wang, W., Li, Y., 2023. A new calculation method and model of hydrate slurry flow of the multiphase pipeline in deep water gas field. JPSE. 3 (1) 100104.

Ge, J., Ji, S., Tan, D., 2018. A gas-liquid-solid three-phase abrasive flow processing method based on bubble collapsing. Int. J. Adv. Manuf. Technol. 95 (1-4), 1069-1085.

Ghaffarkhah, A., Shahrabi, M.A., Moraveji, M.K., 2018. 3D computational-fluid-dynamics modeling of horizontal three-phase separators: An approach for estimating the optimal dimensions. SPE Prod. Oper. 33 (4), 879-895.

Götz, M., Lefebvre, J., Mörs, F., Reimert, R., Graf, F., Kolb, T., 2016. Hydrodynamics of organic and ionic liquids in a slurry bubble column reactor operated at elevated temperatures. Chem. Eng. J. 286, 348-360.

Große, S., Schröder, W., 2008. Dynamic wall-shear stress measurements in turbulent pipe flow using the micro-pillar sensor MPS3. Int. J. Heat Fluid Flow 29(3), 830-840.

Gruber, M.C., Radl, S., Khinast, J.G., 2016. Effect of bubble-particle interaction models on flow predictions in three-phase bubble columns. Chem. Eng. Sci. 146, 226-243.

Gui, M., Liu, Z., Liao, B., Wang, T., Wang, Y., Sui, Z., Bi, Q., Wang, J., 2019. Void fraction measurements of steam-water two-phase flow in vertical rod bundle: Comparison among different techniques. Exp. Therm. Fluid Sci. 109, 109881.

Gvozdić, B., Dung, O.Y., Alméras, E., van Gils, D.P.M., Lohse, D., Huisman, S.G., Sun, C., 2019. Experimental investigation of heat transport in inhomogeneous bubbly flow. Chem. Eng. Sci. 198, 260–267.

Haider, A., Levenspiel, O., 1989. Drag coefficient and terminal velocity of spherical and nonspherical particles. Powder Technol. 58, 63-70.

Hall, N., Elenany, M., Zhu, D.Z., Rajaratnam, N., 2010. Experimental study of sand and slurry jets in water. J. Hydraul. Eng. 136(10), 727-738.

Hansen, L.S., Pedersen, S., Durdevic, P., 2019. Multi-phase flow metering in offshore oil and gas transportation pipelines: Trends and perspectives. Sensors 19(9), 2184.

Hassanzadeh, A., Firouzi, M., Albijanic, B., Celik, M.S., 2018. A review on determination of particle–bubble encounter using analytical, experimental and numerical methods. Miner. Eng. 122 296–311.

Hodgson, J.E., Rajaratnam, N., 1992. An experimental study of jet dilution in crossflows. Can. J. Civ. Eng. 19 (5), 733-743.

Hu, X., Ilgun, A.D., Passalacqua, A., Fox, R.O., Bertola, F., Milosevic, M., Visscher, F., 2021. CFD simulations of stirred-tank reactors for gas-liquid and gas-liquid-solid systems using OpenFOAM®. Int. J. Chem. React. Eng. 19 (2), 193-207.

Huai, W.X., Xue, W.Y., Qian, Z.D., 2013. Numerical simulation of slurry jets using mixture model. Water Sci. Eng. 6(1), 78-90.

Huang, J., Sun, L., Du, M., Liang, Z., Mo, Z., Tang, J., Xie, G., 2020. An investigation on the performance of a micro-scale Venturi bubble generator. Chem. Eng. J. 386, 120980.

Hui, P., Yuan-Xing, L., Zheng-Hong, L., 2019. Computational fluid dynamics simulation of gas–liquid–solid polyethylene fluidized bed reactors incorporating with a dynamic polymerization kinetic model. Asia-Pacific J. Chem. Eng. 14 (1), 1-20.

Hussain, N.A. and Narang, B.S., 1984. Simplified Analysis of Air-Bubble Plumes in Moderately Stratified Environments. 26, 543–551.

Ishii, M., Zuber, N., 1979. Drag coefficient and relative velocity in bubbly, droplet or particulate flows. AIChE J. 25 (5), 843-855.

Issa, R.I., 1986. Solution of the implicitly discretised fluid flow equations by opera- tor-splitting. J. Comput. Phys. 62(1), 40–65.

Jakobsen, H.A., Sannes, B.H., Grevskott, S., Svendsen, H.F., 1997. Modeling of vertical bubble-driven flows. Ind. Eng. Chem. Res. 36 (10), 4052-4074.

James, C.B., Mingotti, N., Woods, A.W., 2022. On particle separation from turbulent particle plumes in a cross-flow. J. Fluid Mech. 932, A45.

Jasak, H., 2009. OpenFOAM: Open source CFD in research and industry. Int. J. Nav. Archit. Ocean Eng. 1 (2), 89-94.

Jeldres, R.I., Fawell, P.D., Florio, B.J., 2018. Population balance modelling to describe the particle aggregation process: a review. Powder Technol. 326 190–207.

Jernelöv, A., 2010. How to defend against future oil spills. Nature 466(7303), 182-183.

Ji, L., Chu, K., Kuang, S., Chen, J., Yu, A., 2018. Modeling the multiphase flow in hydrocyclones using the coarse-grained volume of fluid - discrete element method and mixture-discrete element method approaches. Ind. Eng. Chem. Res. 57 (29), 9641-9655.

Jin, H., Han, Y., Yang, S., He, G., 2010. Electrical resistance tomography coupled with differential pressure measurement to determine phase hold-ups in gas–liquid–solid outer loop bubble column. Flow Meas. Instrum. 21(3), 228-232.

Jobehdar, M.H., Siddiqui, K., Gadallah, A.H., Chishty, W.A., 2016. Bubble formation process from a novel nozzle design in liquid cross-flow. Int. J. Heat Fluid Flow 61, 599–609.

Joshi, J.B., Vitankar, V.S., Kulkarni, A.A., Dhotre, M.T., Ekambara, K., 2002. Coherent flow structures in bubble column reactors. Chem. Eng. Sci. 57 (16), 3157-3183.

Kamotani, Y., Greber, I., 1972. Experiments on a turbulent jet in a cross flow. AIAA J. 10(11), 1425-1429.

Kan, X.Y., Zhang, A.M., Yan, J.L., Wu, W.B., Liu, Y.L., 2020. Numerical investigation of ice breaking by a high-pressure bubble based on a coupled BEM-PD model. J. Fluid Struct. 96, 103016.

Kang, C., Zhang, W., Ji, Y.G., Cui, Y., 2019. Geometry and motion characteristics of bubbles released in liquid cross flow. J. Appl. Fluid Mech. 12(3), 667-677.

Kang, Y., Kim, M.K., Yang, S.W., Kim, S.D., 2018. Characteristics of three-phase (gas–liquid–solid) circulating fluidized beds. J. Chem. Eng. Japan 51(9), 740-761.

Kannan, V., Naren, P.R., Buwa, V.V., Dutta, A., 2019. Effect of drag correlation and bubble - induced turbulence closure on the gas hold-up in a bubble column reactor. J. Chem. Technol. Biot. 94 (9), 2944-2954.

Karagozian, A.R., 2014. The jet in crossflow. Phys. Fluids 26(10), 1–47.

Keane, R.D. and Adrian, R.J., 1990. Optimization of particle image velocimeters. I. Double pulsed systems. Meas. Sci. Technol. 1(11), 1202.

Khalil, A., Rosso, D., DeGroot, C.T., 2021. Effects of flow velocity and bubble size distribution on oxygen mass transfer in bubble column reactors—A critical evaluation of the computational fluid dynamics-population balance model. Water Environ. Res. 93 (10), 2274-2297.

Kiambi, S.L., Duquenne, A.M., Dupont, J.B., Colin, C., Risso, F., Delmas, H., 2003. Measurements of bubble characteristics: comparison between double optical probe and imaging. Can. J. Chem. Eng. 81(3-4), 764-770.

Kim, D., Schanz, D., Novara, M., Seo, H., Kim, Y., Schröder, A., Kim, K.C., 2022. Experimental study of turbulent bubbly jet. Part 1. Simultaneous measurement of three-dimensional velocity fields of bubbles and water. J. Fluid Mech. 941, A42.

Kodak, 1972. Optical formulas and their application, Kodak Publication No. AA-26, Rev. 11-72-BX. Rochester, New York.

Koh, P.T.L., Schwarz, M.P., 2006. CFD modelling of bubble–particle attachments in flotation cells. Miner. Eng. 19 (6–8) 619–626.

Kong, W., Yang, J., Niu, X., Wen, L., Li, H., Ma, Y., Chen, S., 2023. Experimental study of flow kinematics and impacting pressures on a suspended horizontal plate by extreme waves. Water 15(15), 2771.

Kostoglou, M., Karapantsios, T.D., Evgenidis, S., 2020. On a generalized framework for turbulent collision frequency models in flotation: the road from past inconsistencies to a concise algebraic expression for fine particles. Adv. Colloid Interf. Sci. 284 102270.

Kulkarni, A.A., Joshi, J.B., Kumar, V.R., Kulkarni, B.D., 2001. Application of multiresolution analysis for simultaneous measurement of gas and liquid velocities and fractional gas hold-up in bubble column using LDA. Chem. Eng. Sci. 56(17), 5037–5048.

Kumar, S., Ramkrishna, D., 1996. On the solution of population balance by discretization I. A fixed pivot technique. Chem. Eng. Sci. 51 (8), 1311-1332.

Kwon, S.J., Seo, I.W., 2005. Reynolds number effects on the behavior of a non-buoyant round jet. Exp. Fluids 38(6), 801-812.

Laakkonen, M., Alopaeus, V., Aittamaa, J., 2006. Validation of bubble breakage, coalescence and mass transfer models for gas-liquid dispersion in agitated vessel. Chem. Eng. Sci. 61 (1), 218-228.

Lain, S., Ernst, M., Sommerfeld, M., 2020. Study of colliding particle-pair velocity correlation in homogeneous isotropic turbulence. Appl. Sci. 10(24), 9095.

Laupsien, D., Le Men, C., Cockx, A., Liné, A., 2022. Effects of liquid viscosity and bubble size distribution on bubble plume hydrodynamics. Chem. Eng. Res. Des. 180, 451-469.

Le Corre, J.M., Bergmann, U.C., Hallehn, A., Tejne, H., Waldemarsson, F., Morenius, B., Baghai, R., 2018. Measurements of local two-phase flow parameters in fuel bundle under BWR operating conditions. Nucl. Eng. Des. 336, 15-23.

Le Moullec, Y., Potier, O., Gentric, C., Leclerc, J.P., 2008. Flow field and residence time distribution simulation of a cross-flow gas-liquid wastewater treatment reactor using CFD. Chem. Eng. Sci. 63 (9), 2436-2449.

Leandro, J., Bung, D.B., Carvalho, R., 2014. Measuring void fraction and velocity fields of a stepped spillway for skimming flow using non-intrusive methods. Exp. Fluids 55, 1-17.

Lee, J.H.W., Chu, V.H., 2003. Turbulent Jets and Plumes – A Lagrangian Approach. Kluwer Academic Publisher, Norwell, Massachusetts, USA.

Lehr, F., Millies, M., Mewes, D., 2002. Bubble-size distributions and flow fields in bubble columns. AIChE J. 48 (11), 2426-2443.

Li, L., Li, B., 2018. Implementation and validation of a volume-of-fluid and discrete-element-method combined solver in OpenFOAM. Particuology 39 109–115.

Li, L., Liu, Z., Li, B., Matsuura, H., Tsukihashi, F., 2015. Water model and CFD-PBM coupled model of gas-liquid-slag three-phase flow in ladle metallurgy. ISIJ Int. 55 (7), 1337-1346.

Li, T., Wang, Y., Wei, Z., Wang, L., Zeng, J., Yu, G., 2022a. Radial distribution of solid holdup and its fluctuation characteristics in a three-phase scrubbing-cooling chamber. Chem. Eng. Sci. 248, 117130.

Li, X., Hao, Y., Zhao, P., Fan, M., Song, S., 2022b. Simulation study on the phase holdup characteristics of the gas–liquid-solid mini-fluidized beds with bubbling flow. Chem. Eng. J. 427, 131488.

Li, X., Ma, X., Zhang, L., Zhang, H., 2016. Dynamic characteristics of ventilated bubble moving in micro scale venturi. Chem. Eng. Process. 100, 79-86.

Li, Y., Cao, R., Chen, H., Mu, L., Lv, X., 2022c. Impact of oil− sediment interaction on transport of underwater spilled oil in the Bohai Sea. Ocean Eng. 247, 110687.

Liang, X.F., Pan, H., Su, Y.H., Luo, Z.H., 2016. CFD-PBM approach with modified drag model for the gas–liquid flow in a bubble column. Chem. Eng. Res. Des. 112, 88-102.

Lim, H.J., Chang, K.A., Huang, Z.C., Na, B., 2015. Experimental study on plunging breaking waves in deep water. J. Geophys. Res. Oceans 120(3), 2007-2049.

Lima Neto, I.E., Zhu, D.Z., Rajaratnam, N., 2008a. Bubbly jets in stagnant water. Int. J. Multiph. Flow 34(12), 1130-1141.

Lima Neto, I.E., Zhu, D.Z., Rajaratnam, N., 2008b. Effect of Tank Size and Geometry on the Flow Induced by Circular Bubble Plumes and Water Jets. J. Hydraul. Eng. 134(6), 833–842.

Lima Neto, I.E., Zhu, D.Z., Rajaratnam, N., 2008c. Air injection in water with different nozzles. J. Environ. Eng. 134(4), 283-294.

Lima Neto, I.E., Zhu, D.Z., Rajaratnam, N., Yu, T., Spafford, M., McEachern, P., 2007. Dissolved oxygen downstream of an effluent outfall in an ice-covered river: Natural and artificial aeration. J. Environ. Eng. 133(11), 1051–1060.

Liu, L., Keplinger, O., Ziegenhein, T., Shevchenko, N., Eckert, S., Yan, H., Lucas, D., 2019b. Euler–Euler modeling and X-ray measurement of oscillating bubble chain in liquid metals. Int. J. Multiphase Flow 110, 218-237.

Liu, L., Shi, B., Song, S., Chen, Y., Luo, X., Zhang, S., Huang, H., Yao, H., Chen, G., Gong, J., 2023. Co-deposition characteristics of hydrates and sands in gas-salty water-sands flow system. Fuel 346, 128276.

Liu, M., Wang, T., Yu, W., Wang, J., 2007. An electrical conductivity probe method for measuring the local solid holdup in a slurry system. Chem. Eng. J. 132(1-3), 37-46.

Liu, Q., Luo, Z.H., 2018. CFD-VOF-DPM simulations of bubble rising and coalescence in low hold-up particle-liquid suspension systems. Powder Technol. 339, 459-469.

Liu, Y.X., Zhu, L.T., Luo, Z.H., Tang, J.X., 2019a. Effect of spatial radiation distribution on photocatalytic oxidation of methylene blue in gas-liquid-solid mini-fluidized beds. Chem. Eng. J. 370, 1154-1168.

Liu, Z., Li, B., 2018. Scale-adaptive analysis of Euler-Euler large eddy simulation for laboratory scale dispersed bubbly flows. Chem. Eng. J. 338 (3), 465-477.

Liu, Z., Wu, Y., Li, B., 2020. An assessment on the performance of sub-grid scale models of large eddy simulation in modeling bubbly flows. Powder Technol. 374, 470-481.

Lopez de Bertodano, M., Lahey Jr, R.T., Jones, O.C., 1994. Development of a k-ε model for bubbly two-phase flow. J. Fluids Eng. 116, 128-134.

Loubière, K., Castaignède, V., Hébrard, G., Roustan, M., 2004. Bubble formation at a flexible orifice with liquid cross-flow. Chem. Eng. Process. Process Intensif. 43(6), 717–725.

Ma, Y., Zhang, L., Yang, Y., Wei, P., 2020. Air entrainment by inclined circular plunging water jets with various impingement heights. Water Supply 20(8), 3478-3486.

Manzouri, M., Azimi, A.H., 2019. Laboratory experiments evaluating sedimentation and mound formation of obliquely discharged sand particles in stagnant water. Int. J. Sediment Res. 34(6), 564-576.

Marchisio, D.L., Vigil, R.D., Fox, R.O., 2003. Implementation of the quadrature method of moments in CFD codes for aggregation - breakage problems. Chem. Eng. Sci., 58 (15), 3337-3351.

McGinnis, D.F., Lorke, A., Wüest, A., Stöckli, A., Little, J.C., 2004. Interaction between a bubble plume and the near field in a stratified lake. Water Resour. Res. 40(10), 1-11.

McGraw, R., 1997. Description of aerosol dynamics by the quadrature method of moments. Aerosol Sci. Technol. 27 (2), 255-265.

Mei, R., 1992. An approximate expression for the shear lift force on a spherical particle at finite reynolds number. Int. J. Multiph. Flow 18 (1), 145-147.

Meyer, C.J., Deglon, D.A., 2011. Particle collision modeling–a review. Miner. Eng. 24 (8) 719–730.

Milelli, M., 2002. A numerical analysis of confined turbulent bubble plume. Diss. EH. No. 14799, Swiss Federal Institute of Technology, Zurich.

Milgram, J.H., 1983. Mean flow in round bubble plumes. J. Fluid Mech. 133, 345–376.

Mingotti, N., Woods, A.W., 2020. Stokes settling and particle-laden plumes: implications for deep-sea mining and volcanic eruption plumes. Philos. Trans. Royal Soc. A 378(2179), 20190532.

Mingotti, N., Woods, A.W., 2022. Dynamics of sediment-laden plumes in the ocean. Flow 2, E26.

Mitrou, E., Fraga, B., Stoesser, T., 2018, September. An Eulerian-Lagrangian numerical method to predict bubbly flows. In E3S Web of Conferences (Vol. 40). EDP Sciences.

Mohagheghian, S., Ghajar, A.J., Elbing, B.R., 2020. Effect of vertical vibration on the mixing time of a passive scalar in a sparged bubble column reactor. Fluids 5(1), 6.

Mohammadi, M.H., Sotiropoulos, F., Brinkerhoff, J.R., 2019. Eulerian-Eulerian large eddy simulation of two-phase dilute bubbly flows. Chem. Eng. Sci. 208, 115156.

Mokhtari, M., Chaouki, J., 2019. New technique for simultaneous measurement of the local solid and gas holdup by using optical fiber probes in the slurry bubble column. Chem. Eng. J. 358, 831-841.

Mooneyham, C., Strom, K., 2018. Deposition of suspended clay to open and sand-filled framework gravel beds in a laboratory flume. Water Resour. Res. 54(1), 323-344.

Na, B., Chang, K.A., Lim, H.J., 2020. Flow kinematics and air entrainment under laboratory spilling breaking waves. J. Fluid Mech. 882, A15.

Neal, D.R., Sciacchitano, A., Smith, B.L., Scarano, F., 2015. Collaborative framework for PIV uncertainty quantification: the experimental database. Meas. Sci. Technol. 26(7), 074003.

Newland, E.L., Woods, A.W., 2023. On particle fountains in a crossflow. J. Fluid Mech. 964, A10.

Ngo-Cong, D., Nguyen, A.V., Tran-Cong, T., 2018. Isotropic turbulence surpasses gravity in affecting bubble-particle collision interaction in flotation. Miner. Eng. 122, 165-175.

Niceno, B., Dhotre, M.T., Deen, N.G., 2008. One-equation sub-grid scale (SGS) modelling for Euler-Euler large eddy simulation (EELES) of dispersed bubbly flow. Chem. Eng. Sci. 63 (15), 3923-3931.

Oguz, H.N., Prosperetti, A., 1993. Dynamics of bubble growth and detachment from a needle. J. Fluid Mech. 257, 111–145.

Ouillon, R., Muñoz-Royo, C., Alford, M.H., Peacock, T., 2022a. Advection-diffusion-settling of deep-sea mining sediment plumes. Part 1: Midwater plumes. Flow 2, E22.

Ouillon, R., Muñoz-Royo, C., Alford, M.H., Peacock, T., 2022b. Advection-diffusion-settling of deep-sea mining sediment plumes. Part 2. Collector plumes. Flow, 2, E23.

Pakhomov, M.A., Terekhov, V.I., 2019. Structure of the turbulent flow in a sub- merged axisymmetric gas-saturated jet. J. Appl. Mech. Tech. Phys. 60(5), 805–815.

Pan, H., Liu, Q., Luo, Z.H., 2018. Modeling and simulation of particle size distribution behavior in gas–liquid–solid polyethylene fluidized bed reactors. Powder Technol. 328, 95-107.

Papaioannou, T.G., Stefanadis, C., 2005. Vascular wall shear stress: basic principles and methods. Hell. J. Cardiol. 46(1), 9-15.

Patankar, S.V., Numerical Heat Transfer and Fluid Flow, Electro Skills Series (Hemisphere Publishing Corporation, 1980).

Peacock, T., Ouillon, R., 2023. The fluid mechanics of deep-sea mining. Annu. Rev. Fluid Mech. 55, 403-430.

Peixinho, J., Nouar, C., Desaubry, C., Théron, B., 2005. Laminar transitional and turbulent flow of yield stress fluid in a pipe. J. Nonnewton Fluid Mech. 128(2-3), 172-184.

Pfleger, D., Becker, S., 2001. Modelling and simulation of the dynamic flow behavior in a bubble column. Chem. Eng. Sci. 56 (4), 1737-1747.

Plesniak, M.W., Cusano, D.M., 2005. Scalar mixing in a confined rectangular jet in crossflow. J. Fluid Mech. 524, 1-45.

Pope, S., 2000. Turbulent Flows. Cambridge University Press.

Prince, M.J., Blanch, H.W., 1990. Bubble coalescence and break-up in air-sparged bubble columns. AIChE J. 36 (10), 1485-1499.

Qu, X., Goharzadeh, A., Khezzar, L., Molki, A., 2013. Experimental characterization of air-entrainment in a plunging jet. Exp. Therm. Fluid Sci. 44, 51-61.

Raffel, M., Willert, C. E., Scarano, F., Kähler, C. J., Wereley, S. T., Kompenhans, J., 2018. Particle Image Velocimetry: A Practical Guide, Springer, Berlin, 203-241.

Rasband, W.S. et al., 1997. Imagej.

Razzak, S.A., Barghi, S., Zhu, J.X., Mi, Y., 2009. Phase holdup measurement in a gas–liquid–solid circulating fluidized bed (GLSCFB) riser using electrical resistance tomography and optical fibre probe. Chem. Eng. J. 147(2-3), 210-218.

Razzaque, M.M., Afacan, A., Liu, S., Nandakumar, K., Masliyah, J.H., Sanders, R.S., 2003. Bubble size in coalescence dominant regime of turbulent air-water flow through horizontal pipes. Int. J. Multiph. Flow 29(9), 1451–1471.

RBI Instruments Inc., 2010. User's guide for ISO software (interface software for optical probes), Version 2.05. Meylan, France.

Rek, Z., Gregorc, J., Bouaifi, M., Daniel, C., 2017. Numerical simulation of gas jet in liquid crossflow with high mean jet to crossflow velocity ratio. Chem. Eng. Sci. 172, 667-676.

Rezvani, M., Socolofsky, S.A., 2012. Turbulence properties in bubble plumes in presence of currents. In: Hydraulic Measurement and Experimental Methods Conference, snowbird, Utah.

Risso, F., 2000. The mechanisms of deformation and breakup of drops and bubbles. Multiph. Sci. Technol. 12(1).

Ryu, Y., Chang, K.A., Lim, H.J., 2005. Use of bubble image velocimetry for measurement of plunging wave impinging on structure and associated greenwater. Meas. Sci. Technol. 16(10), 1945.

Saffman, P.G., 1965. The lift on a small sphere in a slow shear flow. J. Fluid Mech. 22 (2), 385-400.

Sarhan, A.R., Naser, J., Brooks, G., 2016. CFD simulation on influence of suspended solid particles on bubbles' coalescence rate in flotation cell. Int. J. Miner. Process. 146 54–64.

Sarhan, A.R., Naser, J., Brooks, G., 2017a. CFD analysis of solid particles properties effect in three-phase flotation column. Sep. Purif. Technol. 185 1–9.

Sarhan, A.R., Naser, J., Brooks, G., 2017b. Numerical simulation of froth formation in aerated slurry coupled with population balance modelling. Can. Metall. Q. 56 (1) 45–57.

Sarhan, A.R., Naser, J., Brooks, G., 2017c. CFD modeling of three-phase flotation column incorporating a population balance model. Proc. Eng. 184 313–317.

Sarhan, A.R., Naser, J., Brooks, G., 2018a. CFD model simulation of bubble surface area flux in flotation column reactor in presence of minerals. Int. J. Min. Sci. Technol. 28 (6) 999–1007.

Sarhan, A.R., Naser, J., Brooks, G., 2018b. Bubbly flow with particle attachment and detachment–a multiphase CFD study. Sep. Sci. Technol. 53 (1) 181–197.

Sarhan, A.R., Naser, J., Brooks, G., 2018c. CFD modeling of bubble column: influence of physico-chemical properties of the gas/liquid phases properties on bubble formation. Sep. Purif. Technol. 201 130–138.

Sarhan, A.R., Naser, J., Brooks, G., 2018d. Effects of particle size and concentration on bubble coalescence and froth formation in a slurry bubble column. Particuology 36 82–95.

Sato, Y., Sekoguchi, K., 1975. Liquid velocity distribution in two-phase bubble flow. Int. J. Multiph. Flow 2 (1), 79-95.

Scharnowski, S., Kähler, C.J., 2020. Particle image velocimetry-classical operating rules from today's perspective. Opt. Lasers Eng. 135, 106185.

Schiller, L., 1933. A drag coefficient correlation. Zeit. Ver. Deutsch. Ing. 77, 318-320.

Schladow, S.G., 1993. Lake Destratification by Bubble‐Plume Systems: Design Methodology. J. Hydraul. Eng. 119(3), 350–368.

Schlichting, H., 1979. Boundary-Layer Theory. 7th edition, McGraw-Hill, New York.

Sedrez, T.A., Shirazi, S.A., 2021. Erosion evaluation of elbows in series with different configurations. Wear 476, 203683.

Sedrez, T.A., Shirazi, S.A., Rajkumar, Y.R., Sambath, K., Subramani, H.J., 2019. Experiments and CFD simulations of erosion of a 90° elbow in liquid-dominated liquid-solid and dispersed-bubble-solid flows. Wear 426, 570-580.

Seo, H., Kim K.C., 2021. Experimental study on flow and turbulence characteris- tics of bubbly jet with low void fraction. Int. J. Multiph. Flow 142, 103738.

Seo, H., Marjanovic, G., Balachandar, S., Kim, K.C., 2022. Influence of slip velocity in a two-phase bubbly jet. J. Fluid Mech. 935, A4.

Seol, D.-G., Bhaumik, T., Bergmann, C., Socolofsky, S.A., 2007. Particle Image Velocimetry Measurements of the Mean Flow Characteristics in a Bubble Plume. J. Eng. Mech. 133(6), 665–676.

Serra, P.L., Masotti, P.H., Rocha, M.S., de Andrade, D.A., Torres, W.M., de Mesquita, R.N., 2020. Two-phase flow void fraction estimation based on bubble image segmentation using Randomized Hough Transform with Neural Network (RHTN). Prog. Nucl. Energy 118, 103133.

Shi, R., Wang, H., Chanson, H., 2018. Bubble convection and bubbly flow turbulent time and length scales in two-dimensional plunging jets. Exp. Therm. Fluid Sci. 98, 278–289.

Shi, R., Wüthrich, D., Chanson, H., 2023. Air–water properties of unsteady breaking bore part 2: Void fraction and bubble statistics. Int. J. Multiph. Flow 159, 104337.

Shi, W., Yang, X., Sommerfeld, M., Yang, J., Cai, X., Li, G., Zong, Y., 2019. Modelling of mass transfer for gas-liquid two-phase flow in bubble column reactor with a bubble breakage model considering bubble-induced turbulence. Chem. Eng. J. 371, 470-485.

Shuai, Y., Guo, X., Wang, H., Huang, Z., Yang, Y., Sun, J., Wang, J., Yang, Y., 2019. Characterization of the bubble swarm trajectory in a jet bubbling reactor. AlChE J. 65(5), e16565.

Singamsetti, S.R., 1966. Diffusion of sediment in a submerged jet. J. Hydraul. Div. 92(2), 153-168.

Socolofsky, S.A., Adams, E.E., 2002. Multi-phase plumes in uniform and stratified crossflow. J. Hydraul. Res. 40 (6), 661-672.

Song, G., Li, Y., Wang, W., Jiang, K., Shi, Z., Yao, S., 2019. Hydrate agglomeration modeling and pipeline hydrate slurry flow behavior simulation. Chin. J. Chem. Eng. 27 (1) 32–43.

Su, X., Yang, X., Yu, Y., Gao, F., Wang, X., 2023. A simulation approach to predict electrostatic coalescence performance of water-in-oil emulsion using population balance model. Sep. Sci. Technol. 58 (3) 538–550.

Sun, T.Y., Faeth, G.M., 1986. Structure of turbulent bubbly jets-II. Phase property profiles. Int. J. Multiph. Flow 12(1), 115–126.

Sun, X.Y., Cao, X.W., 2021. Impact of inter-particle collision on elbow erosion based on DSMC-CFD method. Pet. Sci. 18 909–922.

Swan, C., Moros, A., 1993. The hydrodynamics of a subsea blowout. Appl. Ocean Res. 15(5), 269–280.

Tabib, M.V., Roy, S.A., Joshi, J.B., 2008. CFD simulation of bubble column—an analysis of interphase forces and turbulence models. Chem. Eng. J. 139 (3), 589-614.

Tabib, M.V., Schwarz, P., 2011. Quantifying sub-grid scale (SGS) turbulent dispersion force and its effect using one-equation SGS large eddy simulation (LES) model in a gas-liquid and a liquid-liquid system. Chem. Eng. Sci. 66 (14), 3071-3086.

Takehara, K., Etoh, T., 1998. A study on particle identification in PTV particle mask correlation method. J. Vis. 1(3), 313-323.

Tan, R.B.H., Chen, W.B., Tan, K.H., 2000. Non-spherical model for bubble formation with liquid cross-flow. Chem. Eng. Sci. 55(24), 6259–6267.

Thielicke, W., Sonntag, R., 2021. Particle Image Velocimetry for MATLAB: Accuracy and enhanced algorithms in PIVlab. J. Open Res. Software 9(1).

Timkin, L.S., Gorelik, R.S., 2020. Local bubble slip velocity in a downward laminar tube flow. Thermophys. Aeromechanics 27(2), 259–268.

Tomiyama, A., Tamai, H., Zun, I., Hosokawa, S., 2002. Transverse migration of single bubbles in simple shear flows. Chem. Eng. Sci. 57 (11), 1849-1858.

Tsuji, Y., Tanaka, T., Ishida, T., 1992. Lagrangian numerical simulation of plug flow of cohesionless particles in a horizontal pipe. Powder Technol. 71 (3), 239-250.

Vejražka, J., Večeř, M., Orvalho, S., Sechet, P., Ruzicka, M.C., Cartellier, A., 2010. Measurement accuracy of a mono-fiber optical probe in a bubbly flow. Int. J. Multiph. Flow 36, 533-548.

Vieira, C.B., Litrico, G., Askari, E., Lemieux, G., Proulx, P., 2018. Hydrodynamics of bubble columns: Turbulence and population balance model. ChemEngineering 2 (1), 1-26.

Wang, A., Hoque, M.M., Moreno-Atanasio, R., Doroodchi, E., Evans, G., Mitra, S., 2021c. Effect of bubble surface loading on bubble rise velocity. Miner. Eng. 174, 107252.

Wang, B., Socolofsky, S.A., 2015. On the bubble rise velocity of a continually released bubble chain in still water and with crossflow. Phys. Fluids 27 (10), 103301.

Wang, L., Cao, Z., Cai, H., Wang, Y., 2021a. Numerical simulation of gas-liquid-solid three phase in bubble column. J. Phys. Conf. Ser. 1739 (1), 012041.

Wang, T., Liu, Z., Gui, M., Bi, Q., Sui, Z., 2021b. Flow regime identification of steam-water two-phase flow using optical probes, based on local parameters in vertical tube bundles. Flow Meas. Instrum. 79, 101928.

Wang, Y., Qin, Y., Yao, X., 2020. A combined experimental and numerical investigation on damage characteristics of ice sheet subjected to underwater explosion load. Appl. Ocean Res. 103, 102347.

Wang, Y.X., Yin, Z.G., Zhang, W., Zhu, D.Z., 2019. Computational study of bubbly jets in stagnant water. J. Hydrodyn. 31 (5), 1021-1033.

Wang, Z., He, Y., Duan, Z., Huang, C., Yuan, Y., Li, M., Liu, S., 2022. Effects of rolling motion on transient flow behaviors of gas-liquid two-phase flow in horizontal pipes. Ocean Eng. 255, 111482.

Warwaruk, L., Ghaemi, S., 2023. Polymer and surfactant flows through a periodically constricted tube. J. Fluid Mech. 960, A19.

Washino, K., Chan, E.L., Kaji, T., Matsuno, Y., Tanaka, T., 2021. On large scale CFD–DEM simulation for gas–liquid–solid three-phase flows. Particuology 59, 2-15.

Wen, J., Lei, P., Huang, L., 2005. Modeling and simulation of gas-liquid-solid three-phase fluidization. Chem. Eng. Commun. 192 (7-9), 941-955.

Wiedemann, P., Döß, A., Schleicher, E., Hampel, U., 2019. Fuzzy flow pattern identification in horizontal air-water two-phase flow based on wire-mesh sensor data. Int. J. Multiph. Flow 117, 153–162.

Xiao, C.N., Fond, B., Beyrau, F., T'Joen, C., Henkes, R., Veenstra, P., van Wachem, B., 2019. Numerical investigation and experimental comparison of the gas dynamics in a highly underexpanded confined real gas jet. Flow Turbul. Combust. 103(1), 141-173.

Xie, L., Zhou, G., Wang, D., Wang, H., Jiang, C., 2022. Machine learning and data-driven modeling to discover the bed expansion ratio correlation for gas–liquid–solid three-phase flows. Ind. Eng. Chem. Res. 62(1), 789-800.

Xu, Y., Aliyu, A.M., Seo, H., Wang, J.J., Kim, K.C., 2018. Effect of crossflow velocity on underwater bubble swarms. Int. J. Multiph. Flow 105, 60-73.

Yan, H., Gong, H., Huang, Z., Zhou, P., Liu, L., 2022. Euler-Euler modeling of reactive bubbly flow in a bubble column. Phys. Fluids 34 (5), 053306.

Yapa, P.D., Dasanayaka, L.K., Bandara, U.C., Nakata, K., 2010. A model to simulate the transport and fate of gas and hydrates released in deepwater. J. Hydraul. Res. 48(5), 559–572.

Yuan, L.L., 1997. Large eddy simulations of a jet in crossflow. PhD thesis, Department of Mechanical Engineering, Stanford University, Stanford, CA.

Yuan, L.L., Street, R.L., Ferziger, J.H., 1999. Large-eddy simulations of a round jet in crossflow. J. Fluid Mech. 379, 71-104.

Zhang, G., Chanson, H., 2018. Application of local optical flow methods to high-velocity free-surface flows: Validation and application to stepped chutes. Exp. Therm. Fluid Sci. 90, 186-199.

Zhang, H., Yin, Z., Chen, M., Zhang, W., 2023a. Experiment on bubble characteristics of turbulent bubbly jets in pipe crossflow. Ocean Eng. 271, 113782.

Zhang, H., Yin, Z., Chi, W., Zhang, W., 2023b. A new Eulerian-Eulerian-Lagrangian solver in OpenFOAM and its application in a three-phase bubble column. Powder Technol. 426, 118661.

Zhang, H., Zhang, W., 2022. Numerical simulation of bubbly jets in crossflow using OpenFOAM. Phys. Fluids 34(12).

Zhang, L., Yang, V., 2017. Flow dynamics and mixing of a transverse jet in crossflow—Part I: Steady crossflow. J. Eng. Gas Turbines Power 139 (8), 082601.

Zhang, W., 2012. Air injection for river water quality improvement. PhD thesis, Department of Civil and Environmental Engineering, University of Alberta, Edmonton, Canada.

Zhang, W., Liu, M., Zhu, D.Z., Rajaratnam, N., 2014. Mean and turbulent bubble velocities in free hydraulic jumps for small to intermediate Froude numbers. J. Hydraul. Eng. 140(11), 04014055.

Zhang, W., Zhu, D.Z., 2013. Bubble characteristics of air-water bubbly jets in crossflow. Int. J. Multiph. Flow 55, 156-171.

Zhang, W., Zhu, D.Z., 2014. Trajectories of air-water bubbly jets in crossflows. J. Hydraul. Eng. 140(7), 1-9.

Zhang, X., Li, S., Yang, B., Wang, N., 2020. Flow structures of over-expanded supersonic gaseous jets for deep-water propulsion. Ocean Eng. 213, 107611.

Zhang, Y., Lu, X.B., Zhang, X.H., 2021. An optimized Eulerian–Lagrangian method for two- phase flow with coarse particles: Implementation in open-source field operation and manipulation, verification, and validation. Phys. Fluids 33 (11) 113307.

Zheng, L., Yapa, P.D., 1998. Simulation of oil spills from underwater accidents II: Model verification. J. Hydraul. Res. 36 (1), 117-134.

Zheng, L., Yapa, P.D., Chen, F., 2003. A model for simulating deepwater oil and gas blowouts-Part I: Theory and model formulation. J. Hydraul. Res. 41 (4), 339-351.

Zhou, W., Xu, X., Yang, Q., Zhao, R., Jin, Y., 2022. Experimental and numerical investigations on the spray characteristics of liquid-gas pintle injector. Aerosp. Sci. Technol. 121, 107354.

Zhou, X., Ma, Y., Liu, M., Zhang, Y., 2020. CFD-PBM simulations on hydrodynamics and gas-liquid mass transfer in a gas-liquid-solid circulating fluidized bed. Powder Technol. 362, 57-74.

Zhu, L., Chen, H., Song, Y., Shi, R., Liu, Z., Wei, X., Zhao, C., Ai, T., 2023. Study on flow characteristics of gas-liquid-solid circulating fluidized bed with central sinusoidal pulsating flow. Powder Technol. 118415.

Zhu, S.J., Ooi, A., Manasseh, R., Skvortsov, A., 2020. Prediction of gas holdup in partially aerated bubble columns using an EE-LES coupled model. Chem. Eng. Sci. 217, 115492.

Ziefle, J., Kleiser, L., 2009. Large-eddy simulation of a round jet in crossflow. AIAA Journal 47 (5), 1158-1172.

Appendix A

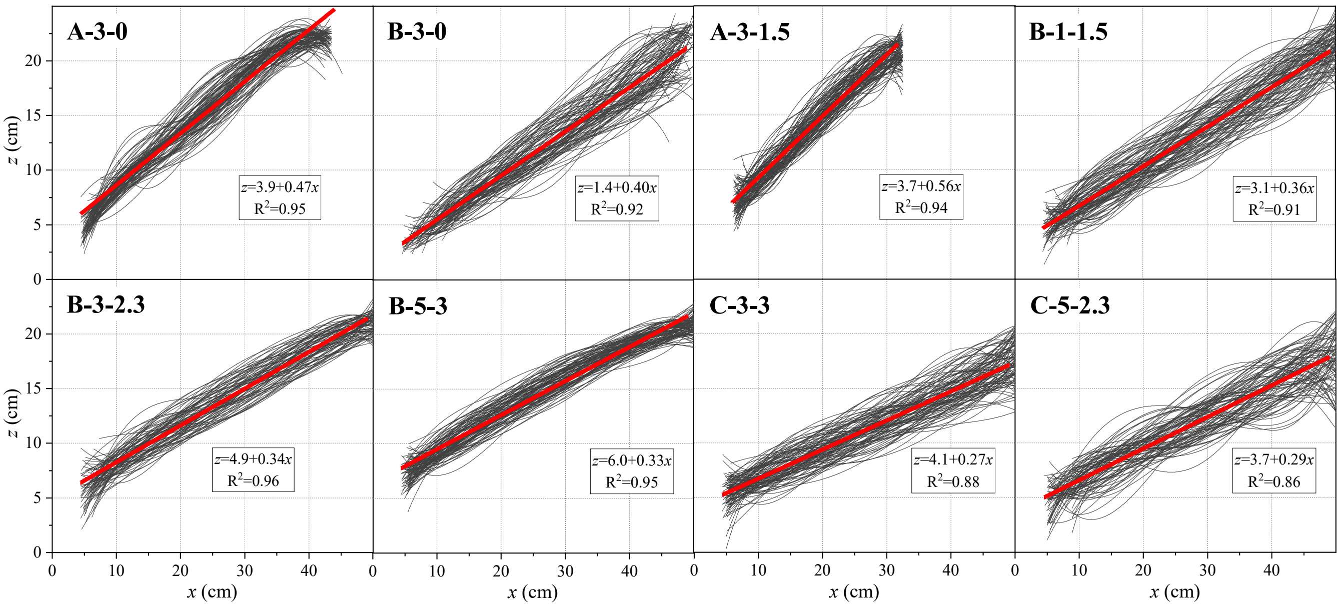

Figure 3-A1. Gas-phase centerline trajectories of bubbly jets in pipe crossflow before bubbles reach the top pipe wall

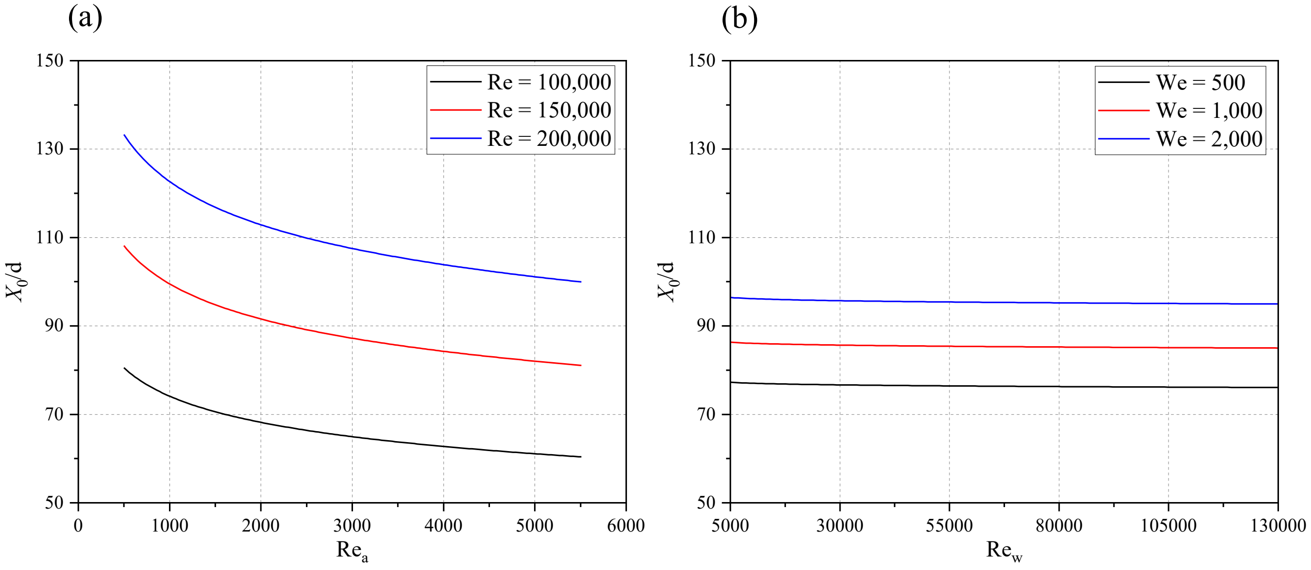

Figure 3-A2. Effects of dimensionless parameters on predicted X_0/d using Eq. (3-5). The fixed parameters are We = 1,500, Re_w = 20,000 in (a); and Re = 150,000, Re_a = 2,000 in (b).

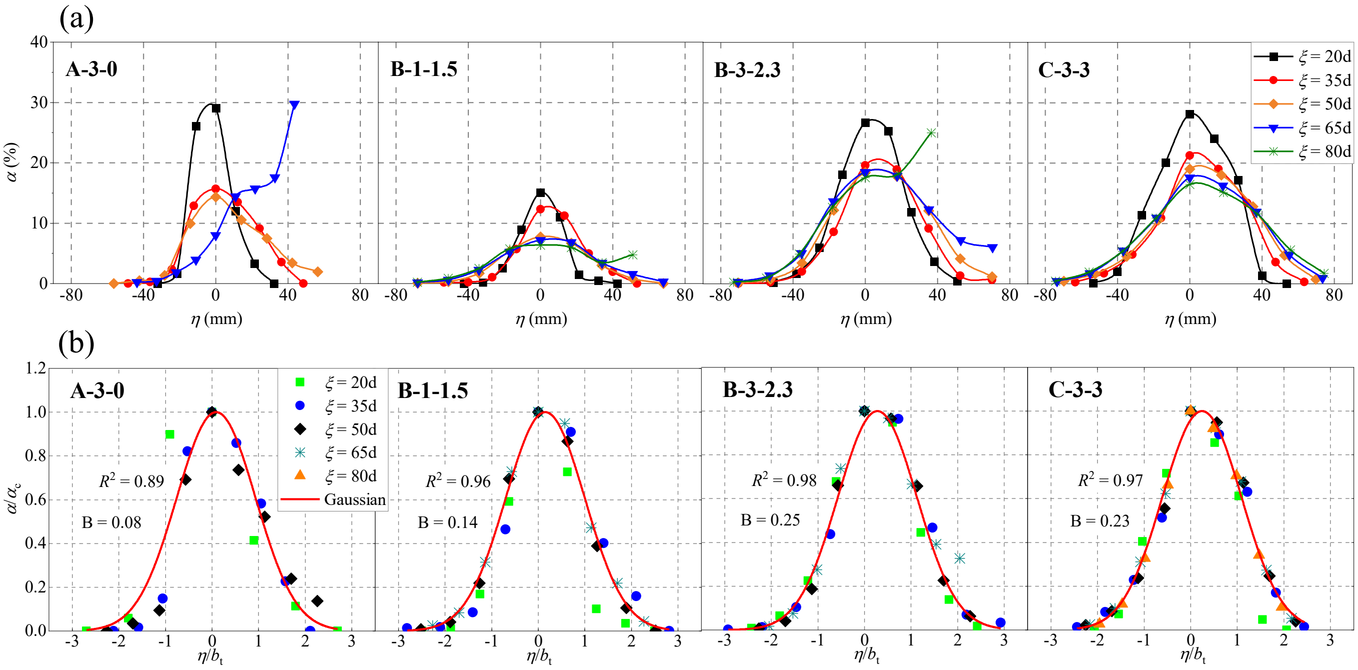

Figure 3-A3. Distributions of (a) gas void fraction and (b) normalized gas void fraction at different sections along η direction from the side view

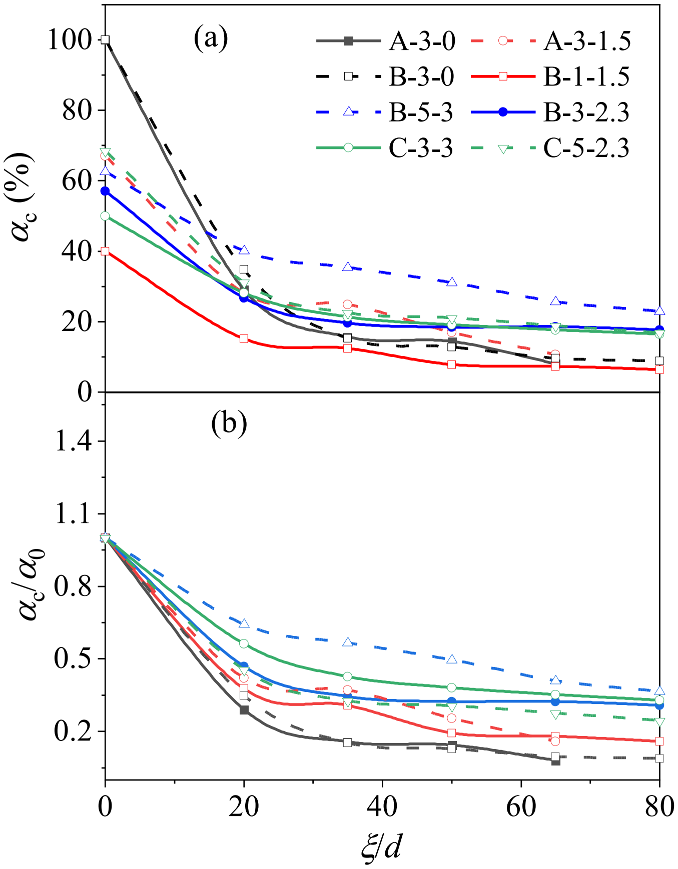

Figure 3-A4. Changes of (a) centerline gas void fraction and (b) normalized centerline gas void fraction along the gas-phase trajectories from the side view

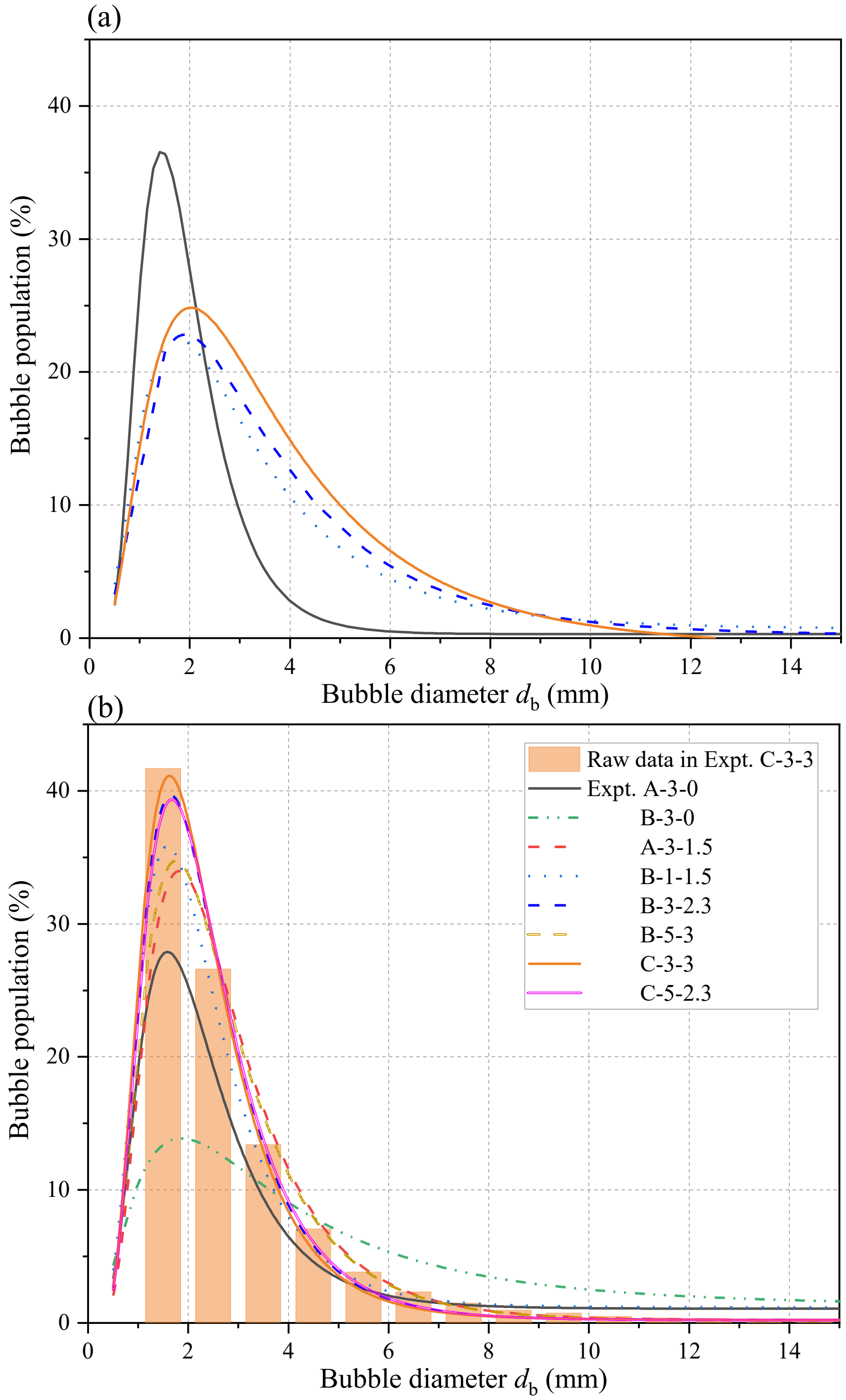

Figure 3-A5. Overall bubble size distribution at all measuring points from the (a) top view; and (b) side view. In Expt. C-3-3, both raw data and numerically fitted data are presented for side view, while in all other scenarios, data are numerically fitted data.

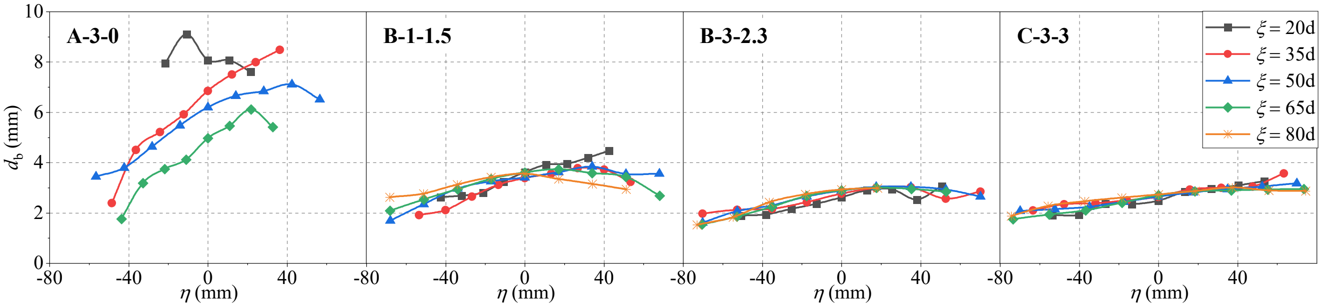

Figure 3-A6. Bubble size distribution at different sections along η direction from the side view

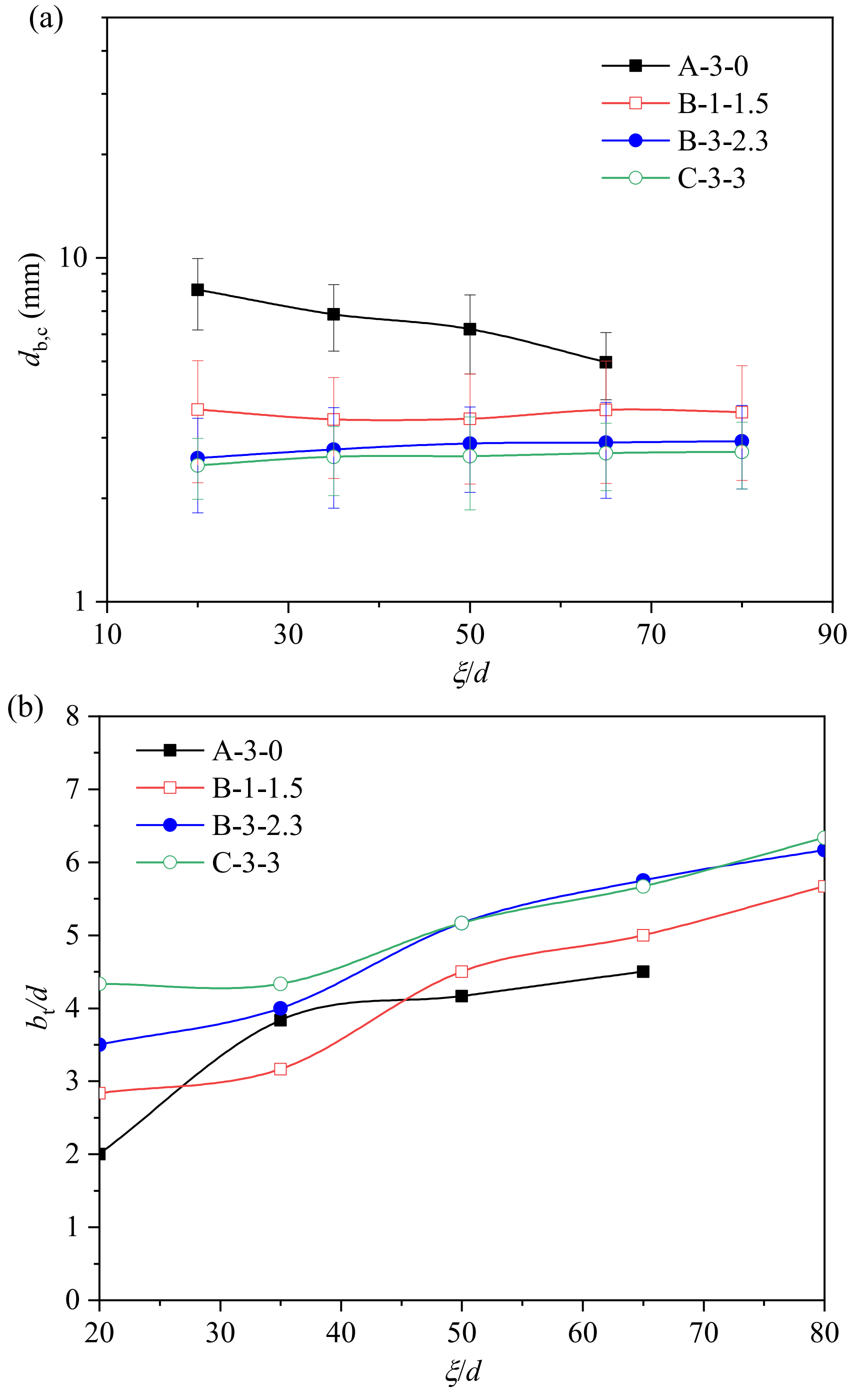

Figure 3-A7. (a) Centerline distribution of bubble size. The error bars represent the standard deviation of the measured bubble diameters; and (b) distributions of gas-phase half-width from the side view

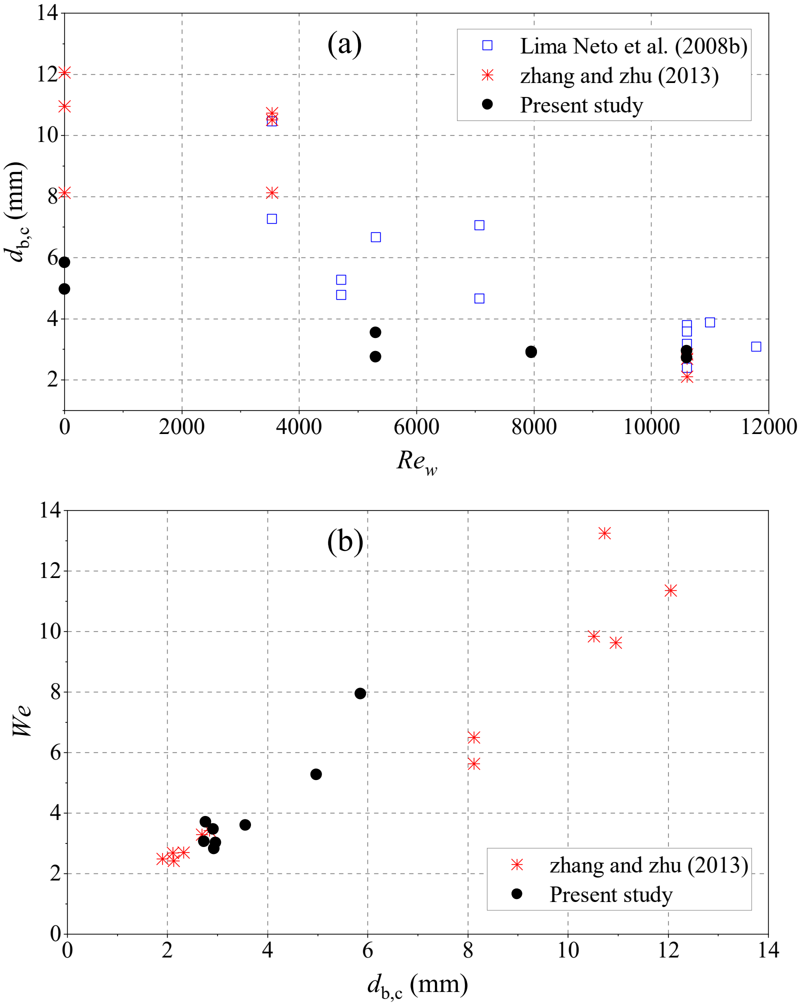

Figure 3-A8. Relationships between (a) $d_{b,c}$ and Re_w; and (b) We and $d_{b,c}$, where We is the Weber number, defined as, $We = \rho U_s^2 d_{b,c}/\sigma$.

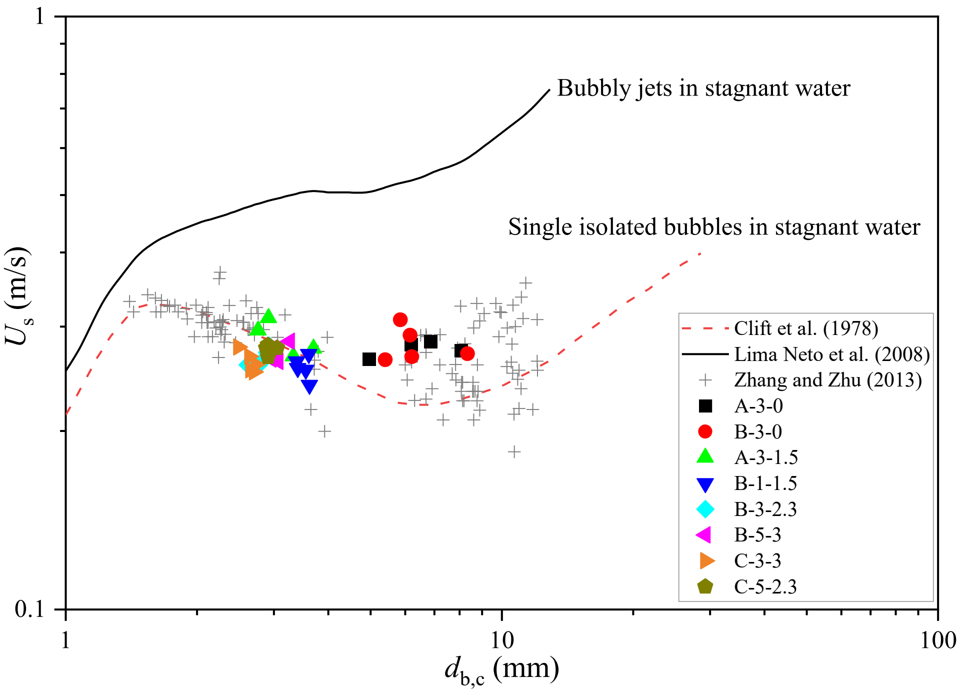

Figure 3-A9. Relationships between bubble slip velocity U_s (U_{bz} in this study) and bubble diameter for bubbly jets in pipe flow

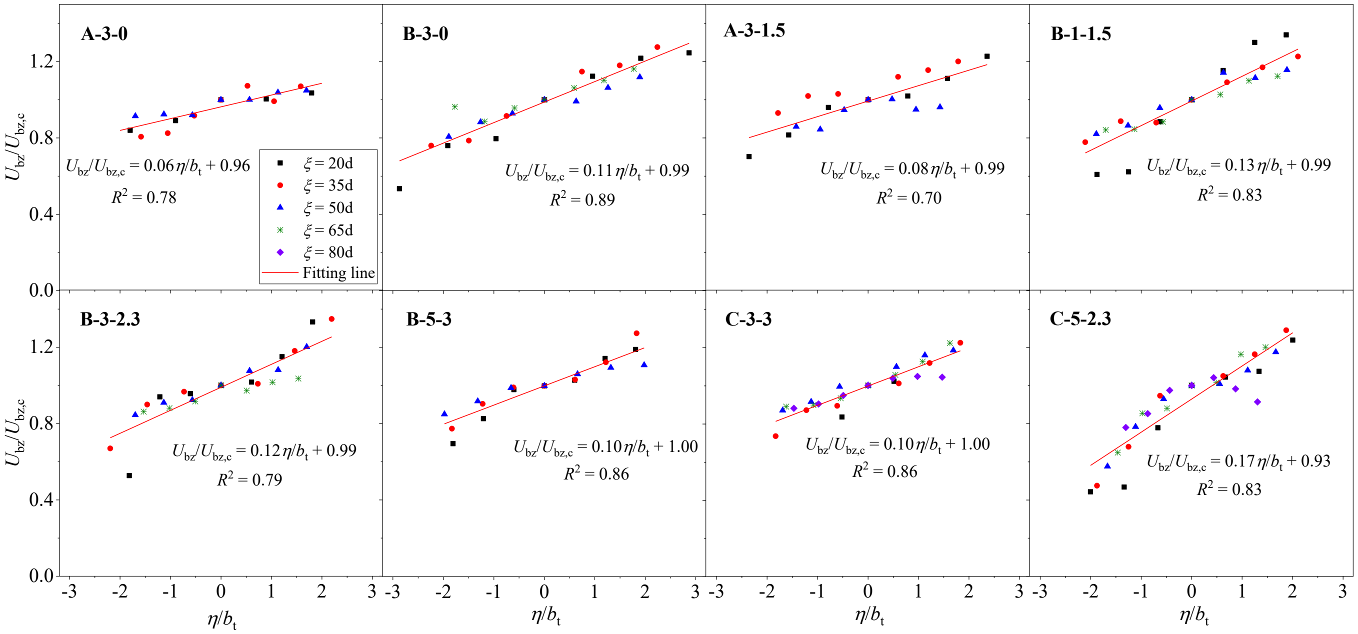

Figure 3-A10. Distribution of normalized rising velocity $U_{bz}/U_{bz,c}$ for different scenarios

Appendix B

Interphase coupling between gas and liquid phases

The drag force describes the resistance experienced by gas bubbles moving in liquid phase. For a bubble swarm, the drag force per unit volume can be written as (Clift et al., 1978):

$$\mathbf{F}_D = \frac{3}{4}\alpha_{\mathrm{g}} C_D \frac{\rho_l}{d_{\mathrm{b}}} \left|\mathbf{U}_g - \mathbf{U}_l\right| \left(\mathbf{U}_g - \mathbf{U}_l\right) \tag{B1}$$

where C_D is the drag coefficient and d_{b} is the gas bubble diameter. Note that α_g considers the effect of solid holdup ($\alpha_g = 1 - \alpha_l - \alpha_p$) in our developed solver. Various drag models have been proposed and compared in the literatures (Schiller, 1933; Ishii and Zuber, 1979), and the widely used Ishii-Zuber drag model (Ishii and Zuber, 1979) was used in our study to calculate C_D. For gas bubbles that are spherical such as in Gan (2013), C_{D} can be determined as:

$$C_D = \frac{24}{Re_m}\left(1 + 0.1 Re_m^{0.75}\right) \tag{B2}$$

where Re_m denotes the mixture Reynolds number of gas and liquid. $Re_m = \rho_l d_b \left|\mathbf{U}_g - \mathbf{U}_l\right| / \mu_m$, where $\mu_m = \mu_l \left(1 - \alpha_g\right)^{-2.5\mu^*}$, and $\mu^* = \left(\mu_g + 0.4\mu_l\right) / \left(\mu_g + \mu_l\right)$.

Due to shear or vorticity effects, gas bubbles travelling through a non-uniform flow field will experience a lift force transverse to the moving direction. The lift force, which tends to produce the radial dispersion of bubbles, can be written as (Drew and Lahey, 1987):

$$\mathbf{F}_L = \alpha_g \rho_l C_L \left(\mathbf{U}_g - \mathbf{U}_l\right) \times \nabla \times \mathbf{U}_l \tag{B3}$$

where C_L is the lift force coefficient. Various studies used a constant or the Tomiyama model (Tomiyama et al., 2002) for C_L. However, there is no consensus on the selection of C_L, and different values of C_L were used in the literature (Lopez de Bertodano et al., 1994; Vieira et al., 2018). The most commonly used constant value of 0.5 was used for C_L in this study, based on sensitivity analysis and comparing to the experimental results.

The virtual mass force is originated from gas bubble acceleration that will accelerate the surrounding fluid during ascent (Jakobsen et al., 1997), and was modeled in this study as:

$$\mathbf{F}_{VM} = \alpha_g \rho_l C_{VM} \left(\frac{\mathrm{D}\mathbf{U}_g}{\mathrm{D}t} - \frac{\mathrm{D}\mathbf{U}_l}{\mathrm{D}t} \right) \tag{B4}$$

where C_{VM} is the virtual mass coefficient. C_{VM} was fixed to 0.5 in this study for individual spherical bubbles (Ničeno et al., 2008).

Under the random influence of turbulent eddies, gas bubbles tend to disperse from high to low void fraction regions. The turbulent dispersion force proposed by Lopez de Bertodano et al. (1994) was used in this work:

$$\mathbf{F}_{TD} = C_{TD} \rho_l k_{l,SGS} \nabla \alpha_g \tag{B5}$$

where $k_{l,SGS}$ is the sub-grid scale turbulent kinetic energy of liquid, and C_{TD} is the turbulent dispersion coefficient. C_{TD} was taken as 0.6 in this study after testing several values to obtain better agreement with the experimental results.

Interphase coupling between fluid and solid phases

The non-spherical drag model proposed by Haider and Levenspiel (1989) was used in this study for the interphase coupling between fluid and particles assuming a shape factor of 0.8. The drag force $\mathbf{F}_{D,p\varphi}$ can be expressed as follows:

$$\mathbf{F}_{D,p\varphi} = \frac{3\mu_\varphi C_{D,p\varphi} Re_p}{4\rho_p d_p^2} (\mathbf{U}_\varphi - \mathbf{U}_p) \tag{B6}$$

where the drag coefficient $C_{D,p\varphi}$ can be calculated by:

$$C_{D,p\varphi} = \frac{24}{Re_p}\left(1 + aRe_p^b\right) + \frac{cRe_p}{d+Re_p} \tag{B7}$$

where μ_φ is the fluid viscosity, Re_p is the particle Reynolds number, ρ_p is the particle density, d_p is the particle diameter, and *a*, *b*, *c*, and *d* are constants that are related to the particle sphericity. More details can be found in Haider and Levenspiel (1989).

The shear lift force $\mathbf{F}_{L,p\varphi}$ acting on a solid particle exists in local shear flow with non-uniform velocity distribution over the particle surface. In this work, the Saffman-Mei lift model was used, which was proposed by Saffman (1965) and developed by Mei (1992):

$$\mathbf{F}_{L,p\varphi} = C_{L,p\varphi}\frac{\rho_\varphi}{\rho_p}(\mathbf{U}_\varphi - \mathbf{U}_p) \times (\nabla \times \mathbf{U}_\varphi) \tag{B8}$$

where $C_{L,p\varphi}$ is the lift coefficient.

$$C_{L,p\varphi} = \frac{3}{2\pi\sqrt{Re_s}}C_{ls} \tag{B9}$$

$$Re_s = \frac{\rho_\varphi d_p^2|\nabla\times\mathbf{U}_\varphi|}{\mu_\varphi} \tag{B10}$$

$$C_{ls} = \begin{cases} 6.46f & \text{if } Re_p < 40 \\ 6.46 \cdot 0.0524\sqrt{\beta Re_p} & \text{if } Re_p \geq 40 \end{cases} \tag{B11}$$

$$f = (1-\gamma)\exp\left(-0.1Re_p\right) + \gamma \tag{B12}$$

$$\beta = 0.5\frac{Re_s}{Re_p},\ \gamma = 0.3314\sqrt{\beta} \tag{B13}$$

The virtual mass force $\mathbf{F}_{VM,p\varphi}$ can be expressed by (Sedrez and Shirazi, 2021):

$$\mathbf{F}_{VM,p\varphi} = C_{VM,p\varphi}\frac{\rho_\varphi}{\rho_p}\left(\frac{D\mathbf{U}_\varphi}{Dt} - \frac{d\mathbf{U}_p}{dt}\right) \tag{B14}$$

where $C_{VM,p\varphi}$ is the virtual mass coefficient. The commonly-used value of 0.5 was used for $C_{VM,p\varphi}$ in this work.

Population balance model for gas phase

The coalescence and breakage source terms can be modeled as:

$$B_{i,co} = \frac{1}{2}\int_0^V a(V-V',V')n(V-V')n(V')dV' \quad \text{(B15)}$$

$$D_{i,co} = n(V)\int_0^{+\infty} a(V,V')n(V')dV' \quad \text{(B16)}$$

$$B_{i,br} = \int_V^{+\infty} m(V')b(V')p(V,V')n(V')dV' \quad \text{(B17)}$$

$$D_{i,br} = b(V)n(V) \quad \text{(B18)}$$

where $a(V-V',V')$ denotes the coalescence rate between bubble size $V-V'$ and V', $n(V')$ represents the bubble density of bubble size V', $m(V')$ is the number of daughter bubble generated by the breakup of the bubble with size V', $b(V')$ is the breakup rate of bubble size V', and $p(V,V')$ is the probability density function of the bubble with size V due to the breakup of the bubble with size V'.

Appendix C

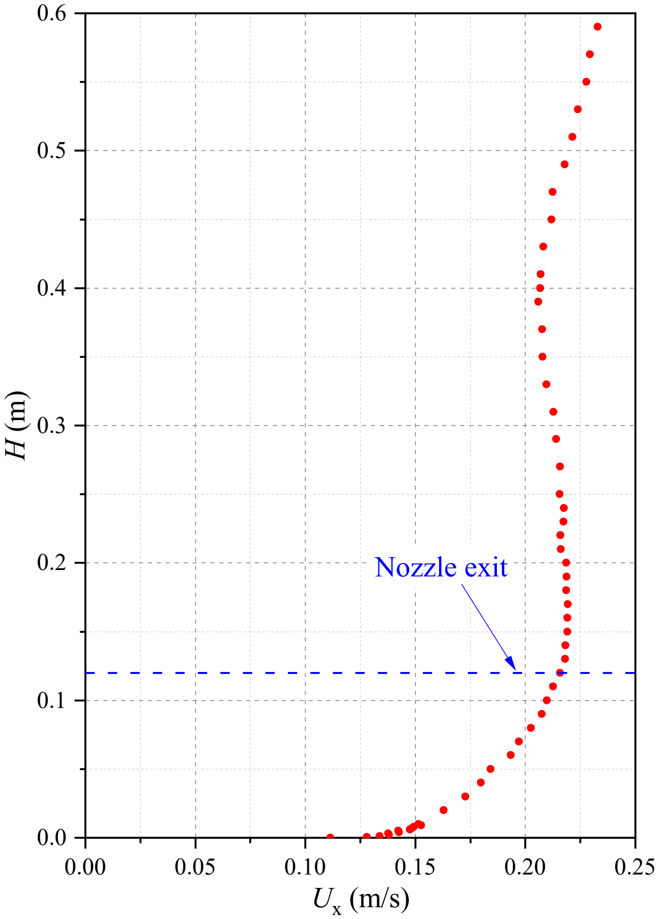

Figure 5-C1. Distribution of mean longitudinal water velocity U_x along the water depth H at 0.25 m upstream from the nozzle.

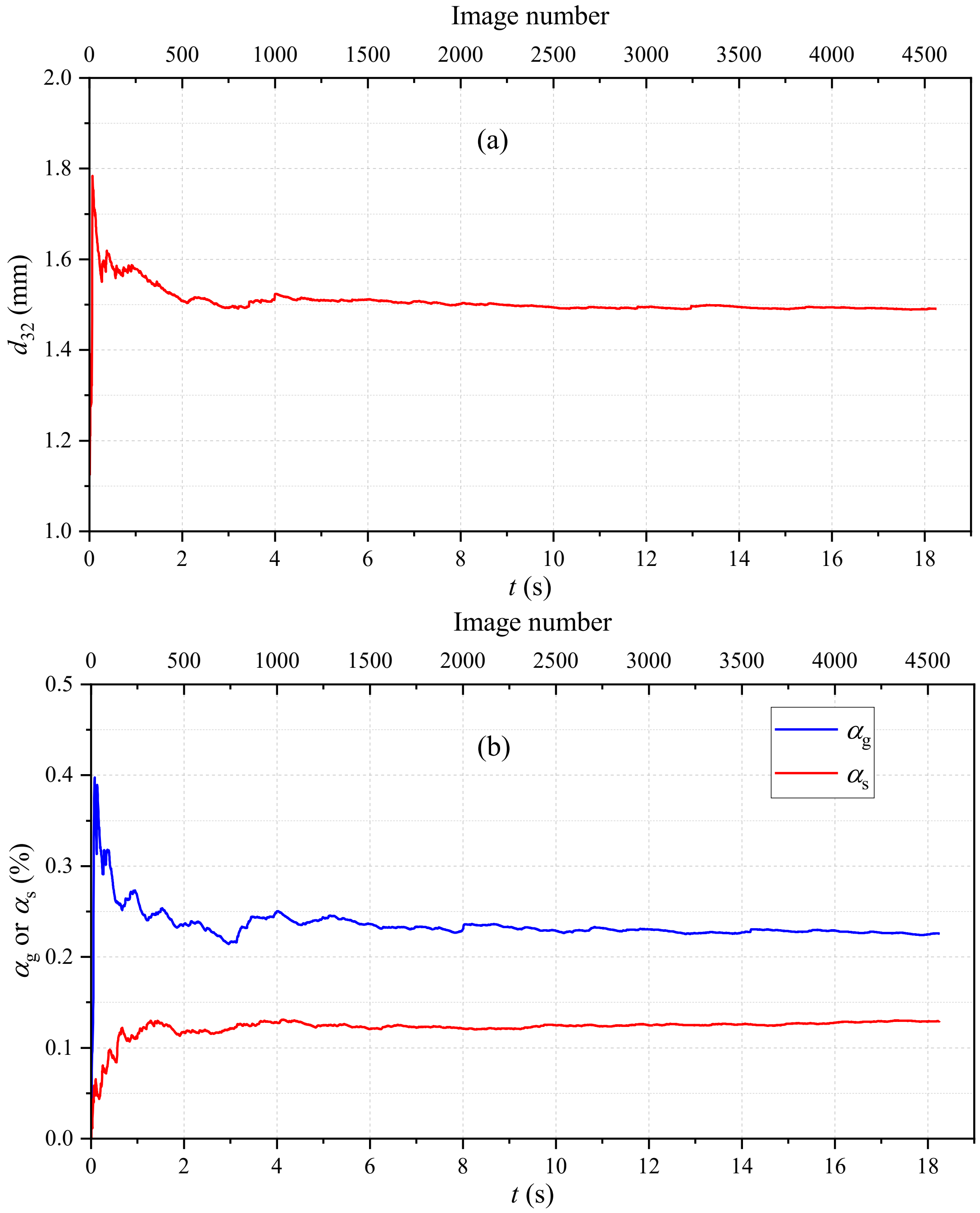

Figure 5-C2. An example of the variations of measured parameters with time or image number: (a) Sauter mean diameter d_{32}; and (b) gas void fraction α_g or sand concentration α_s. Experiment Scenario: Expt. C-24-0.4; and measurement location: 18d from the nozzle exit along the gas-phase centerline. A total of 4,565 images were analyzed by selecting every other image from the total of 9,130 images, with an interval of 0.004 s.

Appendix D

The DOF in this study can be calculated from the near distance of acceptable sharpness D_n and far distance of acceptable sharpness D_f (Wang et al., 2021c):

$$\text{DOF} = D_f - D_n \tag{5-D1}$$

$$D_f = \frac{L(H-f)}{H-L} \tag{5-D2}$$

$$D_n = \frac{L(H-f)}{H+L-2f} \tag{5-D3}$$

where L is the working distance 640 mm, f is the lens focal length 60 mm, and H is the hyperfocal distance expressed as:

$$H = \frac{f^2}{Nc} + f \tag{5-D4}$$

where N is the aperture f-number 2.8, and c is the circle of confusion of 0.035 mm which is calculated by $f/1720$ (Kodak, 1972).

From the above equations, the DOF is calculated as 20 mm in this study.

Appendix E

```
macro "Separate solid and bubbles"
{
    for (n=1; n<=nSlices; n++) {
// Step 1 :Detect solids
setSlice(n);
selectWindow("2");
setBackgroundColor(0,0,0);
setOption("BlackBackground",true);
run("Invert", "slice");
setThreshold(0, 135);
run("Make Binary", "slice");
setOption("BlackBackground", true);
run("Convert to Mask", "slice");
run("Analyze Particles...", "size=10-infinity circularity=0.60-1.00 exclude clear add slice");
roiManager("Show All without labels");
b=roiManager("count");
roiManager("select",Array.getSequence(b));
roiManager("Combine");
roiManager("Add");
roiManager("Delete");
roiManager("Select",0);
setBackgroundColor(0, 0,0);
run("Clear Outside", "slice");
roiManager("Show None");
run("Select None");
// Step 2 :Image with solids
selectWindow("2");
run("Create Selection");
selectWindow("1");
setSlice(n);
run("Restore Selection");
run("Enlarge...", "enlarge=1");
setBackgroundColor(255,255,255);
run("Clear Outside", "slice");
run("Select None");
//Step 3:  Image with bubbles
selectWindow("0");
setSlice(n);
run("Restore Selection");
run("Enlarge...", "enlarge=1");
setForegroundColor(255, 255, 255);
run("Fill", "slice");
selectWindow("2");
run("Create Selection");
run("Select None");
}}
```

Appendix F

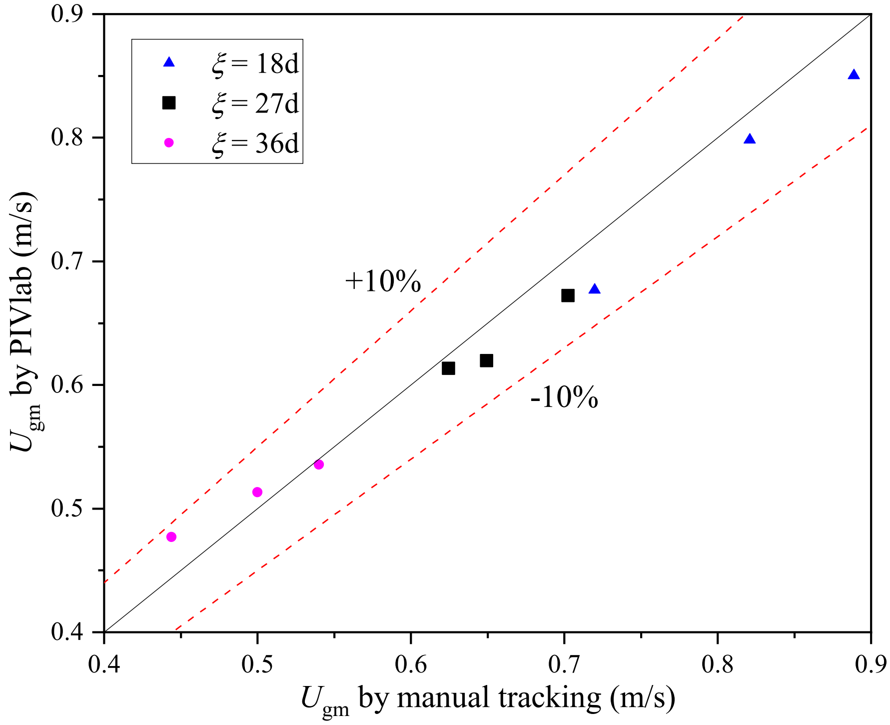

Figure 6-F1. Comparison of mean gas velocity U_{gm} measured by PIVlab and manual tracking in ImageJ.

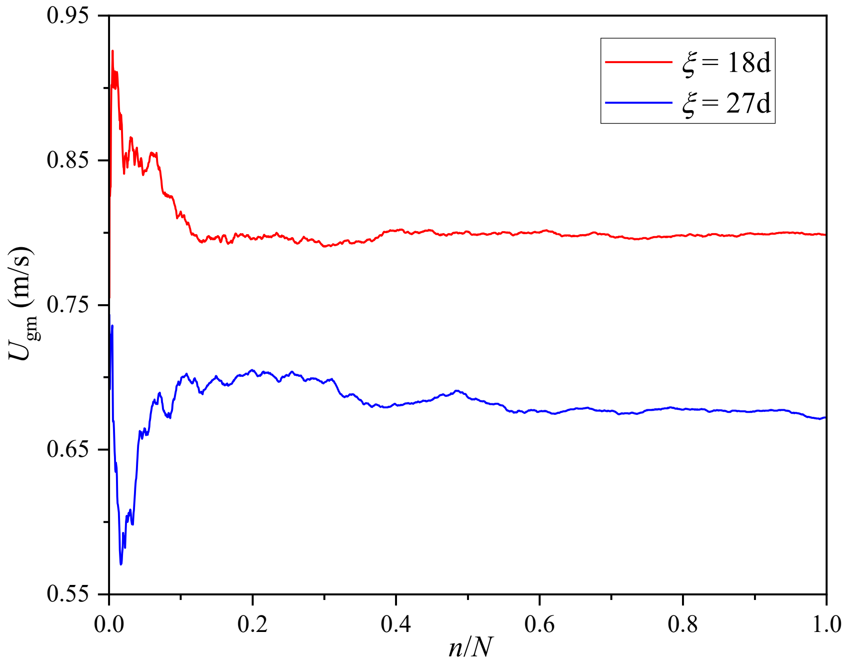

Figure 6-F2. An example of the statistical convergence of mean gas velocity at the centerline of ξ = 18d and 27d

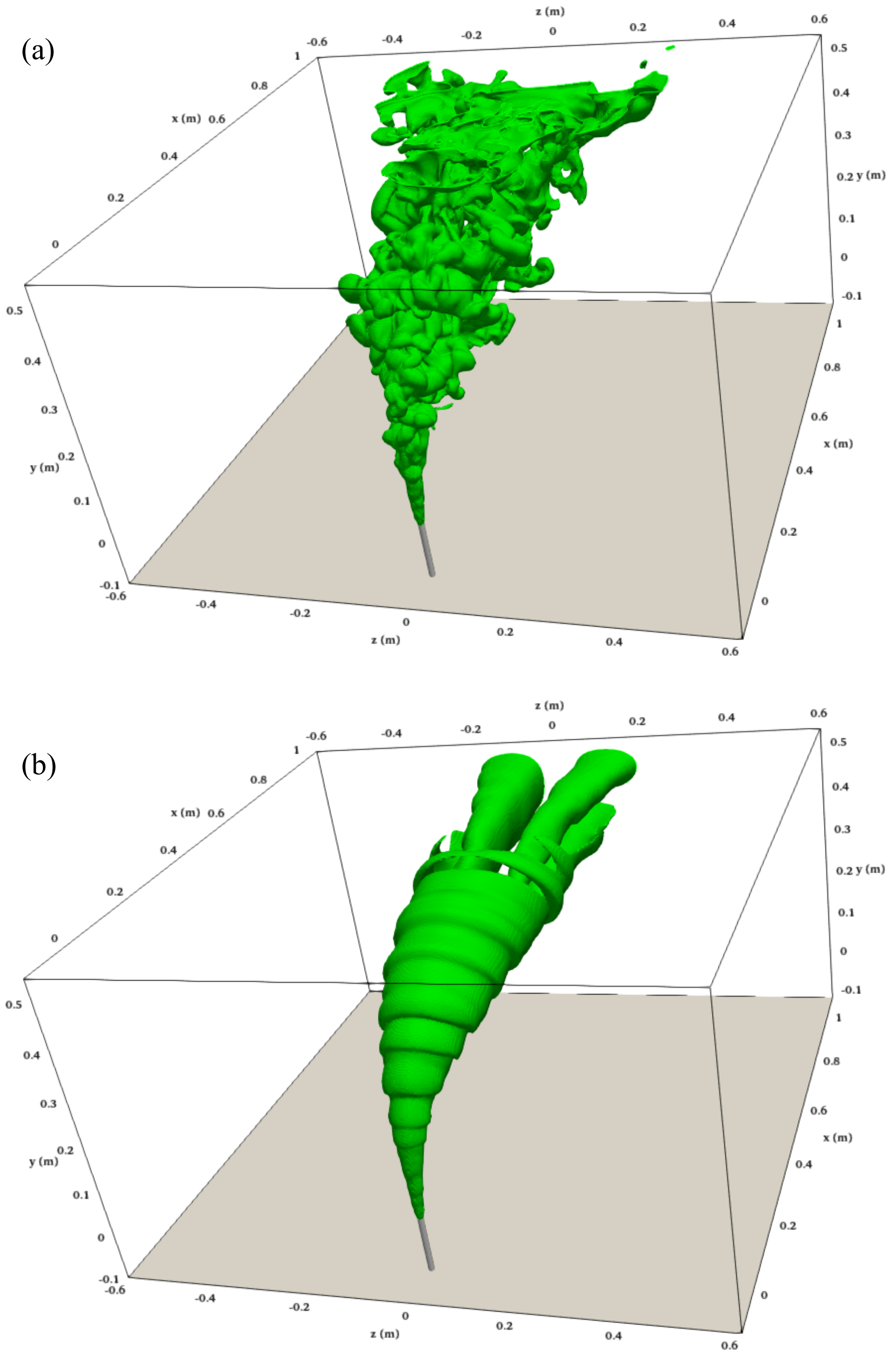

Figure 6-F3. Instantaneous flow structures of the liquid-phase at *t* = 15 s using Grid 3 with the (a) LES model and (b) mixture *k*-*ε* model. The iso-surface is denoted by 3% of the initial scalar concentrations.